A Study of Anisotropy of Magnetic Susceptibility's Effectiveness in Understanding Palaeoflow Systematics in Shale Basins

Matthew W. Galvin

2017

A dissertation submitted to Lancaster University for the degree of Master of Science by Research

Abstract

Understanding sedimentary transport mechanisms in shale-prone basins can be difficult, but anisotropy of magnetic susceptibility (AMS) has the sensitivity and ease of use to be widely applicable. Three distinct shale basins were selected, the turbidite Ainsa Basin, the shelf-edge of the Welsh Borderlands and the hemiplegic Marcellus Shales within the Appalachian Basin. These were chosen to assess the strengths and limitation of AMS as a palaeoflow indicator, focusing mainly on the Ainsa Basin as it has a well characterised palaeoflow and geographically confined depositional model that spans a very short period. This project explored the viability of using Baas et al., (2007) description of the petrofabric's AMS as a means to establish delivery mechanism. The Ainsa System showed two modes of AMS, one that was aligned with the flow direction and a transverse fabric normal to flow direction.

Each site was examined for its minerology; hysteresis tests were performed to observe if the source of magnetic susceptibility was from ferrimagnetic or paramagnetic minerals and to infer if the AMS reflected a grain or crystalline fabric. In the Ainsa case study, the samples had a greater percentage of ferrimagnetic contribution so isothermal remanent magnetism (IRM) and anhysteretic remanent magnetisation (ARM) acquisition was used to determine the ferrimagnetic minerology. The sites were examined for the tectonic impact on the AMS which was largely minimal.

Declaration

I declare that this dissertation is my own work and that is has not previously been submitted for the award of a higher degree at any university.

Acknowledgements

Firstly, I would like to thank the staff at Lancaster University, particularly Mark Hounslow and Vassil Karloukovski, for the help and guidance they provided me during this project. I would like to offer a special thank you to my supervisor Mark Hounslow for allowing me to undertake this study and helping me see it through to the end with his patient assistance.

Secondly, I would like to thank my other tutor Ken Ratcliffe, also Emma Davies and Luke Morgan from Chemostrat Ltd. for their assistance in initiating the project and providing samples and advice during the project.

Thirdly, I would like to thank Andy Biggin and Elliot Hurst from Liverpool University's geomagnetism department for allowing me access to their facilities.

Finally, I am grateful towards my fiancé Eithne and my family who with were very supportive, making the whole project possible.

Contents

List of Figures and Tables

Figures

Tables

1. Sedimentary Basins

Sedimentary basins are by defined as low areas in the Earth's crust, generated by tectonics, which allow the accumulation of sediments (Southard, 2007). Sedimentary basins occur in a diverse range of geological setting such as a within a well confined canyon setting or can be deposited as part of a large gentle uniform slope. The main implicit concept which links sedimentary basins is that they both share prolonged crustal subsidence and accumulation that allow their formation (Southard, 2007).

Sedimentary basins are important for oil and gas exploration as they provide potential reservoirs; therefore it is important to reconstruct the history of the sedimentary basins in order to have a greater chance of successfully describing and predicting reservoir development (Johnson & Stewart, 1985). Studies of basin palaeocurrents are also important they can be used to determine basin-fill history, and to establish the sediment sources, types of facies, and depositional tracts (Johnson & Stewart, 1985). Palaeoflow systematics within marine basins vary depending on the depositional mechanism.

An example of an oil-bearing basin is a hemipelagic basin which is dominated by regular suspension-related deposition of fine sediments (Baas et al., 2007), which contrast with high energy, unidirectional currents of turbidite basins (So et al., 2013). Three different types of depositional basins have been examined in detail:

1.1 Epicontinental Marine Shale Basins

Epicontinental shale basins are important as these are sometimes organic rich (black shales) and potentially provide a source rock for oil and gas (Fleet et al., 1987). Black shales can form at the centre of a bathymetric basin, where the greatest thickness of sediments typically accumulate (Wignall, 1991; Fig. 1.1). Organic rich black shales are created by organic matter being deposited via suspension, falling through the water column, and depositing in the anoxic centre of the basin (Lash & Blood, 2014). The anoxic conditions can be caused by thermal stratification of the water column and the oxygen demand outstripping the supply (Wignall, 1991).

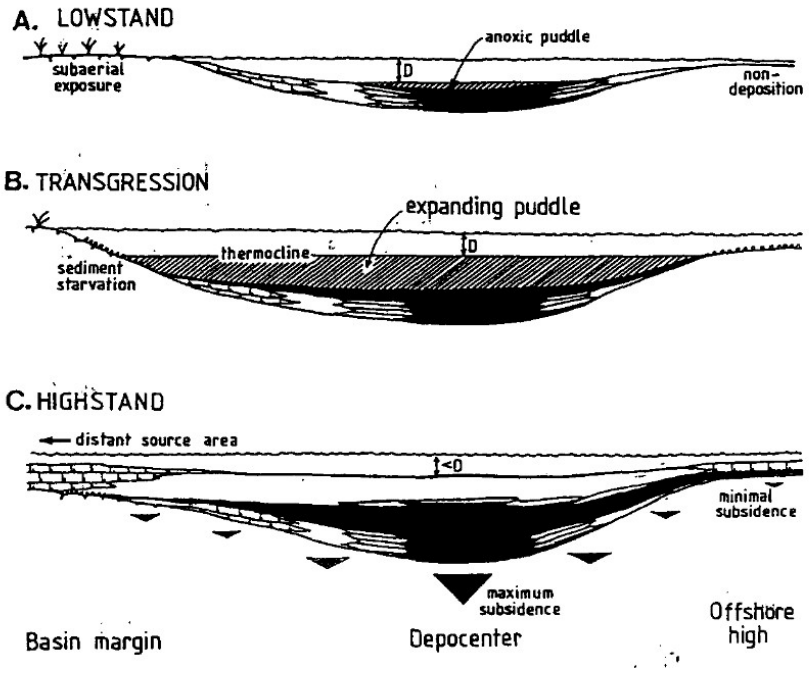

Figure 1.1. A schematic of the deposition of black shales in a bathymetric basin. In this model point D represents the critical depth at which the thermocline is developed. A) Lowstand conditions, this period sees the least deposition, with shales only occurring in the depocenter. B) Transgression conditions see an expansion in deposition of black shales owing to increasing sea levels, sediment starvation and subsidence. C) Highstand conditions, sea level has reached maximum extent and sediment influx causes shallowing of the water column leading to deposition of limestones near the edges of the basin (Wignall, 1991).

Fleet et al., (1986) describe similar models for deposition of the Jurassic Kimmeridge Clay:

i) Coarse, organic detritus input from large amounts of vegetation into bathymetric basins or deltas. In humid climates these produce a gas-prone source rock. An example of this is the Jurassic clastic successions along the coast of Norway and Greenland (Fleet et al., 1987).

ii) A salinity-stratified basin model, where the basin is divided into oxygenated layers depending on salinity. For example, when fresh water runoff flows into a restricted basin and forms a low salinity cap as a result of density discrepancy. The mixing of oxygenated water is then kept near the top of the water column and in the base of the water column the supply of oxygen is outstripped, creating anoxic conditions (Wignall, 1991). Resulting source rocks are derived from aquatic organic matter sinking past the photic zone in hypersaline conditions to oxygen deficient bottom-water conditions (Fleet et al., 1987). A modern example is Lake Maracaibo in Venezuela (Fleet et al., 1987).

iii) Oxygen minimal settings model, this model is characterised by oxygen minimal zones (OMZ). OMZs are where the greatest rate of sinking biological detritus occurs owing to the limited oxygen content (Fleet et al., 1987). They are typically created in warmer climates where the warm saline, epicontinental seas evaporate and are then fed

by low oxygenated intermediate and deep oceans from a lower latitude (Fleet et al., 1987). These basins are heavily influenced by relative sea level changes where transgressions often lead to intensification of the OMZ causing their expansion. The Marcellus Shale in the Appalachian Basin is most similar to this model and is examined in Section 7 (Brown & Kenig, 2004).

1.2 Contourites

Contourites form well below the storm wave base in relatively deep water (>300 m) around the continental rise or in the lower continental slope (Rasmussen & Surlyk, 2012; Stow et al., 2002). Contourite currents are formed by deep sea thermohaline flows (the cooling and sinking of surface water), or are sometimes driven by major wind-driven circulation (Stow et al., 2002). These bottom currents tend to travel slowly at velocities 1-2 cm s^{-1}, but in more confined settings can deposit sediments from muddy to gravel facies (Stow et al., 2002). The accumulation rate of contourite depends upon on sediment supply and this in turn is dependent on several factors such as source area geology, climate and tectonics. Biogenic material supply is controlled by climate, water productivity, deep sea dissolution of shell and the impact of volcanic sources (Faugères et al., 1993).

An example of an ancient contourite deposit can be found on the Welsh borderlands. Mudrock facies were deposited in the Silurian by bottom currents, which were dominated by local topography on the upper continental slope (Soper & Woodcock, 1990). These will form the focus of one of my later studies.

Stow et al. (2002) described several different types of contourite drift deposits depending on the nature of the adjacent continental rise (Fig. 1.2 and Table 1.1).

i) Contourite sheet drifts

Sheet drifts form in very low-relief environments and are composed of layers of constant thickness that occur on a scale of 100 m's to 1000 km's (Stow et al., 2002). They represent basin plain fills and decrease in thickness around the margins. These abyssal sheet drifts are typically comprised of fine-grain sediments of silts and muds, biogenic-rich pelagic material or red clay. An example is the Gloria drift in the Argentine Basin in the south Atlantic (Stow et al., 2002).

ii) Elongated mounded drifts

They occur on the outer shelf or upper continental slope and are dominated by flows showing local topographic interactions, producing mounded and elongated deposits with length to width ratios of 2:1 to 10:1. They vary from 10 to 1000 km's in length and are up to 2 km in thickness with an average sedimentation rate of Ca.2-10 cm ka^{-1}. Their

size is determined by local topography, current width, current intensity and the Coriolis Force. The Coriolis Effect constrains water masses against continental slopes on the western margin of basins, thus causing the currents to become more restricted and intense, increasing their velocities to 10-20 cm s^{-1} (Stow et al., 2002). An example of an elongated mounded drifts are found east of New Zealand, where they occur on the outer shelf or upper slope. These types of deposit also appear on the abyssal plains, and are common throughout the North Atlantic (Stow et al., 2002).

iii) Channel-related drifts

These deposits are controlled by deep channels that constrain the bottom circulation. This increases the current velocities which leads to the erosion of the substrate and the deposition of sand and gravel. Examples include the Kane gap, in the Faroe-Shetland Channel (Stow et al., 2002)

iv) Others

Confined drifts are tectonically confined deposits that have rarely been recorded. Infill drifts are caused by infills of topographic depressions.

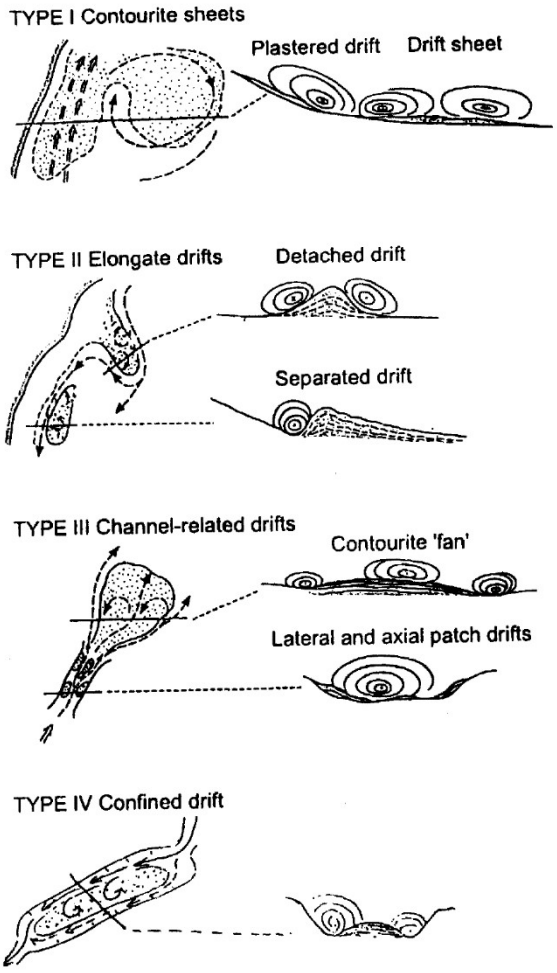

Figure 1.2 Schematic showing the four different types and setting of contourites

Type I Contourite sheet that form in low relief environments associated with basin fills.

Type II Elongate drifts of which deposition is dominated by locally topography, creating elongated mounded deposits.

Type III Channel-related sheet drifts, these are controlled by deep sea channels which tend to deposit sand-gravelly sediments owing to greater current velocity.

Type IV Confined drift, these are rare tectonically confined deposits.

(Stow et al., 2002).

Table 1.1. The different types of contourite describing their subdivisions, where they form, the sizes of that subdivision and examples of each (Stow et al., 2002).

Drift type	Subdivisions	Size	Examples
Contourite sheet drift	a) abyssal sheet	10^5–10^6 km ^{2}	a) Argentine basin; Gloria Drift
	b) slope (plastered sheet)	10^3–10^4 km^2	b) Gulf of Cadiz; Campos margin
	c) slope (patch) sheets	< 10^3 km^2	
Elongated mounded drift	a) detached drift	10^3–10^5 km^2	a) Eirek drift; Blake drift
	b) separated drift	10^3–10^4 km^2	b) Feni drift; Faro drift
Channel-related drift	a) patch-drift	10–10^3 km^2	a) NE Rockall trough
	b) contourite-fan	10^3–10^5 km^2	b) Vema Channel exit
Confined drift		10^3–10^5 km^2	Sumba drift; E Chatham rise
Modified drift – turbidite systems	a) extended turbidite bodies	10^3–10^4 km^2	a) Columbia levee S Brazil Basin; Hikurangi fandrift
	b) sculptured turbidite bodies	10^3–10^4 km^2	b) SE Weddell Sea
	c) intercalated turbidite-contourite bodies	can be very extensive	c) Hatteras rise

1.3 Turbidite Dominated Basins

Turbidites are well-studied ancient depositional systems, although they are difficult to observe in modern deposits owing to their transient nature (Hughes et al., 1995). Turbidite sequences can be on a huge scale, ranging from large turbidite systems such as the Moroccan turbidite system, which is up to 1500 km in width, to smaller individual turbidites that can be on a centimetre scale (Wynn & Stow, 2002).

Turbidite systems are typically created by sediments being transported off the continental shelf by density flows; these density flows travel via feeder channels and then deposit sediments as individual lobe or lobe system deposits in deeper basins. Deep-water turbidite systems can be classified into four categories, with A) being the most proximal to D) the most distal:

A) Canyon or feeder channels that are composed of a mix of poorly sorted coarse and fine clasts (Mulder, 2011); B) An upper fan, with an erosional channel and thick levees; C) A middle fan with smaller depositional channels and thin levees; and D) a lower fan with distal lobes (So et al., 2013). These turbidite deposits are often interbedded with hemipelagic mudstones, which have been deposited by suspension rather than density-flows and represent the background deposition during periods of non-turbidite flow (Bouma, 2000).

Sedimentologists have observed several recurring facies within turbidite deposits, termed Bouma cycles; each facies tend to overlie the one before it and generally fine-up from the base to the top of the cycle (Shanmugan, 1997). Bouma cycles have been divided into five generalised facies from Ta (the base) to Tb, Tc, Td and Te (the top of the cycle; Shanmugan, 1997; Table 1.2, Fig. 1.3).

Table 1.2. Describes the five main facies in a Bouma cycle, with an inferred interpretation of how they formed. Tc has been subdivided owing to differences in sedimentary structures. Modified from So et al., (2013)

Lithology	Thickness	Sedimentary Structure	Boundary and Geometry	Bouma (1962) Division	Inferred Depositional Process
Massive or normally graded sandstone	>30 cm, max. bed thickness of 10's m	Massive, amalgamation, load or flame structure, normal grading (top-only), sole mark, occasional rip-up mud clasts near scoured base	Bounded by flat top and erosive base, tabular bed geometry	T_a	Rapid settling from suspension of sandy low-density turbidity currents, powerful and turbulent flows (Mutti and Ricci Lucchi, 1972, 1975; Lowe, 1982; Kneller and Branney, 1995; Mutti et al., 1999)
Laminated sandstone	10–30 cm	Parallel, wavy or cross-lamination, rip-up mud clast, load structure, sole mark	Bounded by flat or gradational top and erosive base, tabular geometry with considerable lateral continuity	T_b	Rapid mass deposition or traction movement in low-density turbidity currents (Smith, 1971; Paola et al., 1989)
Normally graded silty fine-grained sandstone	<20 cm	Normal grading, alternated with mudstone facies	Bounded by sharp base, sheet-like geometry with good lateral continuity	T_c	Grain-by-grain deposition from suspension, low-density turbidity currents (Piper, 1978; Jipa and Kidd, 1974; Stow and Piper, 1984)
Silty fine-grained sandstone with climbing ripple	<30 cm	Convolute- or wavy-lamination, climbing ripple, flame structure	Bounded by lobate top and flat or irregular base, sheet-like geometry with considerable lateral continuity	T_c	Traction movement with fallout processes from waning turbidity currents (Jopling and Walker, 1968; Muder and Alexander, 2001; Zavala et al., 2011)
Laminated mudstone	30–100 cm	Horizontal or near-horizontal lamination, flame structure	Bounded by sharp top and gradational base, sheet-like geometry with good lateral continuity	T_d	Deposition from suspension during weak turbulent motion in low-density turbidity currents (Arthur et al., 1984; Hill, 1984; Stow & Dean, 1984)
Homogeneous mudstone	3–30 cm	Homogeneous, ball and pillow, flame structure	Bounded by sharp/lobate top and gradational base, sheet-like geometry with considerable lateral continuity	T_e	Hemipelagic settling with lateral transfer by deep-water currents or rapid deposition of floc from mud-rich turbidity currents(Pickering et al., 1986)

Bouma cycles are typically incomplete either because of the erosive nature of overlying high-density turbidites (Hughes et al., 1995), or the local absence of high flow conditions at the base.

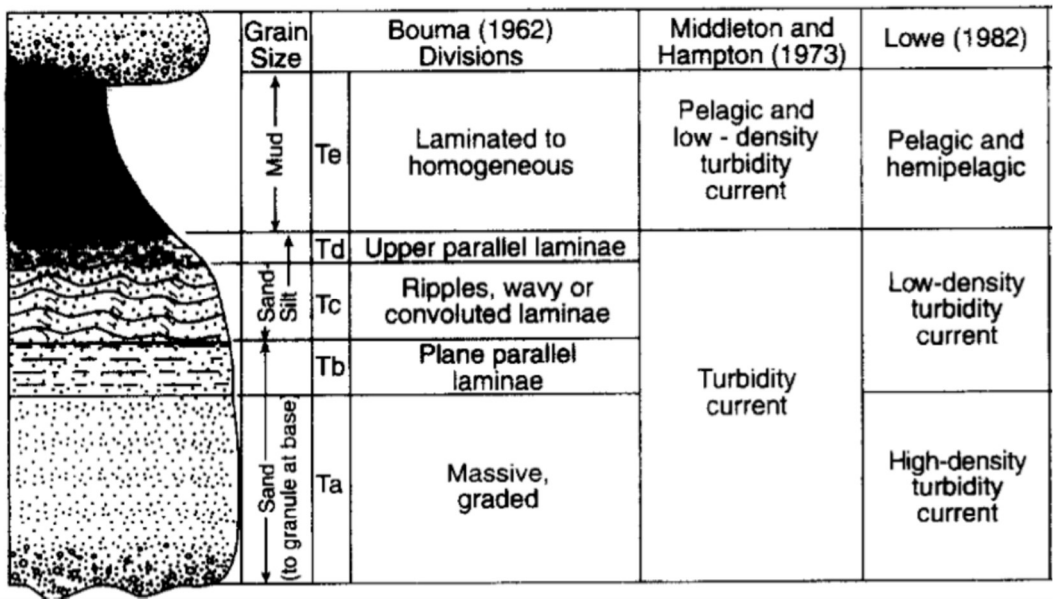

Figure 1.3. An ideal Bouma sequence, displaying a graphical log of the divisions of Ta, Tb, Tc, Td and Te and providing interpretation of how these sedimentary structures were formed. Modified from Shanmugan (1997).

An example of classic turbidite divisions is examined by So et al. (1997), they observed lateral changes of a late Paleozoic turbidite complex, Taean Formation, located in western Korea. They examined the facies and architecture of a lobe complex which they further divided into lobe systems and then further hierarchical subdivisions as lobe elements and beds (Fig. 1.4).

They established that the axes of the lobes were composed mainly of thick bedded Ta facies with thin Te beds (So et al., 2013). The lobe axis has been interpreted as the centre of the turbidity currents with the Ta facies representing the high flow-rate turbulent deposits, and the Te facies representing the background sedimentation from suspension (So et al., 2013). The lobe off-axis deposits overlie the lobe axis which are dominated by medium-grained sandstones (Tb facies) with some Ta and Te facies. The lobe off-axis is interpreted as forming near the main turbidity currents, but distant enough to allow parallel laminations within the sandstone to form (So et al., 2013). The lobe off axis is overlain by the lobe fringe or lobe distal fringe (Fig. 1.5).

The lobe fringe comprises the Ta, Tc, Td and Te facies and is dominated by mudstones with silty-sandstone beds. The lobe fringe is more laterally extensive, showing greater lateral continuity than the lobe axis and off-axis. The lobe distal fringe overlies the lobe fringe and is composed of facies Tc, Td and Te, and is therefore dominated by medium to thick mudstone successions with thin silty-sandstone beds. The lobe distal fringe is interpreted as low-energy, turbiditic deposits that represent the furthest reaches of turbidite sedimentation (Fig. 1.5).

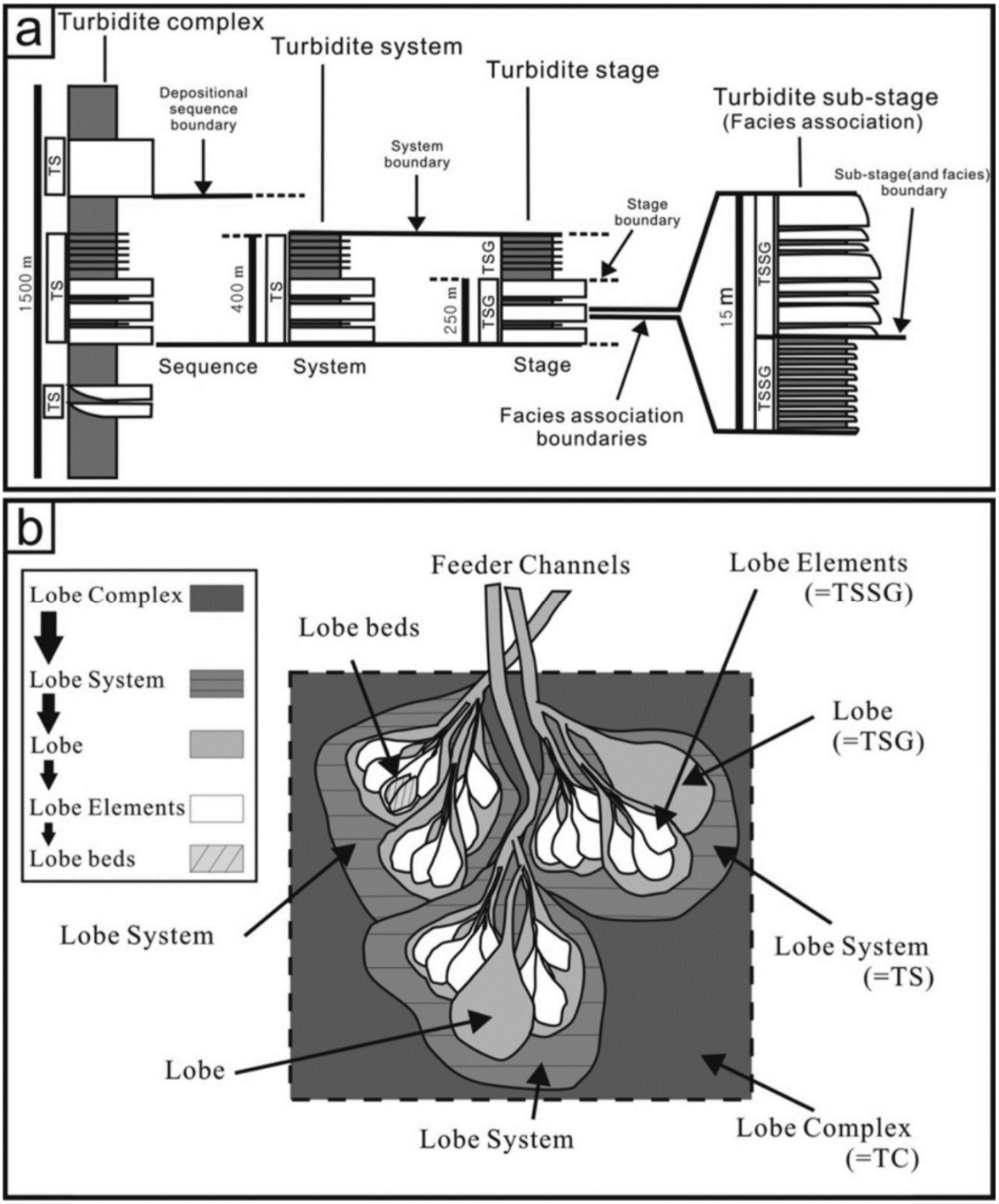

Figure 1.4. a) Shows 4 orders of turbidites within a turbidite complex (TC), 1st-order: turbidite system (TS), 2nd-order: turbidite stage (TSG), 3rd-order: turbidite facies association and component sub-stage (TSSG), 4th-order: turbidite bed, which show Bouma Cycles (So et al., 2013).

b) Displays how orders fit into the architectural hierarchy of each of the lobe deposits, showing the Feeder channels supplying sediment into the large lobe systems which are then divided into different lobe beds. The erosive nature of the turbidite is shown by previous lobes being truncated by younger deposits (So et al., 2013).

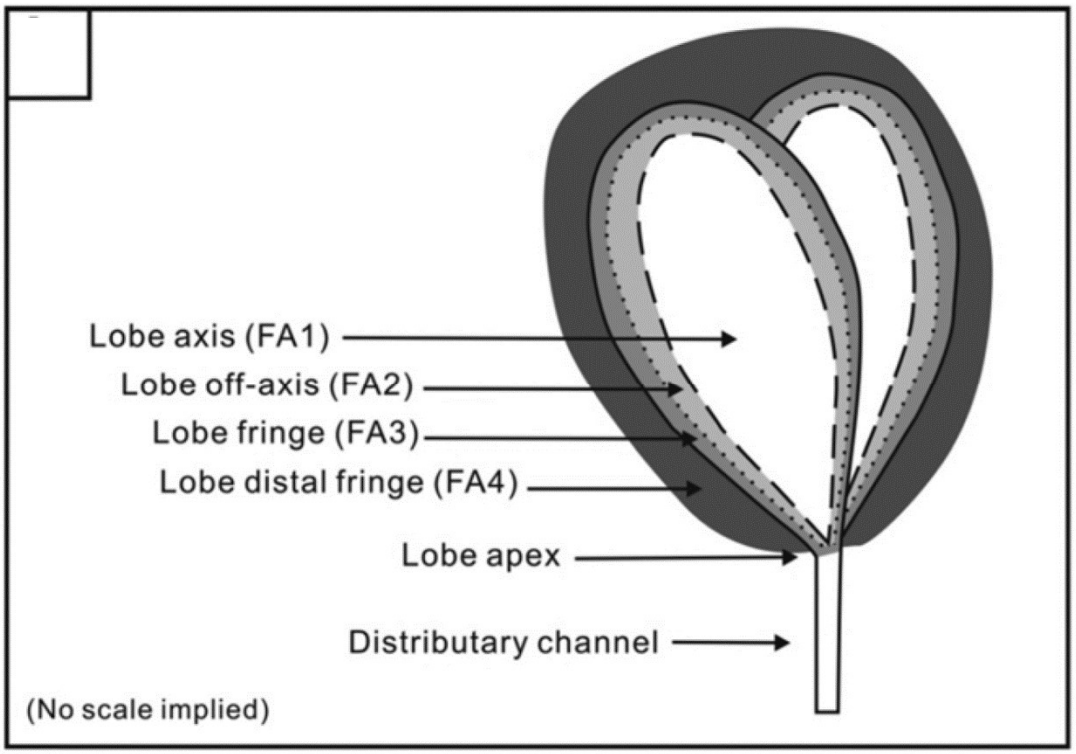

Figure 1.5. A plan view schematic of a lobe deposit. It shows the relations of the facies of the Lobe axis, off axis, fringe and distal fringe (So et al., 2013).

The sedimentation in the supplying canyon system is different from the rest of the turbidite basin and is typically represented by rock-fall or debris flow deposits (So et al., 2013). These are created by the mass movement of sediments caused by slope-failure at the base of the canyon cliffs (Mulder, 2011). The sediments are transported for short periods, leading to the deposition of poorly sorted clasts of various sizes (ranging from millimetres to hectometres) which are typically weakly cemented in a finer-grained matrix (Mulder, 2011). Short travel times cause little internal deformation and sometimes pre-existing bedding is preserved (Mulder, 2011). Example of debris flows are common in the Ainsa Basin (see Section 5).

1.4 Grain Fabrics

Non-spherical clasts deposited in sediments, orientate themselves differently depending on their method of transportation (Baas et al., 2007). There are three main fabric patterns:

1) The horizontal fabric: this is when the long axes of the grains are orientated parallel to the bedding plane, but the long axes do not show a preferred orientation within the bedding plane (Fig. 1.6; Baas et al., 2007). Grains showing this fabric are typical of settling from suspension in still water or in a very weak flow where the drag is insignificant to orientate the grains (Baas et al., 2007). This fabric could be common in sheltered shale basins such as the Jurassic Kimmeridge Shale basin and may be important in the hemipelagic deposits between turbidite beds (Wignalll & Newton, 2001; Shanmugan, 1997).

2) Flow-aligned fabrics: grain long axes are orientated parallel to the main flow direction (Fig. 1.6; Baas et al., 2007). The long axis of the grains may be imbricated and if this is the case, then the grains normally dip upstream (Baas et al., 2007). Extended flows, such as laminar contourite currents or some turbidite flows, have larger shear velocities and are able to lift and transport sediment particles. After such transportation the grains are then deposited so their long axis is aligned approximately parallel with the flow direction, so that they have minimal drag (Mulder, 2011) and are so imbricated. Grains are

orientated owing to their interactions with other grains, as shear forces keep them in stable, imbricated positions (Baas et al., 2007). This fabric is the most common and is normally seen in turbidites in the Tb, Tc, Td facies and also in contourites and epicontinental shale basins, which show dominant unidirectional current flows (Shanmugan, 1997; Stow et al., 2002).

3) Flow-transverse fabrics: grain long-axes are aligned perpendicular to the flow direction (in the bedding plane) and the intermediate grain axis dips upstream (Fig. 1.6; Baas et al., 2007). Flow-transverse fabrics are produced in high velocity flows such as the Ta facies in turbidites, as the grains experience a greater rate of rotation owing to more grain interaction (Hughes et al., 1995). The greater shear forces cause the grains to roll along the bed, causing some grains to orientate so that they are perpendicular to the main flow direction (Hughes et al., 1995). Debris flows can show weakly flow-aligned fabrics or they are isotropic owing to the higher rate of granular collisions and short travel time of the grains, not allowing them to fully re-orientate or imbricate (Baas et al., 2007).

Oblique fabrics are produced when the grain long-axes are parallel to both the imbrication and to oblique orientation of the framework grains (Baas et al., 2007). These fabrics are believed to be caused by several factors including spatial changes in current direction, incomplete reorientation of the flow-transverse fabric, changes in bed roughness or post-depositional modification such as bioturbation and soft-sediment

deformation (Baas et al., 2007). The latter works by partiality re-orientating the deposited grains' long axes, therefore these fabrics cannot be trusted to accurately establish flow direction (Baas et al., 2007).

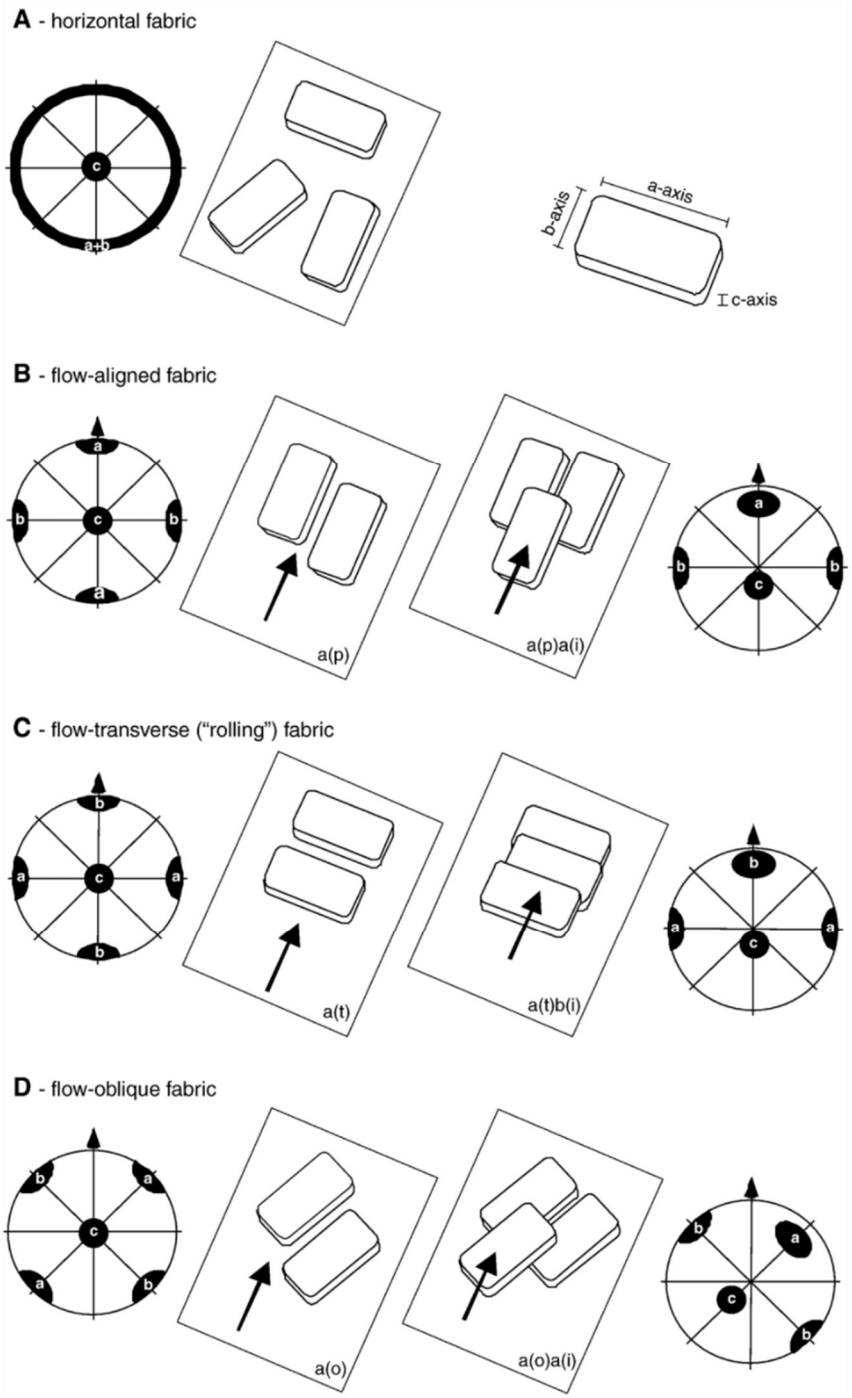

Figure 1.6. The main grain fabric types, as schematic drawings of the orientation of elongated grains (middle) and by the orientation of the three principal orthogonal axes in upper hemisphere stereograms (left shows non-imbricated samples, right shows imbricated samples). Where a=long grain axis; b=grain axis of intermediate length; c=short grain axis; p=parallel; t=transverse; o=oblique; i=imbricated. Black arrows in drawings and stereograms denote flow direction. Horizontal fabrics cannot be imbricated by definition (Baas et al., 2007).

1.5 Establishing Palaeoflow

Understanding and determining the orientation of palaeoflow is important for oil and gas exploration. Examining palaeoflow allows the reconstruction of sediment geometries in ancient basins which is important for establishing and describing potential reservoirs for oil and gas (Johnson & Stewart, 1985). Several methods have been used to establish palaeoflow, ranging from: i) macroscopic methods such cross-stratification directions and fossil orientations (Schieber & Ellwood, 1988; Duke et al., 1992); ii) flow reconstruction using sediment tracing methods such as examining dispersal of zircon grains (Cawood & Nemchin, 2001); iii) establishing flow from grain fabrics using laboratory methods such as petrographic examination, X-ray goniometry (Table 1.3; Baas et al., 2007; Van der Pluijm et al., 1994) and magnetic methods.

i) Macroscopic

Macroscopic field-based methods have been most widely used to determine paleoflow direction in marine basins. Primary sedimentary structures such as cross-lamination or current ripple trends can be used to indicate the paleogeography of the basin (Schieber & Ellwood, 1988). Structures such as hummocky cross-stratification in sandstone beds commonly reflect storm-generated flows; the modal crest is often orientated parallel to the shoreline and the direction of palaeoflow is normal to this (Duke et al., 1992). The cross-bedding angle and size of

the ripples can also be used to determine the speed of the current or oscillatory motion produced by waves (Fig. 1.7; Duke et al., 1992).

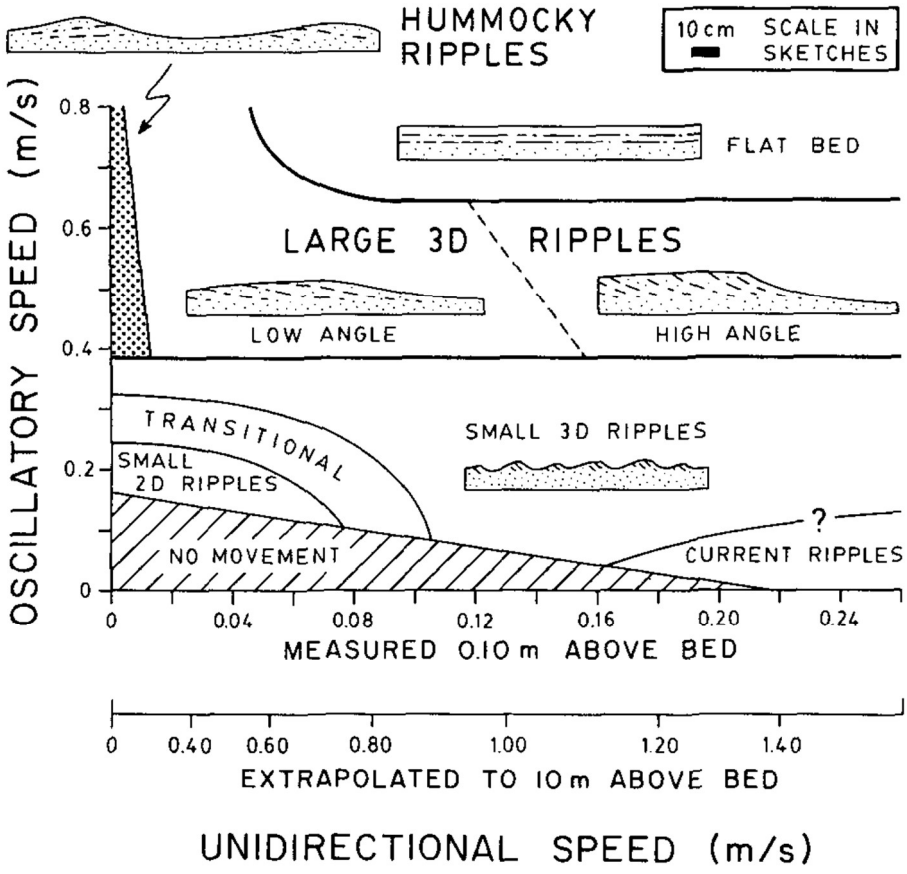

Figure 1.7. Stability fields for different types of ripples that are stable in certain environments. Current ripples are only stable when there is a dominant unidirectional current, whereas the hummocky ripples indicate more oscillatory conditions suggesting tides and storm events (Duke et al., 1991)

The orientation of sole marks (mainly tool marks) has been widely used in turbidite basins to establish palaeoflow (Duke, 1990). These are created as the unidirectional current drags and bounces detritus material along the seabed, with the detritus producing drag and tool-marks on the underlying bed (Duke, 1990). Oriented erosional flute marks are also commonly produced.

Fossil orientation and elongated larger clasts can also be used to determine palaeoflow direction, elongated fossils, such as belemnites or graptolites, will be aligned to lie parallel to unidirectional currents (Schieber & Ellwood, 1988; Underwood, 1994).

ii) Sediment tracing

Tracing sediment transport geographically across a basin can be used to establish palaeoflows (Fedo et al., 2003). Cawood & Nemchin (2001) used detrital zircon crystals to map the basin-wide distribution of sediments, as the U-Pb isotopes of the zircons are used to date the source grains and so find the zircon's initial source region. Similar basin-wide tracing methods can be applied to other detrital materials such as heavy mineral assemblages. Their compositions are determined by the composition of the parent rock, hydraulic and diagenetic conditions (Morton & Hallsworth, 1999). Thus, if these assemblages share similar hydraulic and diagenetic conditions then their composition can be used to establish the location of the source (Morton & Hallsworth, 1999). Fossilised microfauna or microflora can also restrict the provenance of sediments to a certain source, from which transport pathways can be established. This method has been used to establish pathways from the Old World Realm into the Appalachian Basin (DeSantis & Brett, 2011).

iii) Grain fabric methods

Grain based techniques involve examining the grain fabric to establish flow direction (Borradaile, 2001). These fabrics can be observed by petrographic examination which requires manually examining grain preferred orientation through suitably oriented thin sections (Baas et al., 2007). This is performed using a microscope and is a relatively simple method of measuring grain orientation, where post-depositional alterations to the sample such as fracturing can also be assessed immediately (Baas et al., 2007). However thin section methods are only 2D and are often limited to sand sized grains only (Baas et al., 2007), although image analysis methods can work with finer-grained materials.

In shale basins, concretion orientation can be used to estimate flow direction, this method assumes the concretion orientation is a response to the grain-fabric anisotropy in the host sediment. This method also assumes the fabric anisotropy represents depositing currents rather than fractures within the shale (Schieber & Ellwood, 1988). Anisotropy of magnetic susceptibility (AMS), and similar magnetic methods, can be also be used to establish the fabric of the sediment grains and is covered in more detail in Section 3 (Borradaile, 2001).

X-ray texture goniometry can be used to determine rock textures and the preferred crystallographic orientation of specific minerals (Van der Pluijm et al., 1994). This can be performed on sediments, using grains up to 10's of microns in size (Van der Pluijm et al., 1994). X-rays are

emitted onto the sample which are then diffracted, the goniometer records both the direction and intensity of diffracted X-rays (using a specific diffraction lattice) and position of the sample as it is rotated by the goniometer (Fig. 1.8; Battey & Pring, 1997). The resulting data can measure the preferred orientation of fabric-forming phyllosilicates, chlorite and mica which can represent the depositing current (Lüneburg et al., 1999).

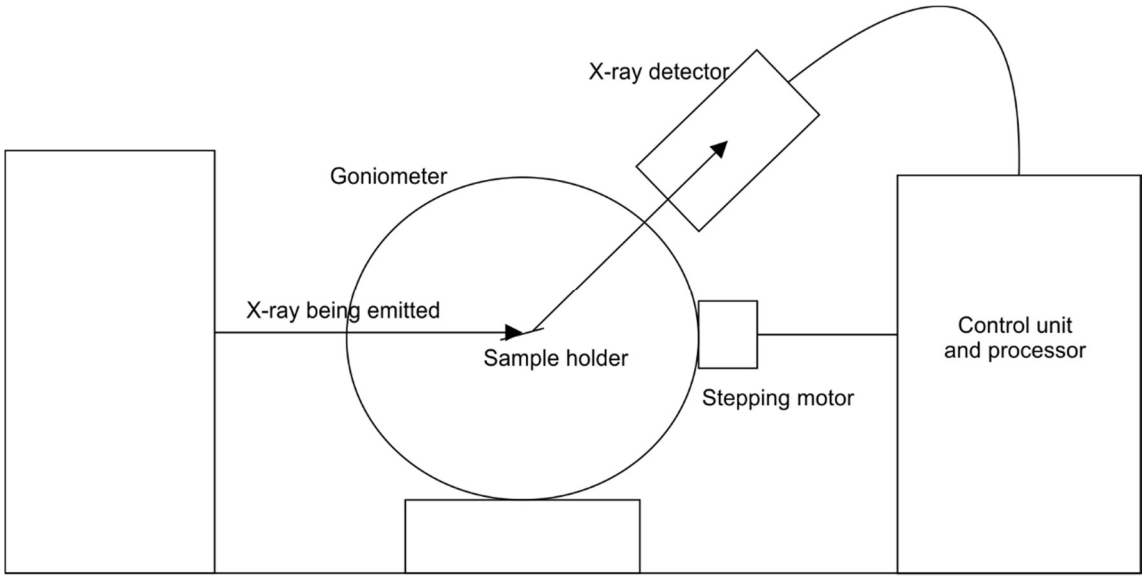

Figure 1.8. Schematic showing the typical setup for X-ray goniometry (from Battey & Pring, 1997).

High-resolution X-ray computed tomography can also be used to produce a 3-dimensional grain-shape (Ketcham, 2005). An X-ray fan beam is directed at a hand sample through all orientations in a plane; the decrease in X-ray intensity caused by going through the rock is then measured by a linear array of detectors (Fig. 1.9; Ketcham, 2005). The resulting data is reconstructed to create a cross sectional image across the plane, this process can be done several times to produce a

3-dimensional ‘texture and absorption’ ellipsoid (Ketcham, 2005). This 3-dimensional ellipsoid can be used to determine grain-shape and anisotropy of different minerals within the sample. These minerals can separated in the initial stages using software.

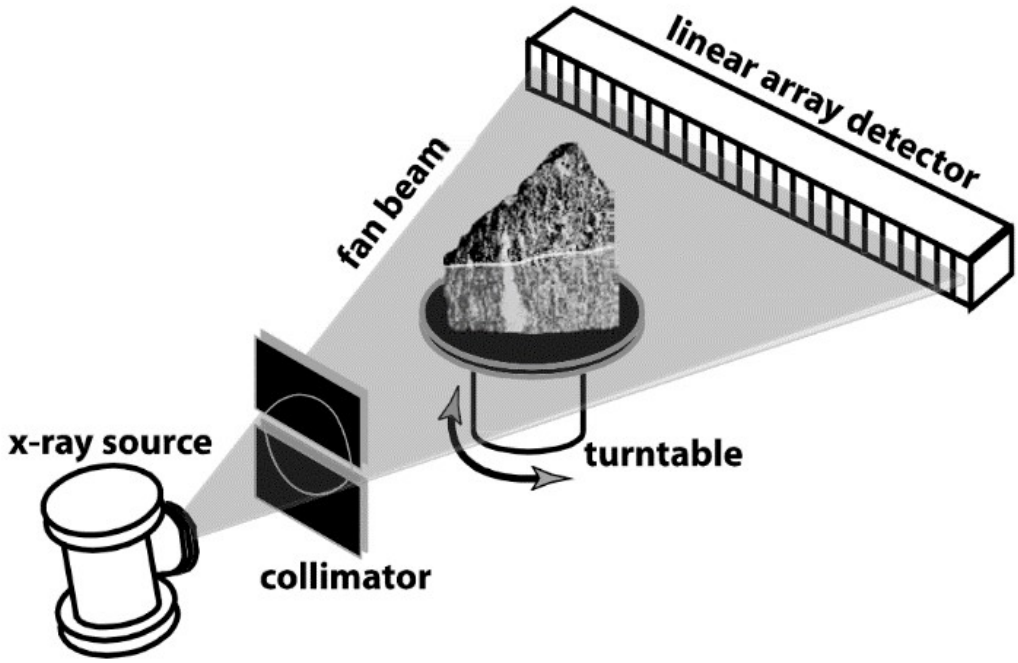

Figure 1.9. A schematic of an X-ray CT. A collimated planar X-ray fan beam is directed at a rotating sample and is recorded by the linear array detector. The data collected can be used to construct a tomographic sample cross-section along a slice plane (Ketcham, 2005).

Sonic methods use the principle that the preferred orientation of the grains will affect the shape parameter of the seismic waves (Tilmann & Bennett, 1973), and it is the degree of elastic anisotropy which is recorded (Hirt et al., 1995). Thus the quickest sonic transmission will be parallel to the preferred long axis grain fabric in sedimentary rocks and overall will reflect the grain shape anisotropy (Hirt et al., 1995). Engelder (1979) used X-ray diffraction goniometry and sonic methods to analyse residual strain within Grimsby sandstone in the Appalachian foreland fold and thrust belt.

Table 1.3. Summary table describing each macroscopic, sediment tracing and grain fabric method for determining palaeoflow in sediments. Anisotropy of magnetic susceptibility will be described in greater detail in Section 3.

Types of methods	methods	Description
Macroscopic Methods	Sedimentary structures	Using the orientation of current ripples, hummocky cross-stratification and flat-laminated beds in siltstone or sandstone facies to establish flow direction, a method widely used by sedimentologists (Schieber & Ellwood, 1988; Duke et al., 1992).
	Tool marks	Created by turbidity flows, as large detrital material scours the sea bed as it is dragged along the substrate. The imprint left by scouring and the tools is parallel to flow direction. This is found in turbidite basins (Duke, 1990).
	Fossil orientation	Using fossil orientation of elongated fossils which align parallel to flow direction. These are found in shale and sandstones. Rarely used for basin-wide flow mechanisms owing to sparse fossil occurrence (Schieber & Ellwood, 1988; Underwood, 1994).
Sediment Tracing Methods	Heavy mineral distributions	Examines the distribution of heavy mineral grains through a basin, e.g. using radiogenic isotopes to establish the zircon age and so infer their source and transfer directions (Fedo et al., 2003; Cawood & Nemchin, 2001).
	Fossil distribution	Examines the distribution of fossils that are restricted to certain source and establish the pathways throughout the basin (DeSantis & Brett, 2011)
Grain fabric Methods	Petrographic methods	Thin sections to examine the anisotropy of the grain long-axes of siltstones and sandstones facies (Baas et al., 2007).
	X-ray texture goniometry	Diffracted X-rays from a specific lattice plane within a specific mineral are recorded as a function of goniometer direction and sample rotation. Crystallographic preferred orientation is determined with the method (Battey & Pring, 1997).
	High-resolution X-rays computed tomography	An X-ray beam is directed at a hand sample through all orientations in a sample rotation plane. The relative changes in X-ray intensity reconstructs a 3-dimenisional model of the grain absorption fabric (Ketcham, 2005).
	Sonic anisotropy	Sonic waves record the degree of elastic anisotropy. Grain fabrics with preferred orientations will have fastest anisotropies in that preferred direction (Hirt et al., 1995).
	Anisotropy of magnetic susceptibility (AMS)	AMS measures the directional variations of magnetic susceptibility which can be expressed as a magnetic ellipsoid. This ellipsoid represents the magnetic grain and can be used to determine the grain's anisotropy (Baas et al., 2007)

2. The Earth's Geomagnetic Field and Magnetostratigraphy

The Earth's geomagnetic field is caused by the motion of the outer core, which generates electrical currents to form a self-exciting dynamo (Butler, 1992).

2.1 Basic Magnetic Concepts and the Earth's Geomagnetic Field

A magnetic moment (*M*) is generated by magnetic field (*H*). When examining the Earth's geomagnetic field, a scalar magnetic potential (*V)* of magnetic dipole is examined (Tauxe, 2005):

$$V = \frac{M\ cos\theta}{r^2}$$

Equation 2.1. A gradient of scalar magnetic potential (*V*) is a function of the radial distance (*r*) and the angle away from the pole (*θ*) (Tauxe, 2005).

Using this equation, the magnetic field vector on the surface of the earth can be broken down into several trigonomic components (Fig. 2.1). The total magnetic field vector (*H*) is composed into a vertical component of $H_v = H \sin I$ and horizontal component $H_h = H \cos I$. Inclination (*I*) is the angle (dip) between the horizontal and *H*. *The inclination, I,* will increase with latitude which ranges from 0° at the magnetic equator and peaking at the magnetic poles (+90 at the magnetic North Pole, -90 at the magnetic South Pole). Declination (*D*) is the angle between the horizontal component of *H* and geographic north (Fig. 2.1; Butler, 2004).

The Earth's magnetic field can be modelled using two components 1) a Geocentric Axial Dipole (GAD) and 2) secular variation (Butler, 1992).

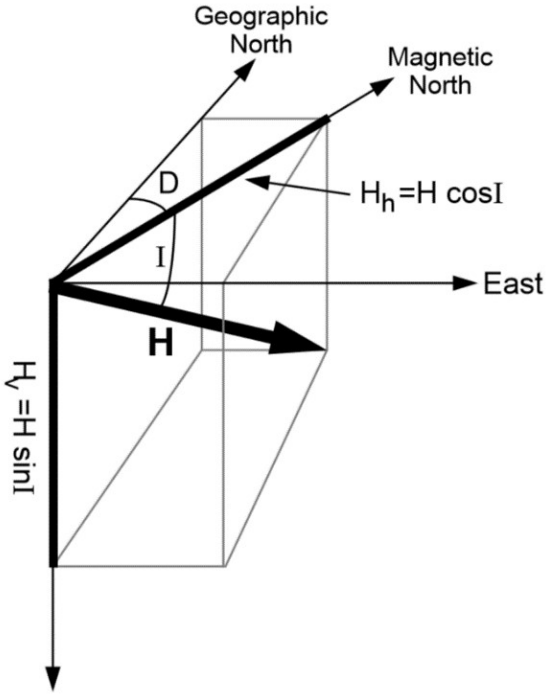

Figure 2.1. Schematic of the different components that compose of the Earth's total magnetic field. Total magnetic field vector (H), Declination (D), Inclination (I) (Butler, 1992).

2.1.2 The GAD Model

The GAD model uses the concept that the Earth's geomagnetic field is a single dipole at the centre of the Earth, similar to a bar magnet (Figs. 2.2, 2.3; Butler, 2004; Langereis et al., 2010). This model uses the equation 2.1 and can be used to derive *H* and its horizontal and vertical components. Thus the geographic latitude, λ, can be determined by "the dipole equation":

$$\tan I = 2 \tan \lambda$$

Equation 2.2. λ is the geographic latitude. The magnetic field strength increase by a factor of two from the equator to the magnetic poles (Butler, 1992).

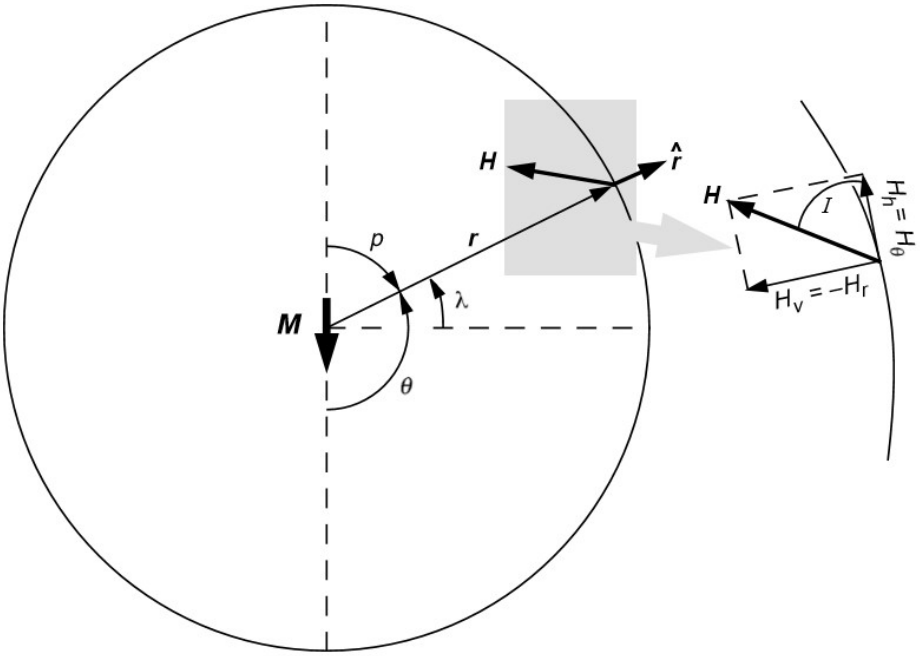

Figure 2.2. Schematic of the different components of the geocentric axial dipole. The components are Magnetic dipole (M), angle from the positive magnetic pole (θ), magnetic colatitude (ρ), geographic latitude (λ), radial distance from the dipole (r), total magnetic field vector (H), unit vector (r^) in the direction r, Inclination (I). The magnetic field vector H can be broken into a vertical component (Hv = –Hr) and horizontal component (Hh = Hθ) (Butler, 1992).

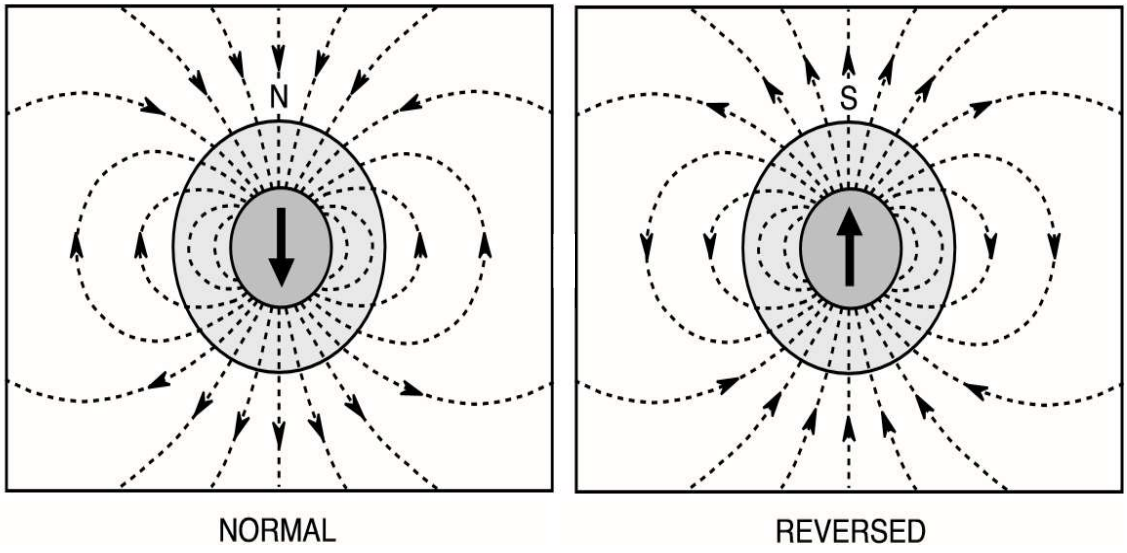

Figure 2.3. The GAD model and the Earth's geomagnetic field during normal and reversed polarity. During normal polarity (when in the northern hemisphere), the inclination is positive (downward directed). The reverse is the case during reversed polarity with the inclination being negative when in the northern hemisphere (Langereis et al., 2010).

However, this model does not fully fit the current magnetic field. Instead, the field deviates from the GAD model, with the current magnetic poles offset from the geographic poles (Fig 2.4; Butler, 2004). Even with an inclined geocentric axial dipole, ~90% of the surface field can be accounted for (Butler, 1992). The best-fitting dipole is the eccentric dipole, in which the field is described marginally better (Butler, 1992).

This dipole varies largely across regions as the best-fitting eccentric dipole can accurately describe the geomagnetic field when applied to most locations, although some areas it cannot explain Ca.20% of the geomagnetic field suggesting a non-dipole field is also present. However, over long time scales (>3000 years) these variations will average to zero, thus the average magnetic field can be represented using the GAD model and the historical positions of geomagnetic poles can be located (Butler, 1992).

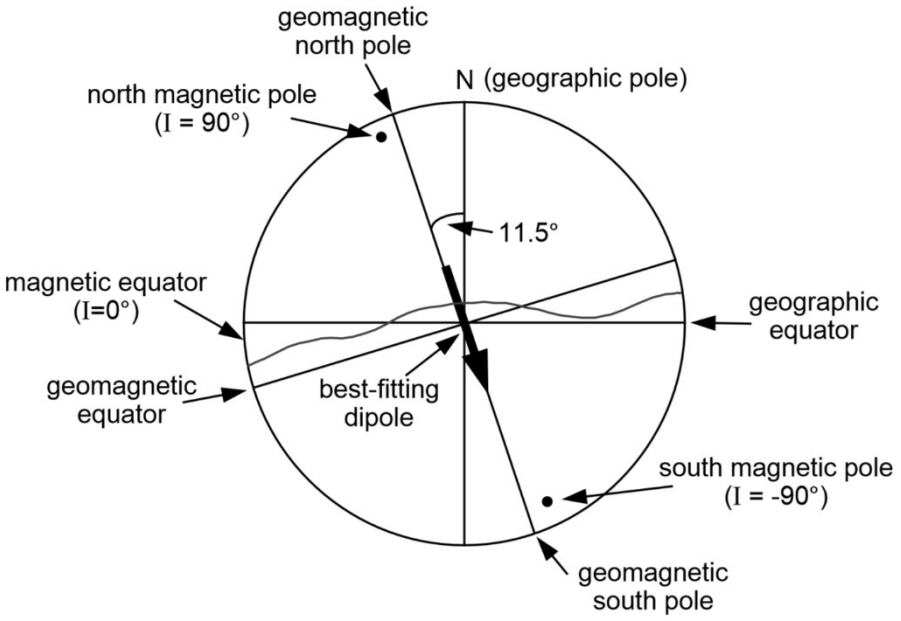

Figure 2.4. A more realistic inclined dipole model for the Earth's current magnetic field, showing the relationship between the geographic, magnetic and geomagnetic poles. The key point is that the geomagnetic poles for the best-fitting dipole are distinct from the magnetic poles (Butler, 1992).

2.1.3 Secular Variation

Geomagnetic secular variation is the change in direction and magnitude of the Earth's magnetic field on a 1-100,000 year scale (Butler, 1992). These changes have been witnessed over the last 400 years in London (latitude 51.5° N), where inclination has varied between 66-75° and declination has varied from -25° to +10° (Butler, 2004; Jacobs, 1989). These findings differ significantly from data acquired at Holbart, Tasmania (latitude 42.9° S), which showed less variation with declination varying from 0° to 14° (Fig. 2.5; Jacobs, 1989). Secular variation is probably the result of local disturbances in fluid flow near the core-mantle boundary (McElhinny & Merrill, 1975).

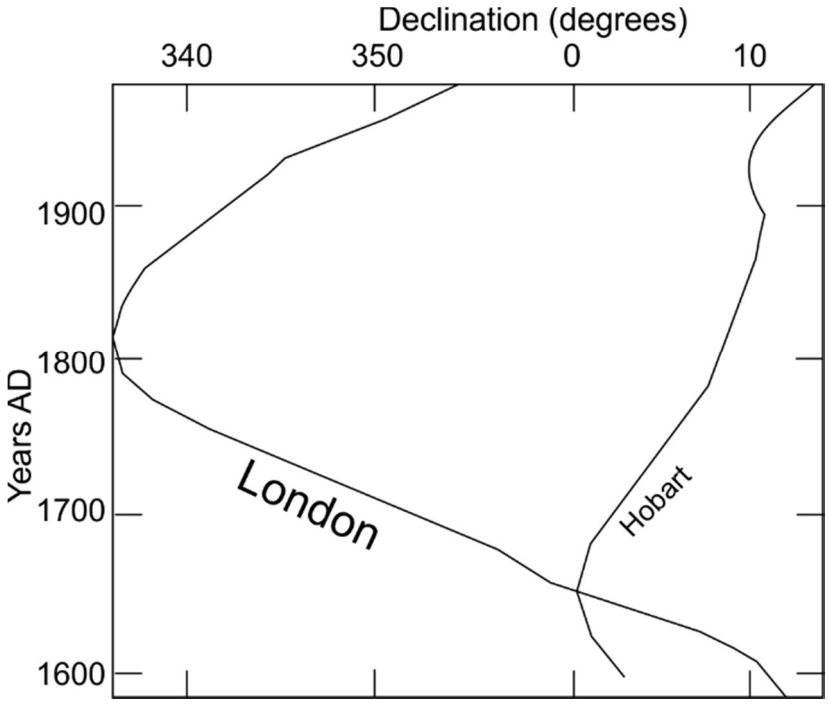

Figure 2.5. Variations in declination of London (51.5° N) and Hobart, Tasmania (42.9° S). (Jacobs, 1989).

2.2 Continental Motion and Apparent Polar Wandering

During deposition magnetic grains will orientate themselves to the geomagnetic field at that time (Collinson, 1965). This palaeomagnetic direction is recorded for each site and can be plotted onto a stereograph as a virtual geomagnetic pole (VGP), assuming a dipole field (Jacobs, 1989).

When the plates move, the previously recorded palaeomagnetic directions will be carried along with the moving plate. Consequently, when plotting palaeomagnetic data with a fixed continent, this change in continental position appears as if the poles are 'wandering' (Fig. 2.6; Jacobs, 1989). Plates which travel in different directions will therefore have dissimilar polar wander paths (Torsvik et al., 2012). These paths can be compared to establish where plates have been and how they have moved relative to each other.

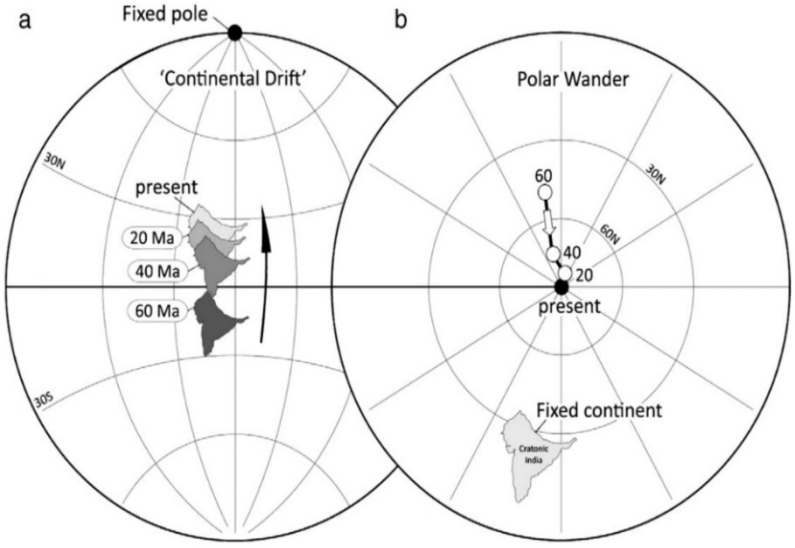

Figure 2.6. The Indian continent movements over the last 60 Ma. a) Is using the declinations and inclinations recorded by rocks during India's movement. Using a fixed pole location during this period allows the movement to be shown. b) In this diagram the continent remains fixed throughout the period and the apparent polar axis is allowed to wander, creating an apparent polar wander path. This is significant as apparent polar wander paths can be compared with other continent apparent paths (Torsvik et al., 2012).

2.3 Polarity Reversals

Magnetostratigraphy uses magnetic field reversals to correlate rocks on a global scale (Langereis et al., 2010). The direction of magnetism in sediment and igneous strata can be measured to determine intervals when the rocks were deposited in the Earth's present field configuration (normal polarity) or in a field 180º from the present field (reverse polarity) (Fig. 2. 7; Langereis et al., 2010; Opdyke & Channell, 1996). Reversals of the Earth's magnetic field are aperiodic, with reversals occurring on average every 0.5 Ma years during the Palaeocene, and becoming more frequent in the Miocene occurring every c. 0.15 Ma (Barton, 1989).

These aperiodic changes in polarity (magnetochrons) have been labelled to help provide a systematic convention for identifying individual polarity events as chrons (Opdyke & Channell, 1996). To establish the absolute age of each magnetochron, biostratigraphy or radiometric dating can be used. Pre-Cambrian reversals can be more difficult to constrain in age as there is no biostratigraphic evidence of age (Pavlov & Gallet, 2005). Other stratigraphic methods such as stable-isotopes of $\delta^{13}C$ and $\delta^{18}O$ are used to provide more accurate dates and to correlate geomagnetic polarity reversals (Pavlov & Gallet, 2005; Ripperdan et al. 1993). In a few cases polarity magnetochrons can last ~10 million years. These intervals are called superchrons, an example of this is the interval between the mid Carboniferous and the mid Permian. The Earth's magnetic field kept a constant reverse polarity over a ~50 Ma interval, known as the Kiaman Superchron.

Owing to the long time scale between reversals, there is limited scope for stratigraphic correlation and dating in superchrons (Pavlov & Gallet, 2005).

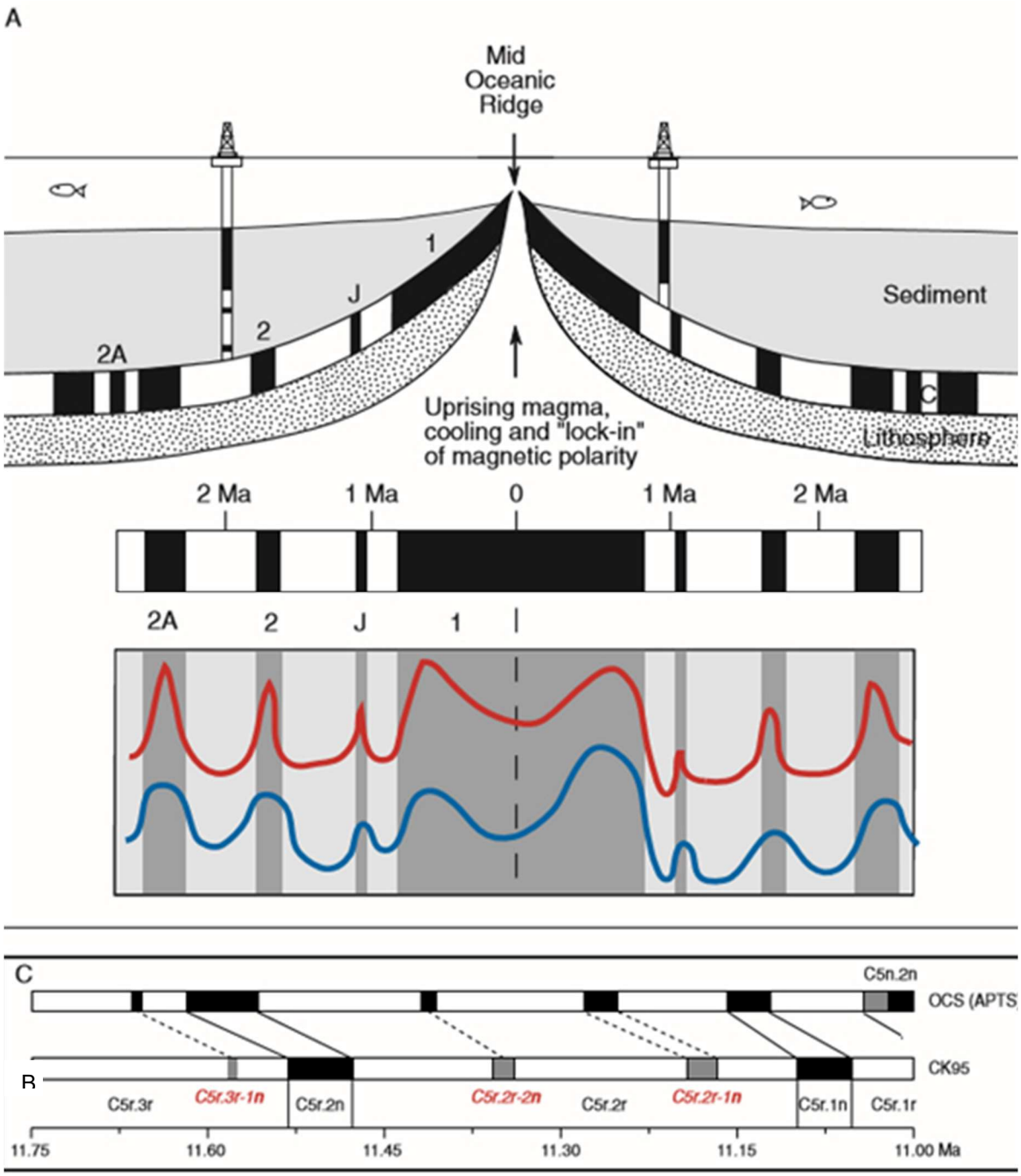

Figure 2.7. A) The creation of magnetic anomalies during sea floor spreading and the changes in polarity as crust is created. As new crust is created magnetic minerals acquire geomagnetic directions as align to the ambient field. Black represent magnetic minerals that have a positive inclination (normal polarity), white represent negative inclination (reverse polarity). Owing to the symmetrical nature of sea floor spreading this creates a symmetrical barcode pattern with each interval representing long periods of the same polarity. B) The barcode pattern can be used to correlate different successions using magnetostratigraphy (Langereis et al., 2010).

2.4 Magnetic Minerals

All matter has a magnetic susceptibility and shares diamagnetic properties where an applied magnetic field will alter the orbit of electrons to produce a small magnetisation antiparallel to the applied field (Butler, 1992; Maher & Thompson, 2010). Paramagnetic and ferrimagnetic solids behave differently to an applied magnetic field. They contain atoms with atomic magnetic moments on account of their unpaired electrons which produces a magnetisation which aligns parallel to the applied field.

Paramagnetic minerals have no interaction between adjacent atoms, an example is shown by Fe atoms of paramagnetic minerals such as fayalite (Butler, 1992). These Fe atoms will have strong magnetic moments when a field is applied but when the field is removed, atoms will react independently from one another and net magnetisation will be reduced to zero again (Butler, 1992).

Ferromagnetic minerals have an unfilled 3d electron orbital that causes the atoms to strongly interact with each other. This characteristic allows a magnetisation several magnitudes greater than paramagnetic minerals. They are able to maintain this magnetisation after a magnetic field is removed, making such minerals remanence-carriers (Butler, 1992). The Fe-Ti oxides, Ti-magnetite, Ti-haematite and sulphides are the main carriers of remanence properties within rocks (Jacobs, 1989).

The properties that dominate magnetic mineral behaviour are their grain size and coercivity. Magnetic grains build up a surface magnetic charge, so in order to reduce this charge the grain subdivides into magnetic domains, this will occur once grains reach a certain size. The size of the grain will define how many domains a ferromagnetic magnetic grain has. Single-domain (SD) grains are when the grain size is so small that the energy required to make a domain wall is larger than the decrease in magnetostatic energy (Butler, 1992). Differences in number of domains have dramatic changes on their properties (Maher & Thompson, 2010). Néel (1955) studied relaxation times of (SD) grains and was able to characterise relaxation time (τ) as:

$$2.3)\ \tau = \frac{1}{C} exp\ \frac{v\ Hc\ Ms}{2kT}$$

Equation 2.3. Where C is the frequency factor, v is volume of SD grain, Hc is the microscopic coercive force of SD grain, Ms is the saturation magnetization of the ferromagnetic material and kT is thermal energy (Néel, 1955).

Néel's (1955) studies found that relaxation time was controlled by a ratio of blocking energy (vHcMs) to thermal energy (kT). Magnetic grains have a blocking temperature which is threshold of energy required to move the magnetic moments. For example magnetite ultrafine crystals (<0.03 μm) are dominated by thermal energy rather than magnetic energy, therefore carry no remanence at room temperatures (Maher & Thompson, 2010). These are called superparamagnetic (SP) as they behave similarly to paramagnetic minerals but with greater magnetisation (Maher & Thompson, 2010).

Magnetite SD grains are typically 0.1 μm in size and very efficient carriers of remanent magnetism; as they have higher intensity remanences and have greater resistance to resetting by later events (Butler, 1992; Maher & Thompson, 2010). As the size of the magnetic grain increases magnetic stability decreases, but grains are still able to maintain a stable remanence and referred to as pseudo-single domain grains (Maher & Thompson, 2010). Multi-Domain (MD) grains are larger grains and are subdivided into several domains owing to energetically favourable circumstances (Butler, 1992). MD grains carry lower intensity and stability remanences compared to SD grains.

Coercivity is a measure of the field necessary to reset a grain's direction of remanent magnetism (without rotating the grain), and is controlled by grain size in Ti-magnetites. Coercivity can be established by a hysteresis loop by determining a magnetising field versus magnetisation (Butler, 1992). Where the coercivity (Hc), the remanence coercivity (Hcr), magnetic saturation (Ms) and magnetic saturation remanence (Mrs) are obtained is shown in Fig. 2.8 (Maher & Thompson, 2010; Leonhardt, 2005). The magnetic ratio Mr/Ms and remanence Hcr/Hc ratio can be used in a domain state plot, establishing the domain state (grain size) of the ferromagnetic magnetic minerals (Fig. 2.9; Dunlop, 2002).

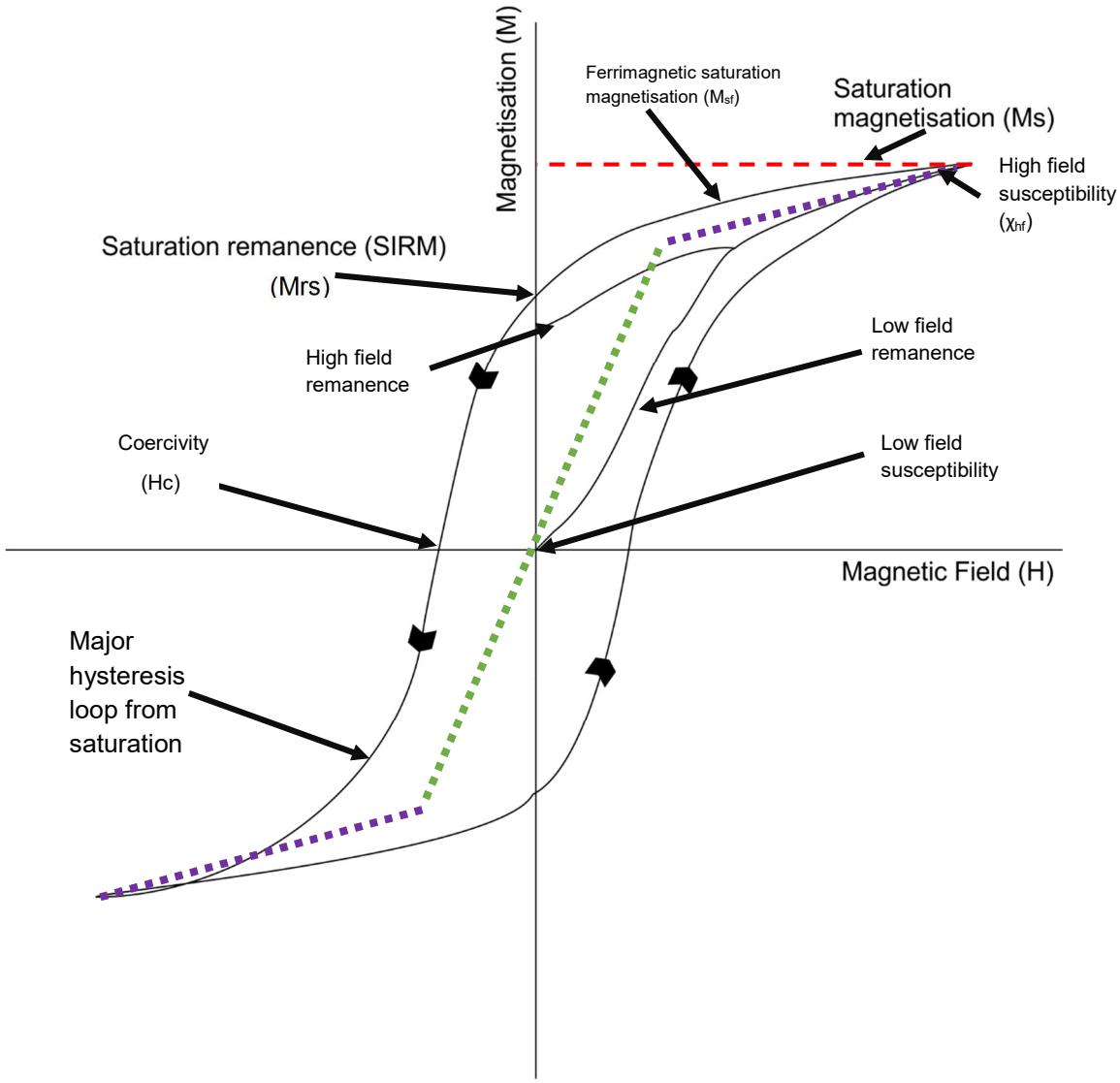

Figure 2.8. An example of hysteresis plot. Shows ferromagnetic and paramagnetic components of a sandstone sample. Hc is the coercivity, the remanence coercivity (Hcr), Ms is the magnetic saturation and Mrs is the magnetic saturation remanence. The green and purple dotted lines are the ferrimagnetic and paramagnetic contribution, respectively (Maher & Thompson, 2010; Leonhardt, 2005).

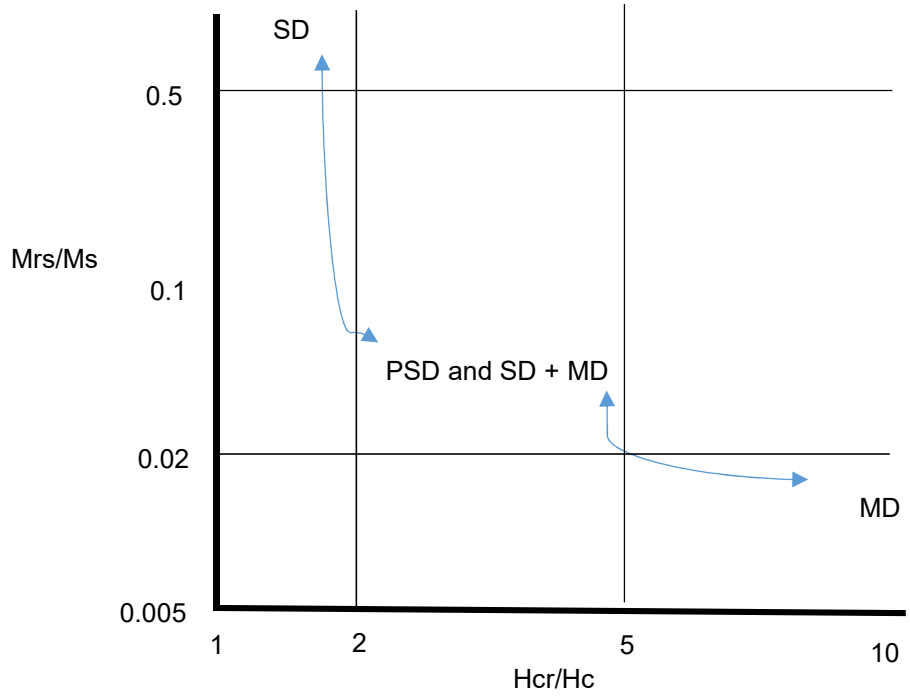

Figure 2.9. A generalised Day plot that uses the ratio of the remanence coercivity (Hcr) and the coercivity (Hc) against the ratio of magnetic saturation remanence (Mrs) and magnetic saturation (Ms). The positions of single-domain (SD), pseudo-domain (PSD) and multi-domain (MD) are shown (not to scale) (Day, 1977).

All magnetic remanences decay over time, this is called magnetic relaxation. The magnetic relaxation is largely controlled by thermal energy (Butler, 1992). More thermal energy leads to greater oscillation of the magnetic grains and can, in turn, overcome the blocking temperature in shorter periods of time (Butler, 1992). When examining ancient magnetic fields recorded in rocks, magnetic minerals with the longer relaxation times (therefore greater blocking energy), such as SD grains, are more useful as these will retain their remanences longer.

Types of remanences

Table 2.1. The major remanence carrying minerals (Collinson, 1983; Opdyke & Channell, 1996).

Magnetic Minerals	Composition	Origin	Curie Temperature	Magnetic characteristics
Magnetite/ Titanomagnetite	(Fe_3O_4)/ (xFe_2TiO_4.[1-x]Fe_3O_4)	Common in igneous, metamorphic rocks and a detrital component in sedimentary rocks	580ºC/ -150ºC to 580ºC	Ferrimagnetic, High saturation magnetism. Coercivity varies on size of grains but generally low.
Haematite/ Titanohaematite	(α-Fe_2O_3)/ ($xFeTiO_3$.[1-x]Fe_2O_3)	Common mainly in igneous and metamorphic rocks but also detrital and diagenetic component in sedimentary rocks	675ºC/-218ºC to 675ºC	Variable characteristics depending on composition but mainly antiferromagnetic. Lower saturation than magnetite but has a moderate to high coercivity
Maghematite	(γ-Fe_2O_3)	Low temperature Oxidation product of magnetite in sedimentary, igneous and metamorphic rocks	~640ºC/ but hard to establish as it will invert to magnetite or haematite above 250ºC	Similar to magnetite but lower saturation magnetisation and comparable remanence coercivity to magnetite
Goethite Magnetisation	(α-FeOOH)	Low temperature oxidation of iron sulphides & Fe-silicates	~120ºC (Converts to haematite c.350ºC)	Antiferromagnetic/ weak saturation magnetism and very high coercivity
Pyrrhotite Magnetisation c.0.10<x<0.14	(FeS_{1+x}) Where x =0-0.14	In basic igneous, sedimentary (reducing environment) and metamorphic rocks	~325ºC	Monoclinic and ferrimagnetic. Saturation 10 times haematite and ½ of magnetite Coercivity is similar to magnetite. Sensitive to oxidation and heat.
Greigite	(Fe_3S_4)	Diagenesis of lake sediments and some rapidly deposited clastic marine sediments	~320ºC	Ferrimagnetic, stable magnetisation. Coercivity is similar to magnetite. Very sensitive to oxidation and heat.

Natural Remanent Magnetisation (NRM) is the remanent magnetism in the rock sample before it has been altered by laboratory treatment (Jacobs, 1989). The NRM is determined by exposure to the geomagnetic field and the geological processes that have occurred during its formation and subsequent history. There are often at least two or more components of NRM in a sample. The primary component known as Characteristic Remanent Magnetism (ChRM), and secondary NRM which may result from various changes such as long-term exposures to the geomagnetic field since formation (Butler, 1992). The three basic forms of primary NRM are Thermo- Remanent Magnetisation (TRM), Chemical Remanent Magnetisation (CRM) and Detrital Remanent Magnetisation (DRM) (Butler, 1992).

TRM is the remanent magnetism, usually gained during igneous rock formation by the grain during cooling through its blocking, or Curie temperature (Opdyke & Channell, 1996). Blocking temperatures are determined by the size and composition of the grains (Opdyke & Channell, 1996).

CRMs are produced below the blocking temperature during chemical growth. Magnetic minerals can grow authigenically during diagenesis, or by processes of weathering. These additional magnetic minerals may have formed and aligned in the ambient magnetic field and so can add to the NRM (Opdyke & Channell, 1996).

DRM is found in sediments and is the remanence of detrital or biogenic magnetic mineral grains as they were deposited in an ambient field during deposition (Opdyke & Channell, 1996). DRM is complex and can be modified by many processes such as bioturbation and compaction (Butler, 1992). Magnetites, haematites and maghaematites are the common carriers of DRM. DRM has a lock-in depth of 10-20 cm below the sediment/water interface, however this is strongly dependent on the rate of sedimentation, grain size and bioturbation depth (Opdyke & Channell, 1996).

Secondary magnetisations in natural samples often derive from Viscous Remanent Magnetisation (VRM) (Opdyke & Channell, 1996). This is acquired in grains with small relaxation times, as the magnetic grains will become remagnetised in the ambient field (Opdyke & Channell, 1996). The magnetic viscosity can also be increased by higher temperatures, such as those found during burial. This is the reason why VRM in sediments is common in modern NRMs and is referred to as Thermo-Viscous Remanent Viscosity (tVRM) (Opdyke & Channell, 1996).

There are two more remanences of note that are produced artificially. These are Isothermal Remanent Magnetisation (IRM) and Anhysteretic Remanent Magnetisation (ARM). IRM is produced by exposing the sample to a strong magnetic field and occurs naturally in circumstances such as lightning strikes. IRM is mostly generated in a laboratory using pulse magnetisers or electromagnet (Opdyke & Channell, 1996). This is a high-field magnetisation process that is used to measure magnetic mineralogy and grain size. The IRM will increase in strength as the magnetising field increases until it reaches saturation IRM (SIRM) (Opdyke & Channell, 1996).

ARM is produced when placing a specimen in an alternating high field that ramps down to zero in the present of a small direct current field (Opdyke & Channell, 1996). ARM shares similar characteristics with TRM in that it results from a small bias field (the dc field in an ARM experiment or the Earth's magnetic field in a natural TRM) in the presence of a randomising factor (the AF field in the ARM experiments; the thermal agitation in the natural TRM) (Opdyke & Channell, 1996).

3. Anisotropy of Magnetic Susceptibility

Anisotropy of Magnetic Susceptibility (AMS) measures the distribution of susceptibility within a sample, and has been used since the 1940's in studies such as Borradaile & Henry (1997); Cifelli et al. (2009); Hailwood & Dowling (1987); Rees et al. (1982) Rochette et al. (1992) and Schieber & Ellwood (1993). AMS determines the susceptibility distribution which can be used as a non-destructive method to determine paleoflow (and grain orientation) within un-deformed sediments and as a useful strain indicator in deformed sediments. AMS measures the directional variations of magnetic susceptibility and is expressed as a symmetric second rank tensor. This, in turn, can be expressed as a magnitude ellipsoid that will represent the magnetic grain preferred orientation in the sample and the strength of the preferred alignment (Park et al., 2013). The AMS tensor is represented by the maximum (Kmax, K1), intermediate (Kint, K2) and minimum (Kmin, K3) principal susceptibility values and these can be expressed graphically as a triaxial ellipsoid (Fig. 3.1; Baas et al., 2007).

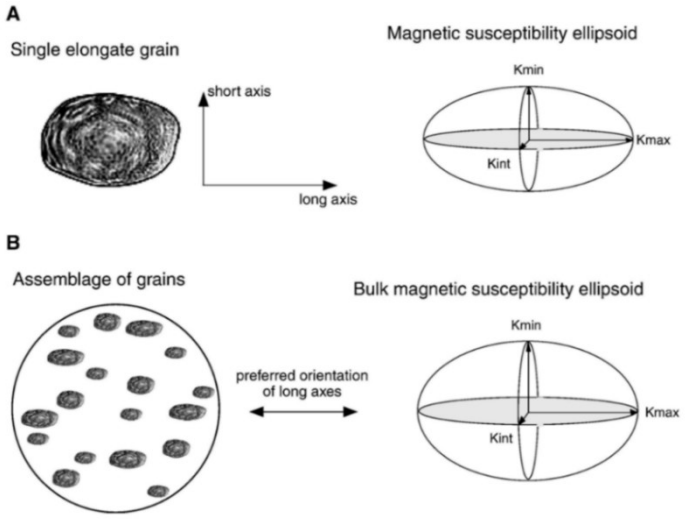

Figure 3.1. The relationship between anisotropy of grains and their magnetic susceptibility anisotropy, showing the Kmax, Kint and Kmin susceptibilities of, A) a single elongate grain and B) an assemblage of elongated grains (Baas et al., 2007).

3.1 AMS Parameters

AMS is dependent on intrinsic magnetic susceptibility and degree of preferred orientation of the individual magnetic minerals (Chadima et al., 2006). Therefore differences in AMS reflect changes in the rock fabric and magnetic mineralogical differences. Anisotropy parameters are used to characterise AMS results; structural geologists use magnetic lineation (L), magnetic foliation (F) and degree of anisotropy (P) which are defined as (Borradaile, 1994):

$$3.1)\ L = K1/K2 \qquad 3.2)\ F = K2/K3 \qquad 3.3)\ P = K1/K3$$

Equation 3.1, 3.2, 3.3 (Jelinek, 1981)

These are used to determine the AMS ellipsoid shape, however Jelinek (1981) and Hrouda (1982) recommended using the corrected degree of anisotropy (Pj) and shape parameter (T) to best define the anisotropy ellipsoid.

$$3.4)\ Pj = exp\sqrt{\{2[(n_1-n)^2 + (n_2-n)^2 + (n_3-n)^2]\}}$$

Where n_1, n_2 and n_3 are the natural logarithms of K1, K2, and K3, respectively and $n = (n_1 + n_2 + n_3)/3$ (Jelinek, 1981).

$$3.5)\ T = \frac{\ln F - \ln L}{\ln F + \ln L}$$

When T <0 the sample has a prolate shaped AMS ellipsoid and when T>0 the sample has an oblate shaped AMS ellipsoid (Jelinek, 1981).

The different shape fabrics can be categorised as normal, inverse, intermediate or anomalous fabrics (Chadima et al., 2006; Hrouda et al., 2002). Normal fabrics will have a magnetic fabric whose K1 (Kmax) direction is parallel to structural lineation such as flow or current directions and the K3 (Kmin) direction is normal to a structural foliation such as a bedding plane or plane of compaction (Borradaile & Henry, 1996; Chadima et al., 2006).

Inverse fabrics are caused when the maximum and minimum axes are inverted (Chadina et al., 2006). Therefore the magnetic lineation is perpendicular to bedding and the fabric is distinctly prolate (Hrouda et al., 2002). These inverse magnetic fabrics can be caused by i) post-deposition deformation; ii) when the fabric is carried by single domain (SD) magnetite and iii) when the fabric is carried by iron-bearing carbonates including siderite (Rochette 1988, 1992).

3.2 AMS Contributors

The magnitude of the fabric is dependent on two factors: the anisotropy of the particles and their degree of alignment (Tarling & Hrouda, 1993). The individual particle anisotropy can relate to either crystalline anisotropy or shape anisotropy (Hrouda, 1992). Shape anisotropy is primarily generated by ferrimagnetic particles with high susceptibility (Borradaile & Werner, 1994; Tarling & Hrouda, 1993). Crystalline anisotropy is intrinsic to the lattice structure and dominant in antiferromagnetic, paramagnetic and diamagnetic minerals (Tarling & Hrouda, 1993).

Shape anisotropy is dominant in magnetite which has a weak crystalline anisotropy, whereas in haematite, other antiferromagnetic iron oxides and paramagnetic minerals crystalline anisotropy dominates (Baas et al., 2007; Tarling & Hrouda, 1993). With shape anisotropy the sizes of the magnetic grains will have an effect on the anisotropy ellipsoid shape; single-domain and multi-domain contributions have strong influences on the AMS and can show radically different anisotropies (Baas et al., 2007; Tarling & Hrouda, 1993). Therefore it is important to establish the mineralogy of samples when analysing AMS, as particle size has little impact on preferred crystalline anisotropy (Baas et al., 2007).

At higher induced fields, paramagnetic as well as ferrimagnetic mineral anisotropies can be measured (Tarling & Hrouda, 1993). Hounslow (1985) looked at the magnetic fabric of paramagnetic phyllosilicate minerals in mudstones. With samples lacking in ferrimagnetic minerals, he hypothesised that the K1 axis of the phyllosilicates was controlled by the alignment of the quartz grains and showed an oblate shape, parallel to the bedding. This was caused by the clay particles being ‘draped’ around the quartz grains by compaction (Hounslow, 1985). There was more variation in AMS shape in coarser sediments which showed decreases in the magnitude of susceptibility and T. These variations were explained as belonging to less organic-rich and coarser sediments that had correspondingly less well developed clay orientation.

3.3 Applications of AMS

Kissel et al. (1998) found depth-variations in AMS in their core through sediments in the North Atlantic abyssal plain. During warm periods there was a greater Pj and susceptibility was very oblate in shape, whereas colder periods were marked by lower Pj and T values. Kissel et al. (1998) hypothesised that it was changes in sedimentation rate rather than chemical or biological changes that caused these significant variations during different climate conditions.

AMS of older sediments can be more difficult to interpret as magnetic fabrics are susceptible to alteration by deformation. Deformation events such as compaction and tectonic shortening often increase the degree of anisotropy and change the initial AMS fabric (Hirt et al., 1995), whereas other post-depositional events such as bioturbation and liquefaction can destroy fabrics. Schieber & Ellwood (1993) looked at the K1 directions of the Mid-Proterozoic Newland Formation in Montana, United States. They found divergence in the AMS between different lithologies and concluded that this was because of the different influences on deposition. The shales reflected basin-wide paleoflow directions whereas the sandstones showed two main K1 directions. The coarsest sandstones were deposited by large storms that produced rip-up clasts and flute marks and the K1 direction was orientated seaward. The finer-grained sandstones were located further offshore and represented deposition by smaller storms and the K1 directions showed two main directions caused by the changing direction associated with wave-orbital motion (Schieber & Ellwood 1993).

Tectonic deformation and metamorphism can produce AMS fabrics within meta-sediments; they can show strong strain gradients on small spatial scales caused by ductile shear zones or refracted-cleavage change (Borradaile & Henry, 1997). In meta-sediments AMS will emphasise different micro-fabrics produced by the associated deformation and may respond to the growth of additional minerals. An example of a deformation fabric can be found in the Canadian Shield in North America, where the AMS of iron rich formations and slates were studied by Borradaile & Henry (1997). Both lithologies had experienced similar levels of deformation but the AMS of the micas in slate was different from the iron rich formations dominated by magnetite. The AMS of micas noticeably reflects a deformation fabric highlighted by the AMS having the same orientation of schistosity in the slates (Borradaile & Henry, 1997).

3.4 Alternative Methods of AMS

A different technique to enhance AMS measurements is to coat the grains in a thin film of ultra-fine magnetite particles. This is done by saturating the sample with a pressurised ferrofluid which will dry in the pores and on the surface of accessible grains to leave a thin film (Baas et al., 2007). Enhanced AMS can be used on samples that are magnetically dominated by diamagnetic minerals such as a quartz dominated sandstone (Baas et al., 2007).

Table 3.1. Comparison of the petrographic, natural AMS and 'Enhanced AMS' techniques (Baas et al 2007).

Criterion	Petrographic method	Natural AMS method	Enhanced AMS method
Measurement principle	Particulate method	Bulk grain method	Bulk grain method
Ease of application	Laborious and time consuming	Quickest method	Quick method
Grain types	Sand to silt sized grains only	Yields fabrics of magnetite, (often finer-grained than framework grains) and/or paramagnetic minerals	Yields fabric of all grains
Sensitivity to user bias	Method is sensitive to user bias	Method is largely independent of user input	Method is largely independent of user input
Type of fabric	Used predominantly for measuring grain fabric but may also be used for measuring pore orientation	Used for measuring grain fabric	Used for measuring grain fabric
Fabric dimensionality	Yields apparent grain long axes in two-dimensional sections	Yields three-dimensional fabric	Yields three-dimensional fabric
Number of grains	Measures orientations 10-100's of grains	Measures orientations of 1000's of magnetite particles	Ideally measures the orientation of all grains
Heterogeneity	Susceptible to mm- and micro-scale heterogeneity caused by grain clusters	Susceptible to mm- and cm-scale heterogeneity, often discernible in the sample with the naked eye	Susceptible to mm- and cm-scale heterogeneity, often discernible in the sample with the naked eye
Statistics	Statistical analysis based on grain population	Limited statistical analysis based on bulk properties	Limited statistical analysis based on bulk properties
Sensitivity to the earth's magnetic field	Not applicable	Very small possibility of the SD magnetite being orientated by earth's magnetic field at time of deposition	Magnetic properties of ultrafine magnetite particles camouflage those of natural particles
Magnetite particle size	Not applicable	Samples must contain MD magnetite or paramagnetic particles	Injection with ultrafine magnetic particles guarantees magnetic signal
Significance of other magnetic particles	Not applicable	Possible additional fabrics from paramagnetic particles	Magnetic properties of ultrafine magnetite particles camouflage those of natural particles
Interaction of magnetite particles	Not applicable	Possible interaction between magnetite particles, producing magnetic lineations	Concentrations of magnetite are low enough to prevent particle interaction; surfactant-coated particles to prevent agglomeration

4. Methodology

The methodology section is divided into four parts: 1) sample collection and preparation, 2) palaeomagnetic data, 3) anisotropy of magnetic susceptibility (AMS) and 4) magnetic mineralogy and analysis.

4.1 Field Sample Collection and Preparation

Hand samples were orientated in the field by finding flat surfaces of areas ~20cm^2 or greater. The spirit level of the orientation staff was used to establish the strike direction (fiducial, x-azimuth) and the orientation was determined using a compass. The dip (maximum angle normal to strike) was recorded using a clinometer in the orientation staff. The strike and footprint of the orientation staff were marked on the surface using a pencil. The strike and dip of the bedding was also measured so that data could be corrected to palaeohorizontal (Collinson, 1983). Each sample's position in the section was then drawn on a sedimentary log.

Most of the Ainsa samples used in this study were collected during fieldwork for this project. The Silurian samples had been collected previously by Mark Hounslow and Sam Harris. For the sandstone samples, the corner or the top/base of a bed was removed using hammer and chisel. Shale samples were removed by digging around the shale monolith and then removing the block with care to avoid breaking it. Samples were then wrapped to avoid breakage during transit. The Marcellus Shale samples were acquired by plugging from borehole cores and therefore were not azimuthally orientated.

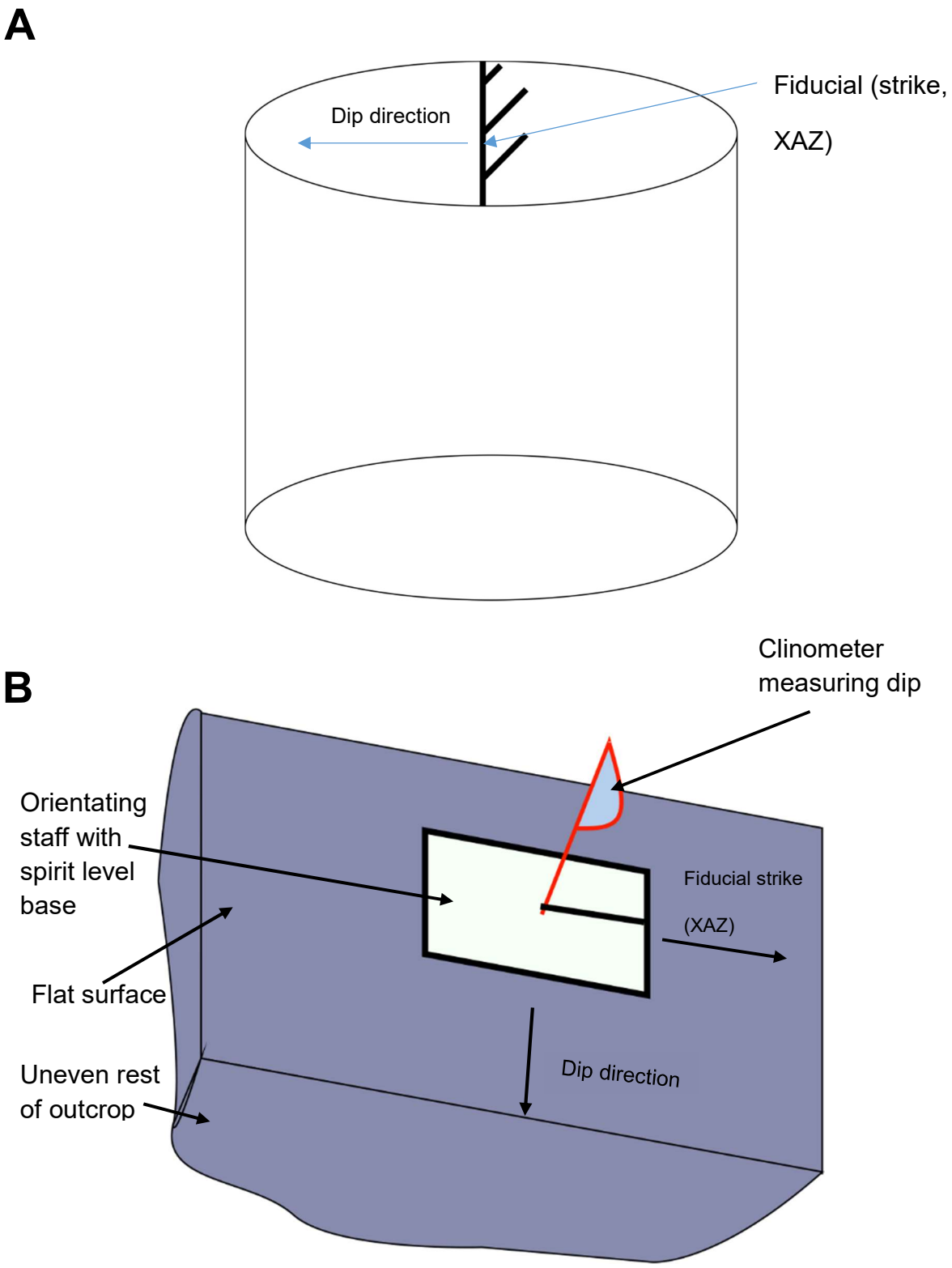

Figure 4.1. A) Example of a cylindrical specimen, with the fiducial mark representing the orientation plane measured in the field. B) Shows the orientating staff being used to mark the fiducial on a flat surface of a sample when in situ.

Once the hand samples had been collected, they were prepared by mounting the samples in dental plaster (chosen for its purity; Thellier, 1967) so that the flat surface marked with the orientation staff-footprint was horizontal. Each sample was then cut (sometimes dry-cut if the samples were fragile) into ‘rods’ using a diamond-edged saw, each strip was cut to a width 22 mm and parallel to the fiducial strike. These strips were then cut again into 22 mm cubic specimens with up to five specimens for each sample. Each specimen was marked by fiducial arrows showing the samples’ X-axis (the strike or XAZ) and labelled appropriately using a waterproof marker (Collinson, 1983). An example of this labelling is AQ17.4 where (AQ = Anisa Quarry, 17=sample number and .4=specimen number 4).

Occasionally during the preparation some of the fissile-shale samples had to be glued using a PVA adhesive and in rare cases a thick solution of sodium silicate was used to strengthen the sample, prior to cutting. The borehole specimens provided to the project were pre-cut to different specifications; therefore these were ground using a flat lap machine and sandpaper to the 22 mm dimensions needed for laboratory use.

4.2 Palaeomagnetic Laboratory Methods

One or two specimens from each sample were chosen to be measured for their natural remanent magnetism (NRM) and were subjected to demagnetisation experiments. Demagnetisation was used to progressively subtract magnetisations with the lowest relaxation times from a specimen (Jacobs, 1989). When this is applied in a stepwise fashion, demagnetisation can be used to extract 1) later, less stable overprints such as the Thermo-viscous remanent magnetism (TVRM) (Collinson, 1983), which is useful for orientating samples and 2) the characteristic remanent magnetism (ChRM) that the specimen acquired during deposition (Jacobs, 1989).

4.2.1 Thermal Demagnetisation

Specimens were progressively heated in several steps using the Magnetic Measurements Thermal Demagnetiser (MMTD1) at Lancaster University, where specimens and the oven are surrounded by a mu-metal shell (Magnetic Measurements, 2016). The MMTD1 is further protected from the Earth's geomagnetic field by a set of Helmholtz coils, all of which nullify the Earth's geomagnetic field to residual field of <10nT.

The MMTD1 heated as many as 13 specimens in one batch and each specimen was held at each heating stage for 20 minutes to allow the specimens to equilibrate at set peak temperatures (Collinson, 1983). Specimens were rapidly air-cooled in the near zero magnetic field to remove the remanence at the set blocking temperature (Collinson, 1983).

The maximum temperature step used was dependent on the specimen's lithology, as some specimens were more susceptible to heat-alteration. This alteration is typically associated with oxidation of other Fe-bearing minerals, such as clays and pyrite (Jacobs, 1989). The alteration was monitored by measuring the magnetic susceptibility between each heating stage, any significant increase was noted and demagnetisation steps that showed that showed significant heat-alteration were not used. Large increases in magnetic susceptibility in the Marcellus samples meant that heating above 200°C was not possible, whereas the Ainsa samples were able to be demagnetised to temperatures of 350°C without significant heat-alteration.

4.2.2 Alternating Field (AF) Demagnetisation

Following the thermal demagnetisation stages, the specimens were further demagnetised using AF. AF demagnetisation places a specimen in a two axis tumbler and subjects it to an alternating magnetic field within a mu-metal shield (to cancel the Earth's geomagnetic field. While the sample is tumbling, the alternating field ramps up to a peak intensity and then smoothly reduces to zero (Collinson, 1983).

This process removes the remanent magnetisation of the ferrimagnetic grains with a coercive force less than the alternating field (Jacobs, 1989). As the field is reduced, the specimen is cycled through demagnetisation increments of decreasing amplitude. This leads to the grains remanence being progressively re-set in random orientations and therefore does not contribute to the NRM (Jacobs, 1989).

Repeating this process with progressively higher magnetic fields successfully removes magnetisation of the grains with coercivity up to the peak field (Jacobs, 1989). The demagnetising field started at 10 mT then increased by 10 mT per step up to 90 mT or until a point when the directional data becomes too scattered (Jacobs, 1989).

4.2.3 Measuring Palaeomagnetic Data

At each stage of demagnetisation the remanent magnetisation was measured using the Cryogenic Consultants Ltd GM400, a highly sensitive, triple axis magnetometer. The GM400 uses three superconducting quantum interference devices (SQUID); these are attached to pick up coils within the GM400 which work as sensitive magnetic field sensors. The GM400 SQUIDS operate at temperature of liquid helium (-269^{o}C) which allows the SQUID to measure magnetic intensity of a specimen along their X, Y and Z axes (Fig. 4.2). The GM400 sensitivity is around $1x10^{-11}$ Am^2 and outputs the declination, inclination and a gamma distribution within 95% confidence limits ($\gamma 95$) for each specimen (Table 4.1).

Table 4.1. Format of the data measured using the GM400 (in bedding corrected coordinates). Four main values are measured with each step, they are (from left to right) the magnetic intensity which is the magnetic moment divided by the volume of the specimen, the declination (the angle between the horizontal component of the specimen and geographic north), the inclination (downward dipping angle between palaeohorizontal and the magnetisation) and $\gamma 95$, an angular measure of the magnetisation variance (Briden & Arthur, 1981).

AQP2.4

Step (°C)	Intensity (mA/m)	Dec	Inc	$\gamma 95$
20	0.264	315.8	18.9	1.3
100	0.105	281.5	6.2	1.6
150	0.103	266.5	-19.3	1.7

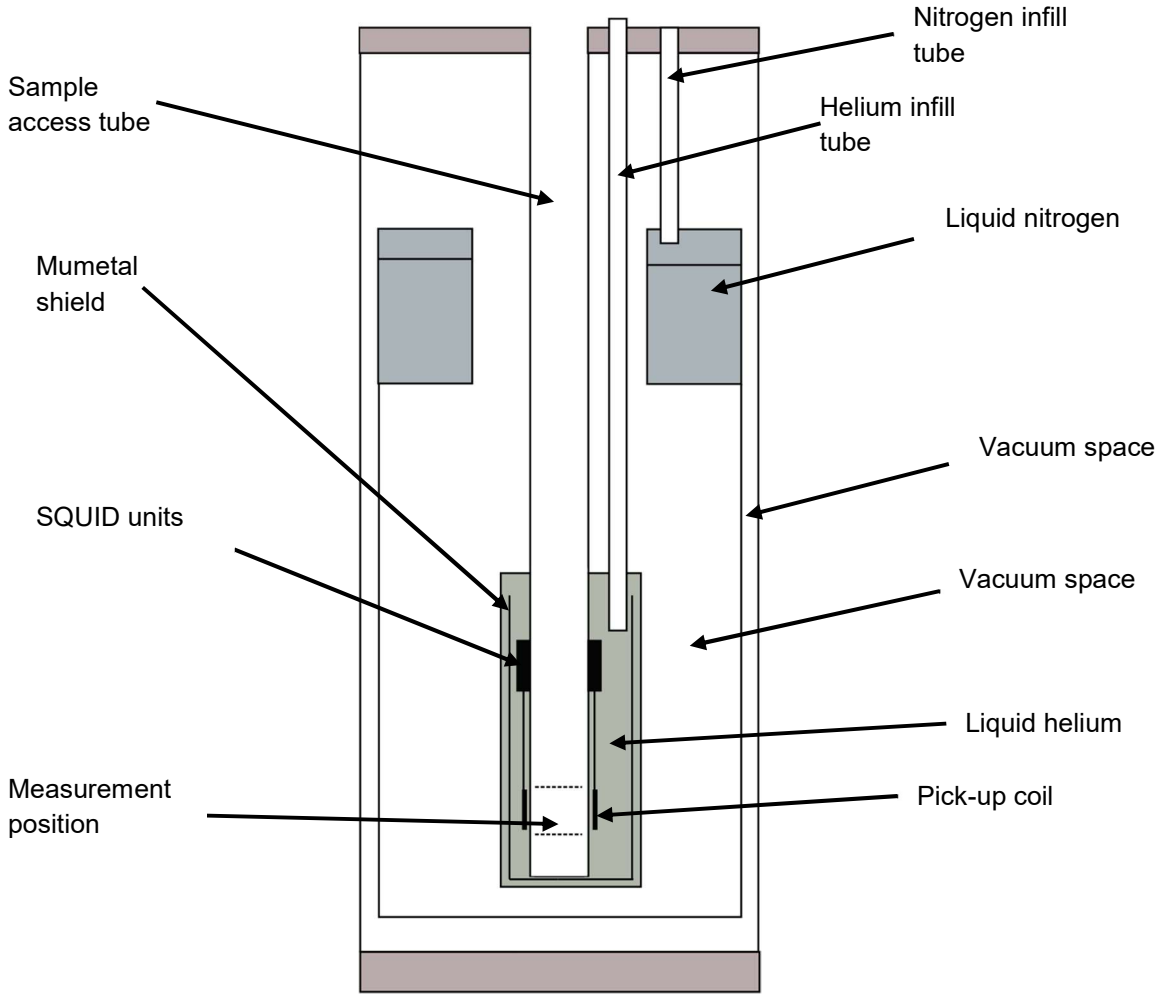

Figure 4.2. A schematic of the GM400 showing the main components (Collinson, 1983).

4.2.4 Presenting Palaeomagnetic Data

The palaeomagnetic data is transformed using the DEMAG program and then plotted into A) Zijderveld diagrams; B) stereographic projections; and C) M/M_o plot (Fig. 4.3).

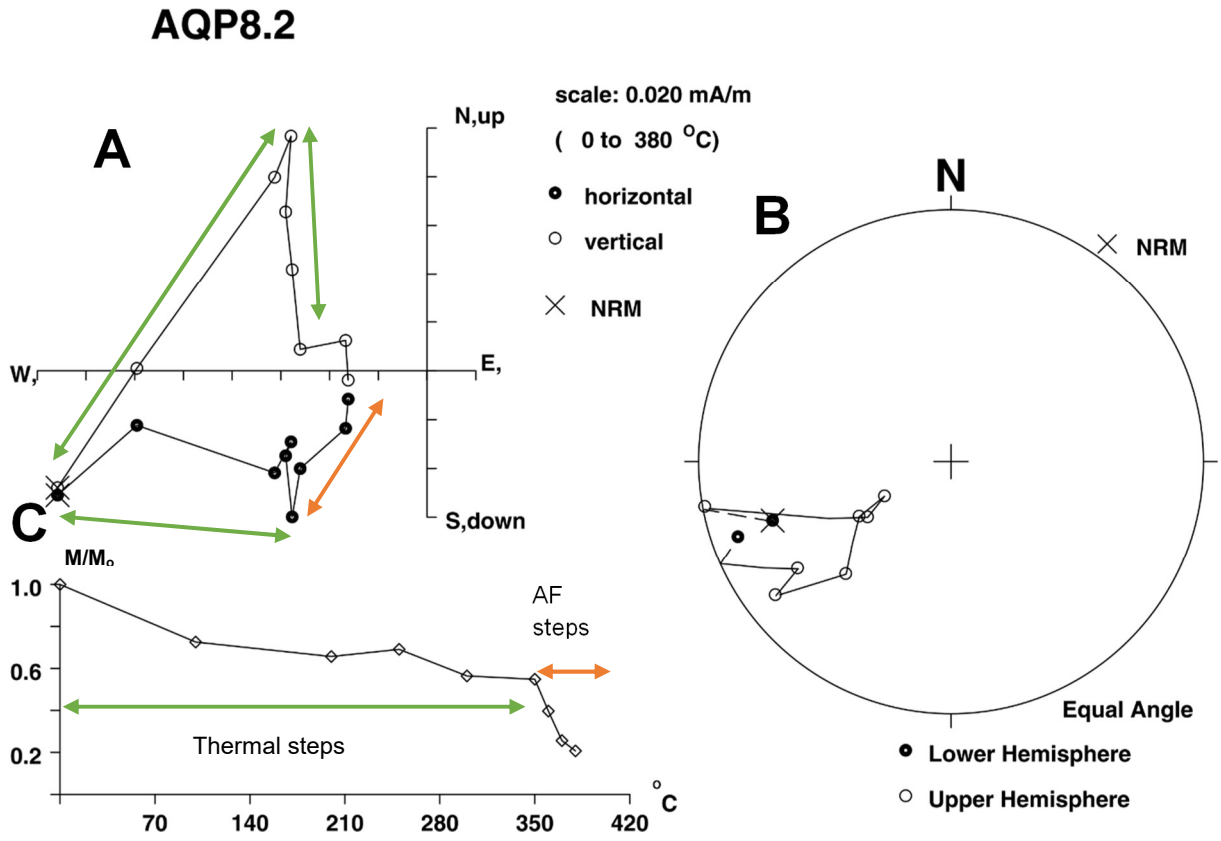

Figure 4.3. A) Zijderveld diagram (Zijderveld, 1967), B) stereograph and C) M/M_o plot. This specimen has been bedding corrected. It has been classed as T2 and the ChRM shows reverse polarity. The green and orange arrows represents the thermal and AF steps respectively.

The Zijderveld diagram displays both intensity and directional changes on to a single plot by plotting them on to orthogonal planes, where the open circles are the vertical projection (on a north-south, Up-Down axes in Fig. 4.3). The filled circles are the horizontal projection (on east-west-north-south axes in Fig. 4.3). Each axis is on an equal intensity scale which is shown at the top right, with the treatment range being indicated beneath this (Collinson, 1983).

As specimens undergo demagnetisation, each step is plotted on the graph according to Dec, Inc and intensity (Collinson, 1983). The distance of each data point from the origin is proportional to the intensity of the remanent magnetism vector plotted onto the plane (Butler, 1992). This means that the initial NRM vector (marked as the crossed circle) will generally plot furthest away from the last demagnetisation point which in turn will plot near the origin. Straight line segments that pass through the origin are normally considered to be the ChRM direction.

The stereographic projection is the 3-dimensional projection of the declination and inclination onto an equal area stereograph. Data with positive and negative inclination is represented as black and white circles, respectively. In the northern hemisphere (in Europe since Carboniferous), normal polarity is usually presented by northerly, positive inclination and reverse polarity is usually presented by southerly, negative inclination.

M/M_o plots show the normalised decay in remanence intensity throughout the demagnetisation process, were M represents the remanence intensity at that current stage and M_o is the initial remanence intensity. Fig. 4.3 shows the decay over the thermal and AF demagnetisations steps.

4.2.5 Palaeomagnetic Data Analysis

Each specimen's demagnetised data was analysed, using the LINEFIND program (Kent et al., 1983) in order to extract the magnetic components for each specimen. When examining demagnetisation data, the specimens have been subdivided into different types to reflect their behaviour:

1) S-type specimens show demagnetisation points that move along straight lines (on Zijderveld plots) corresponding with the components of the primary NRM vector (the ChRM). These are often well defined making them easier to visually interpret (Collinson, 1983). 2) T-type specimens represent results that did not show a linear component, as normal overprints could not be easily removed to isolate the ChRM vectors. Instead, each demagnetising step of these specimens occurs along a great circle path; the ChRM vector is defined as the pole to a great circle (Collinson, 1983). 3) X-type specimens where no directional components are interpreted owing to too much directional scatter or results which show only clear contamination (Table 4.2).

Table 4.2. Description of the different demagnetisation behaviours shown by each group.

Group	Description
S1	Zijderveld diagram show well defined linear component directions that trend towards the origin.
S2	Zijderveld diagram shows less defined linear component directions that trend towards the origin.
S3	Zijderveld diagram shows a vague trend indicating linear ChRM directions, trend towards origin may not be convincing.
T1	Stereographs show well defined demagnetisation path towards the expected ChRM. LINEFIND is used to define great circles (and their respective poles) for the demagnetisation paths.
T2	Similar to T1 but has a less-well defined demagnetisation path.
T3	Similar to T2 but greater directional scatter.
X	No consistent directional components seen in the Zijderveld diagram or stereograph.

4.2.6 Statistics

Initially the palaeomagnetic plots were examined to determine S-type ChRM directions and define these using LINEFIND to provide the declination (D), inclination (I) and $\gamma 95$ for each specimen. Once the S-type data was recorded per specimen wherever possible, the S-type components were then averaged using PMAGTOOL (Hounslow, 2006) (which uses Fisher statistics) to produce an average ChRM direction.

Fisher statistics (Fisher, 1953) were used to provide an α95 value. α95 is a 95% confidence interval about the mean as an angular radius of the cone of confidence (Fisher, 1953). As an example, if the calculated mean ChRM direction is 093,-23; α95= 11°, then there is a 95% probability that the true ChRM direction is within an 11° angular radius about 093,-23.

Specimens that did not show S-type behaviour were analysed using LINEFIND to determine the great circle planes that express their 'unseen' ChRM component. Only T_1 class specimens were used. The T_1 class poles and fixed point S-type ChRM components were then combined using the method of McFadden and McElhinny (1988) using PMAGTOOL (Hounslow, 2006) to provide a directional average of the 'combined' data set. This was converted to a mean virtual geomagnetic pole (VGP) position for the site.

4.2.7 Polarity

To establish the polarity of the samples, the S-type and T_1-class specimens were used to determine the virtual geomagnetic pole (VGP) latitude for each specimen. For S-type data the VGP latitude was calculated using PMAGTOOL (Hounslow, 2006) which utilised the mean VGP pole and site location to calculate the specimen VGP latitude.

Similar for the T-type data the D and I of the point on the great circle nearest to the combined mean was used to determine the specimen VGP latitude. Here a good normal polarity has specimen VGP latitude >60° or reverse polarity <-60°, thus using the VGP latitude to group specimen polarity into classes as in Table 4.3.

Table 4.3. – Description of the different groups which demonstrates different levels of quality shown by the polarity interpretation for Ainsa specimens.

Polarity	Group	Description
Normal	N	ChRM values are within the north east quadrant high VGP latitude >60°.
Normal	N?	Poorer quality ChRM values which are still within the north east quadrant high VGP latitude ~60°.
Normal	N??	Very poor data, indication from the sterograph suggests normal polarity but low VGP latitude values <60°.
Reversed	R	ChRM values are within the south west quadrant low VGP latitude <-60°.
Reversed	R?	Poorer quality ChRM values which are still within the south west quadrant low VGP latitude ~-60°.
Reversed	R??	Very poor data, indication from the stereograph suggests reverse polarity but low VGP latitude values >-60°.
Unknown	U	No clear indication of normal or reverse component. Sample may not have a preserved ChRM component.

4.3 Anisotropy of Magnetic Susceptibility (AMS) Measuring and Analysis

AMS was measured at room temperature using an AGICO MFK1-FA Kappabridge (Fig. 4.4). The specimen was placed in a holder in three positions in order to measure the AMS in each plane perpendicular to axis of the specimen (Hrouda, 1992). The deviatoric susceptibility tensor was measured while rotating the specimen in the susceptibility bridge. This combined with bulk susceptibility is then recorded to obtain the complete susceptibility tensor (AGICO, 2016; Table 4.4).

Five specimens per sample were chosen in order to average out between-specimen variance and to highlight any anomalous specimen data. The AMS directions and parameters obtained were averaged using Anisoft42 (Chadima & Jelinek, 2009). The directional data was then plotted using PMAGTOOL to produce stereoplots (Fig. 4.5).

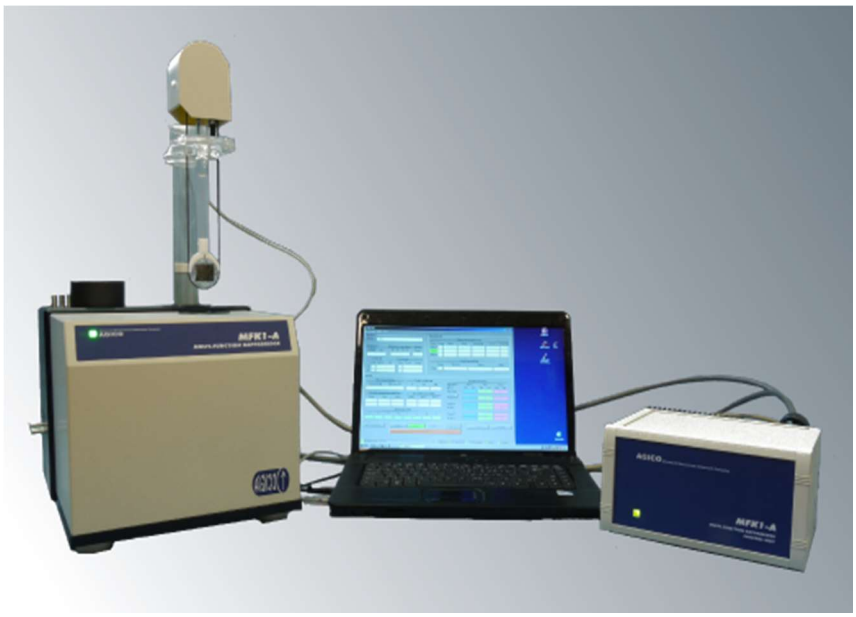

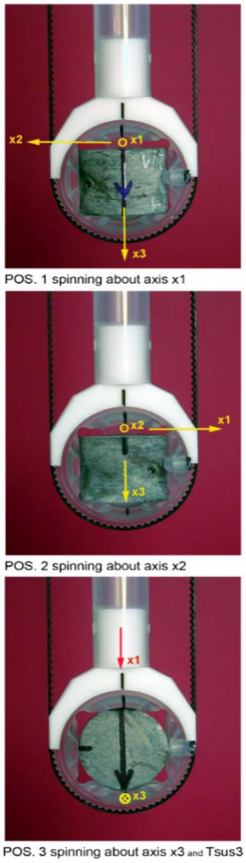

Figure 4.4. A) The Agico MFK1-FA Kappabridge setup. From left to right, the self-contained MFK1-FA Kappabridge with the rotating holder attached; the laptop used to operate, adjust the field and record the data and the power supply (AGICO, 2016). B) Is the three positions that the specimen is placed in the holder (AGICO, 2016).

Table 4.4. Shows the output MFK1-FA Kappabridge. Some key figures are a) Azi is the strike of the fiducial mark recorded in the field. b) Dip is the orientation angle normal to the fiducial mark. c) O.P. is the orientation parameters. d) Nom. Vol. is showing that the volume has been normalised to 10 cm^3. E) Act.vol. is the volume of the specimen measured in cm^3 .

The results are listed below which provide: F) the mean susceptibility. G) The normed principal susceptibilities. H) Eight anisotropy factors calculated from the normed principal susceptibilities. I) The principal directions for the specimen's azimuth given as declination and inclination for the Kmax, Kint and Kmin axes. J) Declinations and inclination that has been corrected accounting for the bedding orientation for the Kmax, Kint and Kmin axes. K) Was the date the sample were measured.

A Azi 230 **C** O.P. : 3 0 3 90 **D** Nom. vol. 10.00

B Dip 16 Demag. fac. : YES Holder -566.E-09 **E** Act. vol. 10.00

Field	**F** Mean	Standard	Tests for anisotropy		
[A/m]	susc.	err. [%]	F	F12	F23
700 F1	106.6E-06	0.0336	2056.8	110.8	3064.0

G Normed principal susceptibilities			95% confidence angles Ax1	Ax2	Ax3
1.0152	1.0087	0.9761	5.9	1.3	1.0
+-0.0003	0.0002	0.0002	1.0	5.9	1.3

H Anisotropy factors (principal values positive)

lnL	lnF	lnP	Pj	T	R	H%	Q
0.006	0.033	0.042	1.043	0.675	0.017	3.852	0.180

		Principal directions			Normed tensor		
		Kmax	Kint	Kmin			
I Specimen	D	245	339	107	1.0095	1.0098	0.9807
System	I	16	13	69	0.0035	-0.0119	0.0025
J Geograph	D	116	206	17	1.0095	1.0098	0.9807
System	I	1	7	83	0.0035	-0.0119	0.0025

K 12-02-2015

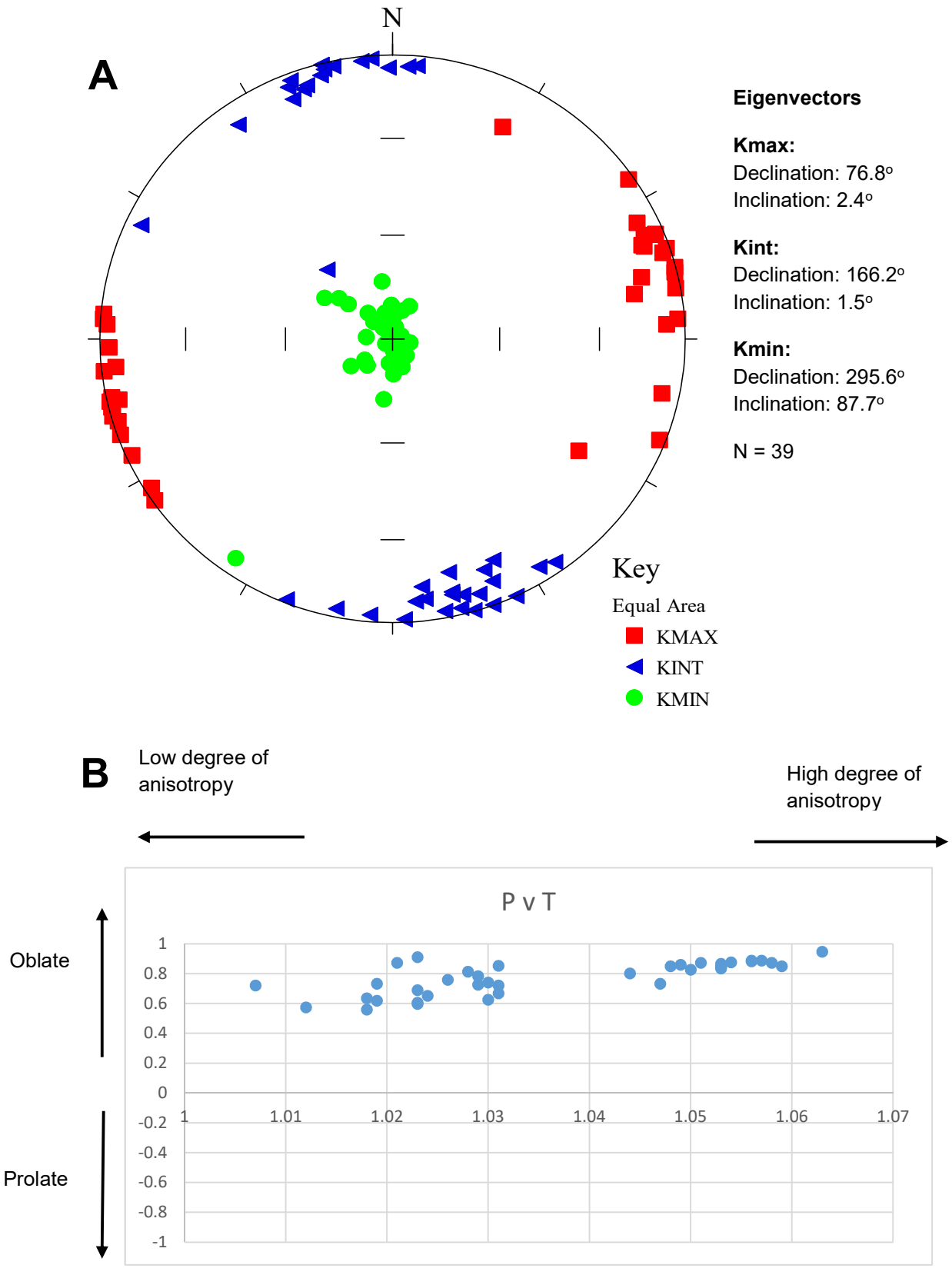

Figure 4.5. An example of a normal AMS data set. A) Is an equal area stereoplot of showing the Kmax (red squares), Kint (blue triangles) and Kmin (green circles) directions for each sample. An eigenvector mean has been given for each of the axes. B) Is a plot comparing the anisotropy parameters of different samples where P is the degree of anisotropy and T is the shape parameter.

4.4 Magnetic Mineralogy Measurements and Analysis

A subgroup of 10 specimens from Ainsa were chosen to identify the magnetic mineralogy (Maher et al., 2010). They were selected from representative lithologies and locations within the section. Specimens were measured for their low frequency mass specific magnetic susceptibility (χ_{lf}), anhysteretic remanent magnetism (ARM) and isothermal remanent magnetism (IRM) acquisition at room temperature (Robertson & France, 1994).

χ_{lf} is calculated by dividing a specimen's low frequency susceptibility by its mass. The specimen's magnetic susceptibility was measured using a Bartington susceptibility meter (MS2B) and the mass was measured using a scientific balance to three decimal places (Fisherbrand PF-203).

ARM was acquired by subjecting specimens to a DC field of 0.1mT in an alternating magnetic field of 80 mT produced by a Molspin AF demagnetiser. Specimen remanence was measured using a Minispin magnetometer. IRM was acquired by subjecting the specimens to an initial 1T magnetic field to produce the saturation isothermal remanent magnetism (SIRM). After the SIRM measurement, the magnetisation was decreased by applying progressively stronger fields in the reverse direction, each step was measured on the Minispin immediately after the field was applied to prevent the viscous loss of remanence. Remanence ratios are used to test the magnetic stability (e.g, 'S'-ratios (IRM_{100mT}/SIRM)) were used to determine the relative contribution of

hard magnetic minerals such as haematite (Maher et al., 2010). High field remanent magnetism (HIRM) is the isothermal remanence growth caused by these fields (e.g. HIRM = SIRM - $IRM100_{mT;}$ Maher et al. 2010). Data acquired can be compared graphically by using biplots of remanent coercivity versus χSIRM. The results of the mineralogical study is then compared with known magnetic parameters of magnetite, titanomagnetite, maghaemite, hematite, goethite, pyrrhotite and greigite which had been established by Hunt et al. (1995), Peters (1995) and Peters & Thomson (1998) (Peters & Dekkers, 2003).

4.4.1 Hysteresis and Thermomagnetic analysis

IRM data can only establish the ferrimagnetic minerology of the specimens, thus hysteresis experiments were used to determine paramagnetic contribution to the susceptibility. Seven representative specimens were chosen from all the case studies. Each specimen was ground into a fine powder and placed into a glass holder that was inserted into the Magnetic Measurements Variable Field Translation Balance (MMVFTB) where a series of hysteresis and thermomagnetic treatments were performed on them.

The data was then analysed using the RockMag Analyzer program (Leonhardt, 2006) which provided the parameters such as values of remanent magnetism/saturation magnetisation (Mrs/Ms) ratio or the remanence coercivity/coercivity (Hcr/Hc) ratio. These ratios can used to graphically show if the magnetite particles are SD or MD (Day et al., 1977). The program also calculates the paramagnetic/diamagnetic gradient which can be converted into a paramagnetic contribution to the induced magnetisation.

5. Case Study: Ainsa Basin

The Ainsa Basin is located in northern Spain, south of the Pyrenees, (Fig. 5.1; Dakin et al., 2013) and forms part of the Graus/Tremp-Ainsa-Jaca complex that developed as a consequence of the thrust activity associated with the Pyrenean mountain building in the Lower Eocene (Pohl & McCann, 2014).

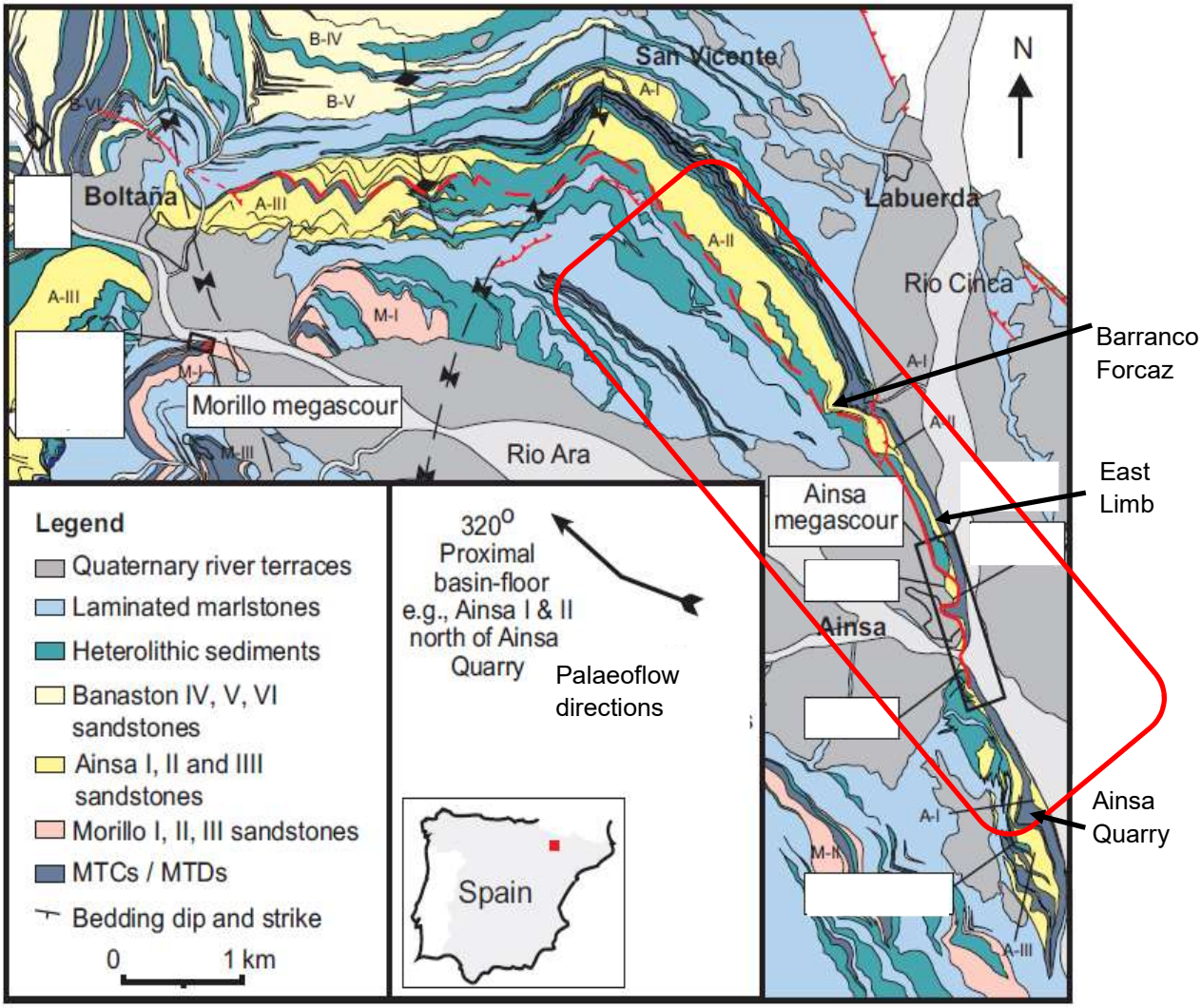

Figure 5.1. A simplified geological overview of the Ainsa Basin and where it is in relation to Spain's geography (lower panel). Modified from Dakin et al., (2013) to highlight the areas of study and show key locations. Palaeoflow directions change from westerly in the proximal erosional channels to northwesterly towards the basin floor where the Ainsa I and II fans are located.

5.1 Development of the Ainsa Basin

The Pyrenees are an asymmetric double wedge alpine fold and thrust belt that trends west-east across northern Spain (Cantalejo & Pickering, 2014). This was generated by the partial subduction of Iberia beneath the European plate, which occurred from the Lower Cretaceous to Upper Palaeogene (Pohl & McCann, 2014), with the shortening occurring between ~58-28 Ma (Pickering & Corregidor, 2005). The structural geology of the orogeny is very complex and can be divided into several sections. Going from north to south, they are the Aquitaine Basin, the northern Pyrenean Thrust System, the Axial Zone, the South Pyrenean Thrust System, and the Ebro Basin. The South Pyrenean Thrust System is characterised by an imbricate system of cover thrust sheets associated with south-verging folds (Mochales et al., 2012); this was the zone that would have influenced the development of the Ainsa Basin (Pohl & McCann, 2014).

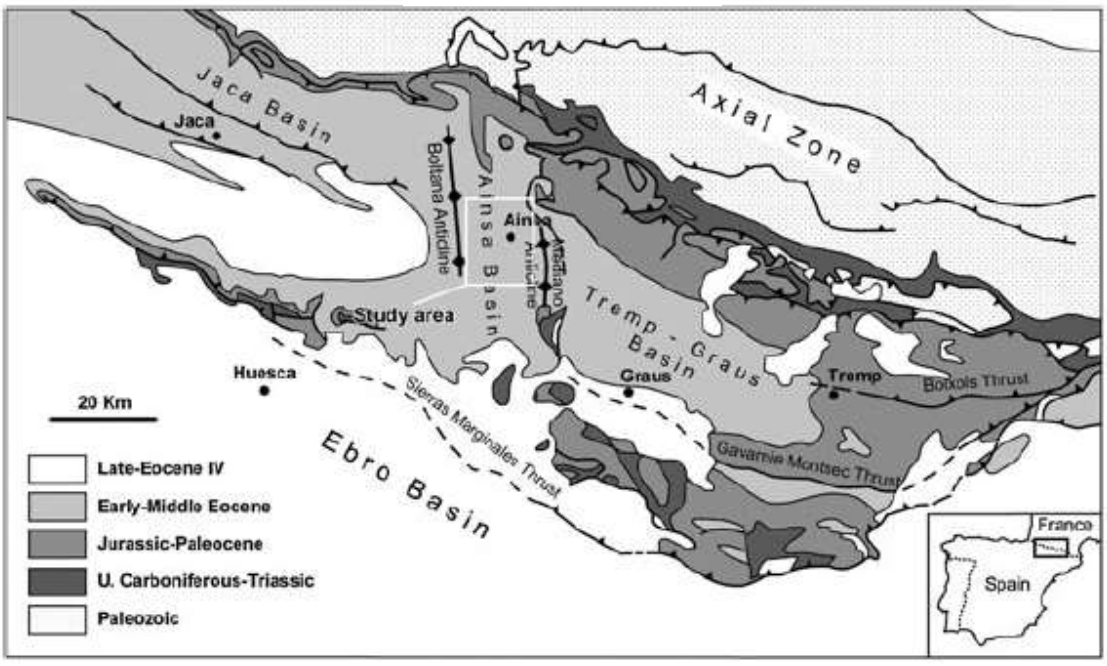

Figure 5.2. Map of the South Pyrenean thrust zone. The white box in the centre of the map represents the study area. It shows the geography of the Graus/Tremp-Ainsa-Jaca basin complex, while also showing the major thrust faults and folds (Pohl & McCann, 2014).

There are three major south facing thrusts: the Sierras Marginales, Montsec, and Bóixols thrusts (Pohl & McCann, 2014). The Ainsa Basin is located on the minor Gavarnie thrust sheet and formed during movement along the thrust sheets in the Palaeocene and Eocene, which produced the Mediano and Boltaña anticlines (Pohl & McCann, 2014). This led to the formation of the Ainsa Basin as an interlinked east-west orientated, deep-marine '*piggy back'* basin (Pohl & McCann, 2014). The Ainsa Basin was locked between the shallow marine basins of Graus/Tremp to the east and the Jaca deep marine basin to the west. The basin is 40 km wide and is dominated by turbiditic deposits and is composed of various sand bodies that are separated by thick shales (Pohl & McCann, 2014). The basin is bounded to the east and west by the Mediano and Boltaña anticlines respectively, with the Buil Syncline between these (Fig. 5.2; Pohl & McCann, 2014). This folding occurred between the Ypresian to late Lutetian owing to movement along the Gavarnie thrust sheet (Pohl & McCann, 2014). The Ainsa Basin is also bound to the north by faulting relating to the South Thrust System and to the south anticline of Sierras Marginales (Fig. 5.2; Pohl & McCann, 2014).

5.2 Factors Controlling Deposition

The Ainsa Basin is divided into four unconformity-bounded units, with the turbidites stratigraphically in the third unit (Falivene et al., 2006). Deposition was influenced by the tectonics of the active basin. The basin shape and position were dominated by the synchronous development of the anticlines and thrust-induced flexure (Falivene et al., 2006). The other major control on sedimentation was glacio-eustatic sea level change and Milankovitch cyclicity. Cantalejo & Pickering (2014) show evidence of 4 recurrent frequencies of eccentricity (c.110 kyr), obliquity (c.40kyr) and precession couplets (c.23 kyr and c.19kyr) on bedding rhythms. These controlling orbital factors would either have increased rates of chemical weathering leading to greater river runoff (and more associated deep-sea turbidites), or Milankovitch cyclicity led to greater river progradiation during low stand tracts in cooler climates, leading to greater amounts of detrital delivery to the shelf edge (Cantalejo & Pickering, 2014).

5.3 The Ainsa Basin

During the Lutetian stage of the Eocene the Ainsa Basin developed from fluvio-deltaic to a deeper continental shelf clastic system (Pickering & Corregidor, 2005). The turbidites were fed from the southeast by a fluvio-deltaic complex, with the mean palaeocurrent direction travelling towards the northwest across the present day Buil syncline (Pickering & Corregidor, 2005) which is supported by gouge-like striations, orientation of residual limestone pebbles and elongated

holes (where pebbles have been eroded out) (Dakin et al., 2013). Therefore most sediments that outcrop on the south east limb represent more proximal deposits. These can be correlated with sediments on the north western-eastern limbs which represent more distal sediments (Dakin et al., 2013).

Each of the four unconformably bounded units is geographically extensive being 20 km in length and up to 9 km wide with strata thicknesses between 80-800 m. These units are composed of a coarse-grained basal unit, capped by fine grained mudstones (Falivene et al., 2006). The Ainsa fans are located above the Banaston and below the Morillo members (Fig. 5.3; Scotchman et al., 2015).

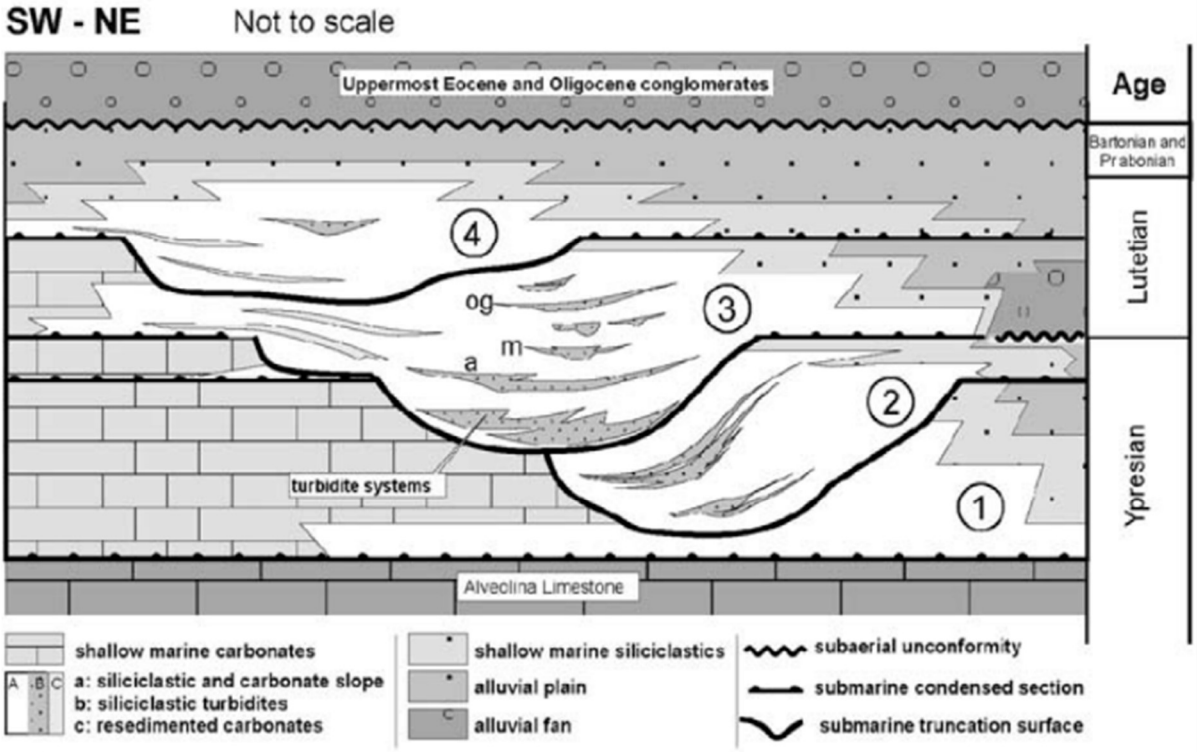

Figure 5.3. General stratigraphy of the Ainsa Basin. Numbers 1-4 represent the four unconformable units. Ainsa (a), Morrilo (m), O Grao (og) turbidite systems occur in the third unit (Falivene et al., 2006).

The base of the turbidites are generally erosional with some showing mixed erosional-depositional channel fills that are related to overbank deposits and muddy slump deposits (Falivene et al., 2006). There are large amounts of carbonate clastics within the sediments; the supply of carbonate is associated with the collapse of the adjacent unstable carbonate platform (Pohl & McCann, 2014). Carbonate clastics are particularly prominent during the deposition of the Morillo turbidite system (Pohl & McCann, 2014).

The major facies of the Ainsa Basin are listed and described in Table 5.1 (Falivene et al., 2006).

Table 5.1. A table summarising features of the main sedimentary facies in the Ainsa Basin (Falivene et al., 2006).

	Main component	Additional components	Main depositional processes
Debrites (D)	Sandy and gravelly mudstone	Clast-supported conglomerates Mud-clast-rich conglomerates Coarse-grained pebbly sandstones	Mainly cohesive debris flows Hyper-concentrated flows High-density turbidity currents
Sandstones (Ss)	Thick-bedded, coarse-to-medium-grained sandstones	Packages formed by thin-bedded turbidite sandstone and mudstone beds Lenticular beds and packages of the facies described in the context of the D facies association	High and low-density turbidity currents
Heterolithics (Ht)	Alternations of fine-grained and thin-bedded sandstones and mudstones	Mudstone beds Medium-to thick-bedded coarse-grained sandstones	Low-density turbidity currents and background settling
Slump-deformed mudstones (Sd)	Thick units made of thin-bedded mudstone with a soft-sediment deformed structure	Thin packages of turbidite sandstones and mudstones	Slumps
Resedimented limestones (Rl)	Mixtures of soft-sediment deformed mudstone and various types of soft-sediment deformed limestone clasts	Meter-thick packages of turbidite sandstones and mudstones	Debris flows

The Ainsa system turbidites are characterised by three fan deposits, Ainsa Fan I, II and III (Pickering & Corregidor, 2005). The palaeogeography of these fans indicates laterally stacked systems towards the foreland in the northeast (Fig. 5.4; Pickering & Corregidor, 2005). The fans tend to have a chaotic basal unit of debrites, sediment slides and/or slump deposits; these basal units are known as mass transport complexes (MTC's) or mass transport deposits (MTD's) for individual deposition events (Scotchman et al., 2015). The fan complexes typically contain 2-3 individual sand bodies which vary in thickness between 30-100 m, separated by mainly thin bedded sandstones and shales (Fig. 5.5; Pickering & Corregidor, 2005).

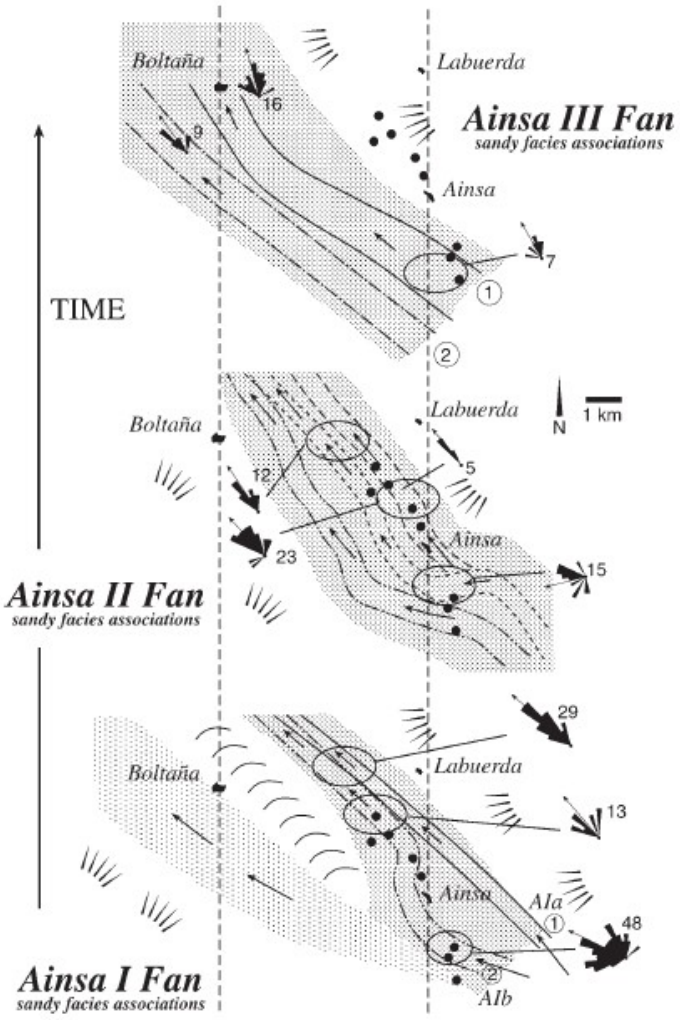

Figure 5.4. Palaeogeography of Ainsa fan I, II and III which are laterally stacked towards the foreland basin (to northeast), highlighted by the progression west of the hashed lines in later fans. The fans have been left unrestored from folding. The palaeocurrent indicators are shown generally orientated northwest in the rose diagrams (from Pickering & Corregidor, 2005).

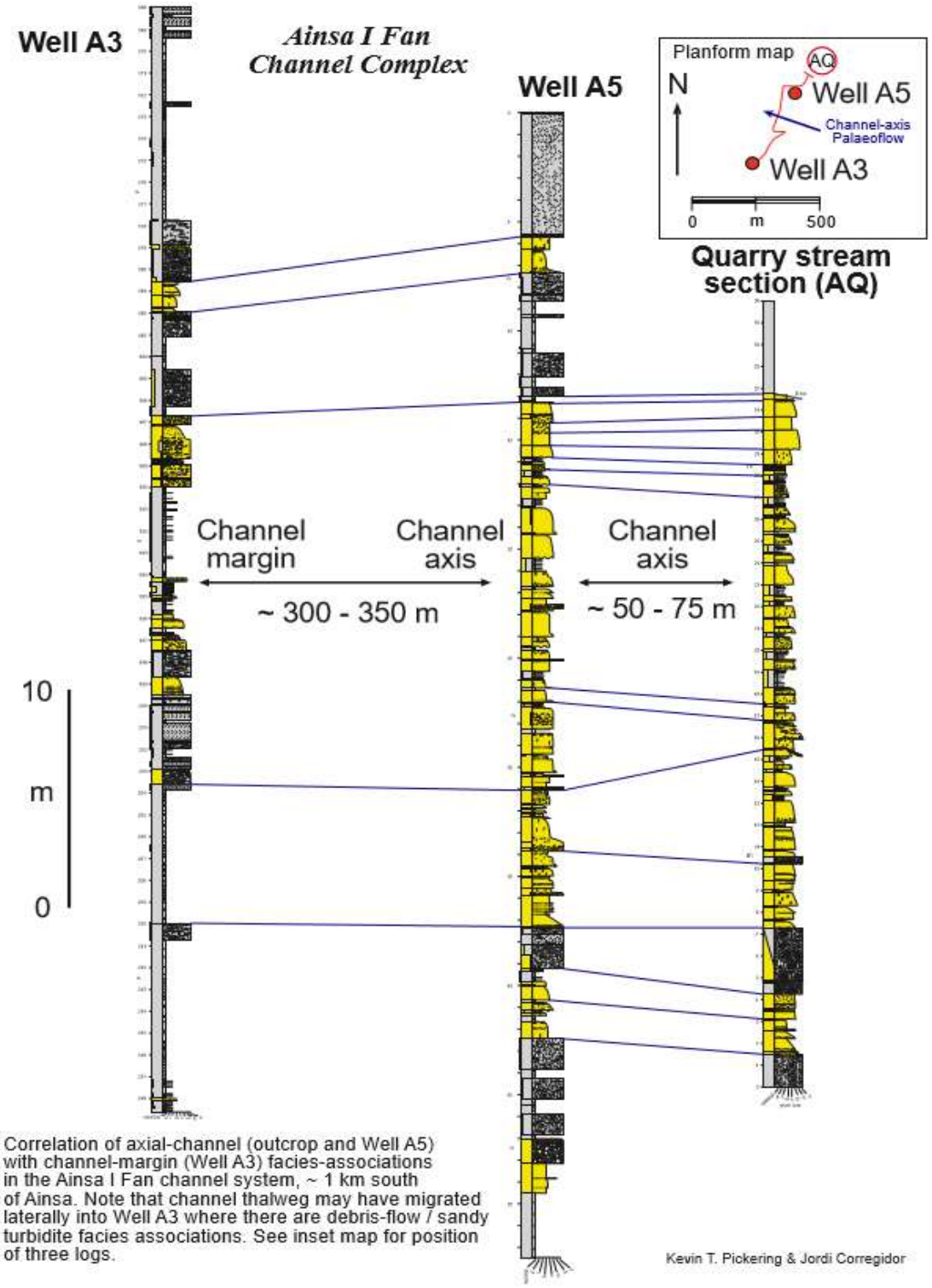

Figure 5.5. Sedimentary logs taken from the Ainsa Quarry site and cores around the area. They have been correlated to provide accurate interpretation of Ainsa fan I (from Pickering & Corregidor, 2005). The location of the Ainsa Quarry is shown in Figure 5.1.

The other deposits within the Ainsa Basin are mass transport complexes (MTC's). MTC's are characterised by debris flows of variable muddy debrites that may contain a large sand content. These deposits have heterogeneous to heterolithic textures (Dakin et al., 2013). Debrites tend to be matrix-supported, disorganised and poorly-sorted (Dakin et al., 2014), commonly with pebbly mudstone facies that are composed of large clasts that vary between >4 mm to 1 m in length. These clasts are well-rounded and composed of limestone, sandstone, chert, quartzite, minor amounts of granite, and angular to sub-angular mud clasts (Dakin et al., 2013). In some cases debrites are composed of angular bioclastic material of reworked corals or fragmented shells (Dakin et al., 2013).

5.4 Biostratigraphy and Age

Pickering & Corregidor (2005) have used foraminiferal assemblages in cores and outcrops to establish that Ainsa Basin sediments were deposited during the mid-Lutetian. They placed the deposits around planktonic foraminiferal zones of P11-12 and calcareous nanofossil zone of NP14-15, suggesting that the Ainsa basin was deposited rapidly in a relatively short time between c.47-46 Ma (Scotchman et al., 2015).

(Pickering & Corregidor, 2005) distinguished 3 major palaeontological events within the Ainsa I fan. The oldest event, A, suggests an upper to mid bathyal environment with normal salinity and aerobic bottom water (Pickering & Corregidor, 2005).

The next event, B, is a period of low diversity among microfauna, with no planktonic foraminifera (Pickering & Corregidor, 2005), suggesting a slightly deeper bathyal environment with dysaerobic conditions (Pickering & Corregidor, 2005). Event C is an acme for planktonic foraminifera and is thought to be caused by increased sea level, making it a contender for a maximum flooding interval. Echinoid, bivalve, gastropod, miliolids, and nummulitic fossils are found frequently and would have been initially from shelf deposits.

Heard et al. (2014) examined the ichnofabrics of the Ainsa System. Ichnofabrics are by controlled several factors such as substrate consistency, nutrient supply, oxygenation levels, salinity, hydrodynamics, rate of sedimentation, and chemical toxicity (Heard et al., 2014). Ichnofacies are used as proxies for diversity and can be used to interpret different sections of a turbidite (Table 5.2). The channel axis and off-axis facies can be identified from the limited biodiversity when compared to the heavily bioturbulated levée-overbank facies (Heard et al., 2014).

Table 5.2. A summary of the environments associated with the Ainsa Turbidite System, describing the lithological differences of the key facies, showing an ichnological summary, highlighting levels of bioturbation and key trace fossils found in these environments (Heard et al., 2014).

Environment	Summary	Ichnology
Channel axis	Thick-bedded coarse-grained to very coarse-grained amalgamated sandstones and mud-clast conglomerates. Normal grading is well-developed in many sandstones, and planar stratification is common in many beds. Pebbly Type II MTCs are common	Low bioturbation intensity and ichnodiversity dominated by *Ophiomorpha, Thalassinoides* and *Planolites. Ophiomorpha* and *Thalassinoides* ichnofabrics dominate
Channel off-axis	Amalgamated to non-amalgamated medium-bedded to thick-bedded sandstone packages several metres thick overlain by non-amalgamated medium-bedded, medium-grained to fine-grained metres thick overlain by non-amalgamated medium-bedded, medium-grained to fine-grained	Low bioturbation intensity and ichnodiversity but slightly higher than channel axis. Commonest ichnotaxa: *Ophiomorpha, Thalassinoides* and *Planolites.* Characterized by *Ophiomorpha–Thalassinoides* and *Thalassinoides* ichnofabrics
Channel margin	Basal amalgamated to non-amalgamated thin-bedded to medium-bedded sandstones overlain by thin-bedded, fine-grained to coarse-grained sandstones. Thick muddy intervals (<1 m thick) associated with siltstone–marlstone laminae, as well as intensely bioturbated sandstones, siltstones and marlstones are developed towards the top forming an overall fining-upward trend.	Moderate bioturbation intensity and moderate to high ichnodiversity dominated by *Thalassinoides, Phycosiphon, Planolites, Chondrites* and *Scolicia. Thalassinoides–Phycosiphon* and *Scolicia* ichnofabrics are most common
Levée-overbank (Ainsa II & III complex set)	Thin-bedded to medium-bedded fine-grained sandstones with relatively thick marlstone partings associated with intensely bioturbated sandstones and siltstones, as well as siltstone–marlstone laminae	Moderate to high bioturbation intensity and ichnodiversity dominated by *Planolites, Phycosiphon, Scolicia, Thalassinoides, Chondrites* and *Skolithos.* Characterized by *Planolites* ichnofabric
Levée-overbank (Ainsa I complex set)	Basal thin-bedded, fine-grained to medium-grained sandstones with thick muddy intervals between the sandstones. Overlain by mottled siltstones and marlstones, forming fining-upward trend. Thin intraformational MTCs occur throughout.	Moderate to high bioturbation intensity and ichnodiversity dominated by *Planolites, Chondrites, Phycosiphon, Thalassinoides* and *Scolicia.* Characterized by the *Planolites–Chondrites* ichnofabric
Abandonment Phase	Thin-bedded sandstones and siltstone–marlstone laminae, as well as intensely bioturbated sandstones, siltstones, marlstones and laminated marlstones	Moderate to high bioturbation intensity and high ichnodiversity dominated by burrow mottling, *Phycosiphon* and *Planolites.* Characterized by the *Phycosiphon–Planolites* ichnofabric
Interfan	Thick type Ia MTCs are abundant in the intrafan between Ainsa I and II. Thick packages of intensely bioturbated, thin-bedded sandstones, marlstones and siltstones occur throughout the interfan and intrafan	High bioturbation intensity and ichnodiversity dominated by burrow mottling, *Phycosiphon, Planolites, Thalassinoides, Chondrites, Nereites* and *Scolicia.* Characterized by burrow mottled-*Phycosiphon* ichnofabric

5.5 Previous Palaeomagnetism Studies

Amorós (2014), Mochales et al. (2012) and Muñoz et al. (2013) have examined the magnetostratigraphy of the Ainsa Basin sediments. They found the main magnetisation carrier was magnetite with variable amounts of iron sulphide. The high-quality ChRM data was mainly carried by magnetite. The Ainsa Basin samples these authors studied were magnetically noisy owing to a sulphide content created during diagenesis.

Mochales et al. (2012) found apparent synform magnetisation (at 80% unfolding which was non-significant with respect to total restoration (Fig 5.6). They observed a significant prefolding ChRM component which was primary in origin (Fig.5.6). The ChRM showed two groups, a northeast positive inclination group representing normal polarity and a southwest negative inclination group representing reverse polarity.

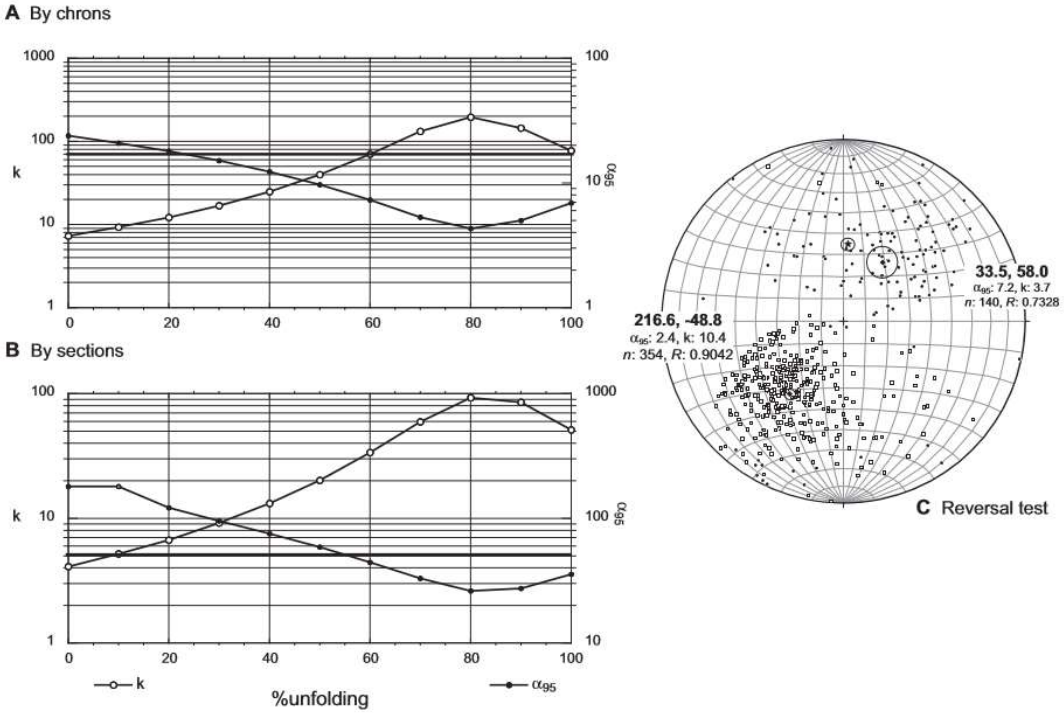

Figure 5.6. There is a slight evidence of synfolding-magnetisation in the fold tests (A-B), likely caused by incomplete component separation. C) Stereograph showing the ChRM data obtained by Mochales et al., (2012) (corrected for the bedding dip).

Micropalaeontology, litho- and magnetostratigraphy have been used to provide a general stratigraphy of the Hecho Group (Fig. 5.7; Scotchman et al., 2015).

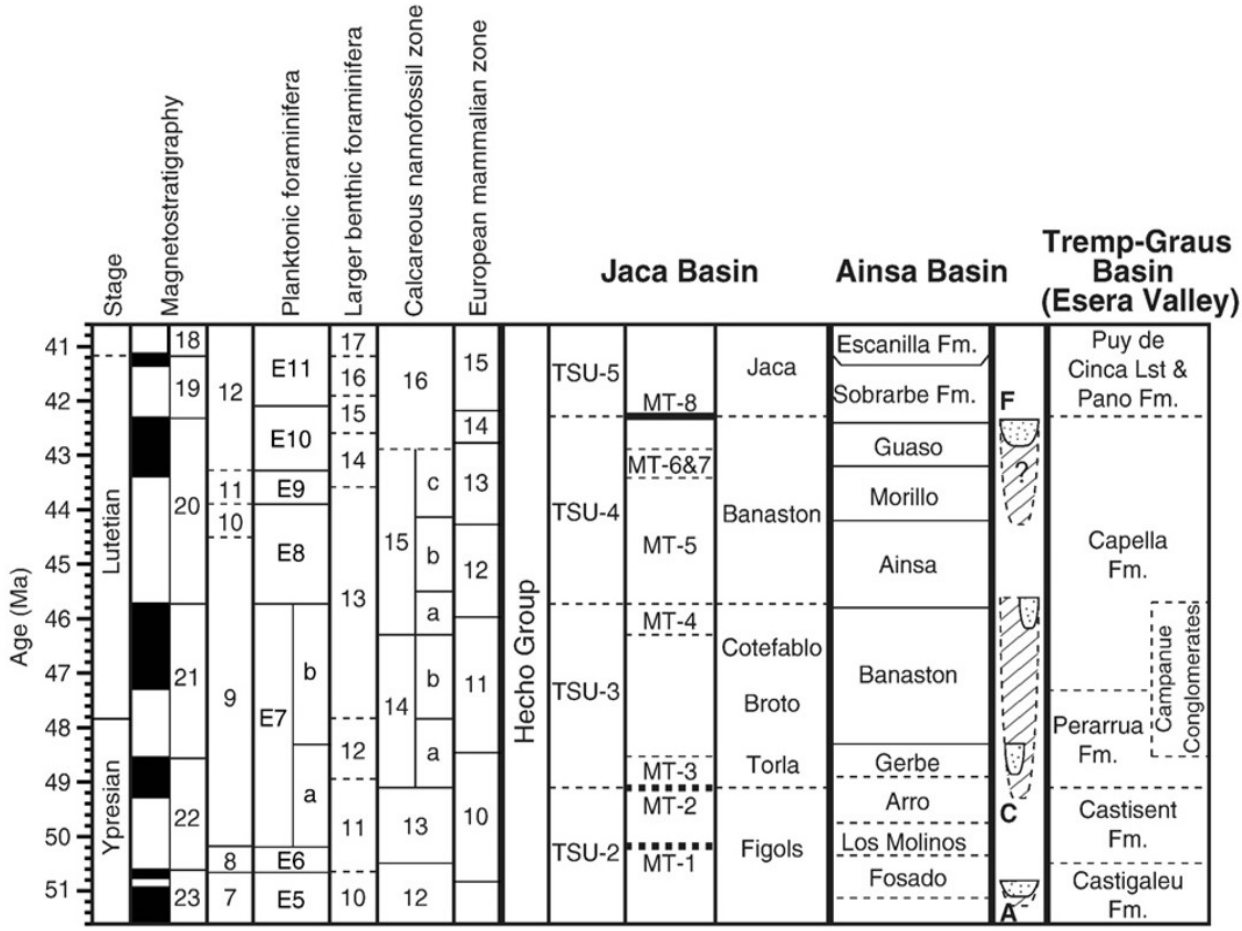

Figure 5.7. Summative chronostratigraphy which compare the Jaca, Ainsa and Tremp-Graus Basins using magnetostratigraphy, palaeontology and micropaleontology (Scotchman et al., 2015). Dating of the Jaca Basin is based upon the dating of megaturbidites (MT) and tectonostratigraphic unit (TSU) divisions taken from Remacha et al., (2003). The dashed and dotted lines represent low confidence in the chronostratigraphic boundaries.

5.6 Ainsa System Study Area

The study focuses on the turbiditic deposits of the Ainsa System, which was chosen because of its well described and well exposed nature. Samples were collected in two stages, the initial set of samples was collected by Luke Morgan and Emma Davies from Chemostrat Limited and the second set was collected during fieldwork 12/10/2015-20/10/2015. Two sites near the town of Ainsa were chosen in the study, the Ainsa Quarry (site A) and the Barranco Forcaz (site B) (Fig. 5.8). Site A is the oldest part of the Ainsa system examined in this study and is a complete outcrop of the Ainsa Fan I (Fig. 5.9).

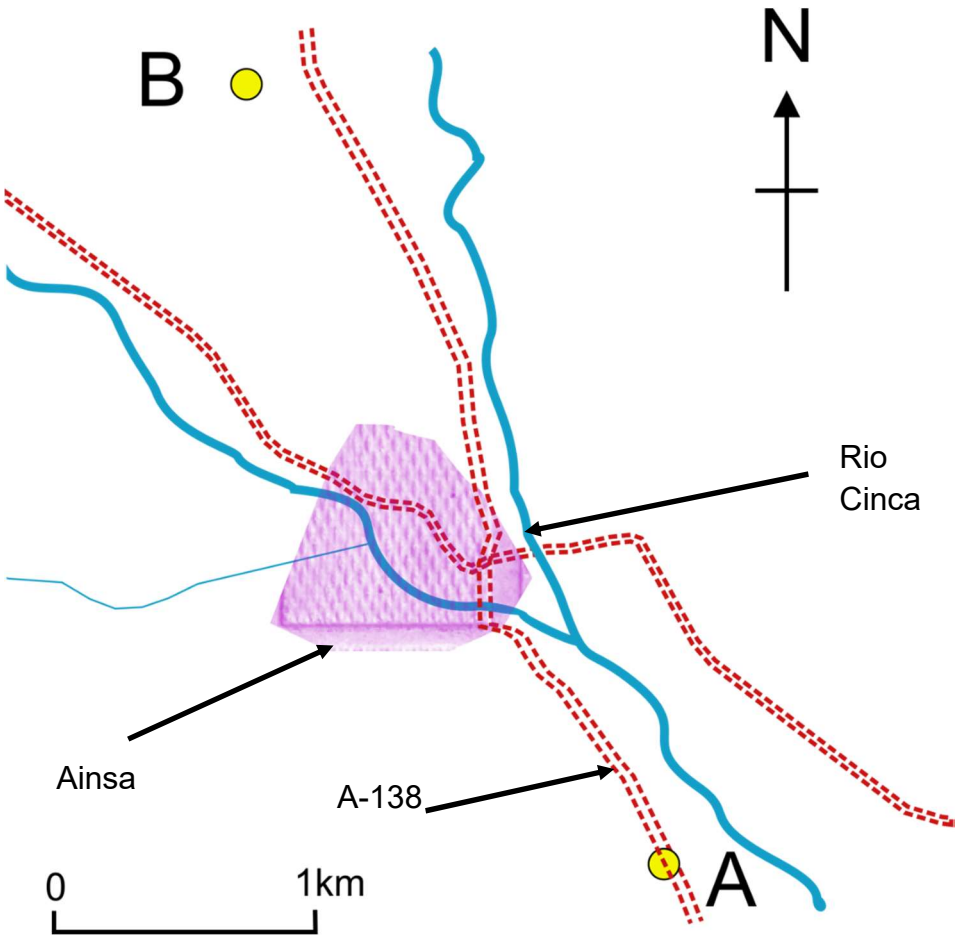

Figure 5.8. Sketch map of Ainsa showing the geographical relationship between the two sites which are labelled A and B. A, the Ainsa Quarry site I located ~1.3 km south west of Ainsa and B: Barranco Forcaz site which is located ~2.4 km NNW of Ainsa. Several other features such as the main roads (in red) and river systems (in blue) are marked on the map.

5.6.1 Ainsa Quarry Site

The lithology of the Ainsa I fan is dominated by highly channelised turbiditic deposits, overlain by an inter-fan shale. A sedimentary log of the Ainsa site is shown in Fig. 5.10 and the relationship of the beds are shown in Fig. 5.11. The lithologies show great amounts of bioturbation (Fig. 5.12), making it difficult to gain palaeoflow data. However, seven tool marks were measured indicating a vector mean towards 342º.

5.6.2 Barranco Forcaz Site

The lithology at this site is part of the Ainsa II fan which succeeds the Ainsa I facies (Fig. 5.9). The lithologies represents more distal turbidite deposition with a greater contribution of mud, highlighted in Fig. 5.13. The bedding demonstrates less variability in thickness than in the Ainsa Quarry owing to a lesser degree of channelisation. The site starts at the top of the Ainsa I interfan-shale and ends at the end of the Ainsa II fan.

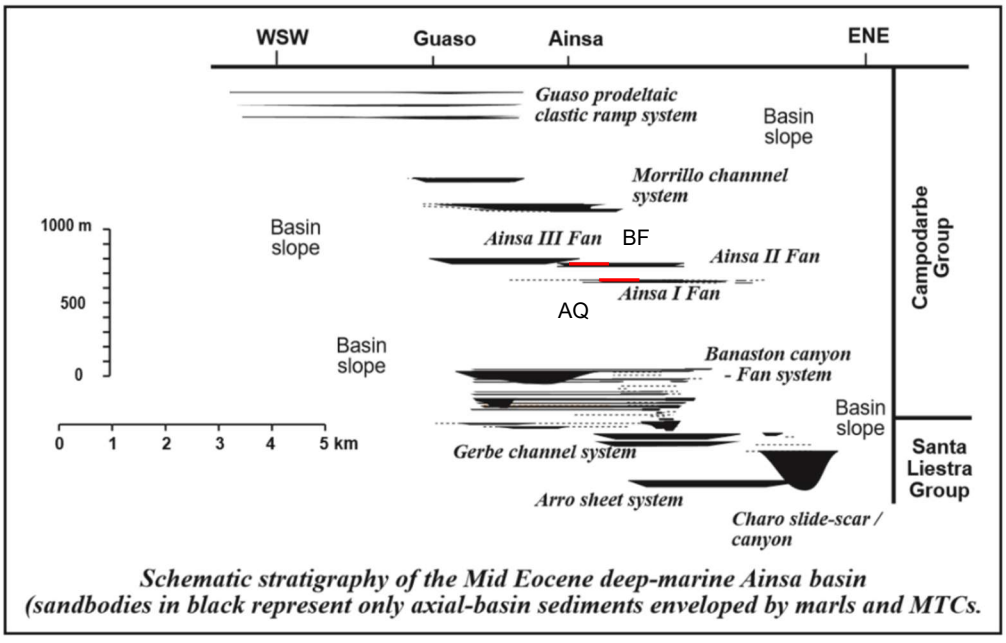

Figure 5.9. Stratigraphy of the Ainsa Basin, showing the size and extent of the Ainsa system. The positions of the Ainsa Quarry (AQ) and Barranco Forcaz (BF) sites have been marked (Pickering & Corregidor, 2005)

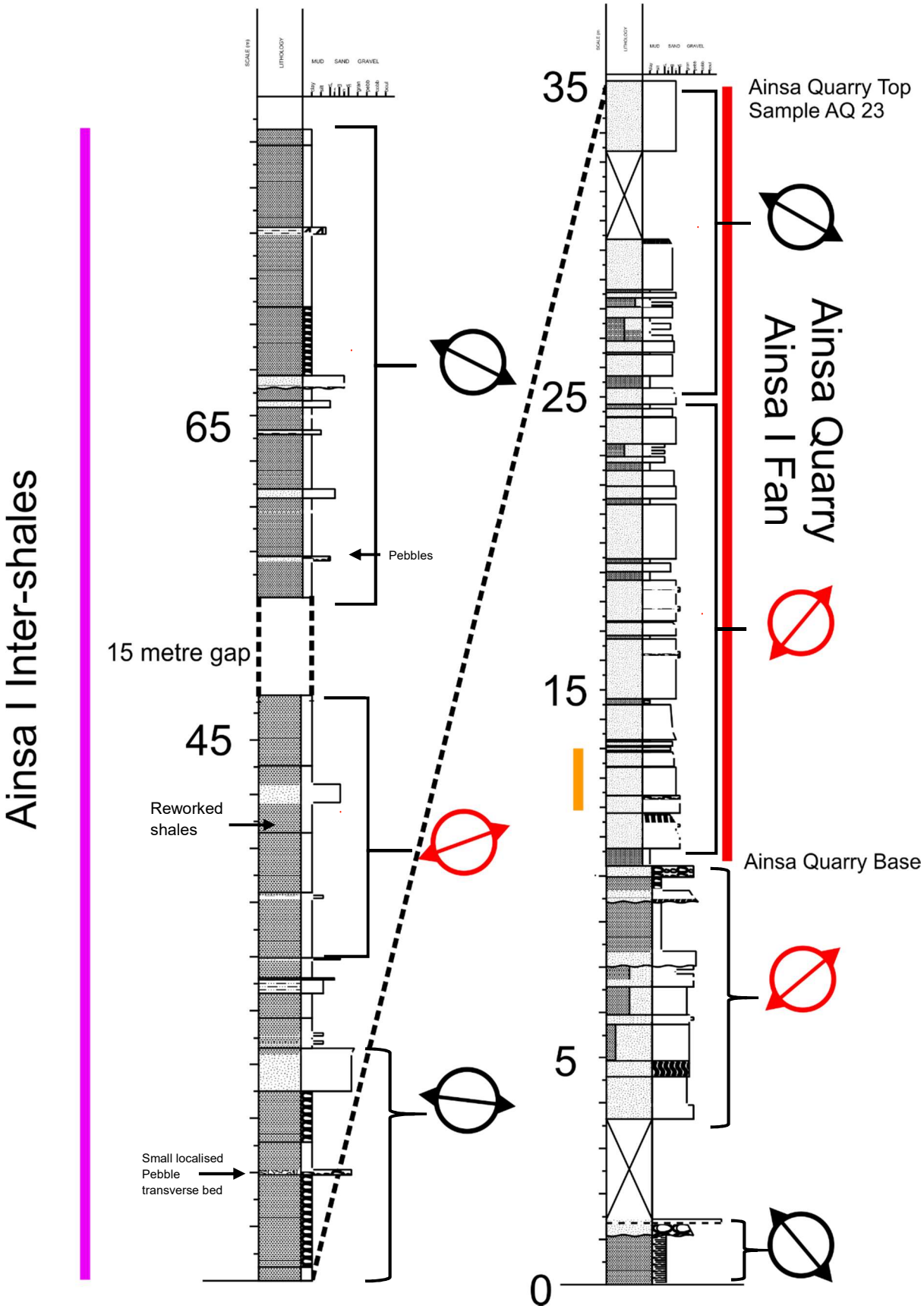

Figure 5.10. Log of the Ainsa Quarry site which has been divided into the Ainsa Quarry composed of the turbiditic Ainsa I Fan and the succeeding Ainsa I Interfan-shales found directly above Ainsa Quarry. Sample mean Kmax directions are shown throughout the sequence by the arrows which have been divided into flow-parallel (black) and transverse (red) Kmax directions. Yellow line is where the individual turbidite was sampled. Some of the shales at the top of the Ainsa Quarry show a transverse direction which would indicate reworking of these shales.

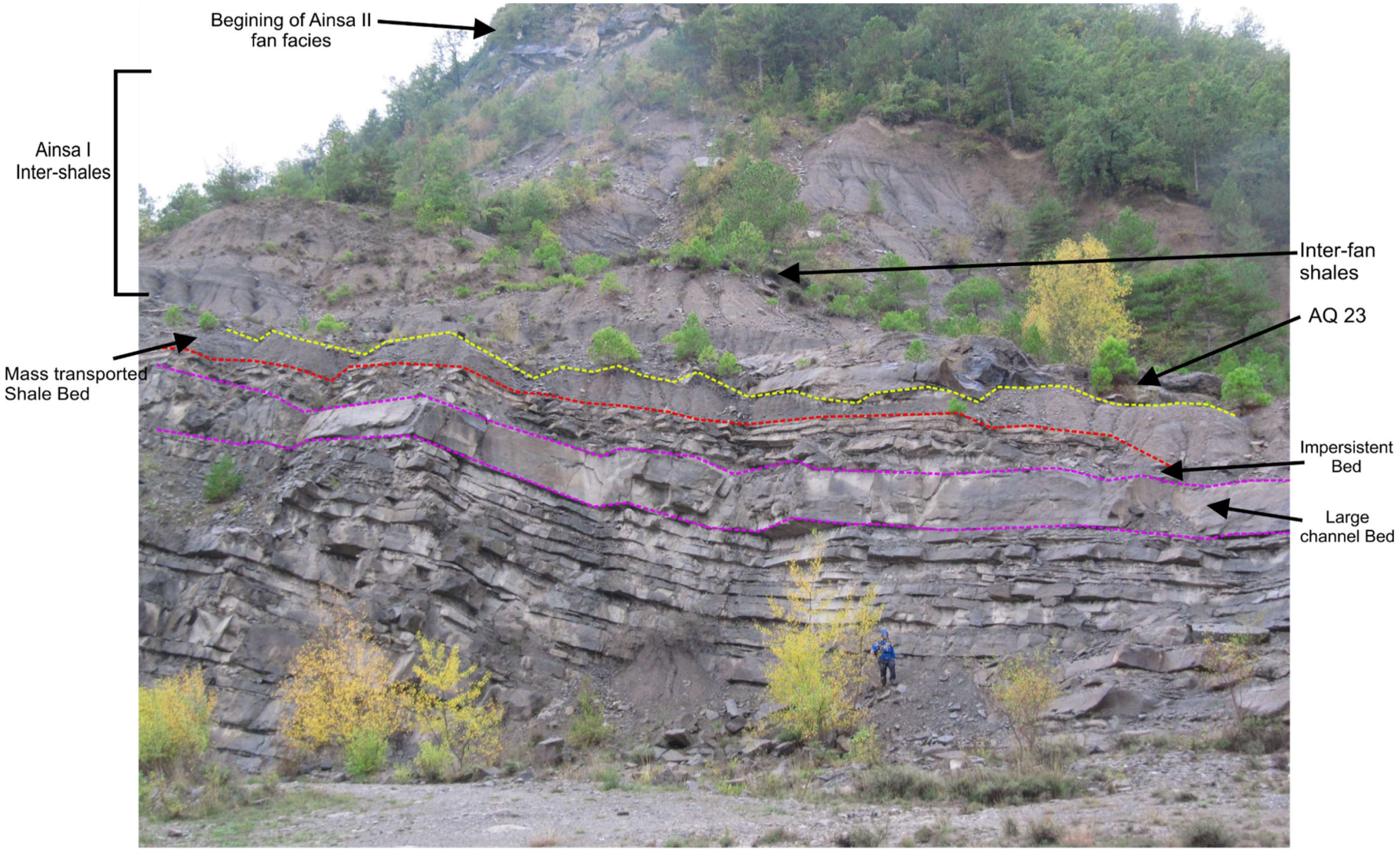

Figure 5.11. Photograph of the Ainsa Quarry, taken adjacent to the road. The photo highlights relationship between the thick sandstone beds of the Ainsa I fan and the mud dominated Ainsa Interfan-shales. The boundary between the two has been marked by a thick sandstone bed where AQ 23 was taken.

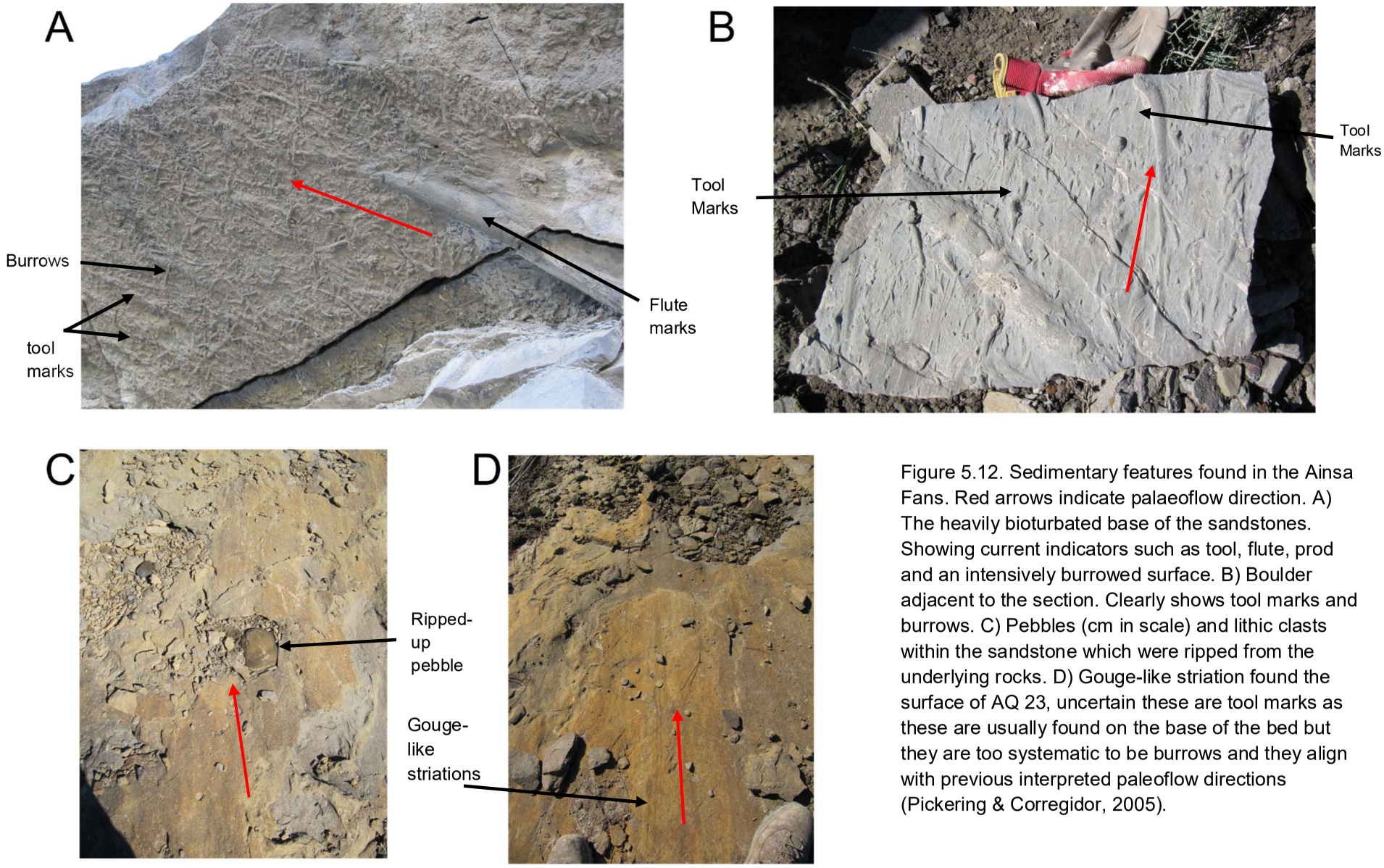

Figure 5.12. Sedimentary features found in the Ainsa Fans. Red arrows indicate palaeoflow direction. A) The heavily bioturbated base of the sandstones. Showing current indicators such as tool, flute, prod and an intensively burrowed surface. B) Boulder adjacent to the section. Clearly shows tool marks and burrows. C) Pebbles (cm in scale) and lithic clasts within the sandstone which were ripped from the underlying rocks. D) Gouge-like striation found the surface of AQ 23, uncertain these are tool marks as these are usually found on the base of the bed but they are too systematic to be burrows and they align with previous interpreted paleoflow directions (Pickering & Corregidor, 2005).

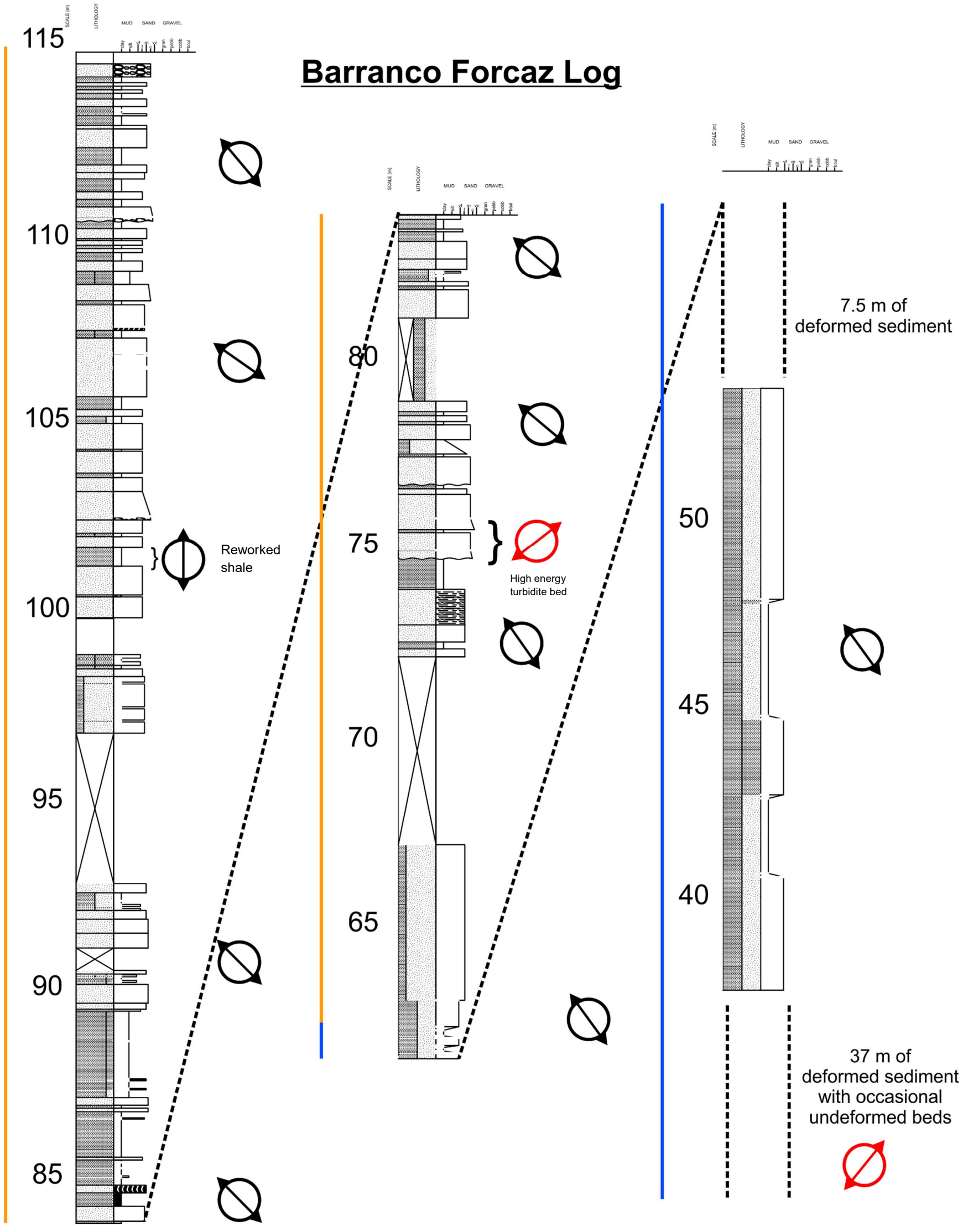

Figure 5.13. Log of the Barranco Forcaz site, the site has been divided into the Ainsa I interfan-shale (blue) and Ainsa II fan (orange). Older parts of the Ainsa I interfan-shale were too deformed to log. Sample mean Kmax directions are shown throughout the sequence by the arrows which have been divided into flow-parallel (black) and transverse (red) Kmax directions. The majority of the samples reflect flow parallel Kmax directions.

5.7 Palaeomagnetism of the Ainsa System

Palaeomagnetic data was obtained from 71 specimens, 29 from the Ainsa Quarry and 42 from Barranco Forcaz. Twenty specimens were initially subjected to full thermal demagnetisation. However, later specimens were only thermally demagnetised to 350-400°C, due to major heat-induced alteration. Data from the initial 20 specimens was too impacted by large increases in intensity and scattered directions to be useful.

Most of the specimens were treated by thermal demagnetisation in regular steps to 350°C, and then using AF demagnetisation in regular steps of 10 mT up to about 90 mT. Specimens were demagnetised until the destruction of magnetic remanence was achieved, destruction was assessed by either increases in magnetic intensity of the specimen or incoherent/random directions.

5.7.1 Palaeomagnetism Results

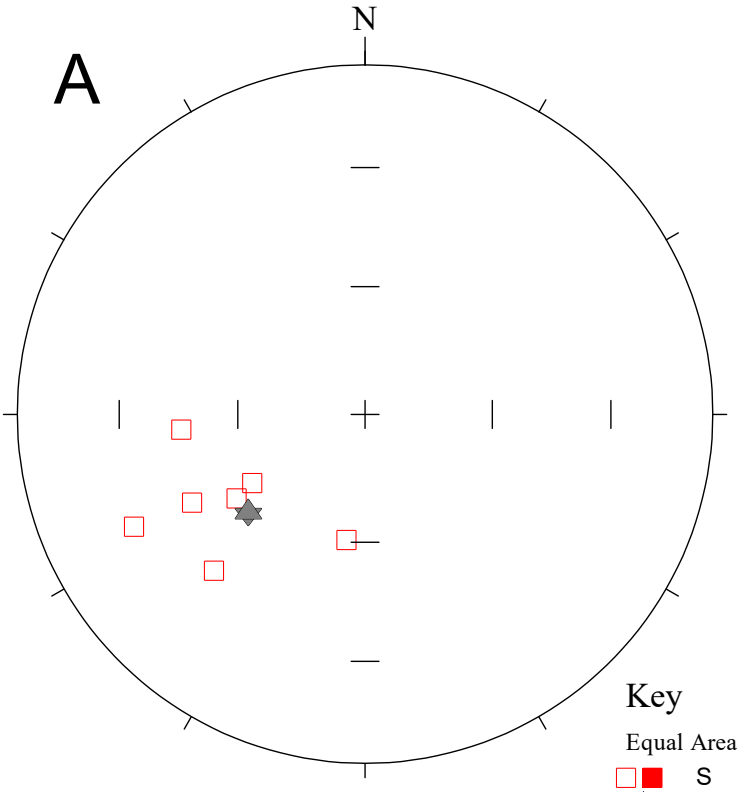

Figure 5.14. A stereonet showing the showing the directions of the ChRM data obtained from the Ainsa Quarry site, these have been corrected for the bedding. These have been subdivided into visually interpreted ChRM directions (S) and the estimated ChRM for the samples was obtained using a combination of the demagnetisating great circle trajectory (T) and (S) values. They show only a reverse polarity with a south westerly directions.

B) A sedimentary log of the measured section and declination, inclination, VGP latitude, and magnetic susceptibility (K_{mean}) ($x10^{-6}$ SI), against stratigraphic height (metres).

Fisher Mean for S class ChRM:
Declination= 236.8°, Inclination= -48.4°,
Alpha(95)= 14.3°, k= 18.7, n= 7

Great circle analysis of T and S values:
Declination= 230.1°,
Inclination= -53.9°, R= 33.0, It = 9, Alpha(95)= 8.0°, k= 9.9,
n(poles)= 28,
n(points)=7

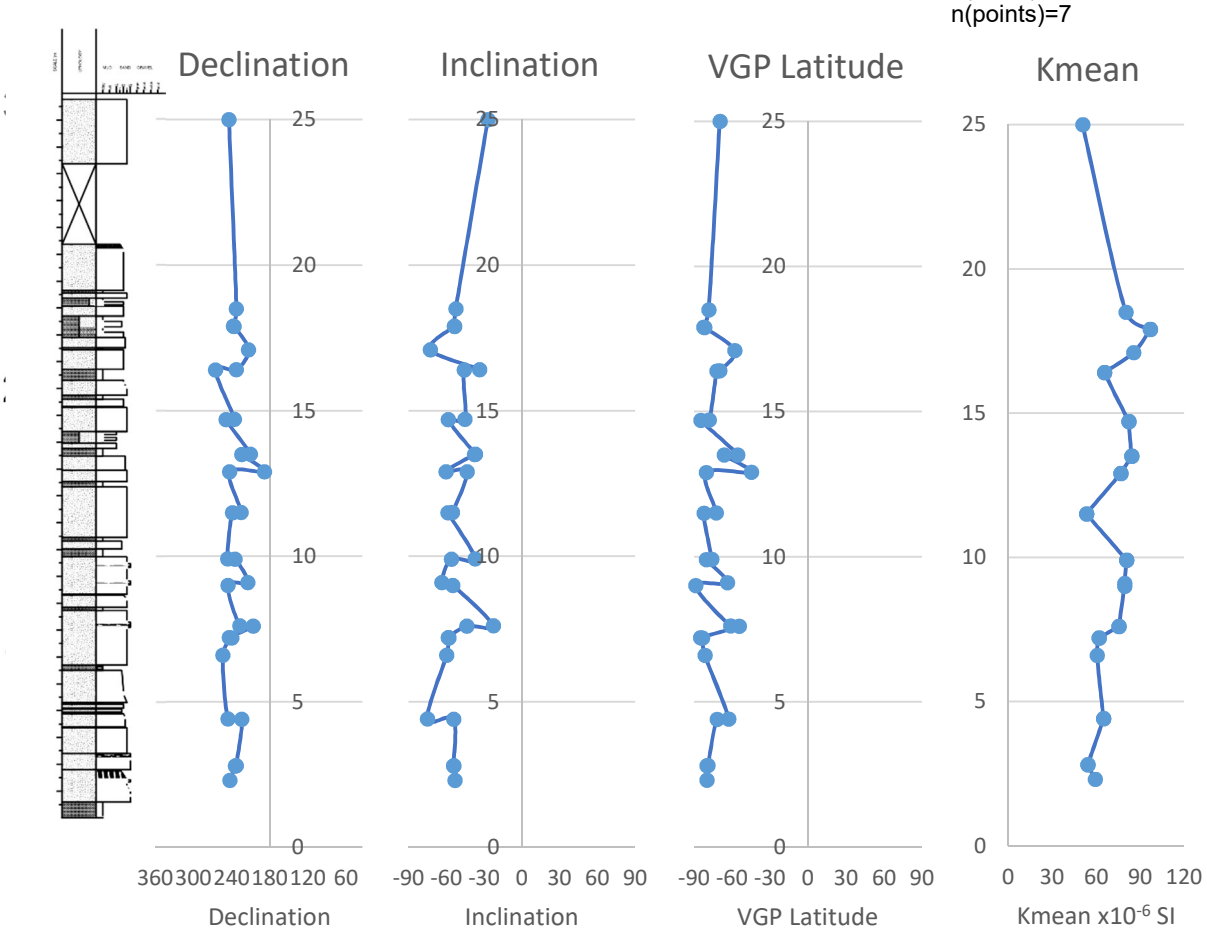

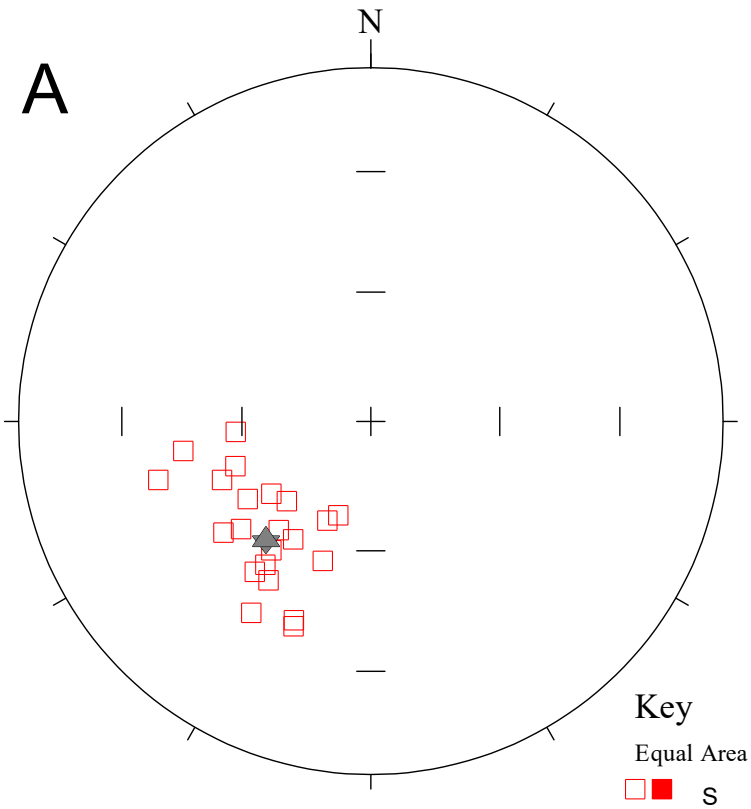

Figure 5.15. A) A stereonet showing the showing the directions of the ChRM data obtained from the Barranco Forcaz site, these have been corrected for the bedding. These have been subdivided into visually interpreted ChRM directions (S) and the estimated ChRM for the sample was obtained using a combination of the demagnetisating great circle trajectory (T) and (S) values. They show only a reverse polarity with a south westerly directions.

B) Declination, inclination, VGP latitude, and magnetic susceptibility (K_{mean}) (x10^{-6} SI), against stratigraphic height (metres). The section-log is shown in Figure 5.13.

Key

Equal Area

S

Fisher mean for s values: Declination= 225.7°, Inclination= -53.7°, Alpha(95)= 6.3°, k= 26.5, n= 22

Great circle analysis of (T) and S components.

Declination= 221.6°,
Inclination= -53.0°,
R= 38.5, Iterations=5
Alpha(95%)= 6.3°,
k=12.2,
N(poles)= 19,
N(points)=22

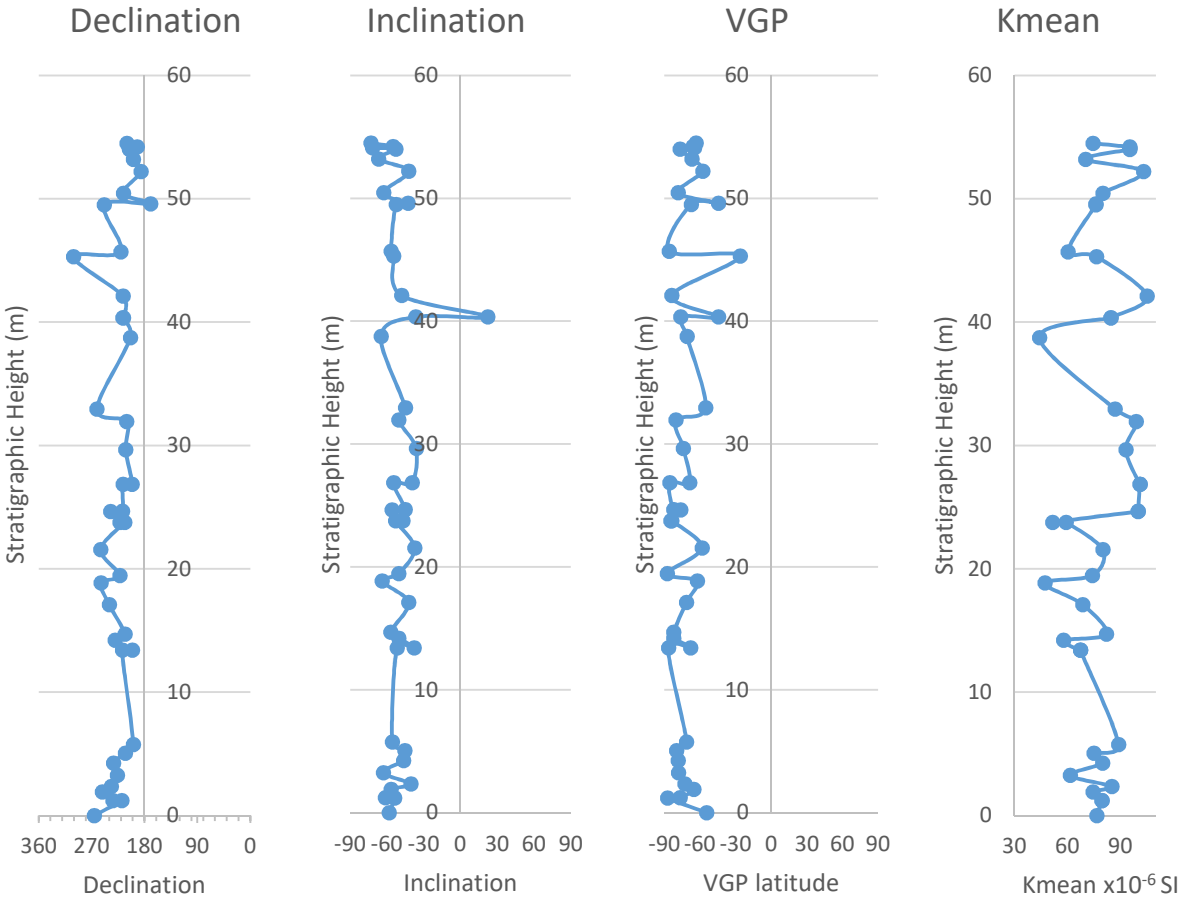

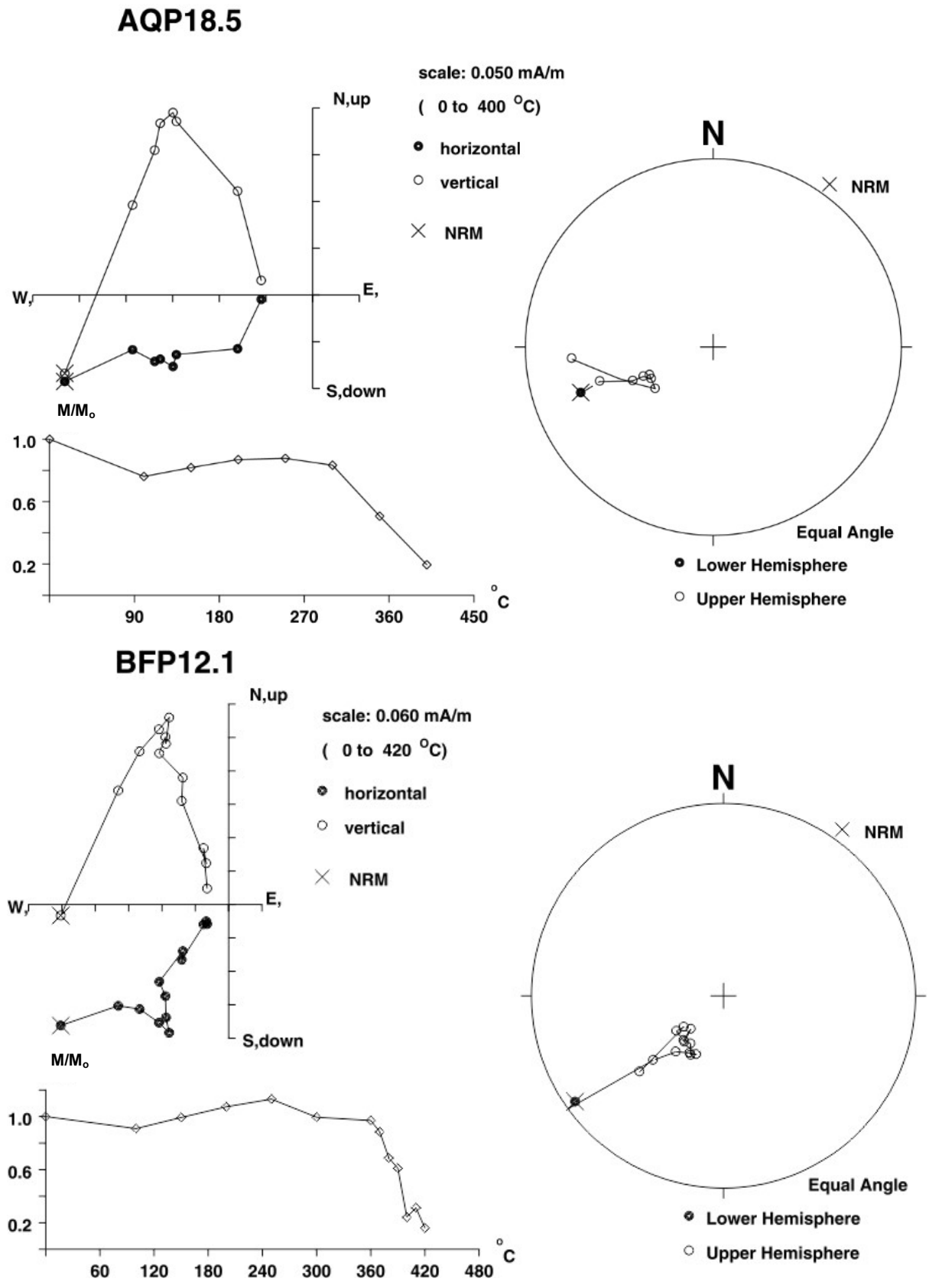

Figure 5.16. Examples of Zijderveld plots of the demagnetisation pattern for each site. AQP 18.5 and BFP 12.1 are taken from the Ainsa Quarry and Barranco Forcaz sites, respectively. Both specimens show a defined reverse, south western ChRM component. The declination of ChRM is slightly different between the two examples with the Ainsa Quarry sample having shallower, more western direction.

Table 5.3. The mean demagnetisation characteristics between the two sites. Fisher (1953) means were used to average the directions from two components: an initial component assumed to be TVRM (thermo-viscous remanent magnetisation, acquired during the Bruhnes); S and T class ChRM data. R is a measure of dispersion and It is the number of iterations.

	Ainsa Quarry	**Barranco Forcaz**
NRM Intensity (mA/m)	From 0.08 to 1.3; average of 0.42	From 0.11 to 1.0; average of 0.44
Average Magnetic Susceptibility (K_m)	91.8 x10^{-6} SI	89.0 x10^{-6} SI
Initial Component	Declination= 317.7°, Inclination= 72.2°, Alpha(95)= 10.8°, k=6.1, n= 29	Declination= 288.9°, Inclination= 73.3°, Alpha(95)= 10.1°, k= 7.1, n= 31
S class ChRM	Declination= 236.8°, Inclination= -48.4°, Alpha(95)= 14.3°, k= 18.7, n= 7	Declination= 225.3°, Inclination= -53.3°, Alpha(95)= 6.0°, k=27.3, n= 22
Combined GC-Fixed Point	Declination= 230.1°, Inclination= -53.9°, R= 33.0, It = 9 Alpha(95)= 8.0°, k= 9.9, n(poles)= 28, n(points)=7	Declination= 221.6°, Inclination= -53°, R=38.5, It = 5, Alpha(95)= 6.3°, k=12.2, n(poles)= 19 n(points) = 22

5.7.2 Palaeomagnetism Analysis

When comparing both data sets from each site, they show similar demagnetisation characteristics (Table 5.3). Both sets show similar NRM intensity and susceptibilities and the ChRM directions show only south-westerly means. The presence of only reverse polarity, similar VGP latitudes and the similar demagnetisation behaviour indicates these sediments were deposited over a short timescale. Mochales et al. (2012) findings suggest the two sites lie in the long reversal chron of C20r and time duration of deposition could be a maximum of c.1 Ma. Muñoz et al. (2013) and Mochales et al. (2012) also found clockwise rotation up to 52° about a vertical axis in the sediments which is similar to values obtained in this study, which would place the time of deposition between 43-45 MA. The similar average NRM intensity and magnetic susceptibility would suggest that the two sites have had similar sources for magnetic minerals.

Samples from the Barranco Forcaz site show greater within-section variation in magnetic susceptibility varying from 35 to 110 ($x10^{-6}$ SI) suggesting that the concentration of these magnetic minerals varies three-fold. This may be attributed to a larger sample size which has a greater mixture of clastic grain size. The specimens with lower susceptibility samples tended to show more scattered ChRM directions, Mochales et al. (2012) suggested that the presence of magnetic sulphides were the cause of this noise, although if these sulphides were prominent in the sediments, there should be a distinct unblocking temperature of ~325^{o}C which is not present in most samples.

5.8 Magnetic Minerology of the Ainsa Basin

Several samples from both Ainsa sites were tested for their magnetic mineralogy in order to examine possible mineralogical influences on the AMS data from different lithologies. Isothermal remanent magnetism (IRM) and anhysteretic remanent magnetisation (ARM) acquisition was used to determine the ferrimagnetic minerology using the room temperature data (Peters & Dekkers, 2003). The back field curve for each of the specimens saturated below 700 mT, suggesting insignificant haematite and goethite contributions to their composition (Maher et al., 2010). ARM ratios such as ARM/SIRM were used to rule out other ferrimagnetic minerals as the main magnetic mineral (Maher et al., 2010).

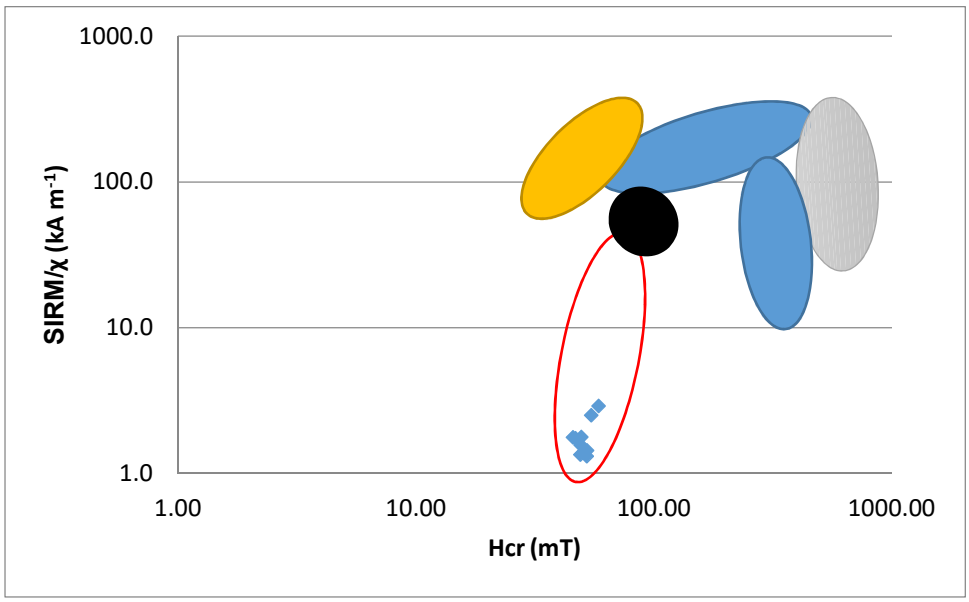

Figure 5.17. Biplot of remanent acquisition coercivity (Hcr) versus saturation remanent magnetism SIRM/χ.The red circle is the typical values for magnetite and Ti-magnetite, orange circle=pyrrhotite, black circle=greigite, blue circles=haematite and grey circle=goethite. All the results lie within the magnetite and Ti-magnetite range (Peters & Dekkers, 2003).

5.8.1 Hysteresis

Three specimens were investigated for their hysteresis properties to evaluate the contribution of paramagnetic minerals to the AMS. If the AMS has a strong contribution from paramagnetic minerals, it should have a linear high-field induced magnetisation, whereas magnetite contributions will be seen as a saturation component at fields less than 300 mT. The low field used (<700 mT) cannot distinguish haematite contributions from paramagnetic contributions, but the IRM/ARM data and AF demagnetisation suggests no significant haematite components.

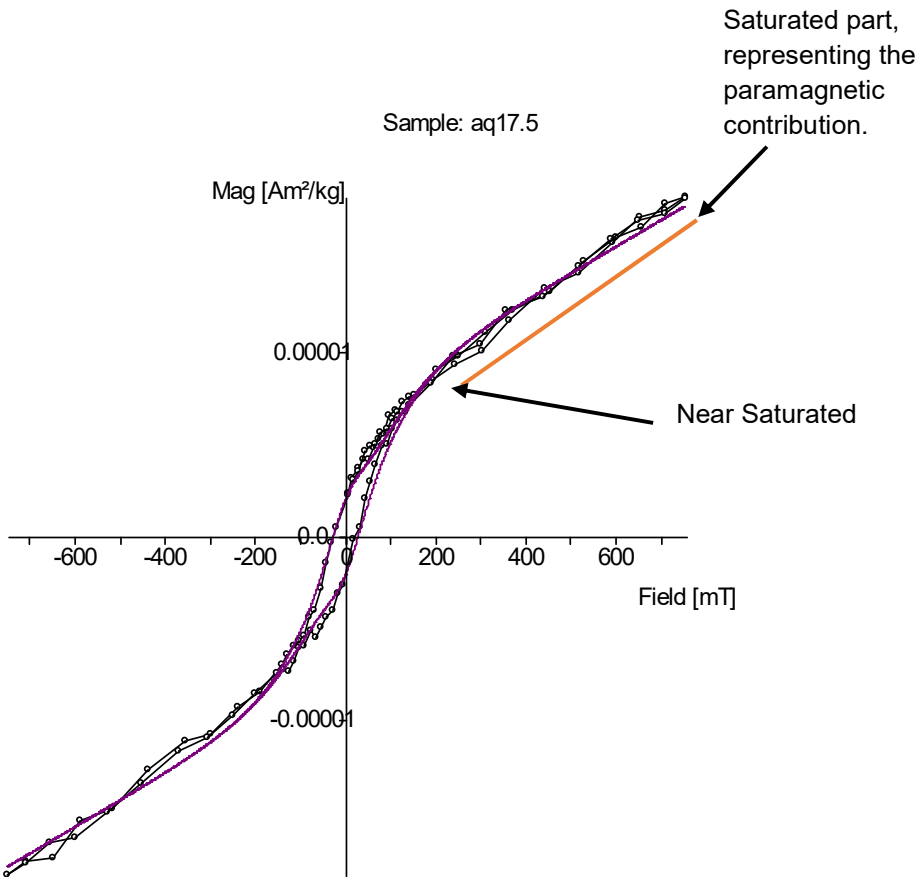

Figure 5.18. Hysteresis plot of coarse sandstone unit from the Ainsa Quarry site. The plot also shows interpreted paramagnetic mineral contribution, above a saturating ferrimagnetic component, which is saturated by c. 200 mT.

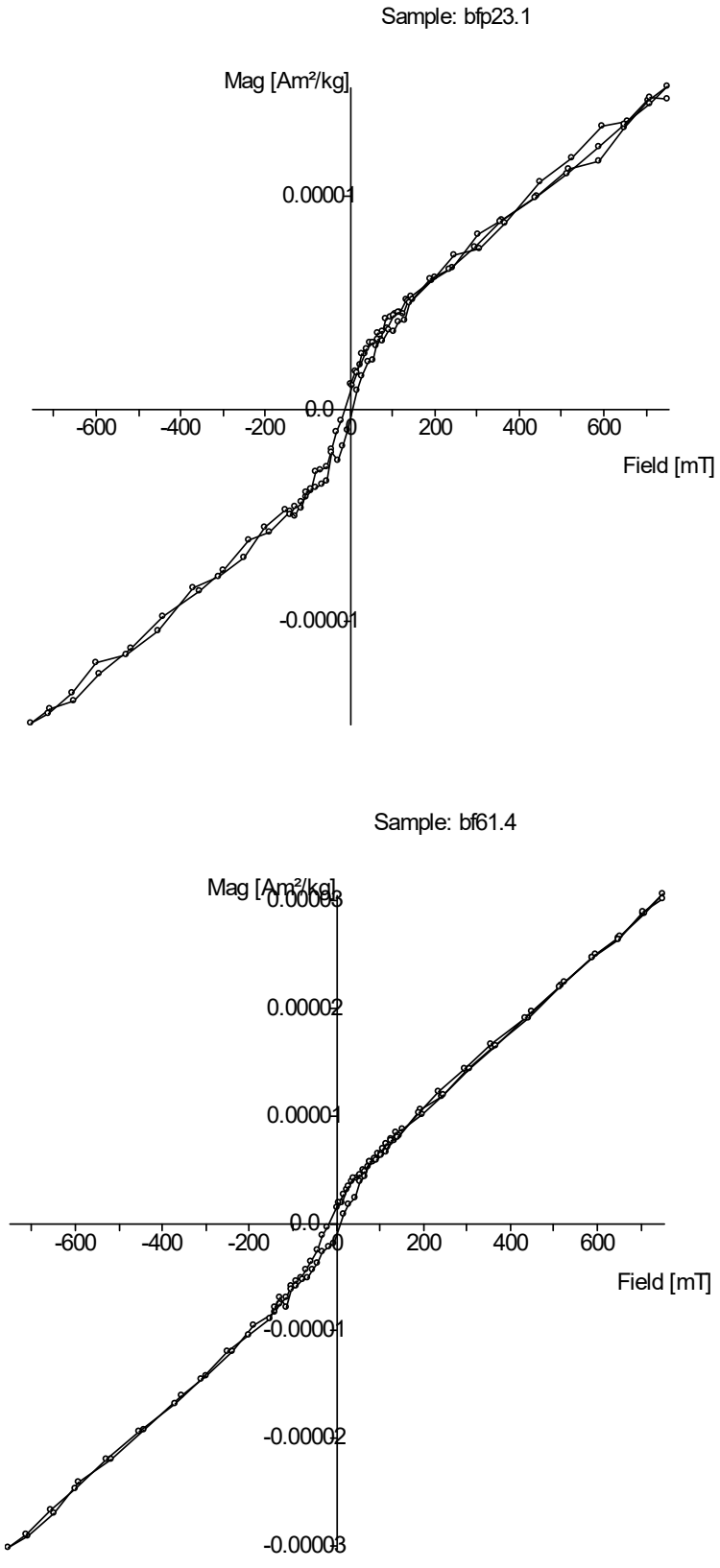

Figure 5.19. Two mud dominated specimens from the Barranco Forcaz site, the upper-data is from a siltstone and shows a mixture of paramagnetic and ferromagnetic minerals. This specimen shows a flow-transverse AMS fabric. The lower plot shows a hysteresis curve dominated by its high paramagnetic mineral content.

Table 5.4. Hysteresis parameters for each of the sediment samples, SST=sandstone, SLST=siltstone and MDST=mudstone. The percentage of ferrimagnetic paramagnetic/diamagnetic content. Ms=Saturation induced magnetisation, Mrs=Saturation remanent magnetisation. Hc/Hcr are coercivity and remanent coercivity.

Spec	**Type**	**Ferrimagnetic content (%)**	**Para/diamagnetic content (%)**	**Ms (Am^2/kg)**	**Mrs (Am^2/kg)**	**Hc (mT)**	**Hcr (mT)**
Aq 17.5	Med-coarse SST	81.9	18.1	$7.63x10^{-3}$	$1.99x10^{-3}$	31.29	57.11
Bf 23.1	SLST	48.7	51.3	$3.52\ x10^{-3}$	$6.51\ x10^{-4}$	11.45	62.37
Bf 61.4	Fine MDST	8.9	91.1	$2.53x10^{-3}$	$1.29x10^{-3}$	20.5	46.11

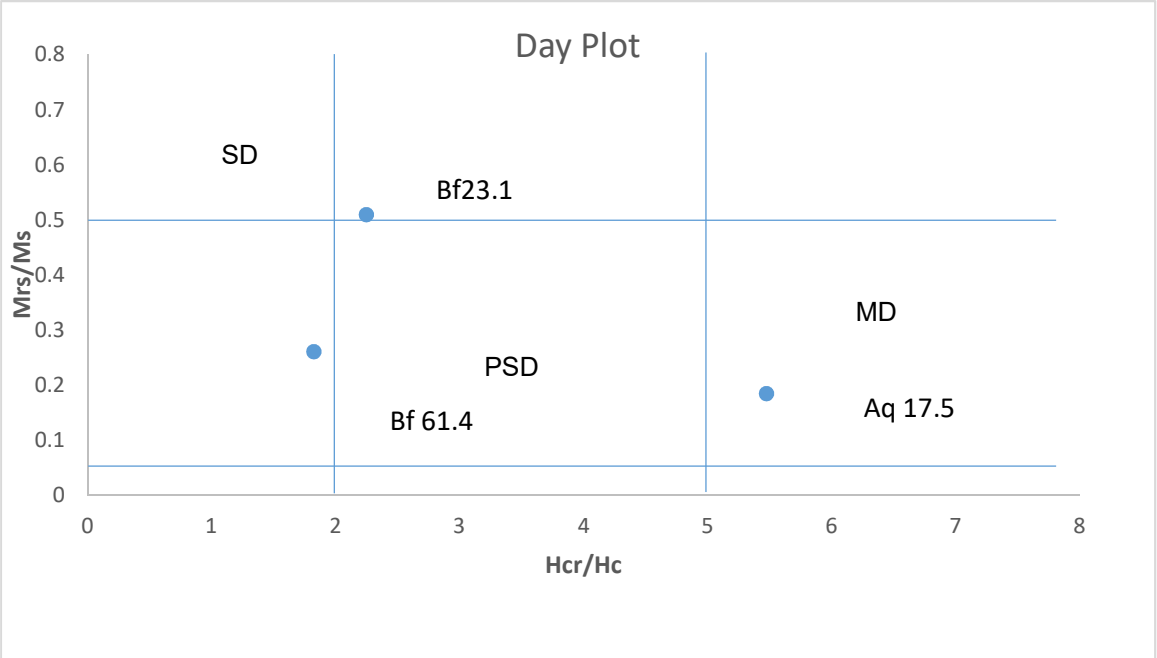

Figure 5.20. Day et al., (1997) plot showing the magnetic grain size of the magnetite for the three samples tested. Where SD=single domain, PSD=pseudo domain and MD=multi-domain. The shales are found in the PSD field and sandstone specimen is in the MD field.

5.8.2 Magnetic Minerology Analysis

The magnetic mineralogy data (Fig. 5.17, 5.19, 5.20) suggests the carrier of the remanence is a pseudo single domain to multi-domain magnetite, which was also found in studies by Mochales et al. (2012) and Muñoz et al. (2013). Paramagnetic minerals appear to contribute between 18% to 91% of the susceptibility, depending on the lithology.

The mudstone samples have coercivities (Hc) less than the sandstone samples, although the coercivity of remanence (Hcr) is similar. The sandstone sample is clearly higher in ferrimagnetic content than the shale samples. This could be due to it being richer in locally eroded intrusive igneous rock (higher concentrations of ferrimagnetic minerals) (Mochales et al., 2012), whereas the mudstone units are probably higher in Fe-rich paramagnetic minerals such as micas and clays.

IRM and ARM acquisition, and Day plots indicate that the magnetite is pseudo-single domain to multi-domain. Overall, the magnetic mineralogy responsible for the magnetic susceptibility appears to be a mix of paramagnetic minerals and magnetite. Mochales et al. (2012) described the presence of sulphides in the underlying sediments but no evidence of this was found during this study.

These differences in contribution could suggest a possible difference in source, thus the AMS may be partly dependent on the source and mineralogy.

5.9 Anisotropy of Magnetic Susceptibility of the Ainsa System

The anisotropy of magnetic susceptibility (AMS) data was measured from 153 samples, 81 from Ainsa Quarry (277 specimens) and 72 from Barranco Forcaz (270). Up to five or more specimens were measured from each sample and averaged using the Anisoft 42 program (Chadima & Jelinek, 2009) which uses Jelinek statistics to average the AMS tensors. Each specimen's AMS was corrected for the bedding orientation, so all directions are with respect to palaeohorizontal and geographic north.

5.9.1 Ainsa Quarry Site

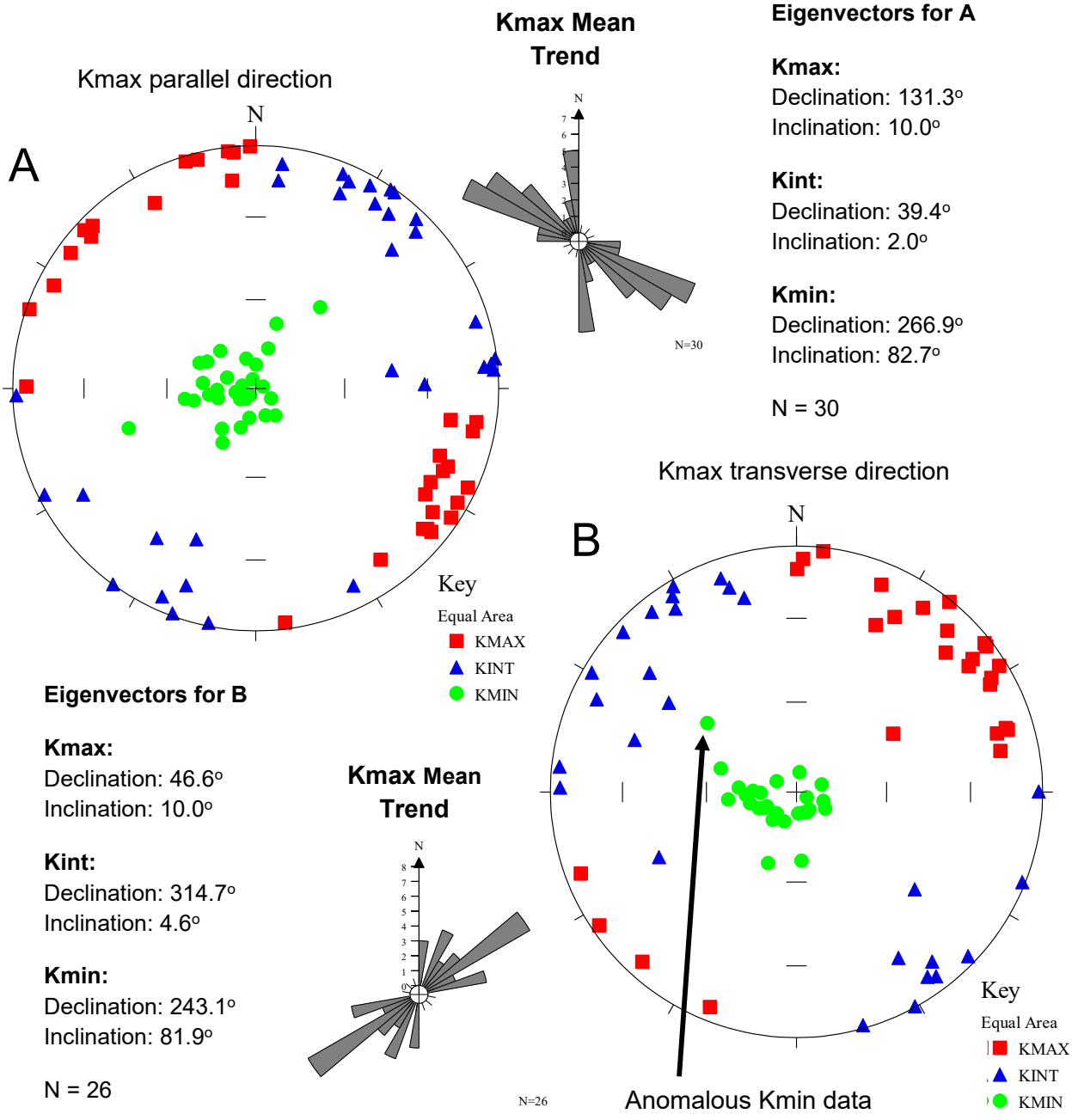

Figure 5.21. Stereoplots of the AMS for each sample that was produced from an average of their specimens from Ainsa Quarry and has been divided into, A) specimens with Kmax direction is parallel to the flow direction orientated southeast-northwest and B) specimens with Kmax direction normal (orientated Northeast-southwest) to the inferred flow. The majority of the AMS directions are orientated parallel to the flow direction c.63%.

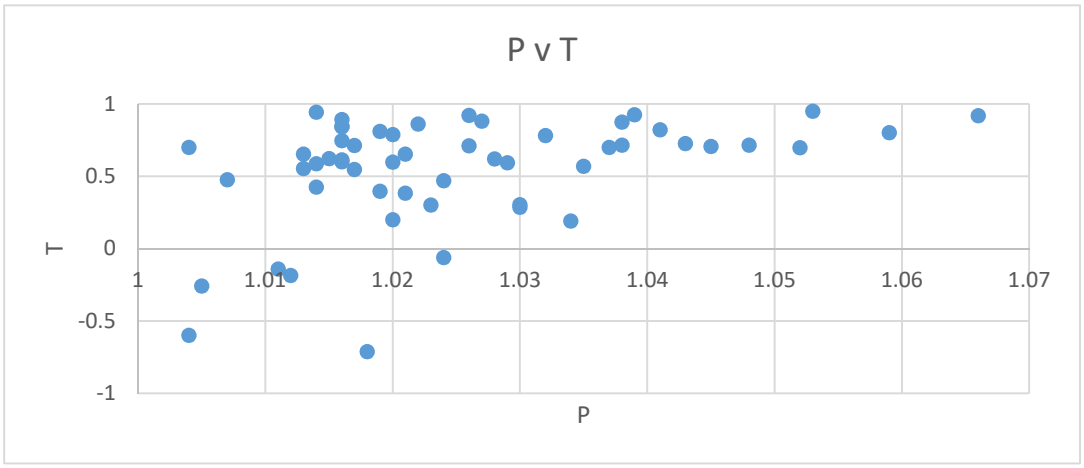

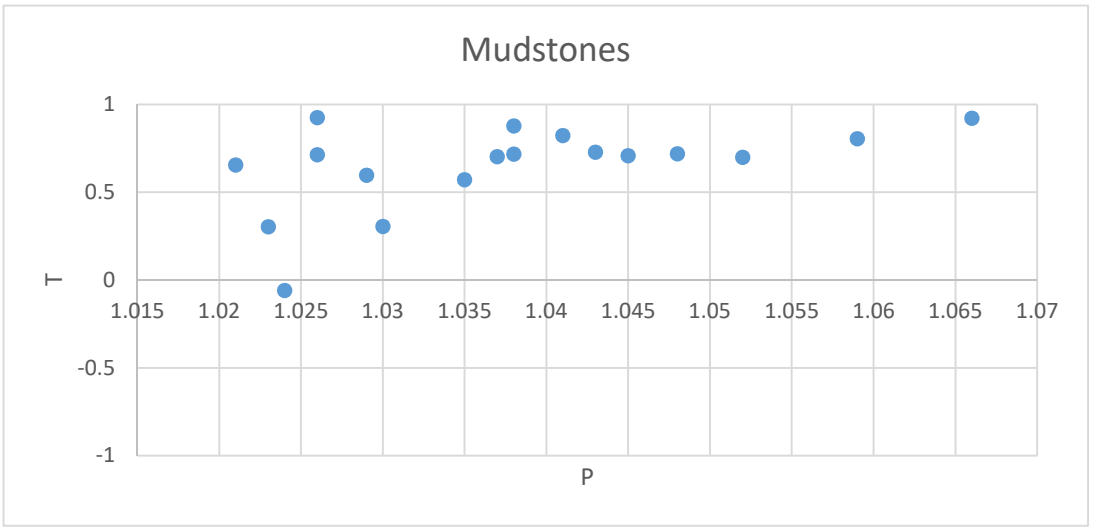

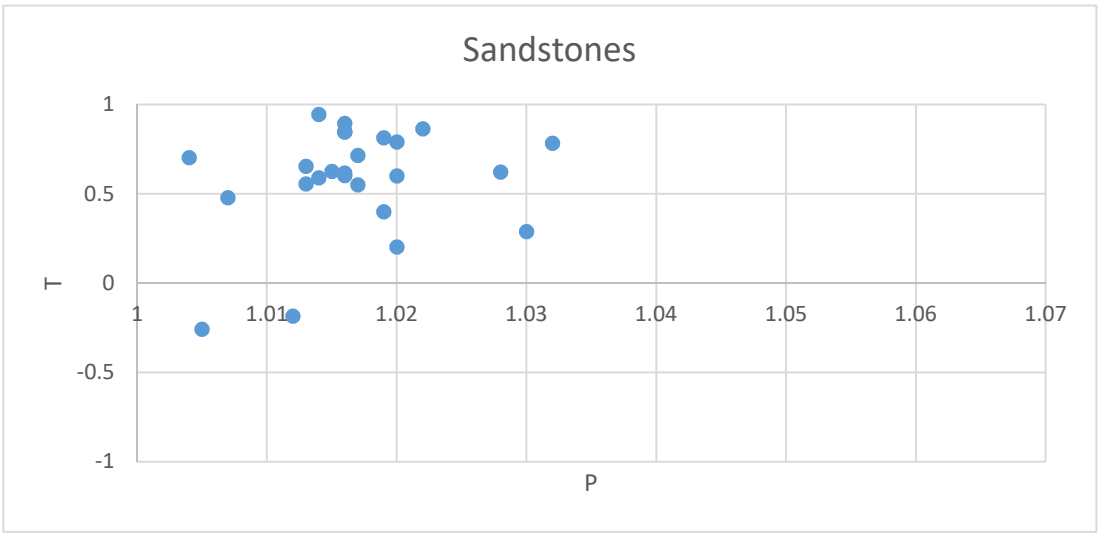

Figure 5.22. The shape and degree of anisotropy of different specimens from the Ainsa Quarry Site. The mudstone has a greater range of the degree of anisotropy and has a significantly more oblate shape shown by large T. Sandstone specimens have a weakly anisotropic fabric and are well constrained as the p values are mostly less than those from mudstones.

The AMS data from the site shows two dominant Kmax trends in the section. The oldest and lower part of the sequence shows Kmax direction trends northeast – southwest, whereas most of the section has Kmax directions trending northwest – southeast. Kmin values have a small imbrication to the southwest with some specimens imbricated to the North West, but in one turbidite bed only.

The magnetic parameters for this section are fairly consistent. The T parameters are mostly between 0.3 - 0.95 for most of the specimens. The degree of AMS shows more variation with P values around throughout the sequence around 1.00 - 1.06.

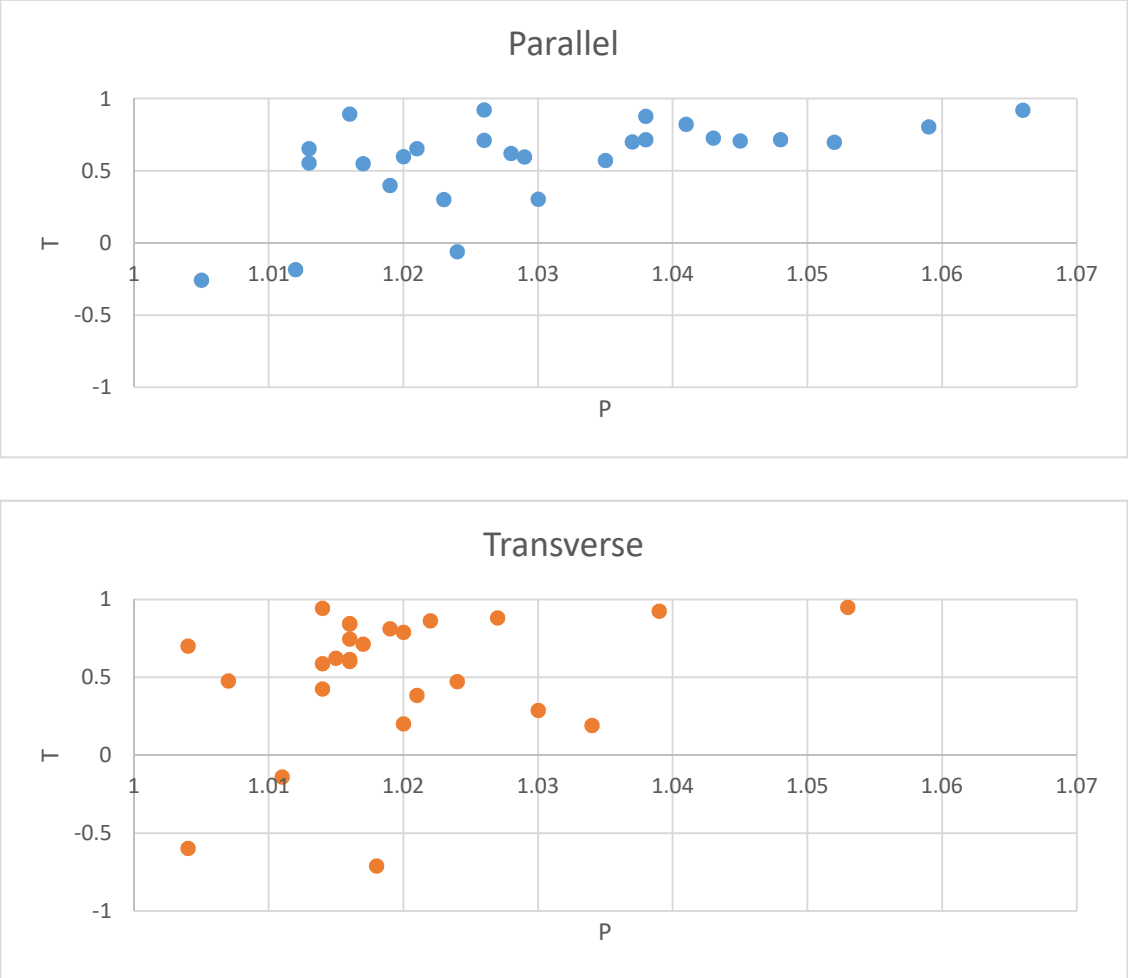

Figure 5.23. The shape (T) and degree of anisotropy (P) of the two Kmax groups of the Ainsa Quarry Site. The flow-parallel groups have an average with higher P and T values than the transverse group of specimens. The flow parallel group also have a greater percentage of mudstone specimens.

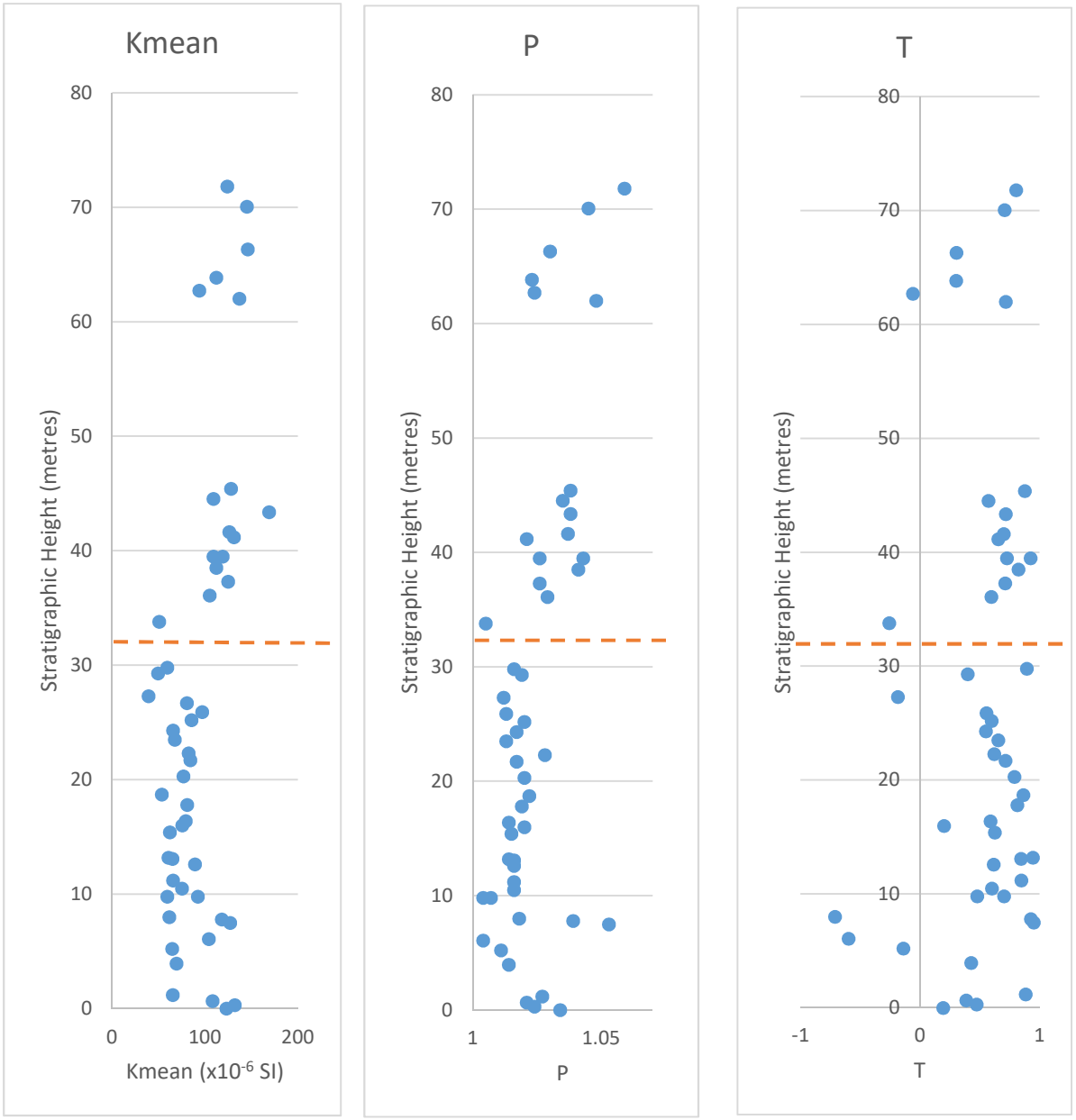

Figure 5.24. The bulk magnetic susceptibility (K_{mean}), shape (T) and degree of anisotropy (P) through the section at the Ainsa Quarry. The magnetic susceptibility, and P increases sharply above the dashed line, this reflects the change in lithology from Ainsa I fan sandstones (below) to the Ainsa I interfan shale above.

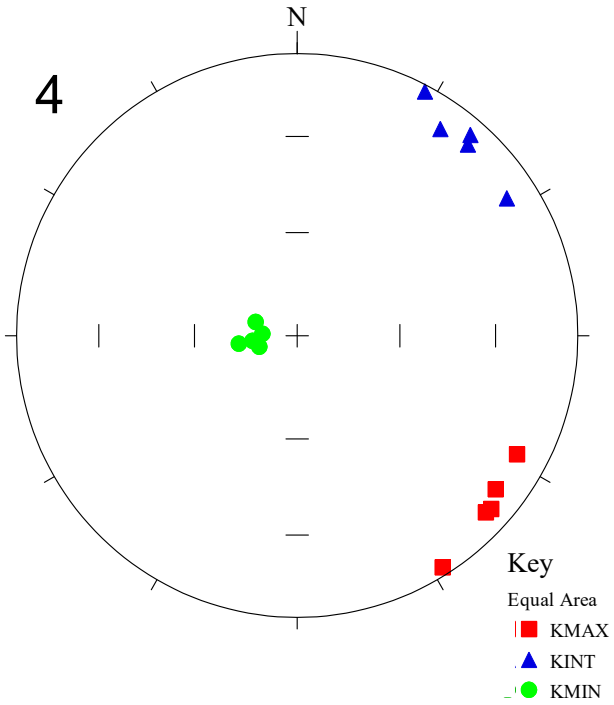

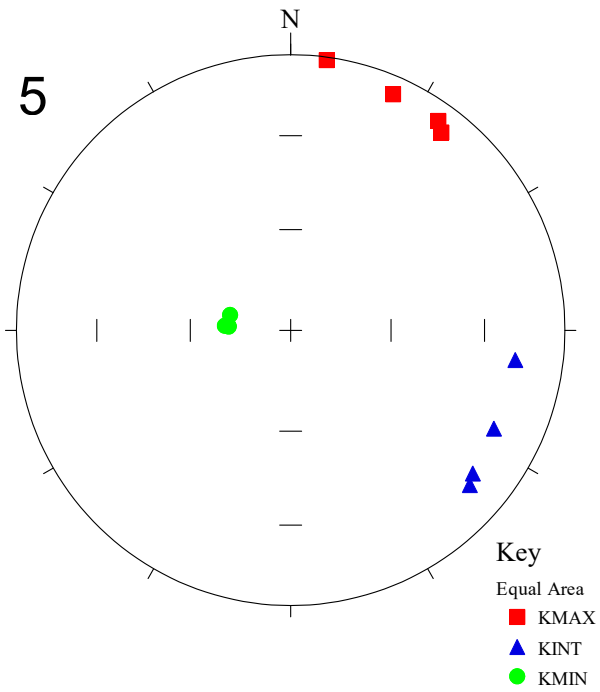

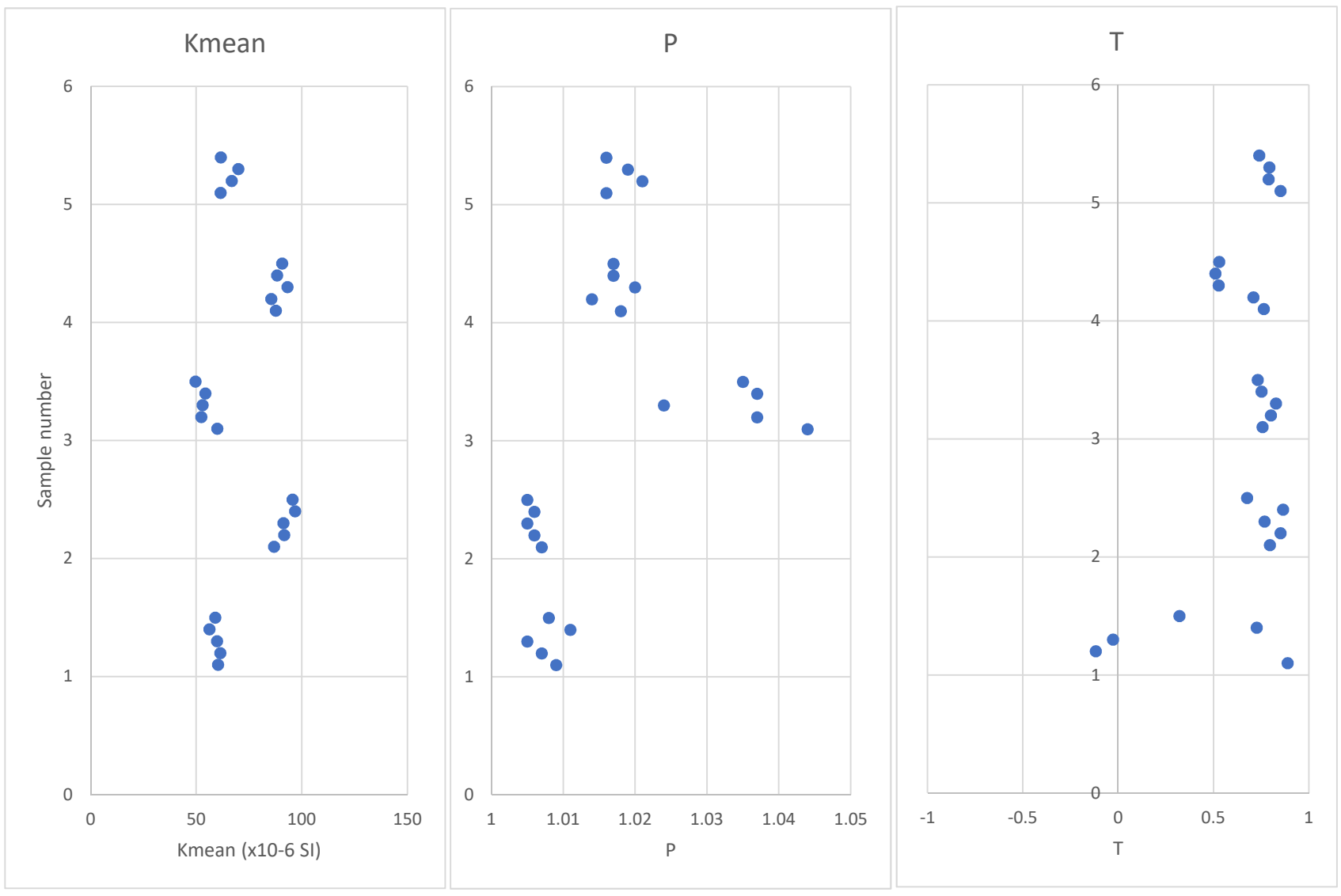

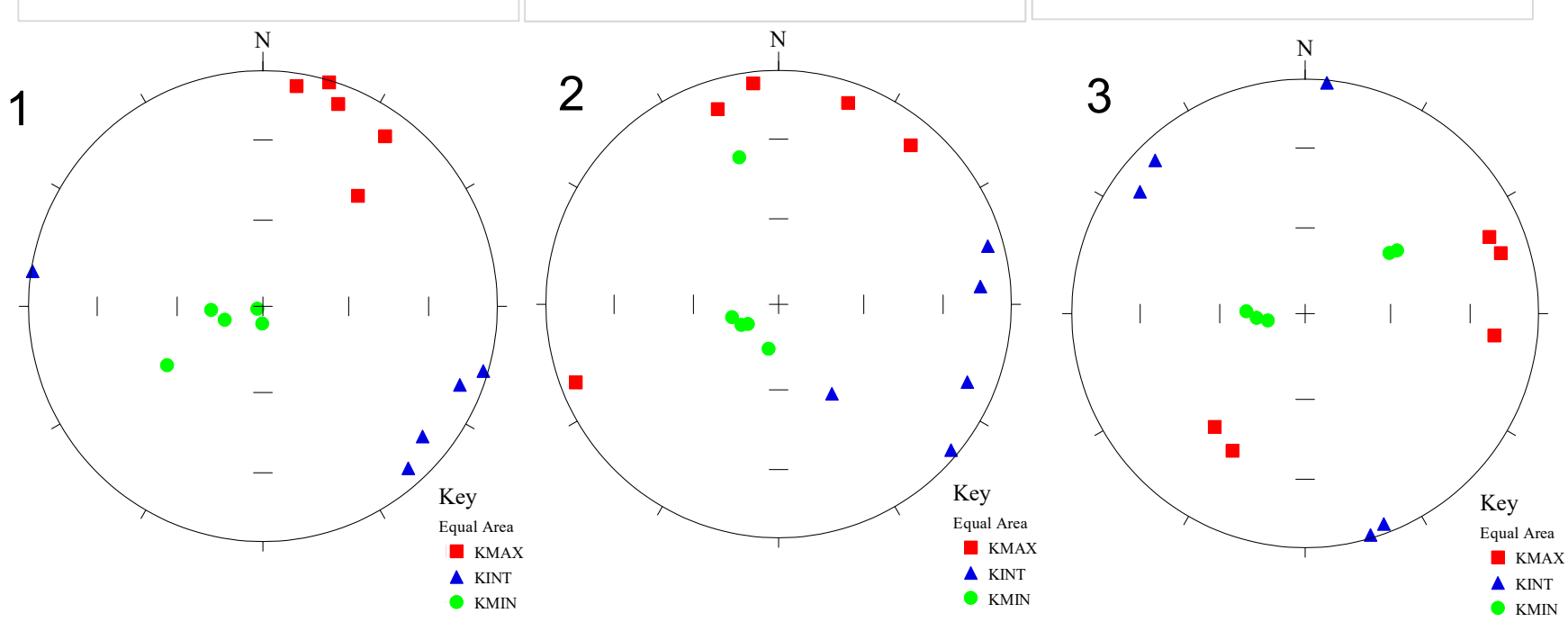

Figure 5.25. The bulk magnetic susceptibility (K_{mean}), shape (T) and degree of anisotropy (P) of different samples through a single turbidite deposit at the base of the Ainsa Quarry, marked on Fig. 5.10. P slightly increases towards the top of turbidite reflecting change in the flow velocity. K_m and T show little change and mainly reflect compositional differences. Stereoplots 1-5 each represent 4-5 specimens from each sample, 1 is at the base and 5 is at the top of bed. 1 & 2) Are at the base of the turbidite and reflect Ta or Tb Bouma facies (So et al., 2013), implying high velocity, low-density flows which is in agreement with smaller degree of anisotropy and displays transverse fabric. 2 shows a less defined transverse mode which indicates a reduced velocity. 3) Is the middle of turbidite and also shows a transverse fabric. 4) Is near the top of the turbidite and has greater P values and would reflect Tc or Td fabrics as it shows flow-aligned fabric (So et al., 2013). 5) Is the start of another turbidite that has eroded the top of this bed, indicated by the transverse fabric.

5.9.2 Barranco Forcaz Site

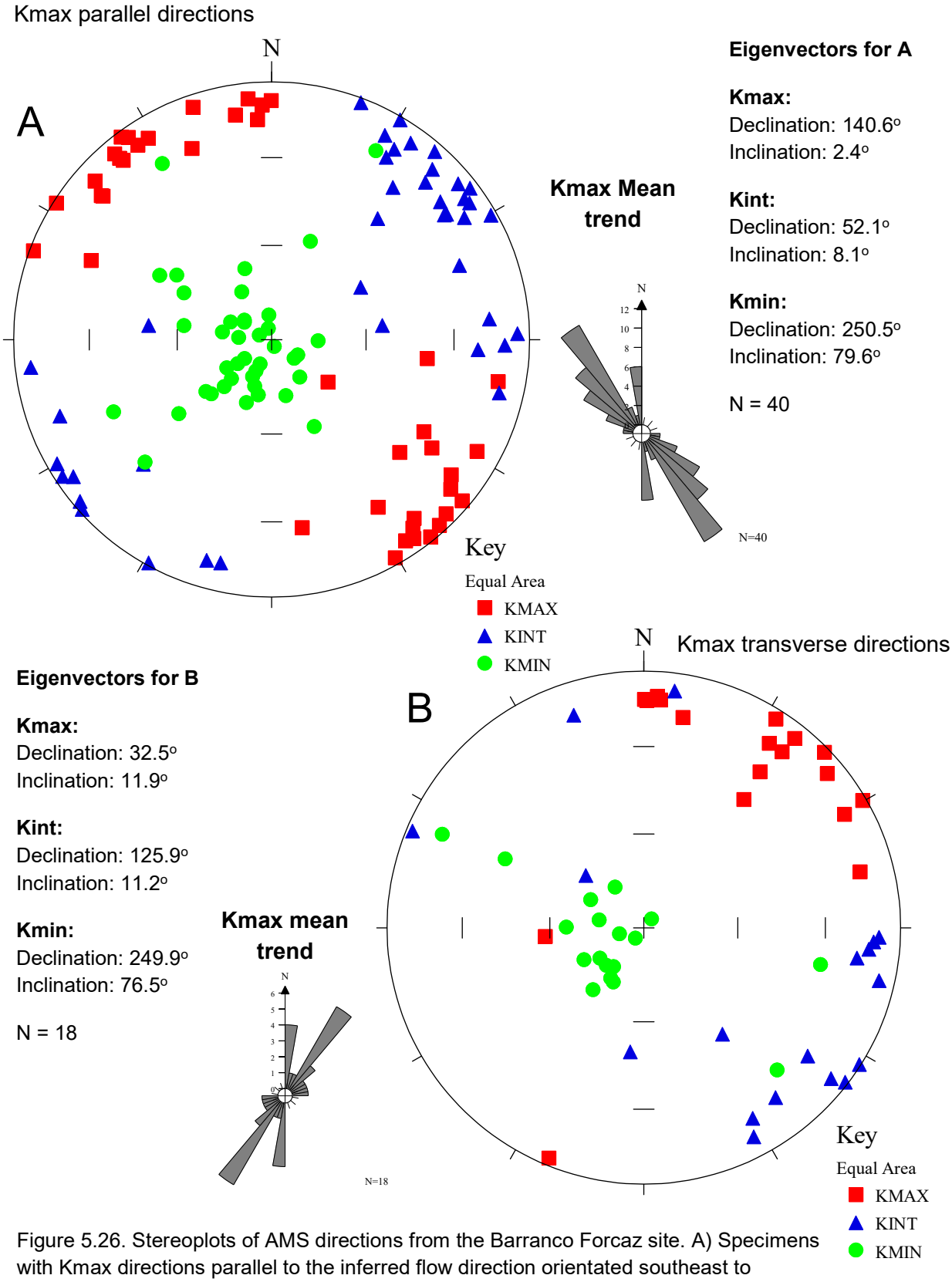

Figure 5.26. Stereoplots of AMS directions from the Barranco Forcaz site. A) Specimens with Kmax directions parallel to the inferred flow direction orientated southeast to northwest and B) specimens with Kmax directions normal to inferred flow. The majority of the specimens examined are orientated parallel to the flow direction c.83%.

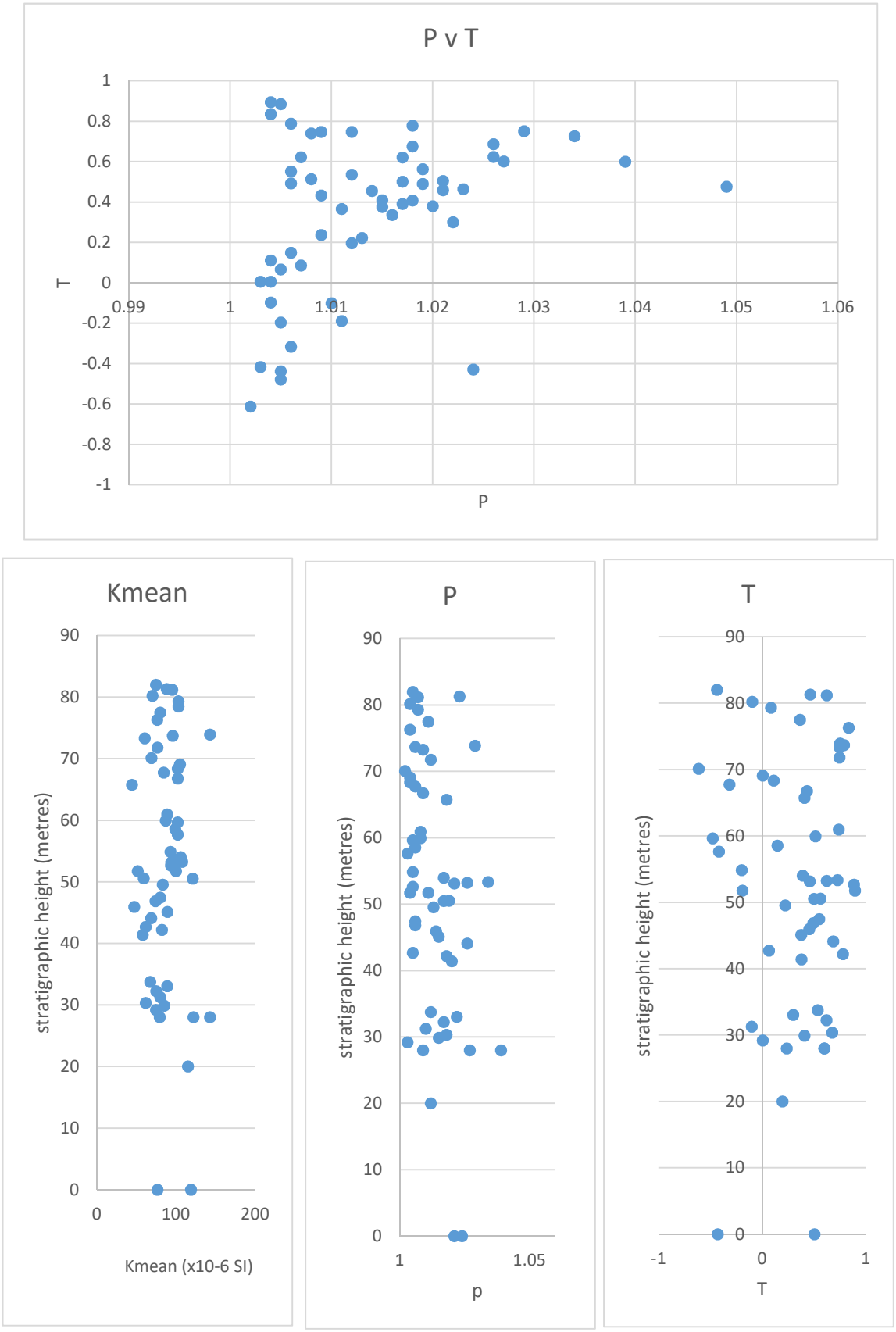

Figure 5.27. Mean bulk magnetic susceptibility (Kmean), shape (T) and degree of anisotropy (P) of samples at the Barranco Forcaz site.

5.9.3 AMS Analysis of Ainsa System

The two sites share a few similarities; they both show two distinct groups for Kmax directions, one that is parallel to flow (as measured by macroscopic indicators; Pickering & Corregidor, 2005) and one that is normal to flow directions. They share similar average magnetic susceptibility and flow-aligned and transverse fabrics can be found within the same bed (Fig. 5.25). The transverse fabrics can be explained using the turbidity models of Baas et al. (2007) which suggest that under low-flow conditions Kmax directions are orientated parallel with flow, but may form normal to flow-aligned fabrics when the fluid velocity is large enough to rotate the grains into a rolling-type fabrics. This high velocity flow does not rotate all the grains and some will be deposited in a stable position parallel to flow, explaining why some beds have both fabric orientations.

In large turbidite beds, there will be several Bouma facies indicating different modes of transport. In the examined bed (Fig. 5.25.), there were at least two different modes of transport indicated by the change from transverse fabrics, with low P values, to a flow-aligned fabric, with greater P values. This change in fabric reflected a transition from low-density flows to weaker turbulent flows and/or deposition from suspension. The top part of the large turbidite bed appears to have been removed by the overlying turbidite, which skews the AMS fabric to reflect transverse flow fabrics. This is consistent with the data in Fig. 5.10 as the Ainsa I Fan has a greater percentage of transverse (grain-

rolling type) Kmax directions compared to Barranco Forcaz, reflecting the high energy channel deposits in the Ainsa Quarry section.

According to the Baas et al. (2007) study, the transverse fabrics should have a smaller degree of anisotropy (P) and be more isotropic (T closer to zero). In the Ainsa Basin, there is a difference between AMS fabrics with normal and transverse Kmax trends, with transverse mode showing smaller average P values but no noticeable difference in T, (Fig. 5.23). In the Ainsa Quarry section the majority of the flow-parallel fabrics show a greater range in the P and T values, whereas the transverse-fabrics P values are more confined with most samples having values between 1.01-1.03. The T values were expected to be more isotropic (closer to 0) than the normal fabrics but this is not the case.

In the interfan- shales above the Ainsa Quarry turbidites there were some shales that had transverse orientations rather than the expected flow-aligned AMS fabrics. There was an expectation that the shales would be flow-aligned as these were assumed to be deposited in low velocity turbidity currents or a hemiplegic setting which would not have rotated the grains. These transverse results can be explained as debris flows within the shales; these are mentioned in Falivene et al. (2006) and would have large enough current velocities to produce these fabrics. The presence of debris flows is further supported by the presence of pebbles or slightly coarser compositions noticed in the field.

There is an association between low P and T values (particularly prolate fabrics with T>0) and low bulk susceptibilities. This is shown in Fig. 5.24., where P and T values increase sharply with the bulk susceptibility, this corresponds to a change in lithology from channelised sandstone and mudstone to hemipelagic shales and debrites. Although the difference in mode of deposition could explain changes in AMS fabric, it does not explain the drop in magnetic susceptibility. Instead the lithological composition may be an overriding factor that decides the shape and degree of anisotropy, as the sandstones' magnetic susceptibility is composed of ferrimagnetic minerals and whereas the mudstones' are dominantly composed of paramagnetic minerals, Table 5.4.

Fig. 5.22 shows a clear grouping for the sandstone samples which have smaller P values reflecting the magnetite composition. Paramagnetic-dominated samples produce a greater scatter with a much higher degree of anisotropy associated with the phyllosilicate minerals (e.g. clays).

The AMS does not appear to show Kmax directions greater than 10^{o} inclination or a Kmin distribution forming a girdle parallel to tectonic shortening which would be expected of tectonic shortening or folding. Therefore the effects of tectonism on the AMS are minimal; the AMS of the phyllosilicate (or magnetite) reflects planar orientation associated with compaction. This is supported by Travé et al. (1998)'s strontium isotopes studies that found an absence of in situ mineral transformation and a study by Parés et al. (1999) of AMS tectonic fabrics.

A limitation of this study is that the samples were mainly taken from the top and base of large beds, while thinner beds were sampled in full. This should not be a problem for the thinner beds as the five specimens from each sample should cancel out the variations from the top and base of the bed. This method was adopted for logistical reasons owing to the difficulty in breaking the well cemented lithology and this sampling may have affected the data, skewing it to reflect erosive conditions at the bases of turbidites and closer to hemiplegic deposition at the top. Baas et al.'s (2007) model suggests there should be more flow-aligned fabrics at the bottom of the Ainsa Quarry. These flow-aligned fabrics would be associated with the top of individual turbidites, instead the base of Ainsa Quarry is nearly entirely composed of transverse fabrics.

Several samples were taken from a large turbidite bed to investigate how AMS may change throughout. The Kmax and Kmin directions are consistent throughout the bed and show a general upwards trend to increased Km, P and T values, reflecting the change in grain size and a greater mud content (Fig. 5.25.). However, these fabrics remain transverse throughout, suggesting that erosion from the overlying turbidite may be removing the top-part of the flow-aligned turbidite fabric.

5.10 Conclusion

Magnetostratigraphy has shown that the Ainsa system between Ainsa fans I and II was deposited within a short time period in chron C20r (<1 Ma; Mochales et al. 2012) which was suggested by the presence of a single magnetic polarity in the ChRM data at the two sites (Fig. 5.14 or 5.15). The magnetic mineralogy data suggests the main carrier of the ChRM is a pseudo-single domain with a small multi domain magnetite influence.

The Baas et al. (2007) model for turbidite grain fabrics can be applied to the Ainsa Basin, meaning that the Kmax directions can be proven to show the direction of palaeoflow in a hemipelagic setting or low velocity turbidity flows. However, in more turbulent and greater flow conditions such as the Ainsa I fan or debris flows, Kmax directions re-orientate normal to the palaeoflow owing to greater rates of grain rotation, which cause grain fabrics to become more isotropic, corresponding to lower T values (Fig.21).

AMS can be used to infer depositional models such as debris flows within the shale facies but the effects of lithological composition on the AMS also needs to be taken into account. Variations in composition have a greater impact on the magnetic fabrics, as the paramagnetic minerology will produce fabrics with much greater degrees of anisotropy and larger magnetic susceptibilities. Tectonism has no apparent impact on the AMS apart from initial vertical compaction associated with burial.

For the AMS the magnetic susceptibility appears to have a contribution between 9 to 82% from paramagnetic minerals, depending on the lithology. These changes in contribution would suggest a change in source as the ferrimagnetic minerals have a detrital origin and the paramagnetic minerals would have been deposited from suspension. Therefore these different depositional mechanisms associated with ferrimagnetic or paramagnetic will affect the AMS fabric. The other observation is that both ferrimagnetic and paramagnetic fabrics were successfully measured using AMS to establish palaeoflow.

6. Case Study: The Welsh Borderlands

One of the main objectives of this project was to examine anisotropy of magnetic susceptibility (AMS) fabrics in different sedimentary environments at varying scales. The Welsh Borderlands was chosen to test the effectiveness of AMS as a palaeocurrent indicator for sediments owing to its geographically larger shallow shelf environment and to examine how local tectonics can affect the AMS fabric. Three study areas were chosen that range in age from the Llandovery of the early Silurian (Hill End Farm & Quarry, Buttington Quarry sections) to the mid Silurian, Wenlock age Eaton Trackway section (Burgess & Richardson 1991; Crossley & Clark 2015).

6.1 Geological History

The early Palaeozoic rocks around the Welsh Borderlands overlie Precambrian basement where the Neoproterozoic (late Precambrian) Uriconian Volcanics are overlain by the thick Longmyndian Supergroup (Brenchley & Rawson, 2006; Woodcock & Strachan, 2000). West of the Wrekin there is evidence of metamorphism of the basement, visible in the Ruston Schists and the Primrose Hill Gniess (Brenchley & Rawson, 2006). These outcrops lie between and along the Church Stretton and Pontesford-Linley faults, the latter displacing units in the Ordovician, while the Church Stretton Fault influenced sedimentation throughout the Lower Palaeozoic (Toghill & Chell, 1984). This Precambrian volcanism and faulting was generated by a subduction zone located near Anglesey; as the crust subducted below the Welsh Basin, this produced the Uricornian Volcanics. Faulting parallel to the subduction

zone formed a rift-basin where the Longmyndian Supergroup was deposited (Toghill & Chell, 1984).

As the Iapetus Ocean began to close in the late Ordovician, southern Britain went through a tectonic episode as eastern Avalonia and Baltica collided (Woodcock & Strachan, 2000). This Shelveian Event, named by Toghill (1992), was the deformation and uplift associated with this collision, which occurred in the early Ashgill, creating an unconformity in the Welsh Borders successions (Cherns et al., 2006; Toghill, 1992). These tectonics created large-scale open folding, during the Upper Ordovician (Toghill, 1992). The subduction led to the creation of basaltic/gabbroic intrusions, while folding led to uplift of the landmass of the Midland Platform. At the end of the Ashgill with global sea-level regression and the glaciation of Gondwana, sea level was at a low although this is not recorded in the Welsh Borderlands (Toghill, 1992; Woodcock & Strachan, 2000).

During the Silurian the closure of the Iapetus Ocean saw the Avalonian sub-continent converge with Laurentia as the former was drifting northwards into lower latitudes (Fig. 6.1, Soper & Woodcock 1990; Cocks, 1989). This is reflected in the deposition of reefal-tropical limestones during the Wenlock (Cocks, 1989). Sedimentation within the Welsh Borderlands was controlled by active faulting that separated the main basin to the NW from the marginal shelf to the SE (Woodcock & Gibbons, 1988).

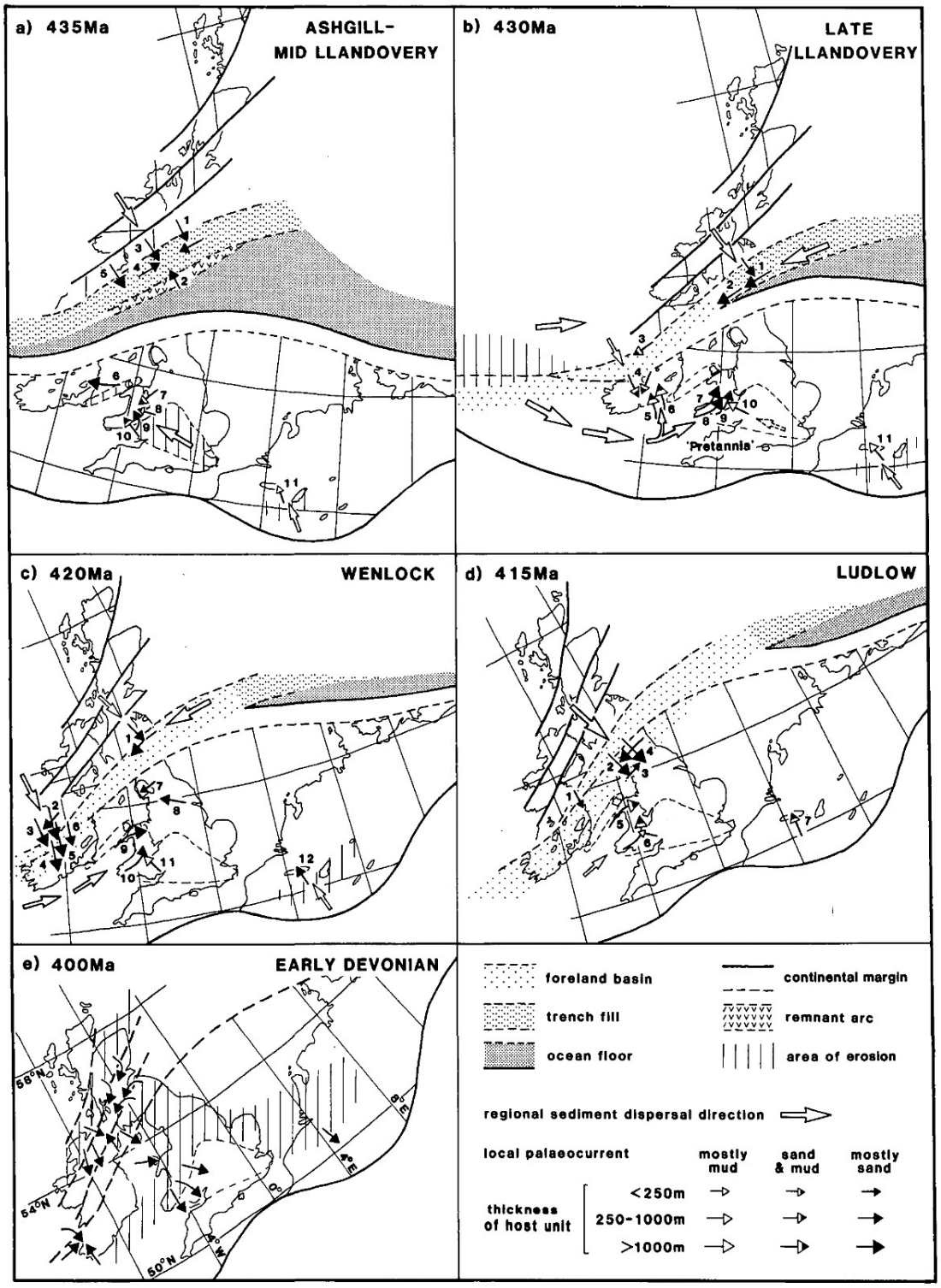

Figure 6.1. Simplified reconstruction of the merging of Eastern Avalonia and Laurentia from 435 to 400 Ma. The figure uses palaeomagnetic and sediment supply data, the latter which is shown by arrows indicating the type of sedimentary supply (Soper & Woodcock, 1990).

6.2 Structure of the Basin

Weaknesses and discontinuities in the crust associated with different terranes influenced and controlled sedimentation (Dewey & Rosenbaum 2008). The Welsh Borderlands are dominated by four fault zones that are orientated northeast - southwest, with the two main ones being the Church Stretton and Pontesford-Linley fault complexes (Cocks, 1989; Dewey & Rosenbaum, 2008; Fig. 6.2). The faults dip steeply and cut deep into the Precambrian basement showing dip-slip and strike-slip displacement (Woodcock & Gibbons, 1998). These faults were then reactivated during the Ashgill Shelveian transpression event that dextrally displaced the rock (Cocks, 1989); extensional faults were also produced at this time by the formation of the Welsh Borderlands, which are orientated north-west.

The Church Stretton fault was the main fault system active during the Silurian (Toghill and Chell 1984). The outcrops to the east of the fault (Fig 6.5) gently dip south-east representing a shallow water shelf facies. However, in mid Wales west of the fault, the formations are much thicker reflecting greater water depth and deposition rates. The dip of the beds west of the Church Stretton fault is much greater, dipping steeply south to south-east; caused by rotation and displacement of the strata associated with the Caledonian folding (Fig. 6.3, Toghill and Chell 1984).

Later Acadian (i.e. mid-Devonian age) deformation had a limited effect in Shropshire showing sinistral transpression (Toghill and Chell 1984). These pre-existing faults were then reactivated again during the Variscan Orogeny (Cocks, 1989).

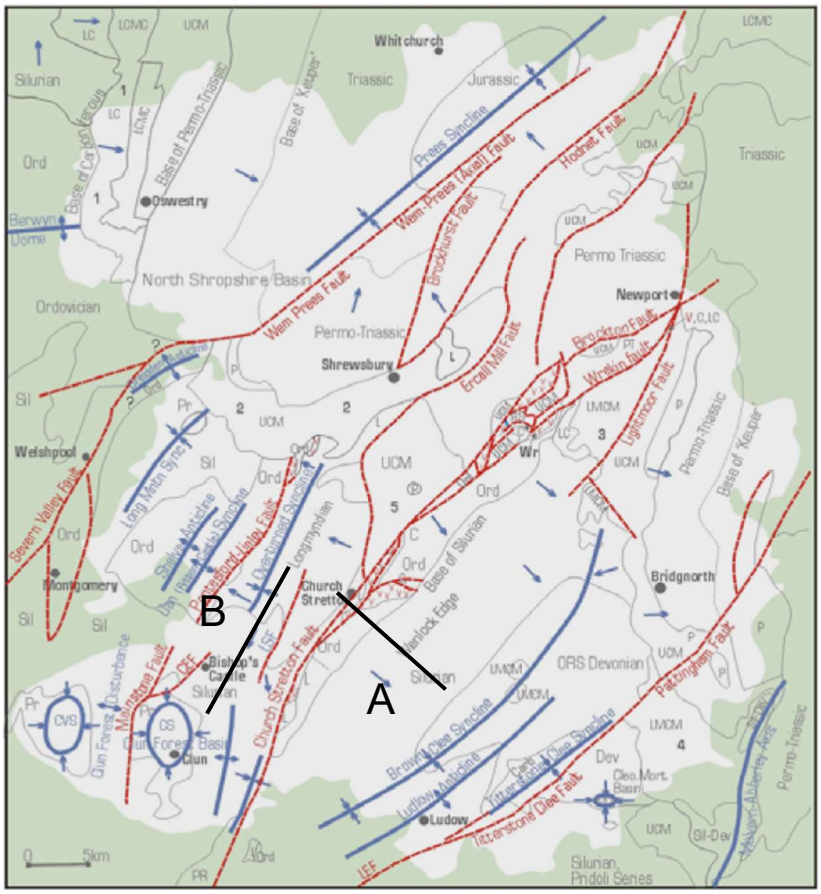

Key

L	Longmyndian	LMCM	Lower & Middle Coal Measures
RS	Ruston Shists	UCM	Upper Coal Measures
C	Cambrian	P	Permian
Ord	Ordovician	LSF	Longmynd Scarp Fault
Sil	Silurian	P-T	Permo-Triassic
Pr	Pridoli	Wr	Wrekin
Dev	Devonian	CVS	Clun Valley Syncline
LC	Lower Carboniferous & Namrian	CS	Cufn Syncline
		CEF	Cufn Erion Fault
		LEF	Leinthall Earls Fault

Figure 6.2. A structural map showing the key folds and faults in the Welsh Borderlands. The major fault is the Church Stretton Fault which was most active during Silurian deposition (Dewey & Rosenbaum 2008).

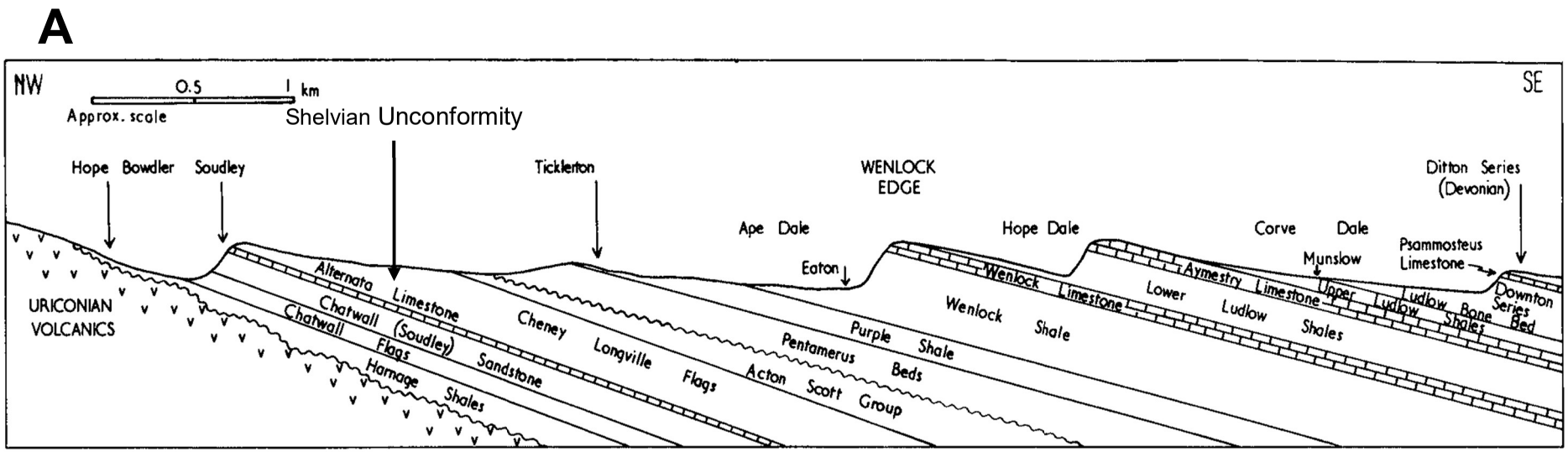

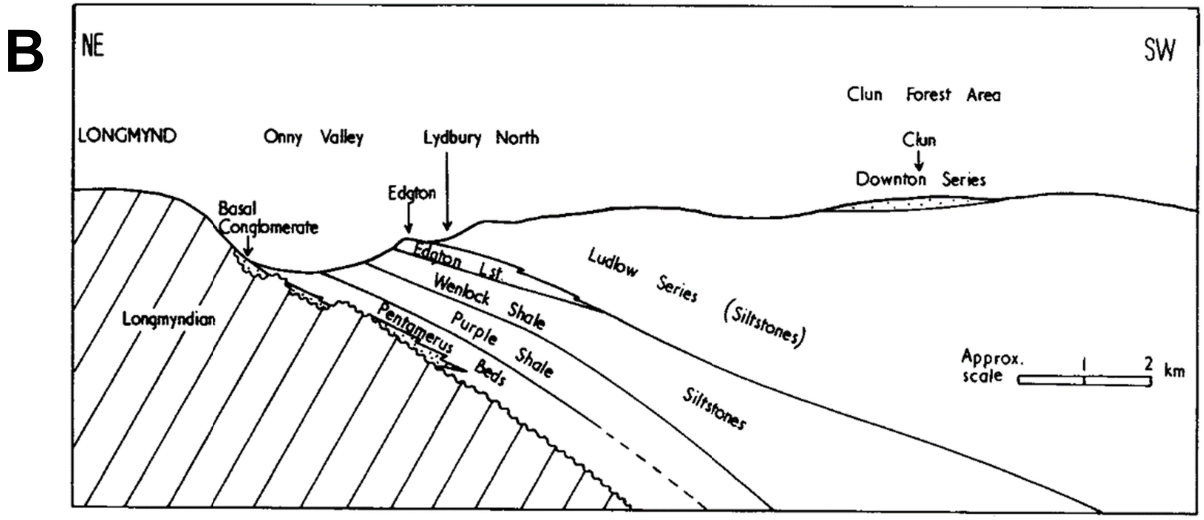

Figure 6.3. A) A cross section from Hope Bowdler to Corve Dale. It shows the strata of the Wenlock Edge east of the Church Stretton Fault. The unconformable boundary between the Precambrian Uriconian Volcanics and the Ordovician beds and the Ashgill unconformity between the Ordovician and Silurian have been highlighted. Thickness of the bed are not to scale. (Toghill & Chell 1984) B) A cross section from Longmynd to Clun Forrest. The Silurian outcrop here uncomfortably overlies the Longmyndian Precambrian and is dipping at a steeper angle (Toghill & Chell 1984).

6.3 Paleoclimate and Palaeobiology

Eustatic sea-level was at a low at the end of the Ordovician owing to the glaciation of Gondwana (Sopher & Woodcock 1990). The sea transgressed at the start of the Silurian and shallow shelf marine facies were deposited in the Wenlock Edge area following the Shelvian unconformity. Sea levels fluctuated during the Llandovery caused by rising global sea-levels and local tectonism associated with the Welsh Borderland Fault System and areas to the west of the Church Stretton Fault (Davis et al., 2011). These fluctuating sea-levels lead to fluvial conglomerates, sandstone and mudstones being deposited locally at the start of the Llandovery.

During the Aeronian, shelf deposition was of sandstone, siltstone and shales which were associated with the Bog Quartzite, Venusbank Formation, Kenley Grit, and Pentamerus Beds (Davis et al., 2011). In the late Aeronian the sea transgressed further leading to geographically extensive shallow marine shales throughout the Telychian, such as the Tarannon ‘purple’ shales which overlie the Cefn Formation sandstones (Mullins & Loydell, 2002). Sea-level reached an acme at the end of the Llandovery and then regressed at the start of the Wenlock (Fig 6.4; Woodcock & Strachan, 2000). In the Wenlock, thick shales of the Coalbrookdale Formation (>200 m thick) formed across the shelf, with deposition of limestone units of the Farley Member above.

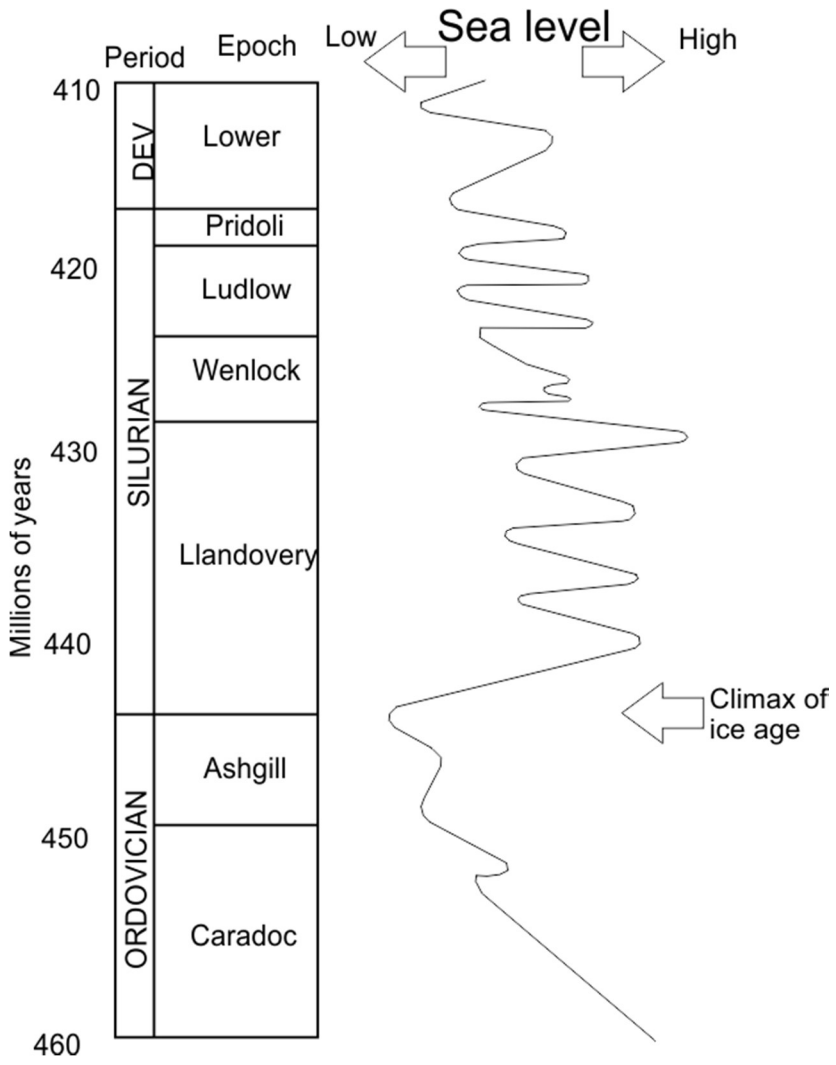

Figure 6.4. A global sea-level curve from the Late Ordovician to the Early Devonian. The Ashgill (Hirnantian) ice age has been highlighted. Modified from Woodcock & Strachan (2000)

Throughout the later Silurian, the Welsh Borderlands represented an interval of deposition in shallow seas. Ziegler et al. (1968) were able to establish five communities of brachiopod: *Lingula, Eocoelia, Pentamerus, Stricklandia*, and *Clorinda*, each of these communities lived in different environmental water depths, Fig 6.5.

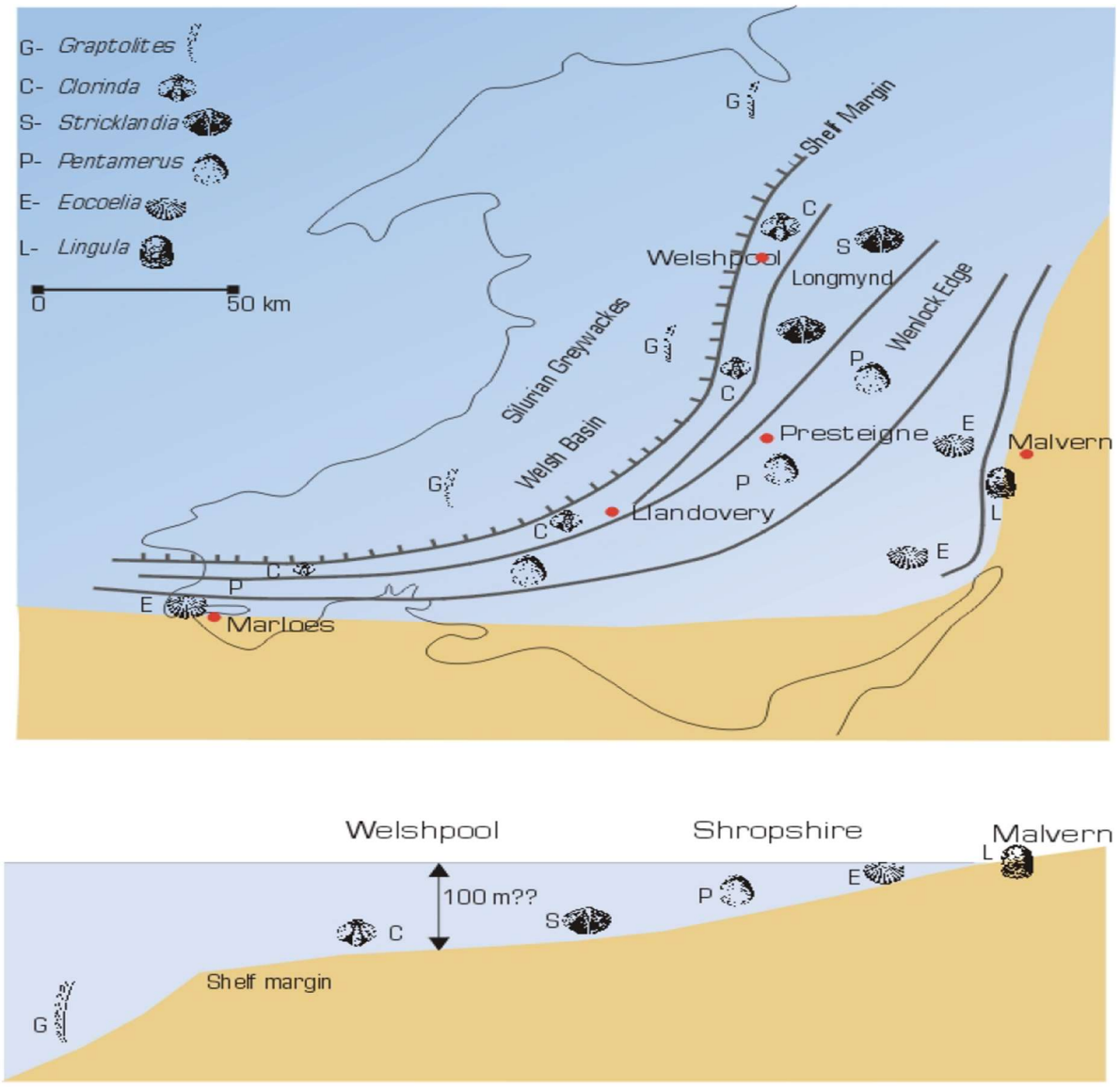

Figure 6.5. The distribution of brachiopod colonies across the Wenlock Edge area and Welsh Basin in the Llandovery. The *Pentamerus* brachiopods are found at c.60 m. These colonies are associated with a series of shale sequences with occasional sandy conglomerates (Ziegler, Cocks & Bambach, 1968; Dewey & Rosenbaum 2008).

6.4 Palaeocurrents and Sediment Transport

Sedimentation in the Welsh Borderlands from the Mid- Llandovery to the Ludlovian is dominated by thinly-bedded, mudstones and sandstones (Basset et al., 1992; Cherns et al., 2006). These mudstones are hemipelagic or turbiditic in origin and are viewed as the lower part of the slope-apron facies (Cherns et al., 2006). Sedimentation was influenced by the formation and uplift of the Pretannia landmass to the south, a result of the convergence of Eastern Avalonia and the Laurentia margin which drove the northerly directed currents (Soper & Woodcock, 1990; Woodcock & Strachan, 2000). Conditions were occasionally anoxic during the Telychian and inter-turbidite and hemipelagic muds are common and are often carbonaceous, containing graptolites (Basset et al., 1992). The area during the Wenlock became dominated by carbonate deposition related to the deepening of the shelf (Basset et al., 1992).

Underwood (1994) used fossil assemblages of benthic fossils e.g. brachiopods and pelagic fossils graptolites in the mudstones to establish the palaeoflow direction (Fig. 6.8). The palaeocurrents indicated by Underwood's (1994) study were orientated parallel to the shoreline. Basset et al. (1992) and Underwood (1994) suggest the dominant palaeoflow mechanism was storm or longshore-directed bottom currents instead of turbiditic.

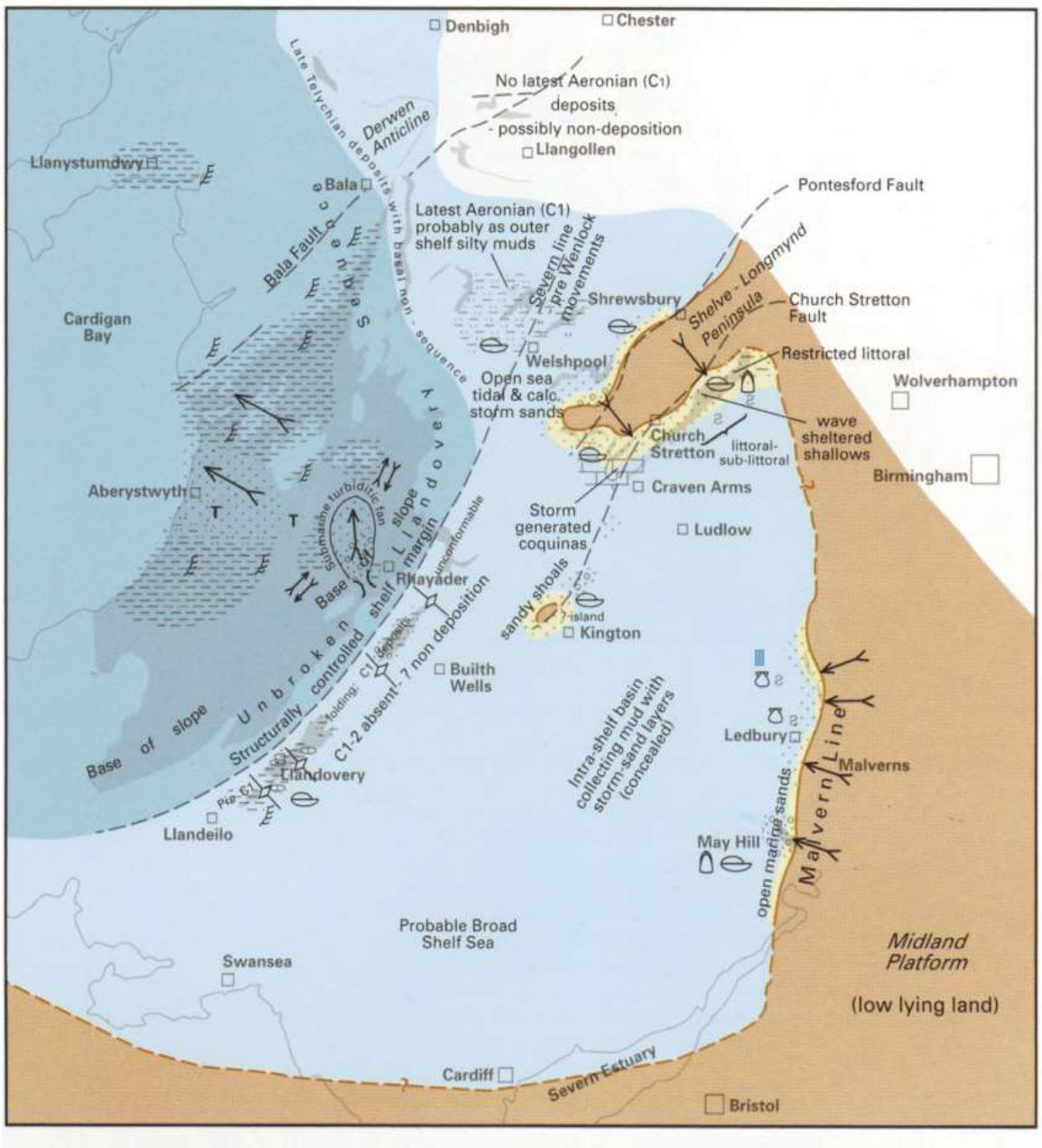

Figure 6.6. Palaeogeographic map showing the shorelines of Wales and the Welsh Borderlands in the late Middle Llandovery (Aeronian) based on different biozones (Basset et al., 1992).

6.5 Welsh Borderlands Study Area

The geographical locations of the three study sites are shown in Fig. 6.7., Fig. 6.8., is a summative Silurian correlation chart showing the main lithological members and the age of each site.

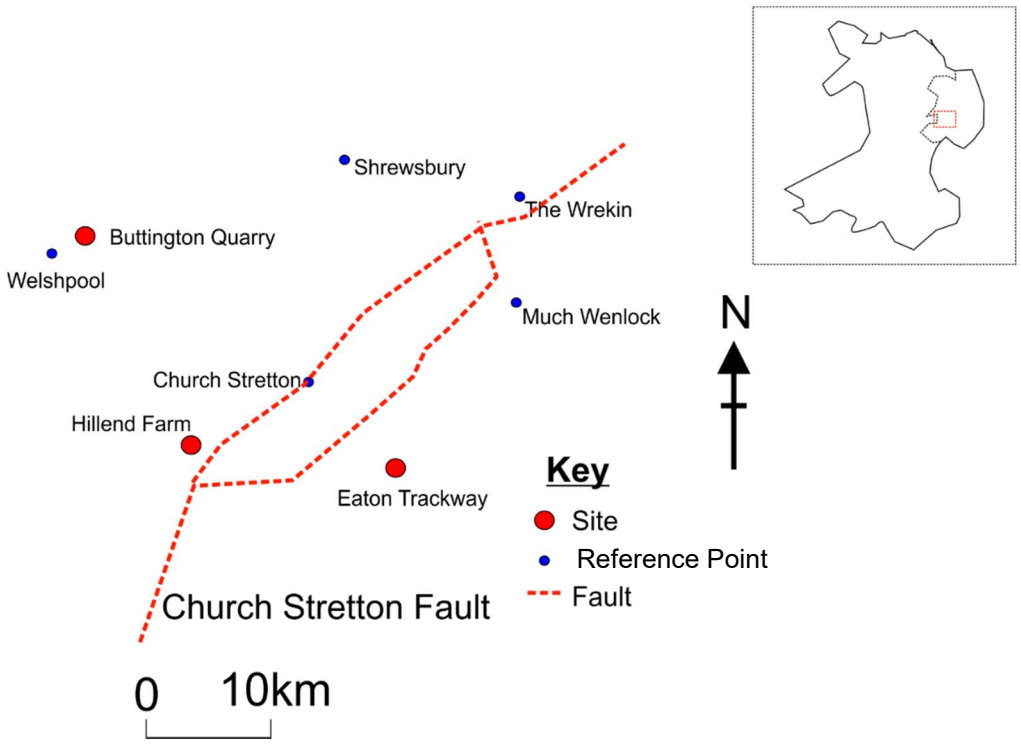

Figure 6.7. Sketch map showing the three sampled sites and the Church Stretton Fault. The location of the Buttington Quarry is west of the Church Stretton fault zone which is shown in the steepness of bedding when compared to other sites.

Figure 6.8. Correlation chart in which columns represent (left to right) the series, stage, sub-stage, graptolite biostratigraphy zone, conodont biostratigraphy zone, members of the Welsh Basin and Wenlock Edge/West Midlands which both have been divided into three different columns depending on geographic areas and the last column is a generalised ^{13}C curve. The study sites are shown on the far right (Davis et al. 2011).

6.6 Hillend Farm

The Hillend Farm outcrops (located, Fig. 6.7) are composed of three sub-sections (Fig. 6.10). At the top are interbedded chocolate-brown to purple silty mudstones with shelly limestones at the base in the Quarry and roadside sections, which are part of the Pentamerus Beds (Fig. 6.10). The Pentamerus Beds thicken basinwards, and are up to 91 m thick (Crossley & Clark 2015). At Hill End the Pentamerus Beds lie metres above the Precambrian unconformity and are Aeronian in age (440.3-438.5 Ma) dated by the presence of graptolite and brachiopod species *Clinoclimacograptus retroversus* and *Eocoelia hemisphaerica* at the base of the outcrop (Crossley & Clark 2015). These findings suggest that these three outcrops only span less than c.1Ma from the Late Aeronian to the earliest Telychian.

Figure 6.9. The outcrop where the Farm yard log was taken on the Hillend Farm site (Fig 6.10). The red line shows the base of the section which dips gently to the right. Sampled outcrop extends for 10 m to the right.

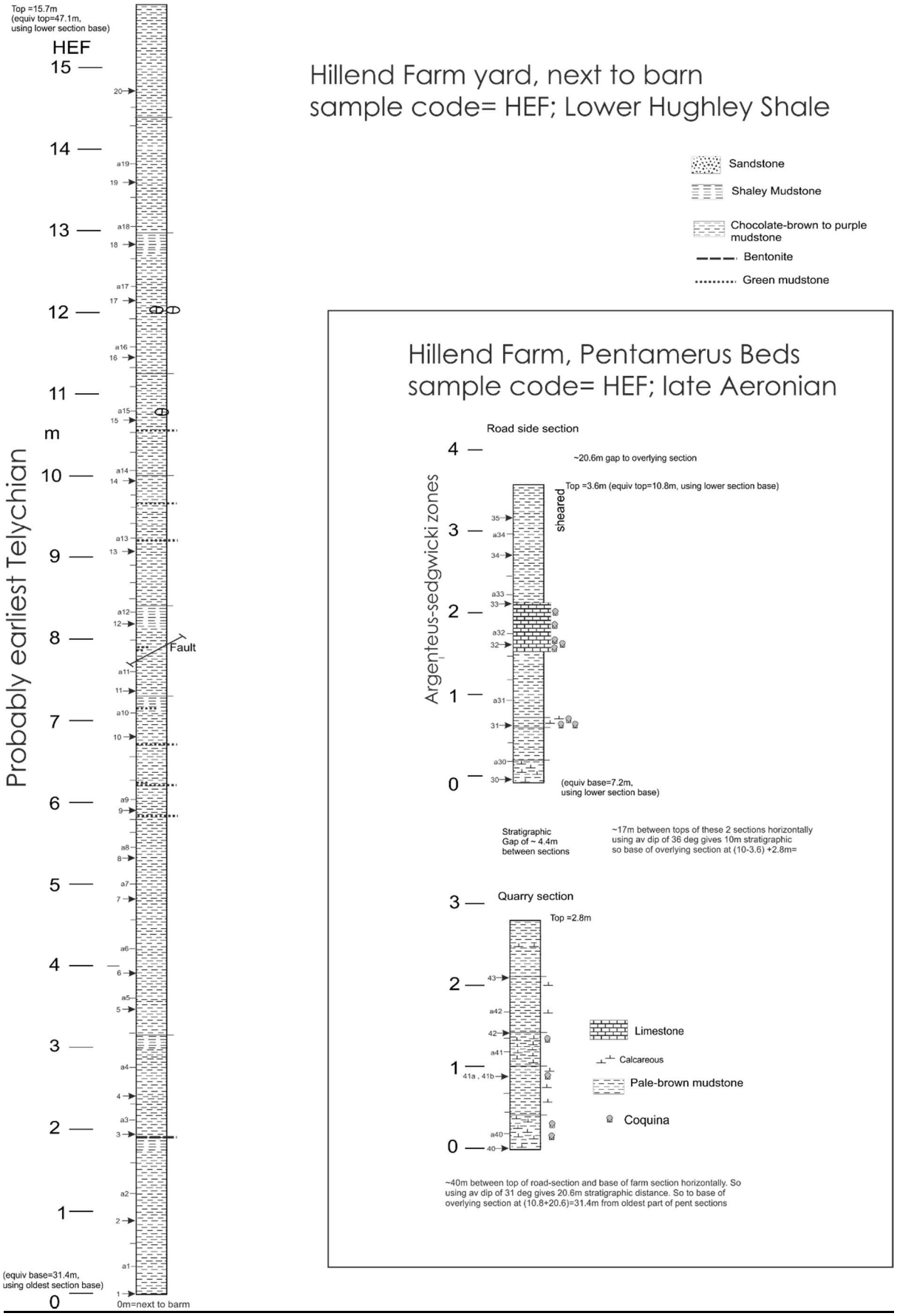

Figure 6.10. Log of the Hillend Farm site, divided into farm, quarry and roadside sections. The sample numbers are shown.

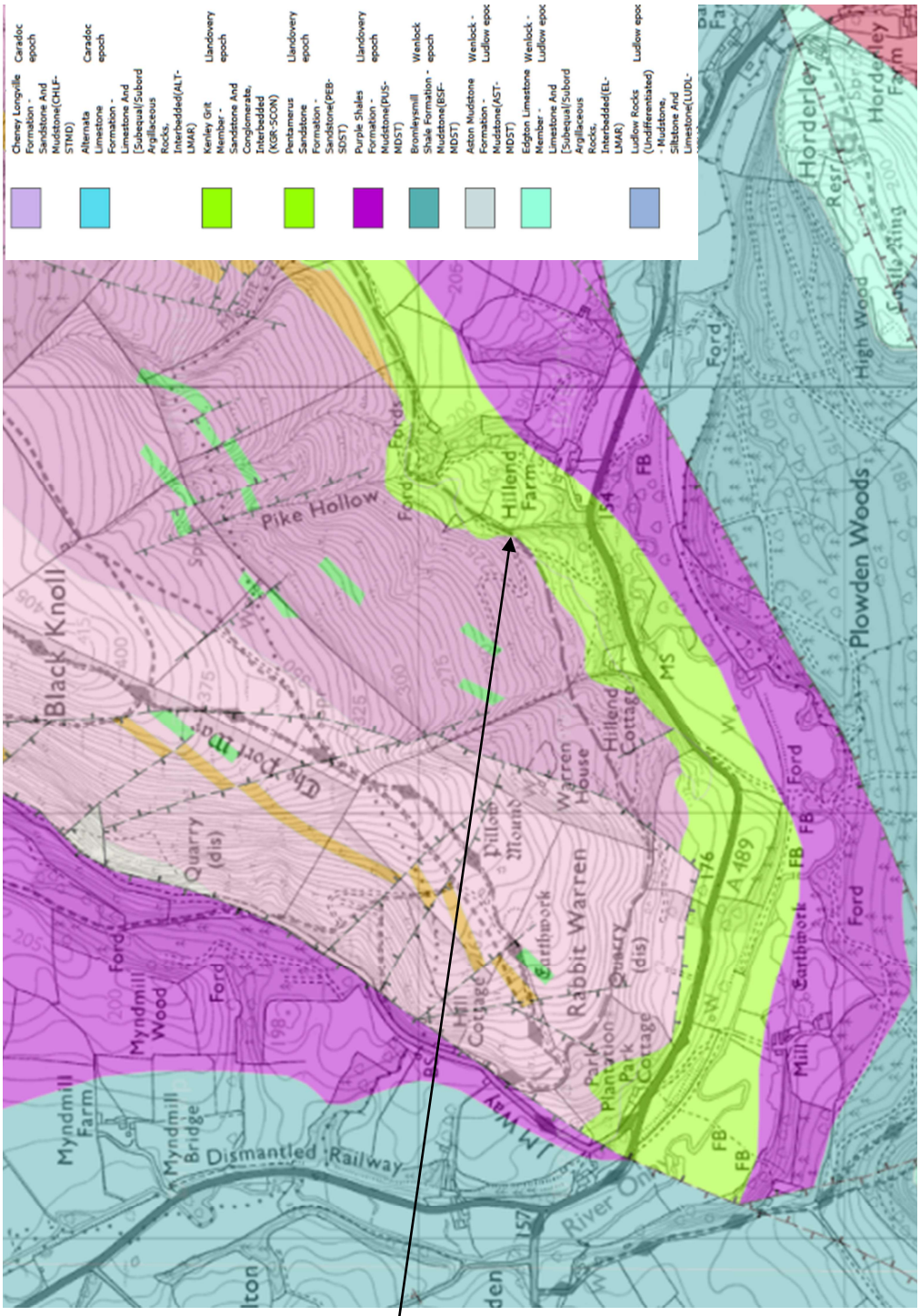

Figure 6.11. Geological map of the area around the Hillend Farm, showing key lithologies and local faulting. A key of the main geological units is shown in the top right. (EDINA. 2016)

6.6.1 Hillend Farm AMS Results

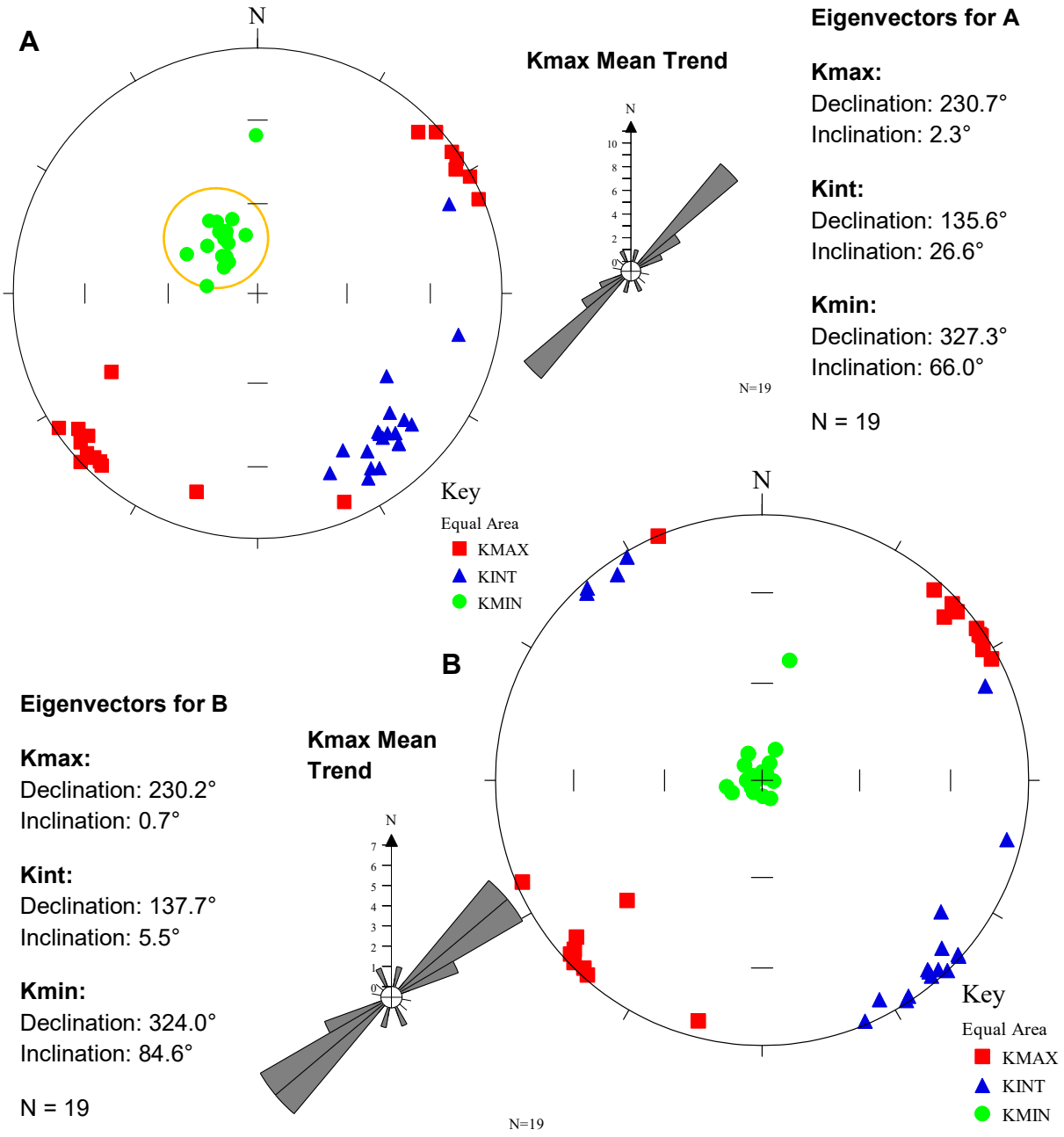

Figure 6.12. Stereoplots of the AMS axes for Hillend Farm and summary Kmax orientation trends. A) The AMS fabric shown in in situ coordinates. B) Corrected for bedding orientation. All the specimens had a NE strike (c.050°) and gentle dip (c.20°) which align with the Kmax direction. Hillend farm next to the barn (Lower Hughley Shales) was the only subsection measured in this AMS study.

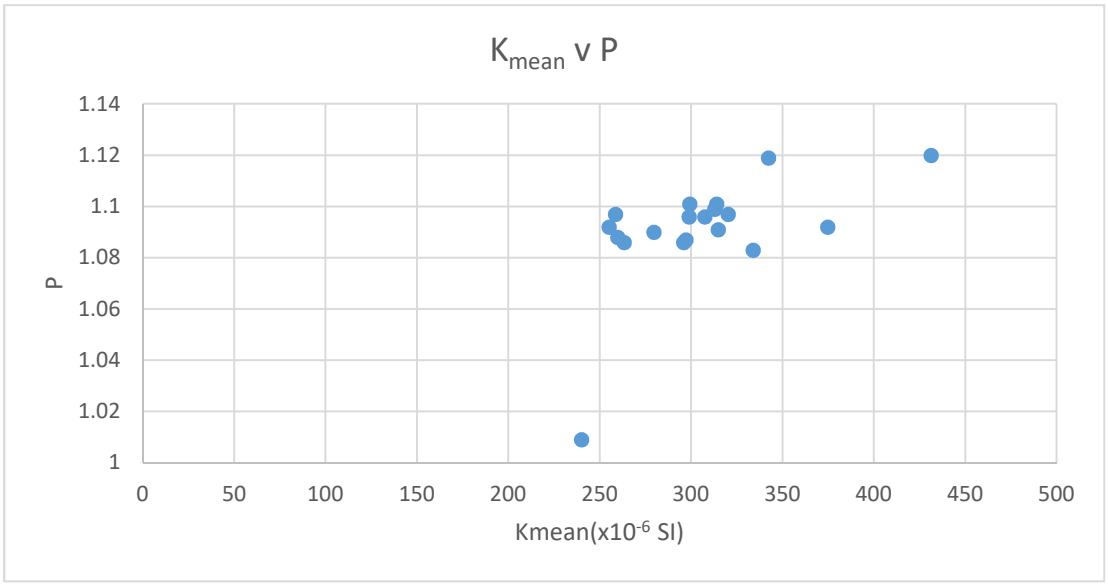

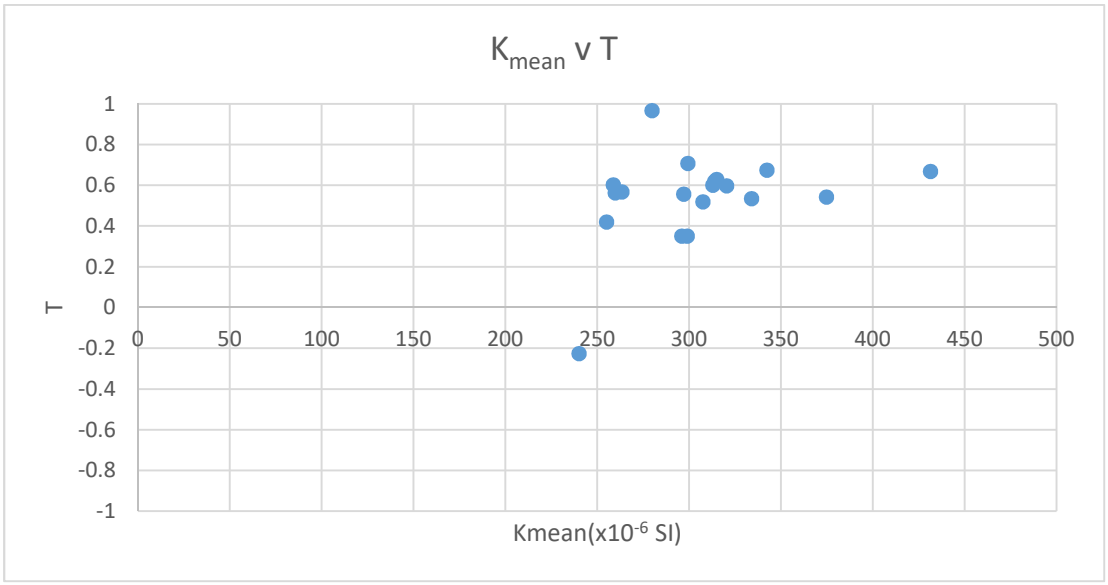

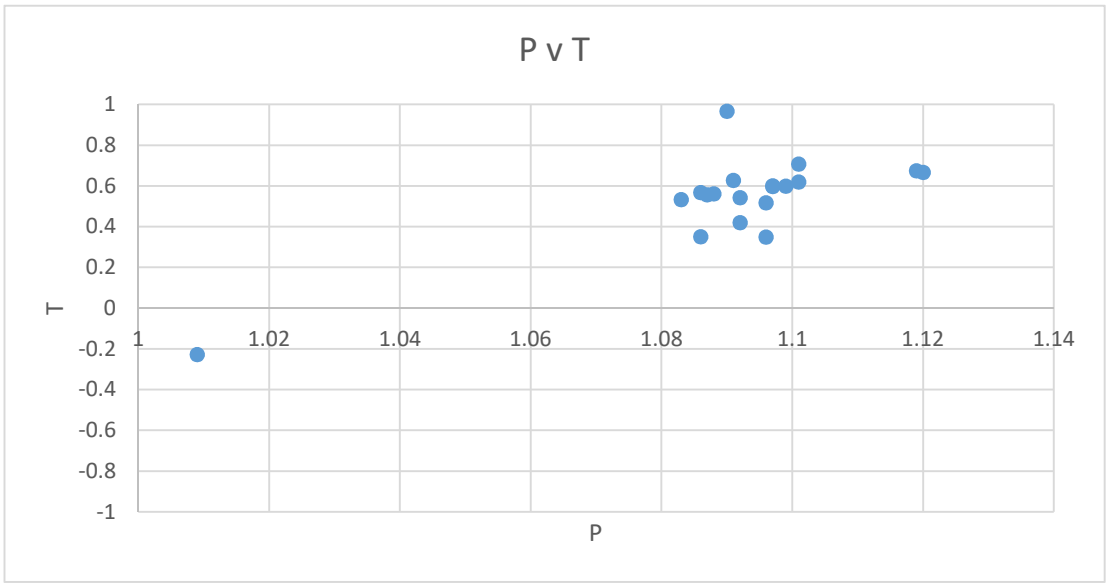

Figure 6.13. Mean magnetic susceptibility (K_{mean}), shape (T) and degree of anisotropy (P) of Hillend Farm specimens. Apart from the single anomalous result, the K_{mean}, T and P values are quite consistent at this site.

The contributions of tectonic activity were examined using a direction-correction (DC) fold test (Enkin J., 2003) in Fig. 6.14. The DC fold test indicates that the Kmin is part of a sedimentary fabric that formed prior to tilting or folding but has been affected to some extent by local tectonism.

Best fitting Slope (Unfolding): 155.8%;
α95% Confidence interval: ± 51.5%,

The DC fold test is positive, indicating the Kmin was probably acquired prior to tilting or folding.

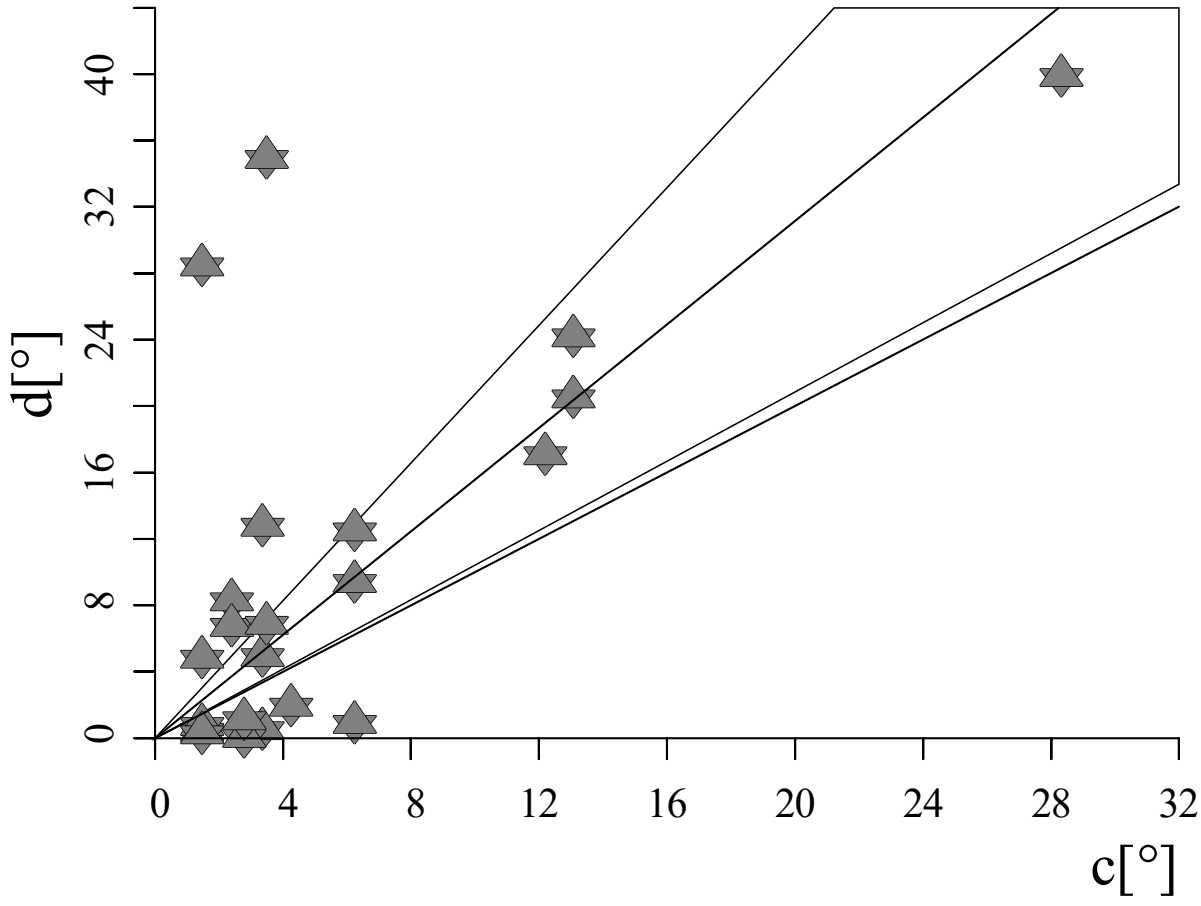

Figure 6.14. Direction-correction (DC) fold test using the declination and inclination of the bedding and the geographically corrected Kmin directions (Enkin J. 2003). The optimal clustering is at 155.8% slope with a α95 ± 51.5% which the high value of the α95 suggest the test is limited in providing a clear-cut result. The DC slope value is 55.8% greater than values expected form undeformed sediments. The results indicate the magnetic fabric of sediments was created prior to the tilting or folding but also suggests the magnetic fabric has been significantly affected by folding.

6.6.2 Hillend Farm Analysis

Low conodont alteration indices (CAI) of 1 to 1.5 in the area east of the Church Stretton faults would seem rule out major heating or deformation of these successions (Aldridge, 1986). The DC fold test was inconclusive suggesting some tectonic influence on the fabric. However, the uniformity of the Kmax axes and bedding-vertical Kmin directions also suggests that the fabric was produced by deposition. Therefore tectonism modifying this fabric seems unlikely as the AMS seems to reflect sedimentary textures associated with deposition and compaction according to Baas et al. (2007) and Borradaile (2001).

There is one dominant Kmax trend orientated northeast-southwest which is aligned parallel to the proposed palaeoshoreline (Fig. 6.6). If this was part of a turbidite deposit, it would have to be low velocity so as not to generate any flow-transverse fabrics that where seen in the Ainsa Quarry. Instead, the AMS fabric is similar to that reported by Shor et al. (1984) from contourites, indicating the AMS is more likely reflective of a shelf current.

The samples have a high T and P values (Fig. 6.13) that could be associated with this hemipelagic/contourite laminar deposition. The high MS values may be reflective of a greater paramagnetic content within the mudstones, suggesting the AMS is caused by preferred crystalline anisotropy of the clay minerals.

6.7 Buttington Quarry

The section in the quarry shows the early Silurian resting unconformably on late Ordovician shales and dolerites. The sediment samples in the quarry are the upper part of the Cefn Formation and all of the Tarannon 'Purple Shales' Formation, (Fig. 6.15; Fig. 6.17; Loydell et al., 2014). The biostratigraphy of the succession in this quarry has been studied by Mullins & Loydell (2001); they used graptolite and chitinozoan biozones to constrain the age from late Aeronian through the entire Telychian c.438-433.5 Ma (Fig 6.16).

Figure 6.15. The relationships between the red- brown and grey mudstones. The bedding is dipping steeply >75°. Shovel is c.70 cm in length.

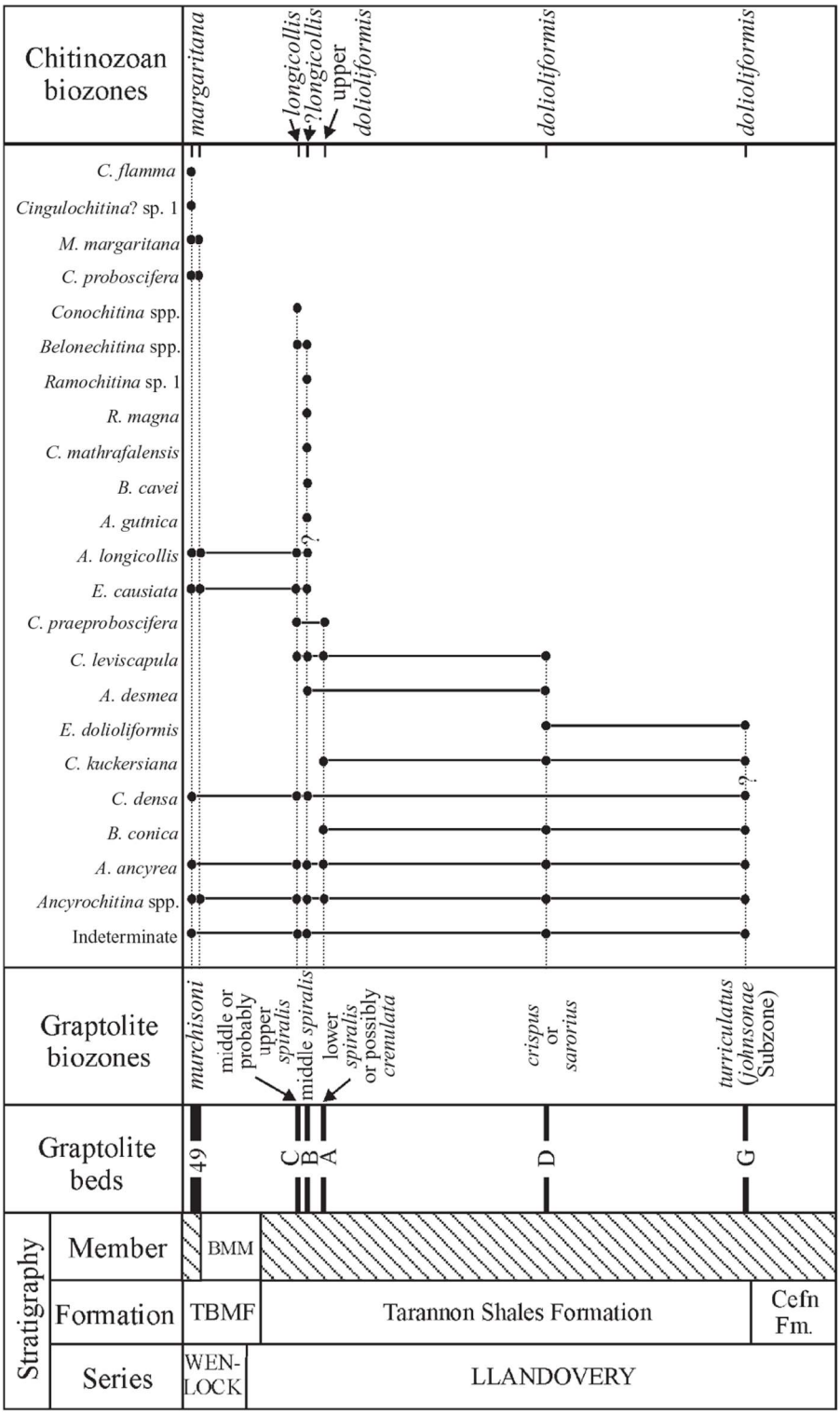

Figure 6.16. Biostratigraphy chart in which columns represent (left to right) the series, formation, member, graptolite beds, graptolite biostratigraphy, recovered chitiozoans and chitiozoan biozones (Mullins & Loydell, 2001).

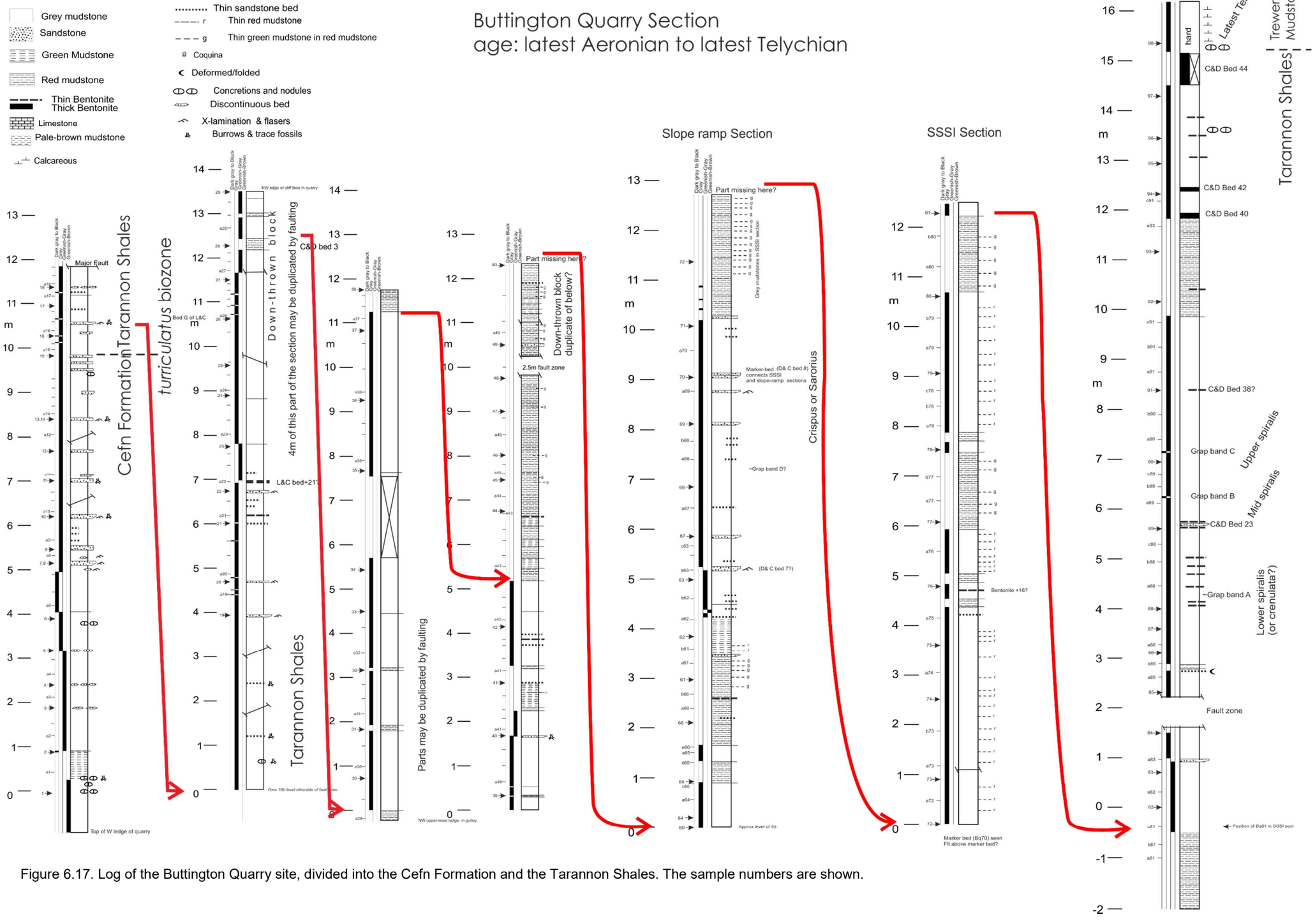

Figure 6.17. Log of the Buttington Quarry site, divided into the Cefn Formation and the Tarannon Shales. The sample numbers are shown.

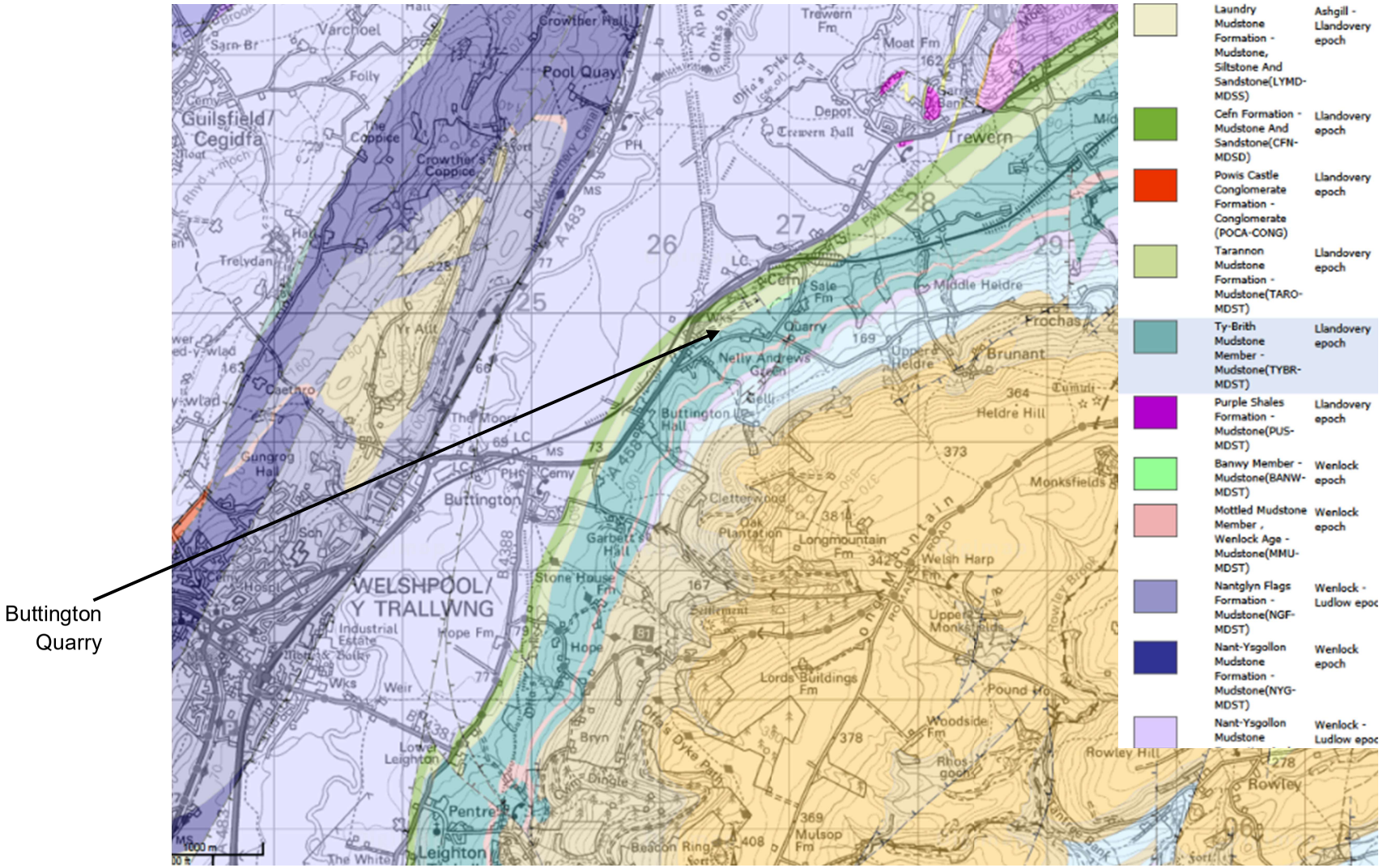

Figure 6.18. Geological map of the area around the Buttington Quarry, showing key lithologies and local faulting. A key of the main geological units is shown in the top right. (EDINA. 2016)

6.7.1 Buttington Quarry AMS Results

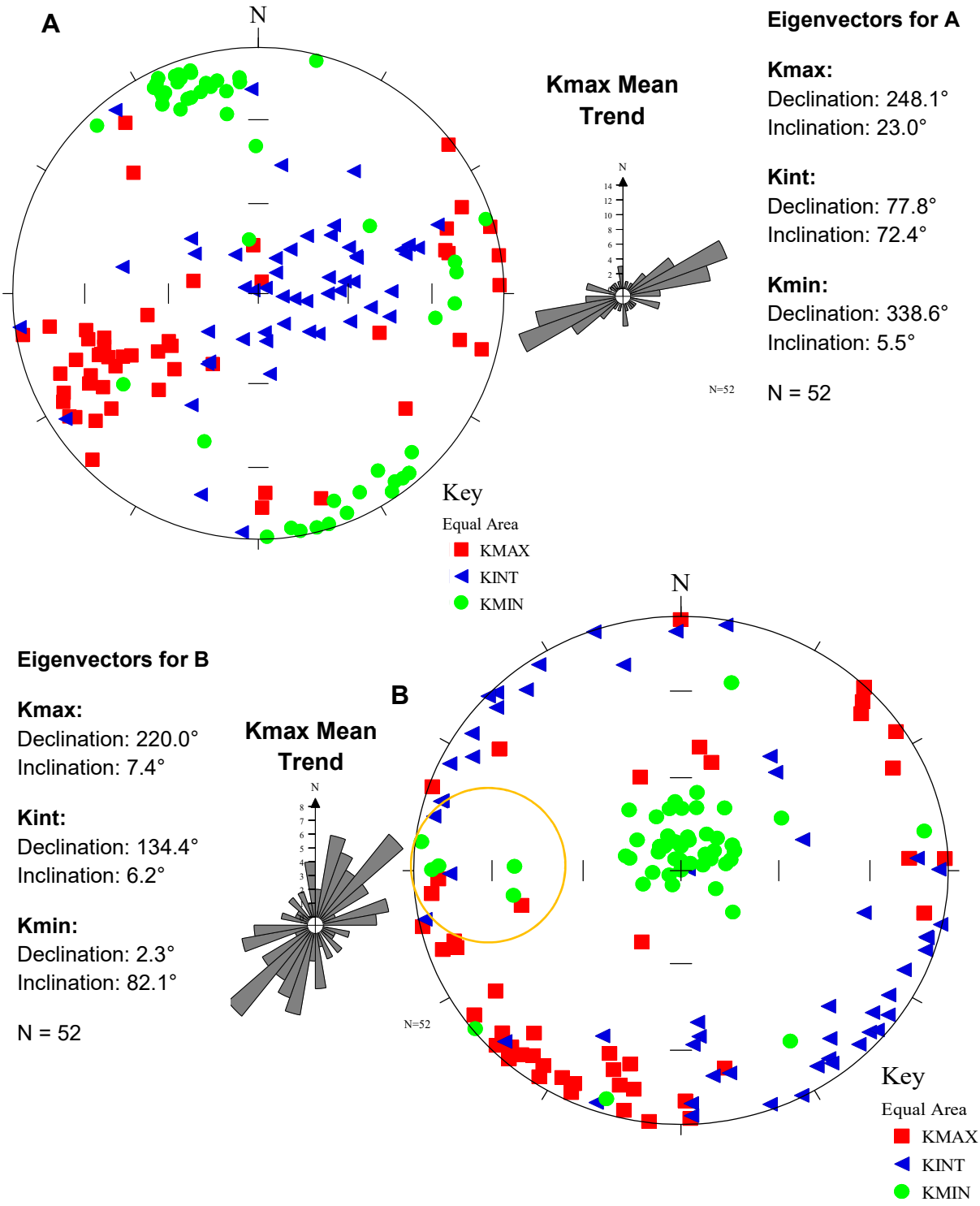

Figure 6.19. Stereoplots of AMS for Buttington Quarry. A) Is the in situ AMS fabric (before bedding correction). B) Corrected for bedding. There is a small minority of anomalous data which are indicated by their shallow Kmin directions (highlighted in the orange circle), these are found throughout the quarry. The bedding varied in strike and dip throughout the quarry, the bottom of the quarry had an average 051/86°, the middle was shallower with an average of 067/75° and the top of the quarry had an average of 080/72°.

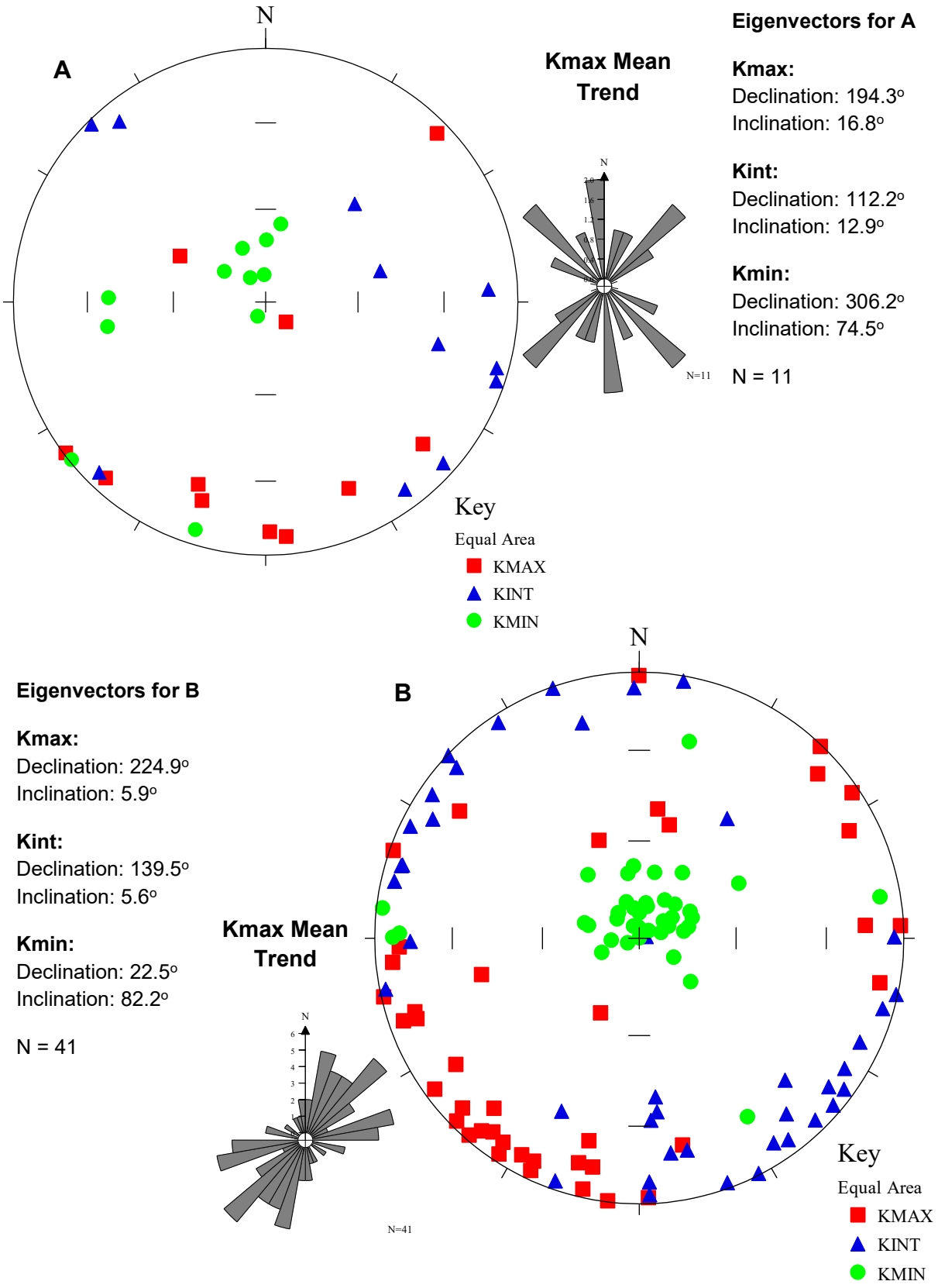

Figure 6.20. Stereoplots of AMS for Buttington Quarry that has been corrected for bedding. A) Cefn Formation B) Tarannon Shales. The Cefn Formation is very scattered and Tarannon shales also show scatter.

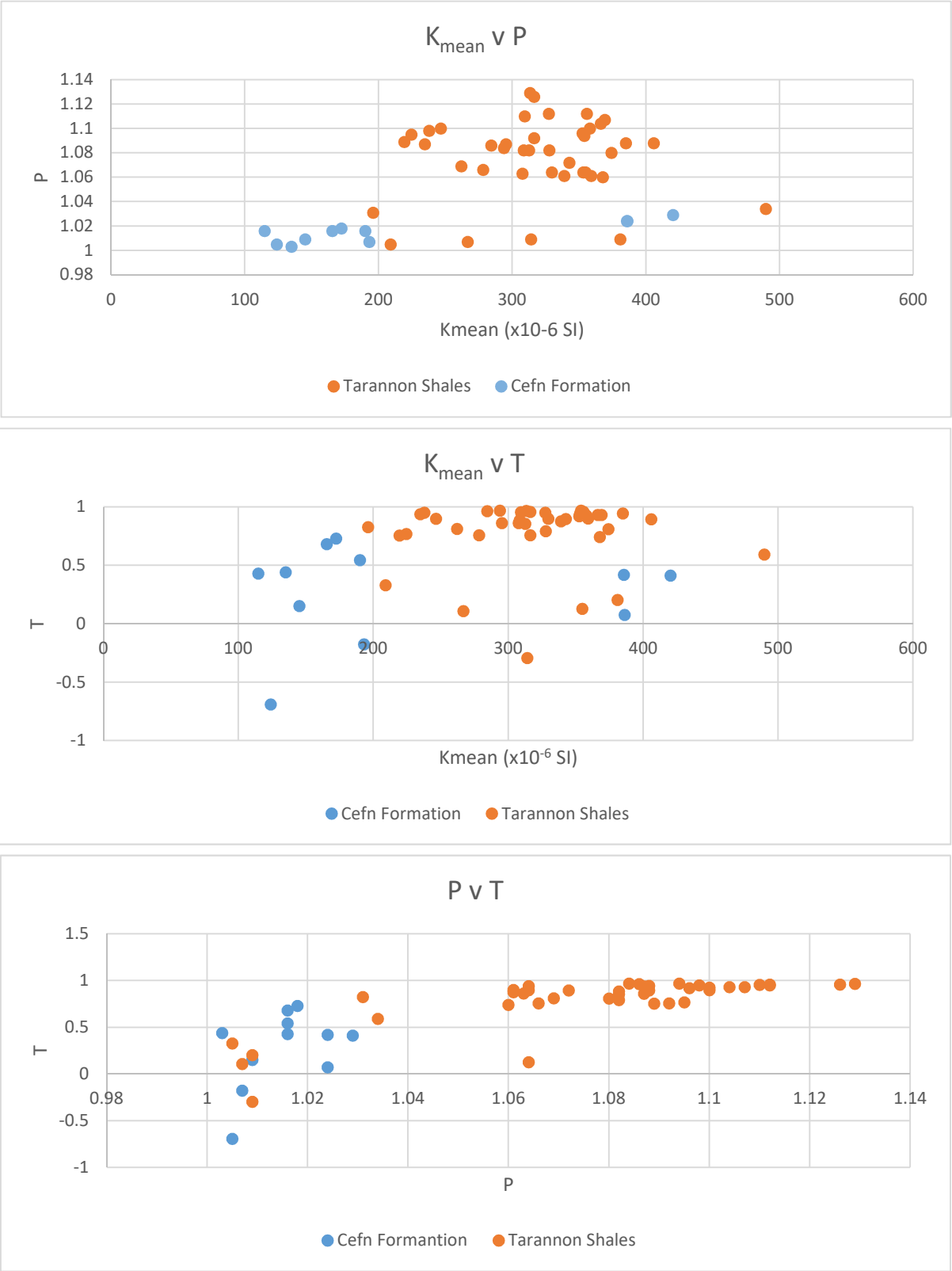

Figure 6.21. Mean magnetic susceptibility (K_{mean}), shape (T) and degree of anisotropy (P) of Buttington Quarry specimens. These have been separated into specimens from the Cefn Formation which have weaker magnetic susceptibility and P values then the Tarannon Shales.

The tectonic activity and presence of girdling of the geographic corrected K-axes at this site (Fig. 6.19) questions if the AMS fabric represents a sedimentary fabric or has it been altered by local tectonic activity. This was tested using a direction-correction (DC) fold test (Enkin J., 2003) in Fig. 6.22.

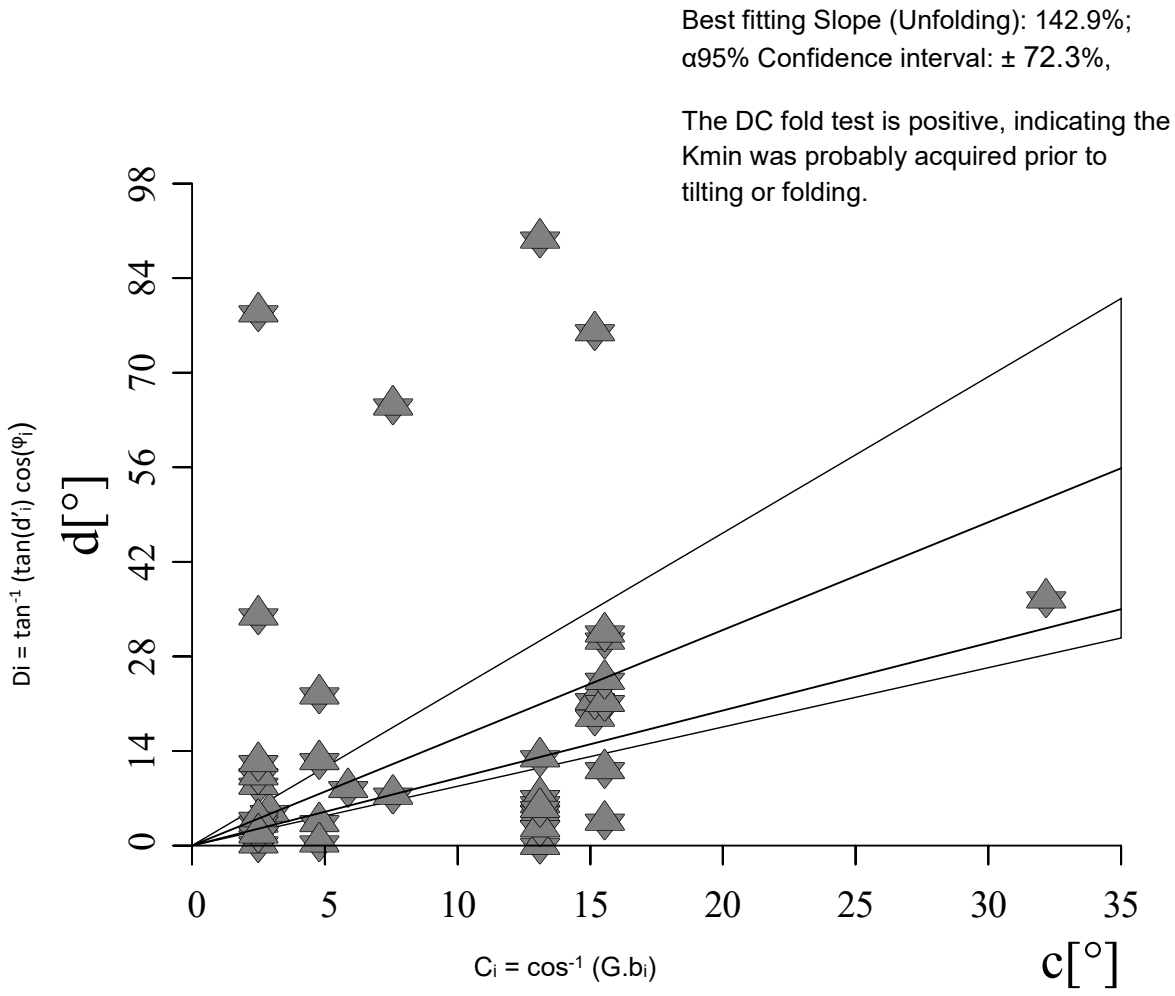

Figure 6.22. Direction-correction (DC) fold test using the declination and inclination of the bedding and the geographically corrected Kmin directions (Enkin J. 2003). The optimal clustering is at 143% slope with a α95 ± 72.3% which the high value of the α95 suggest the test is limited in providing a clear-cut result. The DC slope value is 43% greater than values expected form undeformed sediments. The results indicate the magnetic fabric of sediments was created prior to the tilting or folding but also suggests the magnetic fabric has been significantly affected by folding.

6.7.2 Buttington Quarry Analysis

Tectonism has had a greater impact on the sediments on this site. The beds experienced folding (beds were dipping >75° Fig. 6.19) and faulting but no incipient cleavage has developed. When examining the parameters the P values are high, with some specimens lying within the maximum limits of 1.13 for an underformed shale (Tarling & Hrouda, 1993). These high P values indicate potential for the AMS reflect a tectonic fabric. Evidence of a tectonic influence is also shown in Fig. 6.22 which suggests the AMS fabric of sediments developed before folding but later may have been influenced by tectonics. Thus, when bedding corrections are applied, the AMS axes appear to reflect depositional textures for most of the samples.

There is one dominant Kmax direction orientated northeast-southwest which is aligned parallel to the palaeoshoreline (Fig. 6.19), suggesting a similar depositional mechanism to the succession at Hillend Farm. As both the Cefn Formation and Tarannon Shales share similar AMS fabric it suggests they were deposited within a similar depositional same system. This implies that it is the method of deposition that is controlling the AMS fabric rather than compositional differences.

There was greater scatter in the AMS results at this site compared to others, these anomalous steep Kmax directions tend to have the weak K_m, P values and more isotropic T values. The scatter is mainly found in the Cefn Formation which has a lower magnetically susceptibility than those from the Tarannon Shales (Fig. 6.20.), thus the AMS fabric is not as well defined for each specimen. However, the scatter is present throughout the quarry, this has been attributed to increased deformation shown by its larger CAI value of 2.5 (Aldridge, 1986), that may have diagenetically altered crystalline anisotropy.

6.8 Eaton Trackway

The Eaton Trackway section is located at the base of Wenlock Edge (Burgess & Richardson 1991). This is the youngest study site in the Welsh Borderlands, with the sediments deposited in the Homerian stage of the Wenlock. The units samples are from the Coalbrookdale Formation (Apedale Member) and the overlying carbonate rich Farley Member (Burgess & Richardson 1991). The samples collected were mostly calcareous mudstones (Fig. 6.24).

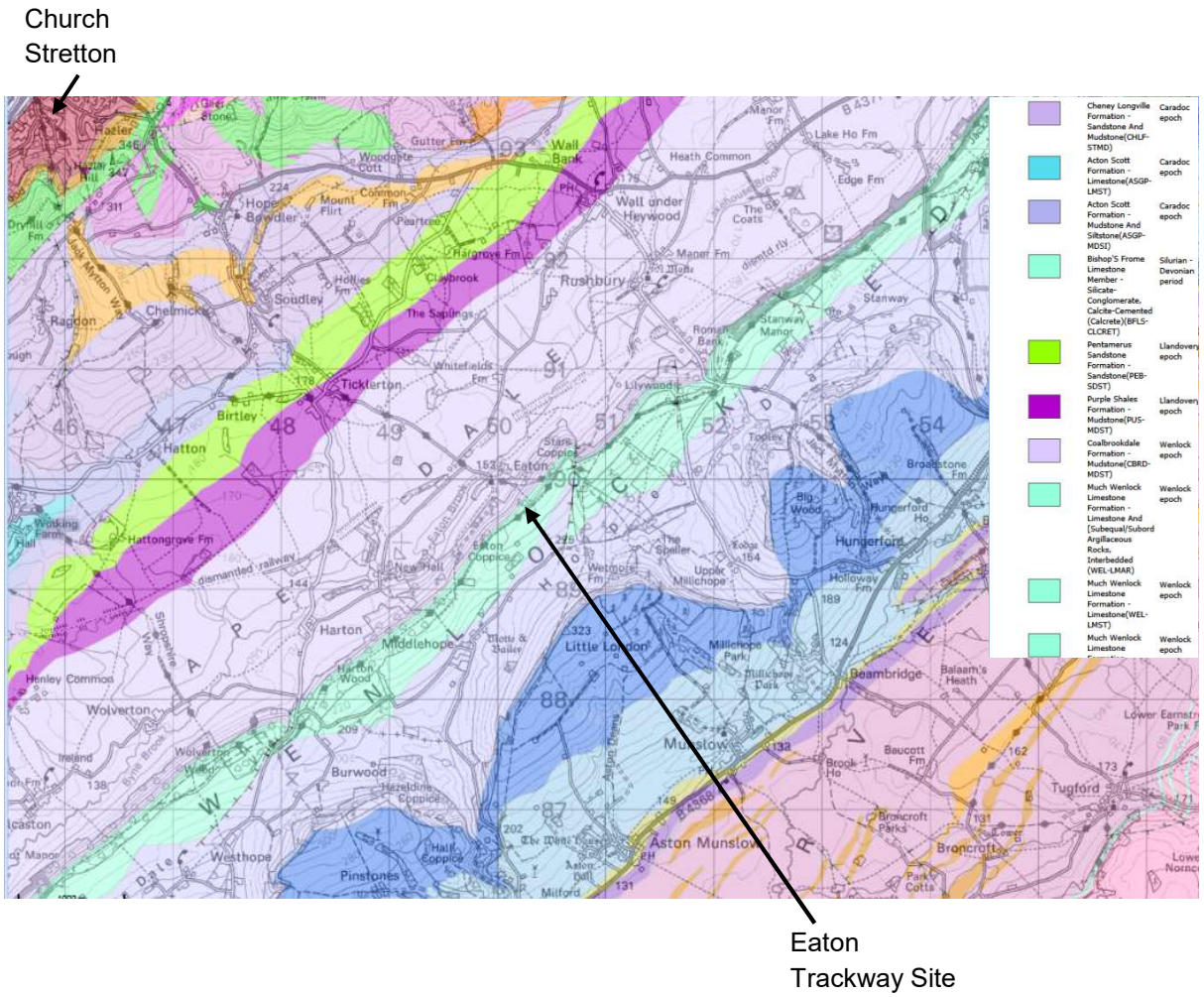

Figure 6.23. Geological map of the area around the Eaton Trackway site, showing key lithologies and minor local faulting. A key of the main geological units is shown in the top right. (EDINA. 2016)

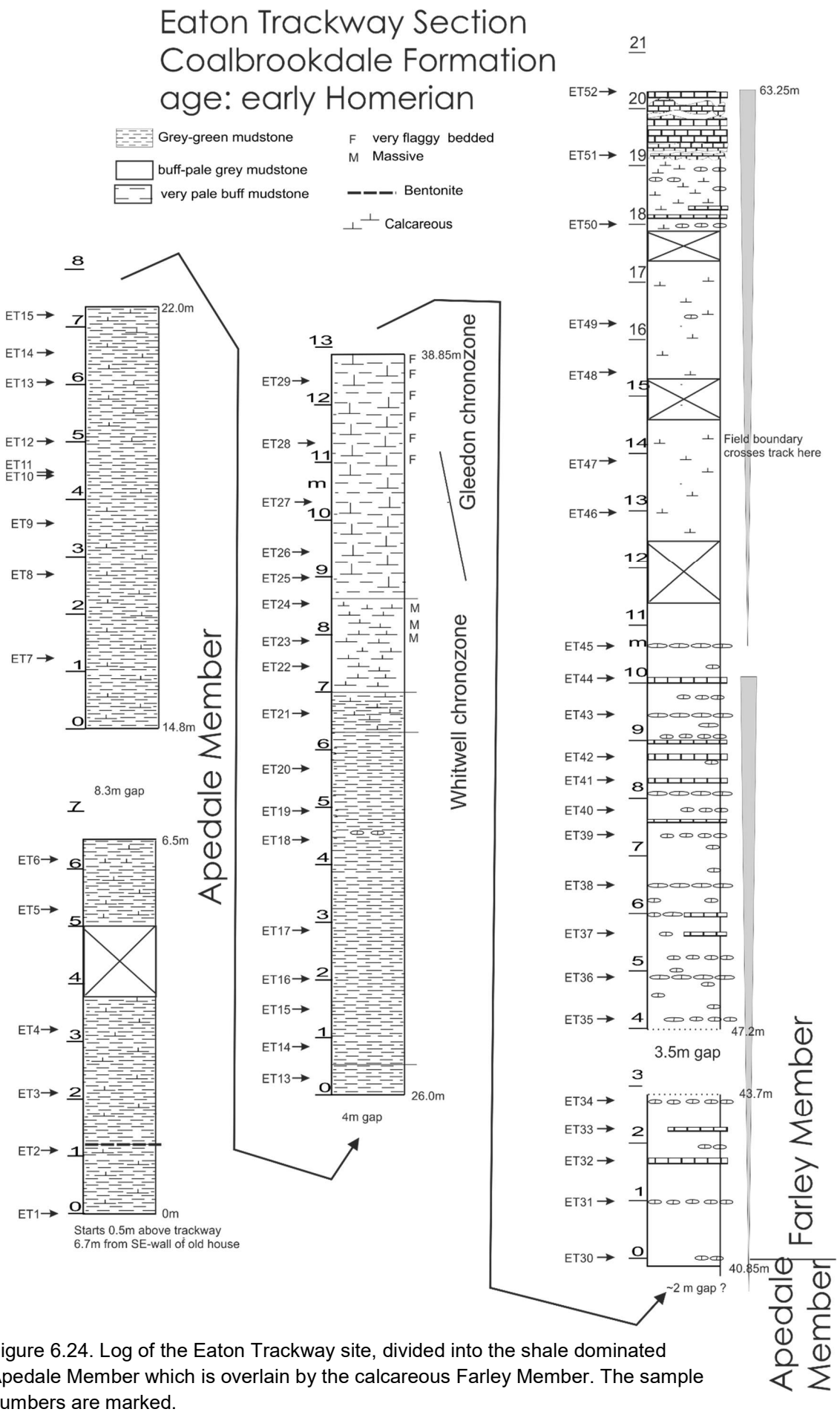

Figure 6.24. Log of the Eaton Trackway site, divided into the shale dominated Apedale Member which is overlain by the calcareous Farley Member. The sample numbers are marked.

6.8.1 Eaton Trackway AMS Results

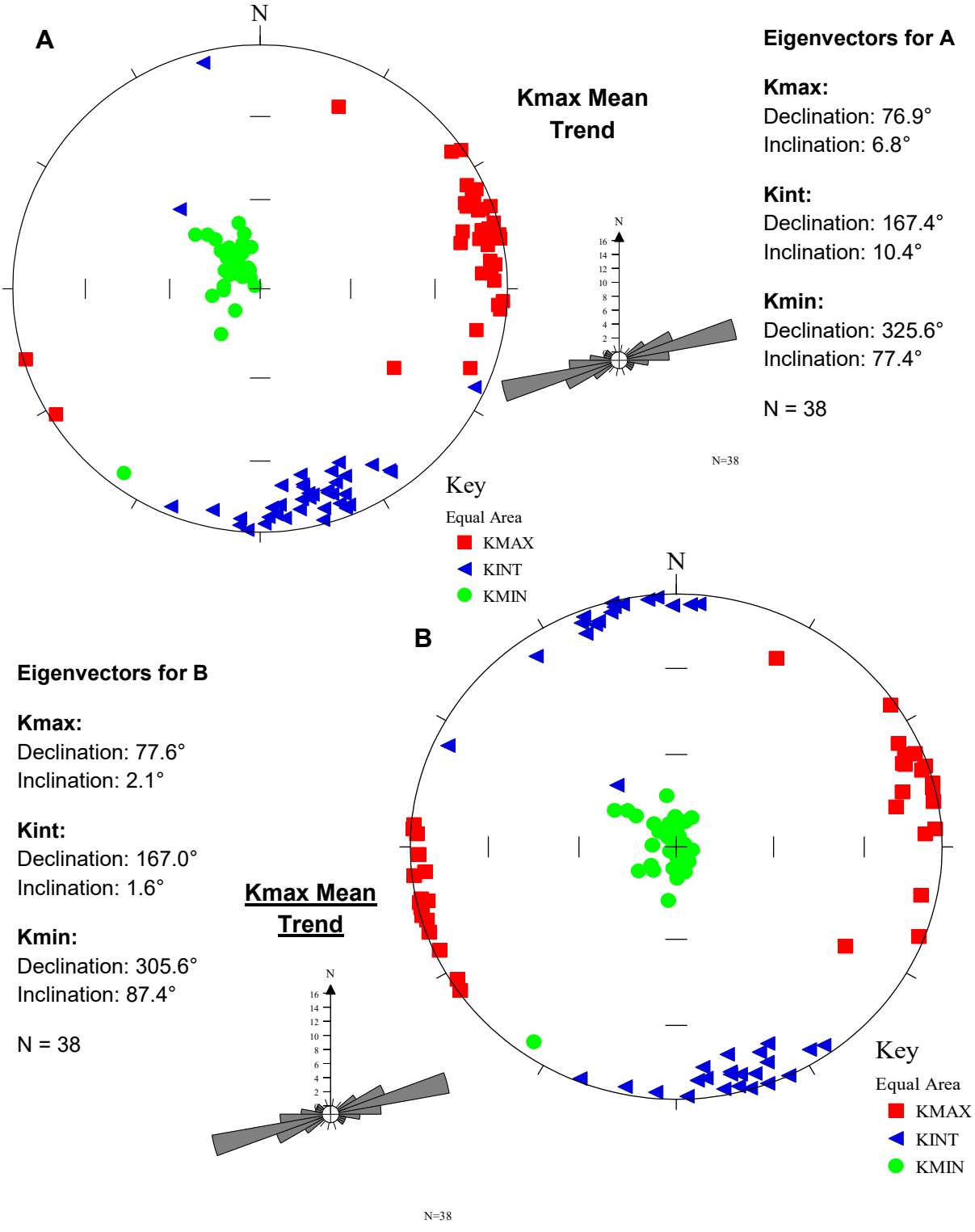

Figure 6.25. Stereoplots of AMS for Eaton Trackway. A) The In situ AMS fabric. B) Corrected for bedding orientation. The bedding dips gently with a maximum dip of 20°.

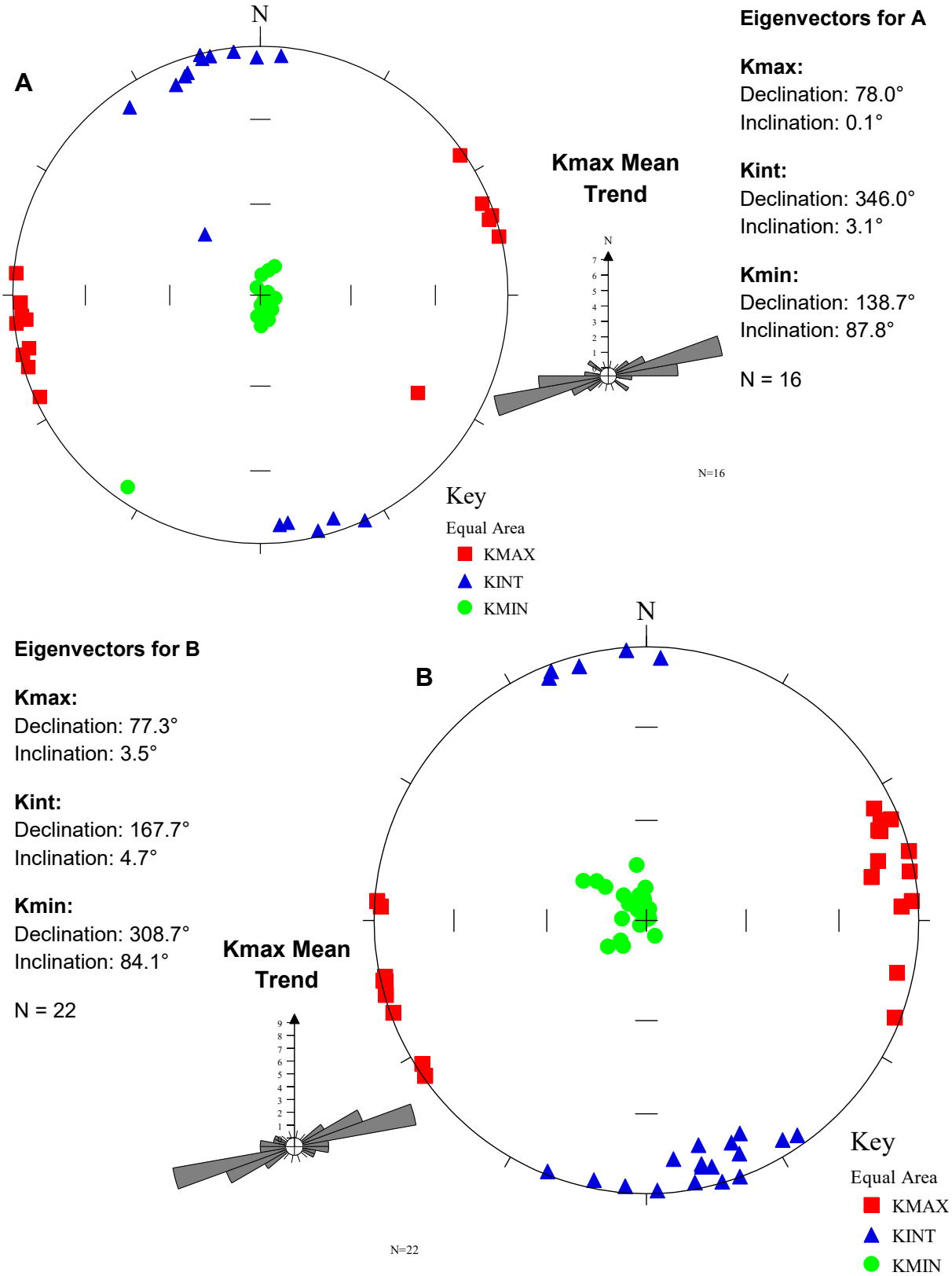

Eigenvectors for A

Kmax:
Declination: 78.0°
Inclination: 0.1°

Kint:
Declination: 346.0°
Inclination: 3.1°

Kmin:
Declination: 138.7°
Inclination: 87.8°

N = 16

Eigenvectors for B

Kmax:
Declination: 77.3°
Inclination: 3.5°

Kint:
Declination: 167.7°
Inclination: 4.7°

Kmin:
Declination: 308.7°
Inclination: 84.1°

N = 22

Figure 6.26. Stereoplots of AMS for Eaton Trackway that has been corrected for bedding. A) Apedale Member B) Farely Member. There is little variations in Kmax directions between the two lithologies.

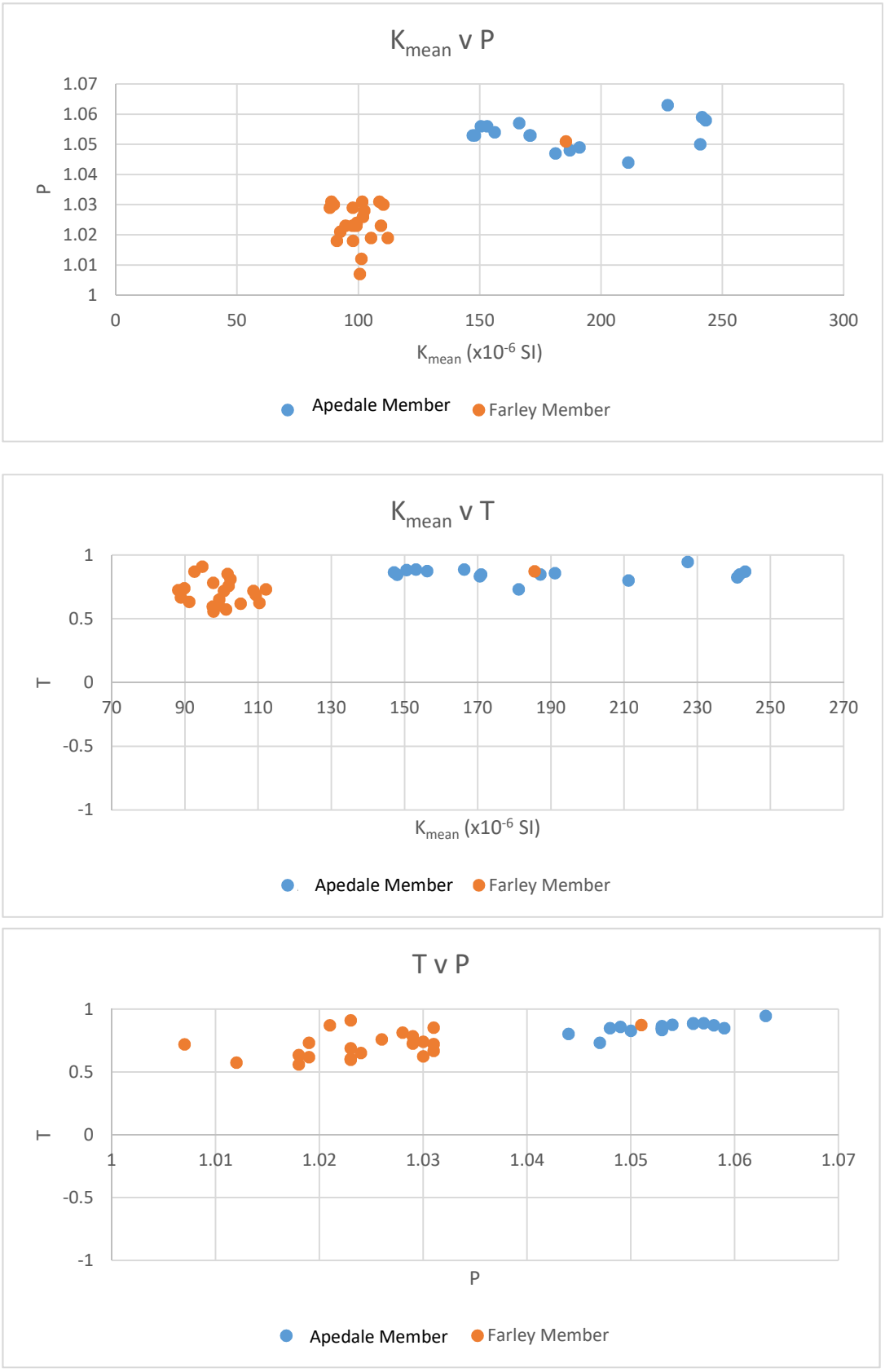

Figure 6.27. The mean magnetic susceptibility (K_{mean}), shape (T) and degree of anisotropy (P) of Eaton Trackway samples. The group circled is the Farley member which has lower magnetic susceptibility and P values then the Apedale Member.

6.8.2 Eaton Trackway Hysteresis Results

A sample from the Apedale Member was selected for hysteresis experiments to examine the paramagnetic contribution to the induced magnetisation.

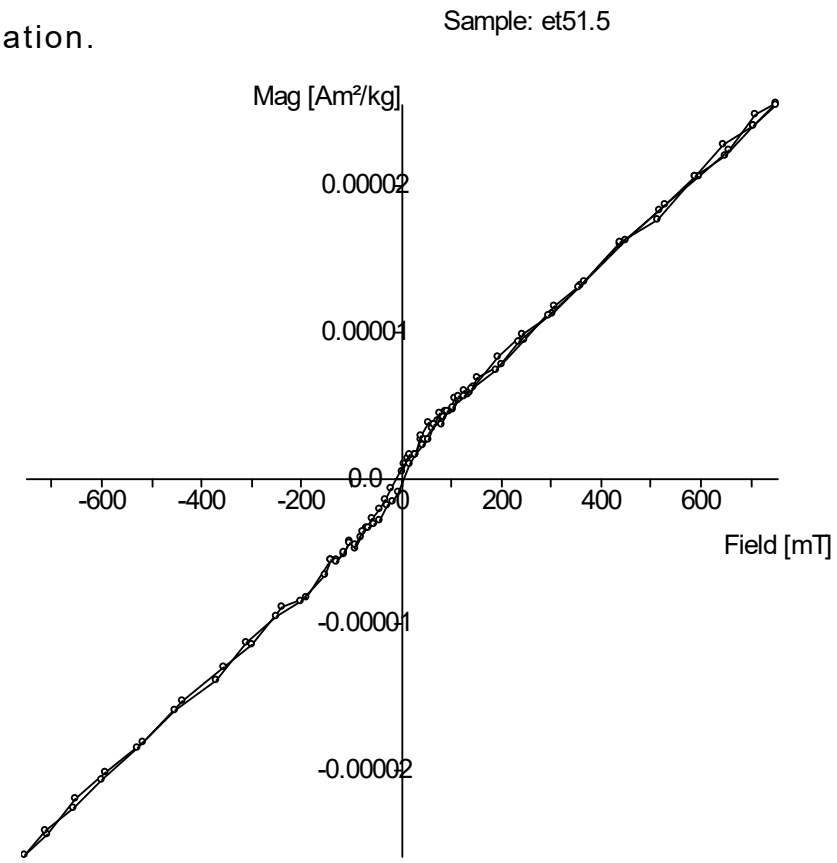

Figure 6.28. Hysteresis plot of a mudstone sample from the Apedale Member in the Eaton Trackway site. The loop shows a paramagnetic dominated mineral contribution, owing to its straight nature with only a small saturating part before c. 100 mT.

Table 6.1. Hysteresis parameters for the Apedale Member sample, MDST=mudstone. The percentage of ferrimagnetic paramagnetic/diamagnetic content. Ms=Saturation induced magnetisation, Mrs=Saturation remanent magnetisation. Hc/Hrh are coercivity and remanent coercivity.

Spec	**Type**	**Ferromagnetic content (%)**	**Para/diamagnetic content (%)**	**Ms (Am^2/kg)**	**Mrs (Am^2/kg)**	**Hc (mt)**	**Hcr (mt)**
Et 51.5	Pale-brown MDST	8.8	91.2	$8.01x10^{-4}$	$5.73x10^{-4}$	14.37	58.77

6.8.3 Eaton Trackway Analysis

The effects of folding and tectonism are insignificant at the Eaton Trackway succession (Fig. 6.25). The very low CAI index (~1.5) would also suggest similar levels of heating as found in the Hillend Farm section (Aldridge, 1986). The Kmax directions only show one dominant trend northeast-southwest which is slightly different from the other sites which may reflect changes in palaeo-topography rather than a different depositional mechanism.

Both the Apedale Member and Farley Member share the same AMS fabric, with similar Kmax directions (Fig.6.26), implying the depositional model has the greatest impact on the AMS fabric. This supports the interpretation of Buttington Quarry where the change in lithology did not change direction of the AMS.

The hysteresis data indicates that the mudstone sample was dominated (c.91%) by a paramagnetic mineralogy suggesting that the magnetic susceptibility is controlled by crystalline anisotropy from clay minerals with a preferred orientation. These clay minerals are probably the dominant source of the AMS fabric in the other Silurian sites in the Welsh Borders, suggested by the similarly high T and P values.

6.9 Conclusion

The effects of tectonism and thermal alteration on the AMS fabric are minimal for most of sites with the exception of the Buttington Quarry site, where it is inconclusive. A fold test and the AMS parameters of the Buttington Quarry potentially reflect a tectonic fabric with the high P values being on the threshold for a 'typical' underformed shale (Tarling & Hrouda, 1993) and the scatter throughout the quarry would suggest the deformation lead to the creation of diagenetically altered crystalline anisotropy. The other sites unaffected by deformation have similar AMS fabrics to the Buttington Quarry site when the bedding correction has been applied, which suggests a sedimentary fabric for the sites. Hence, it is more probable that the AMS fabric for all the sites can be used to infer palaeoflow and a depositional model for the sites (Fig. 6.29).

Cherns et al. (2006); Basset et al. (1992); Soper & Woodcock (1990) and Underwood (1994) have suggested that the depositional model was driven from the uplifting Pretannia landmass leading to northerly currents, where currents were either turbiditic or part of a coast-parallel current system. The AMS data reflects a coast-following contourite system rather than basin-directed low intensity turbidity currents. High velocity turbidity currents would have more than one Kmax direction, showing transverse fabrics associated with grain interactions. Also none of the sites have any significant Kmin imbrication that would be expected in a turbulent flow (Baas et al., 2007). The turbidity transport would be normal to the shoreline, but all the AMS Kmax directions are parallel to the proposed palaeoshore-line (Basset et al., 1992). The

AMS fabrics are similar to those of Shor et al. (1984) contourite study, which found planar AMS representing the bedding of muddy contourites that formed parallel to the shoreline whereas the Kmax directions for the turbidity currents were normal to the shoreline.

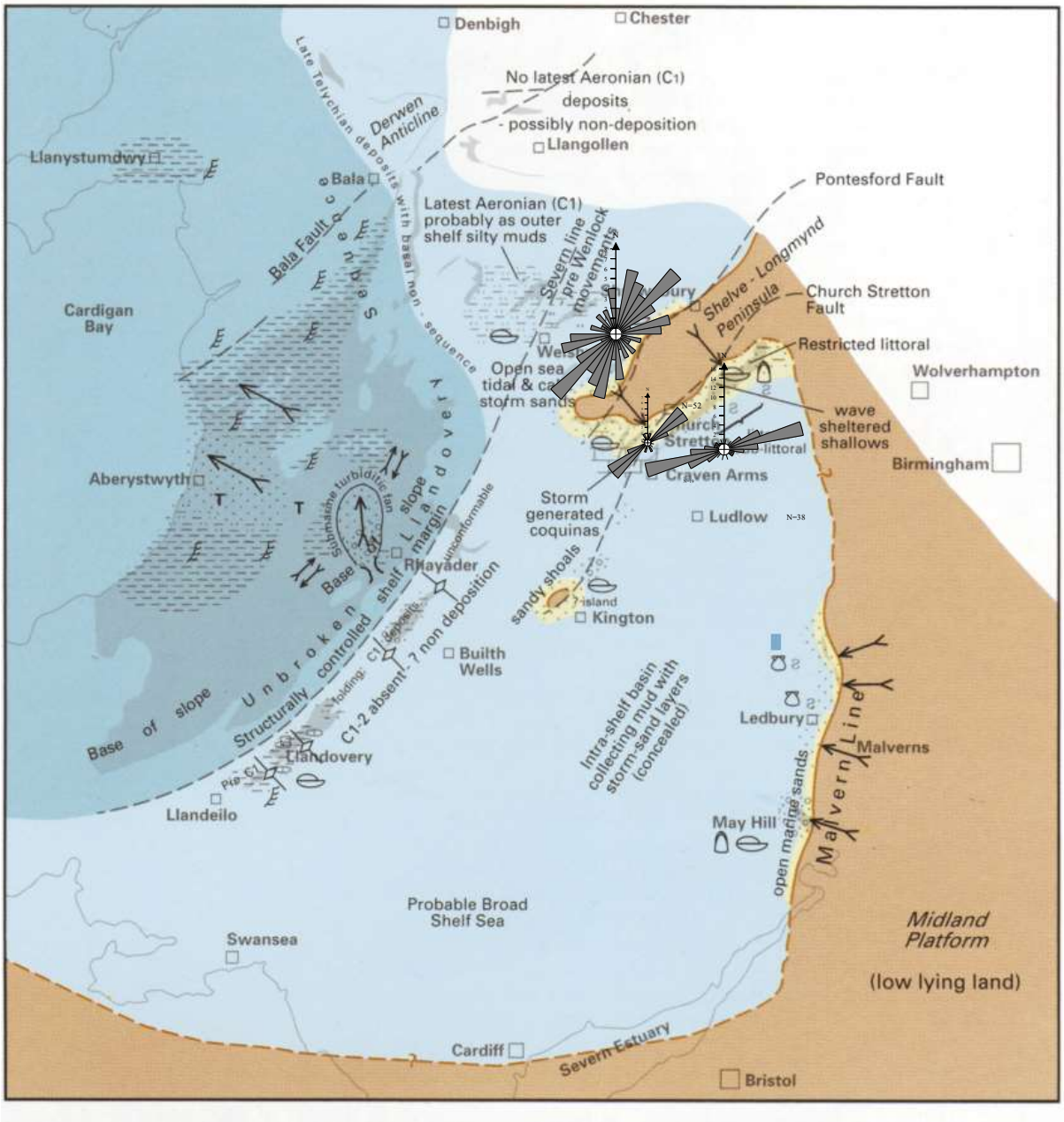

Figure 6.29. Palaeogeographic map showing the shore of Wales and the Welsh Borderlands in the late Middle Llandovery (Basset et al., 1992) with the added rose diagrams of the Kmax directions for each site. The inferred flow from the Kmax direction is aligned with shoreline suggesting a contourite system.

The effects that major lithological differences had on the AMS fabric were examined at the Buttington Quarry and Eaton Trackway sites. The Kmax directions were mostly similar between members and different lithologies. The Cefn Member in the Buttington Quarry has a much weaker susceptibility owing to greater quartz content which probably caused the occasional directional scatter. However, despite changes in composition the AMS fabric was still be successful in indicating palaeoflow.

Hysteresis data on a mudstone sample indicates the dominance of the paramagnetic contribution to the AMS. The crystalline anisotropy could explain the high $K_{M,}$ P and T values when compared to the shape anisotropy of detrital magnetite found in Ainsa. Thus, AMS sourced from crystalline anisotropy can be used to evaluate palaeoflow in these Silurian sediments.

7. Case Study: Marcellus Shale

This section examines AMS as a palaeocurrent indicator in the hemipelagic foreland basin setting of the Appalachian Basin. Samples were taken from two boreholes, borehole A and B located in Western Pennsylvania and north-western West Virginia. The aim of this is to examine the effectiveness of the AMS technique in a deep, organic-rich basin setting where conventional sandstone-based palaeocurrent directions cannot be obtained.

7.1 Appalachian Basin

The Marcellus Shale extensively sub-crops in the Appalachian Basin which is the foreland basin of Appalachian Orogeny (Bret et al., 2011). The fold-axes due to the Appalachian Orogeny are orientated northeast – southwest and folded rocks from the Orogeny cover several states from Northern Alabama to Newfoundland on the east side of North America (Ver Straeten et al., 2011; Fig 7.1).

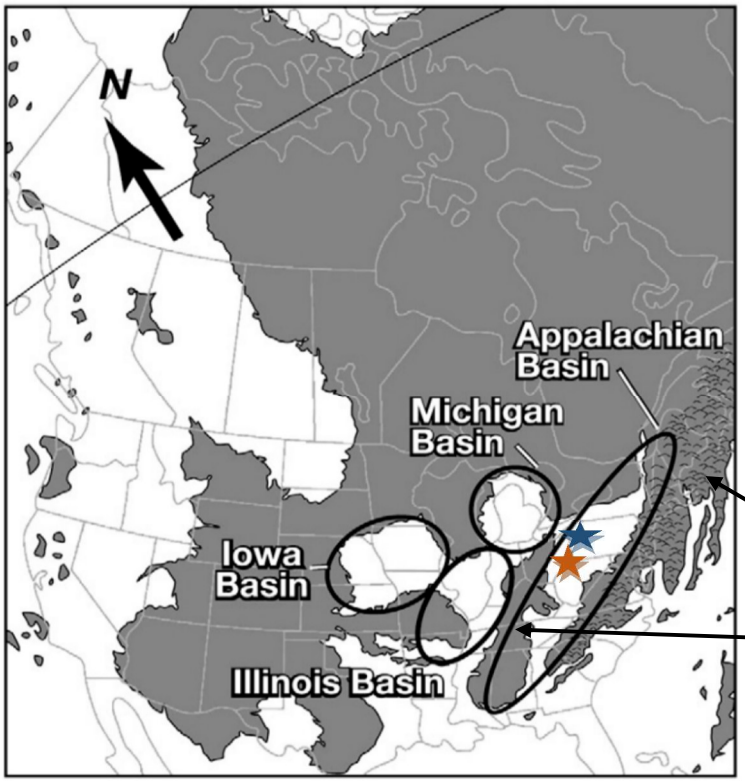

Figure 7.1. A palaeogeographic map of eastern Laurentia during the Middle Devonian. The non-deposition areas are marked in grey and show the Appalachian orogenic relief in the east and the Findlay-Algonquin Arch which separates foreland Appalachian Basin from the Michigan and Illinois basins (Bret et al. 2011). Borehole A and B have been marked on as a blue and orange star, respectively.

7.2 Geological Setting

The Appalachian Basin initially formed during the Lower Devonian and is strongly linked with the collision of the eastern North America and Avalonia landmasses (Ver Straeten et al., 2011). The Appalachian Basin was created by the flexure of lithosphere related to the loading produced by eastward thrusting of the successive Taconic, Acadian and Alleghanian orogenic piles (Manning & Elmore, 2012). The Acadian Orogeny was caused by the oblique convergence of the Avalon terrane and the North American Craton from the mid-Devonian to the early Mississippian (Manning & Elmore, 2012). The Acadian Orogeny has been split into three to four tectonic-phases representing individual pulses of Acadian deformation (Ver Straeten et al., 2011).

7.2.1 Marcellus Subgroup

The Marcellus Subgroup was deposited during the second tectonic-phase of the Acadian deformation and formed the distal part of the Catskill Delta system (Manning & Elmore, 2012). The depositional area of the Marcellus in the Appalachian Basin was dominated by hemi-pelagic deposition which was strongly controlled by tectono-eustatic influences (Lash & Blood, 2014). The tectonic controls happened on longer time scales associated with second to fourth order sedimentary cycles, whereas the eustatic controls reflect the shorter fifth to sixth order sedimentary cycles (Manning & Elmore, 2012).

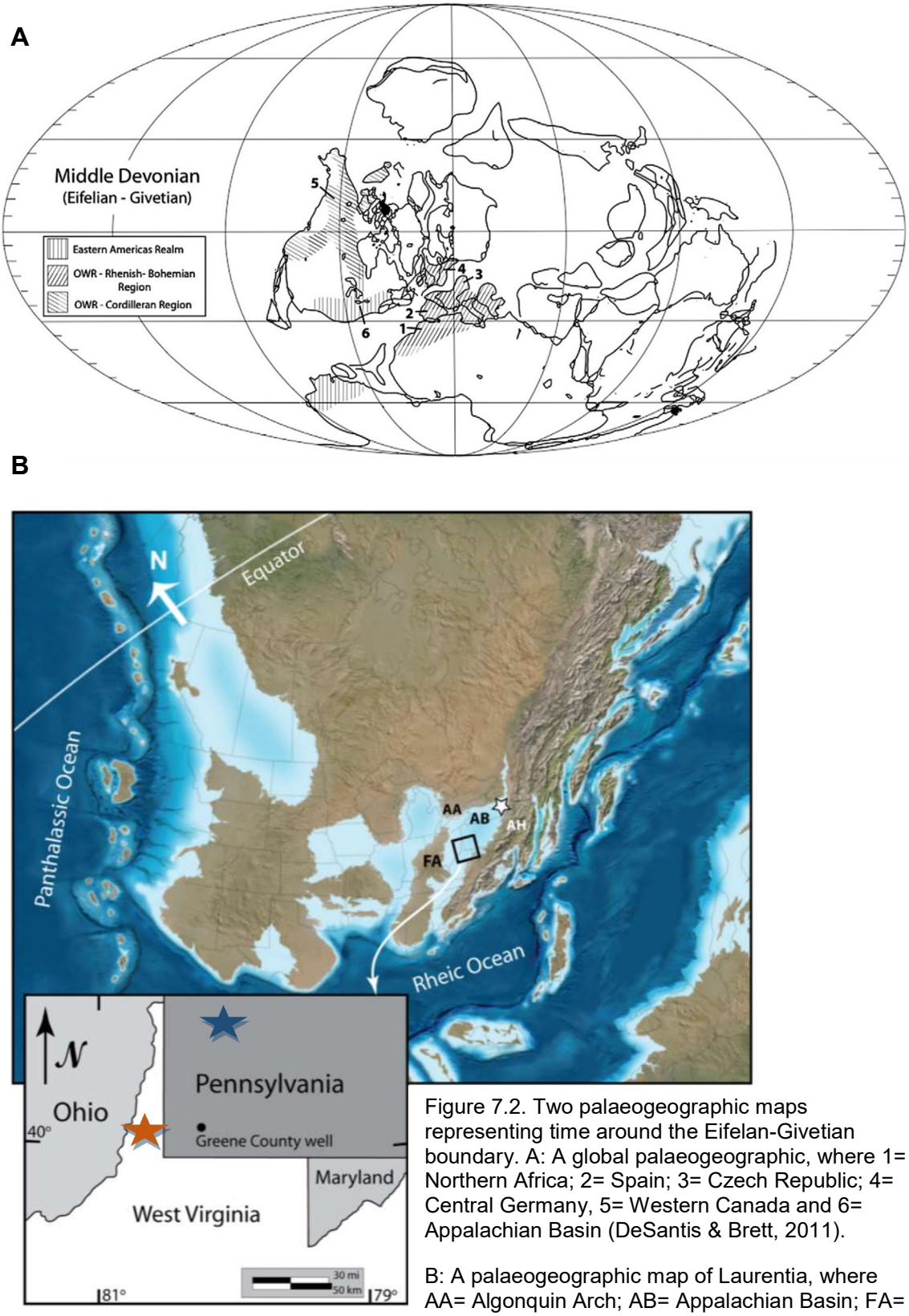

Figure 7.2. Two palaeogeographic maps representing time around the Eifelan-Givetian boundary. A: A global palaeogeographic, where 1= Northern Africa; 2= Spain; 3= Czech Republic; 4= Central Germany, 5= Western Canada and 6= Appalachian Basin (DeSantis & Brett, 2011).

B: A palaeogeographic map of Laurentia, where AA= Algonquin Arch; AB= Appalachian Basin; FA= Findlay Arch; A= Acadian highlands. Borehole A and B have been marked on as a blue and orange star, respectively (Blakey, 2013).

The Marcellus Subgroup is the basal subgroup of the Hamilton Group. The Hamilton Group was deposited in the mid-Devonian, specifically in the Eifelian-Givetian (Manning & Elmore, 2012). The subgroup is succeeded by the Skaneateles Formation, but the underlying unit beneath the subgroup varies across the Appalachian Basin; in Pennsylvania the underlying unit is the Onondaga Limestone Formation (Lash & Blood, 2014; Brett et al., 2011; DeSantis & Brett, 2011; Fig 7.3). The Marcellus Subgroup is divided into two main formations, the Union Springs and Oatka Creek formations which represent two separate transgression events (Brett et al., 2011). Owing to the lack of a lithostratigraphic framework of boreholes A & B, this case study focuses less on the AMS of individual lithologies. Instead, the AMS is used to establish basin-wide patterns, thus the use of a general stratigraphy of Pennsylvania can be justified.

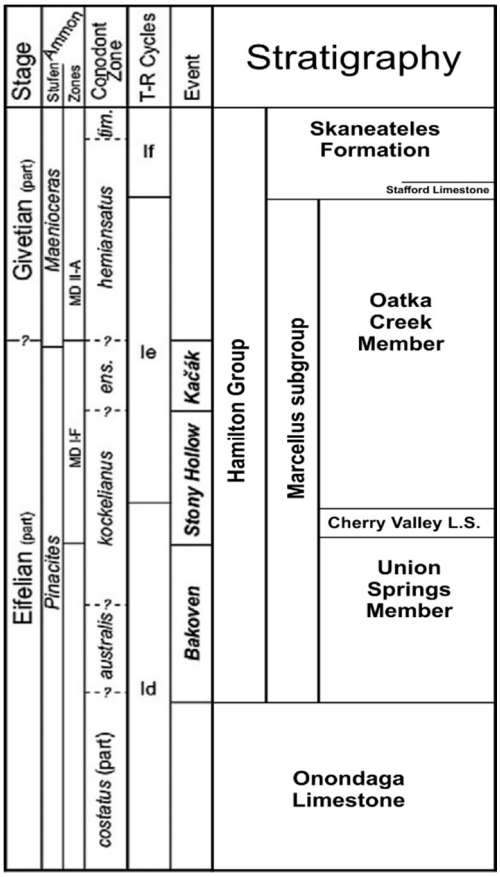

Figure 7.3. Stratigraphic chart of Pennsylvanian stratigraphy in the Eifelan-Givetian stages, columns left to right, stage, Ammonite and Conodont zones, transgression and regression cycles, biostratigraphy events (Carter et al. 2011; DeSantis & Brett, 2011).

7.3 Palaeoclimate & Biostratigraphy

During the mid-Devonian the Appalachian Basin would have been situated in the subtropics, c.25-30° southern latitude (Werne et al., 2002; Ver Straeten et al., 2011). Regional sedimentation patterns were dominated by surrounding archs and highlands (Fig 7.1), but eustatic sea-level changes were connected to the global Rheic Ocean (Lash & Blood, 2014). The Marcellus Shales are the distal part of the Catskill delta and represent a hemipelagic/tidal estuary environment (Slingerland et al., 2009). The dominant flow direction is indicated by fossil orientations of graptolites, brachiopods and ostracods which indicate flow to the SE (Jones & Dennison, 1970).

Throughout the Eifelian-Givetian there is a general rise in global sea-level (Fig. 7.4), a consequence of this being a global 'greenhouse' interval (Brett et al., 2011). Brett et al. (2011) claims there may have been unrecognised glacial periods of low sea-level to explain sea-level fluctuations, although there is no direct evidence of glacial sediments during this period (Brett et al., 2011). The transgressive and regressive cycles in the mid-Devonian have been recorded by Ver Straeten et al. (2011) and Brett et al. (2011) who were able to establish associated biogenic event such as the *Kačák* event.

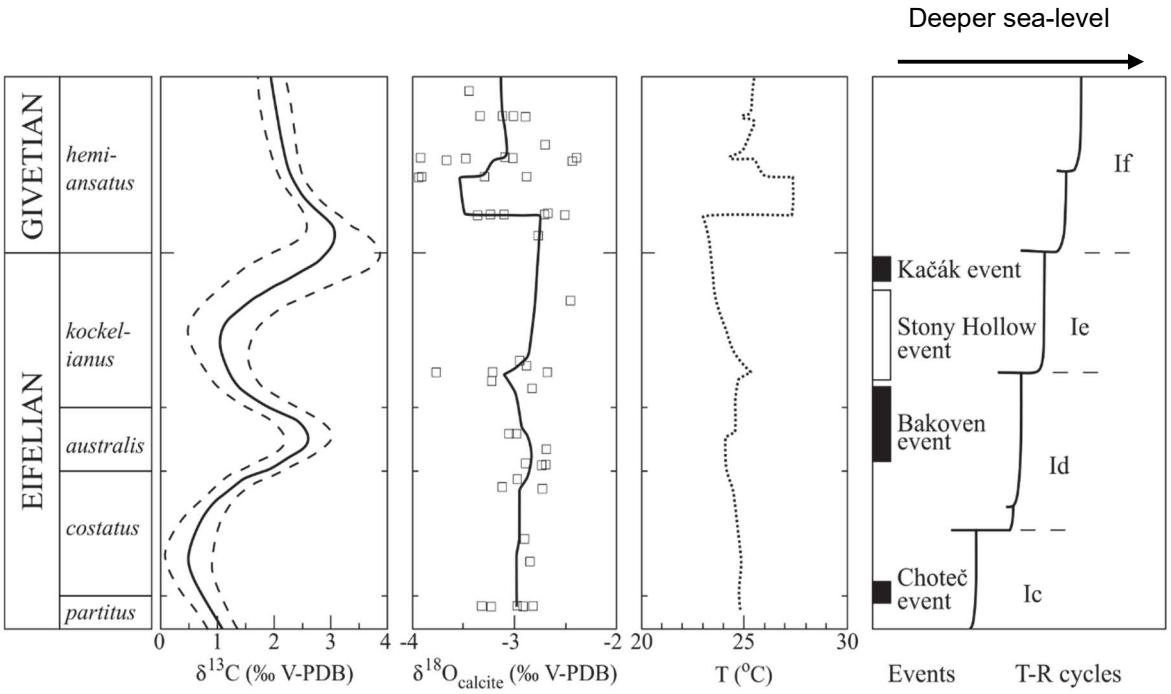

Figure 7.4. Conodont zones, stable oxygen and carbon isotopes and the inferred temperature between the Eifelian-Givetian. On the far right is eustatic sea-level with biogenic events labelled (Desantis & Brett, 2011).

The Eifelian-Givetian stratigraphy is well constrained owing to the presence of conodont zones and sparsely distributed pelagic goniatite fossils. Bentonitic marker beds have been used to correlate the stratigraphy (Brett et al., 2011). Carbon isotope signatures and other proxies have been used to support and confirm biogenic events; e.g. Fig 7.4 (Desantis & Brett, 2011). There were three distinct biogenic events in the late Eifelian.

First, the Bakoven event reflected the abrupt deepening of the basin, with widespread anoxic conditions that led to severe reduction of the Onondaga/Columbus faunas in the Appalachian Basin (Desantis & Brett, 2011). The following, Stony Hallow event, is characterised by the expansion and then contraction of the tropical Cordilleran Province which saw a regression in sea-level and a brief return of certain fauna

particularly *Variatypa* (Desantis & Brett, 2011). These fauna then began to disappear as sea-level deepened, producing anoxic deposition of shales once more (Desantis & Brett 2011). The third event, the *Kačák* event, is recorded by the deposition of dysoxic to anoxic sediments during the late Eifelian which resulted in a strong reduction in diversity in pelagic organisms (Desantis & Brett, 2011).

Brown & Kenig (2004) used molecular fossils, 'biomarkers', to support the interpretation of the palaeoenvironments. An example biomarker, related to the algal '*Chlorobiaceae'* requires light, anoxic, and sulphuric conditions to survive (Brown & Kenig, 2004). The extensive presence of *Chlorobiaceae* in the black shales would suggest geographically widespread euxinia within the water column during the mid-late Devonian (Brown & Kenig, 2004).

The green/grey shales of the Marcellus Subgroup also contain *Chlorobiaceae* bacteria, but these are probably due to synsedimentary re-deposition from nearby black shales or because there were intervals of poor oxygenation (Brown & Kenig, 2004). This increase in algae in black shales can be explained by enhanced phytoplankton productivity, with a stratified sea-water column where the upper column productivity controls the oxygen content and thus organic respiration on the sea floor (Brown & Kenig, 2004).

7.4 Structure of Appalachian Basin

The folding of the plunging Appalachian synform basin was synchronous with the deposition of the Marcellus Subgroup. Sedimentation within the basin was dominated by relative sea-level change which affected biogenic sedimentation and subsidence (Ver Straeten et al., 2011; Manning & Elmore, 2012).

Hirt et al. (1995) examined the P-wave anisotropy of the Appalachian Basin (Fig. 7.5). They concluded that the P-wave anisotropy is dominated by stress relief micro-cracks, these micro-cracks do not reflect in situ stress anisotropy, since during deposition the maximum stress would have been orthogonal to P-wave anisotropy observed. Instead, the anisotropy reflects the crystalline fabric of the chlorite minerals.

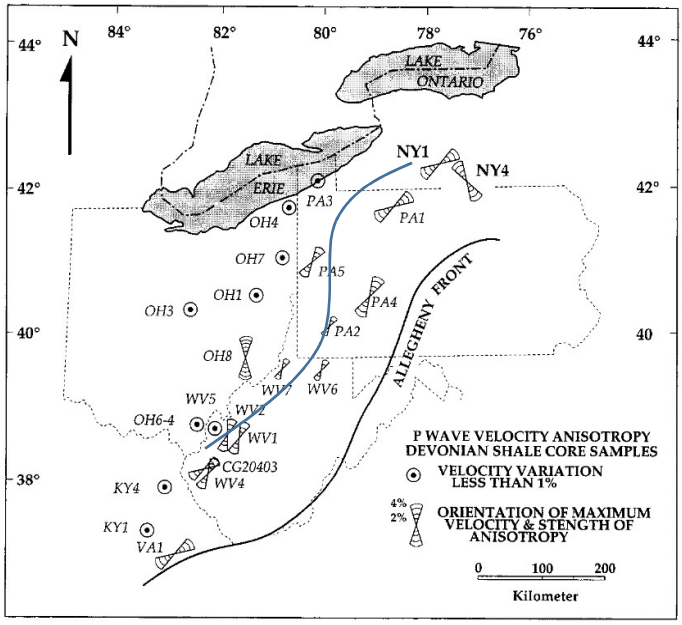

Figure 7.5. Magnitude and anisotropy of P-wave velocity of Devonian sediments (Hamilton Group to Candaway Group) within the Appalachian Basin taken from orientated borehole data gathered by Evans et al. (1989). The general orientation of P-wave is trending east northeast, except the anomalous NY4 borehole which may have been caused by an orientation error. The blue line is the axis of the anticlinal synform which plunges towards the southeast (Stamatakos et al., 1996).

The Marcellus ‘basin’ can be divided into three separate zones that show different depositional mechanisms: the carbonate dominated distal margin (in the west), the basin axis and the proximal margin, in the east (Fig 7.6; Ver Straeten et al., 2011). The Basinal Axis Zone was where the Marcellus shales were deposited, these deposits were mainly composed of dark shales and siltstones. The latter are thought to represent the distal ‘fluvial’ influx of sediment produced from the Acadian Orogenic high to the east (Menning et al., 2006).

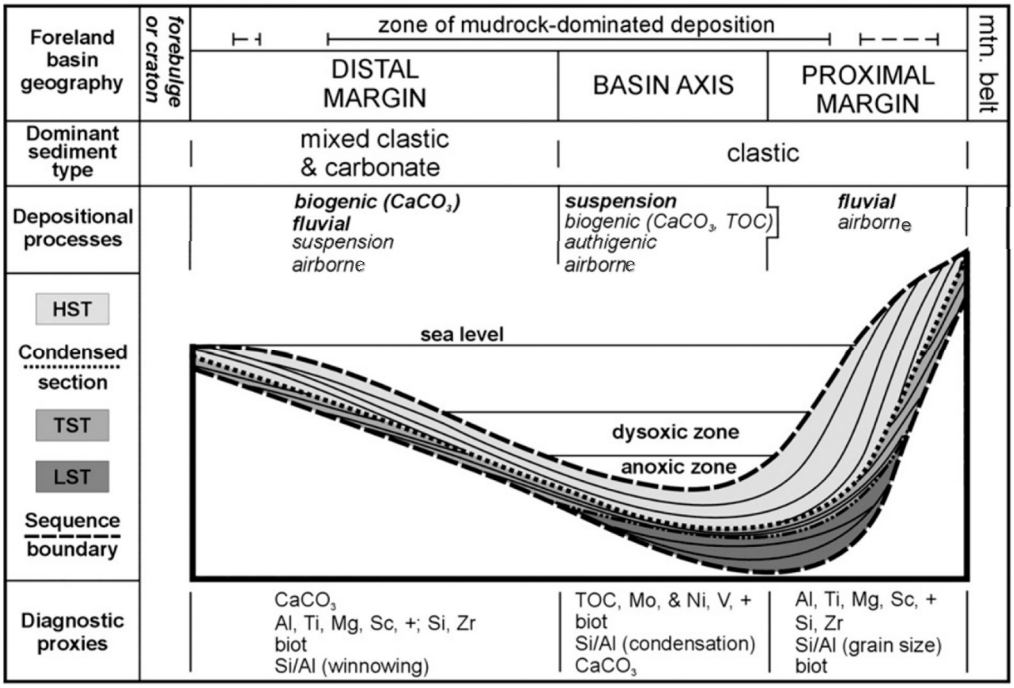

Figure 7.6. Schematic cross section of the Appalachian Basin (Ver Straeten et al. 2011). Mudrock deposition during high-stand and low-stands has been highlighted by different shading. The Marcellus Shale would have been supplied from suspension and biogenic contributions. The carbonates were deposited on the western distal margin and would have been deposited during periods of clastic starvation (Brett et al., 2011).

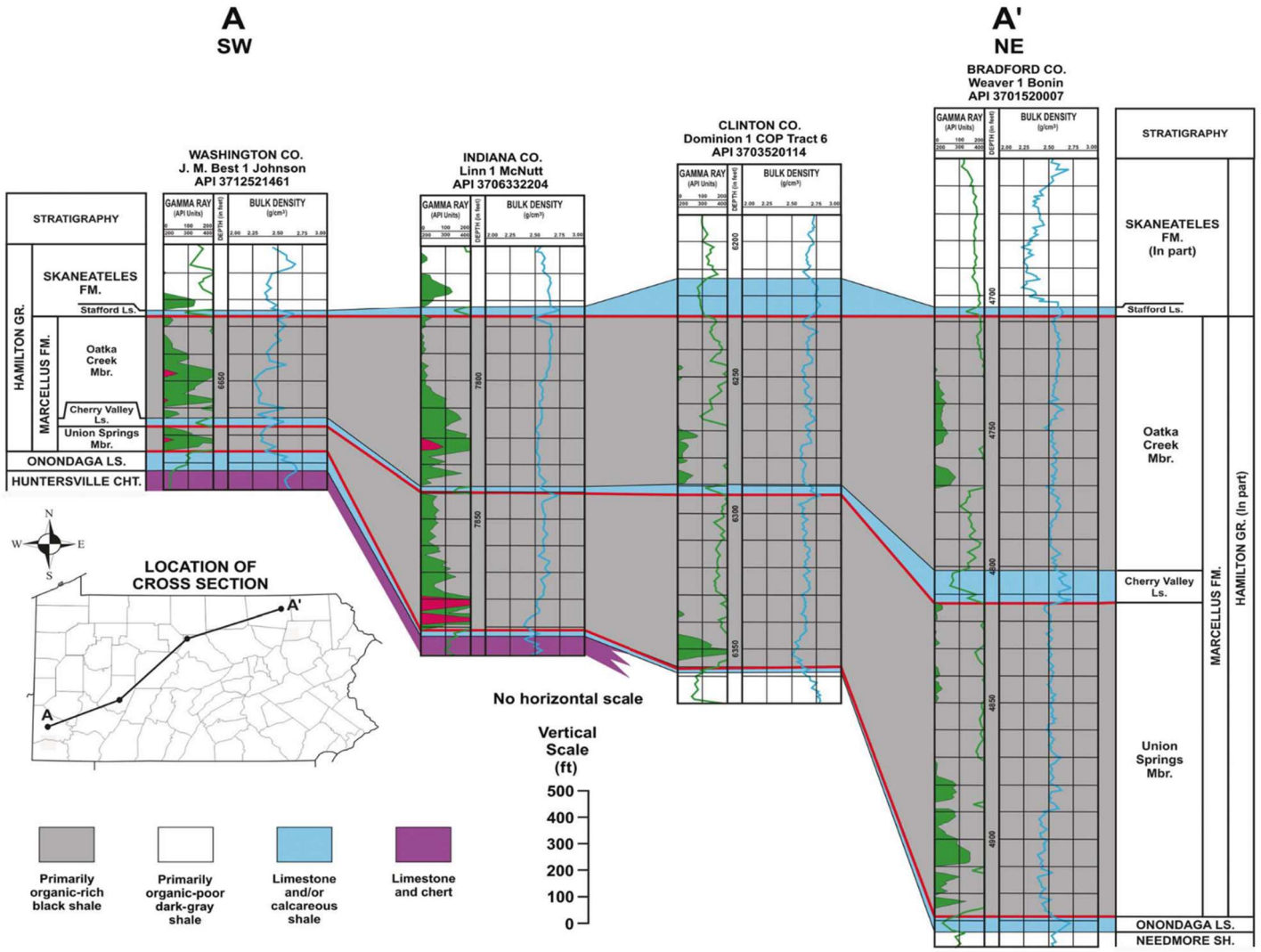

Figure 7.7. Cross section of the Marcellus Formation across the Pennsylvanian State from Washington County (A) to Bradford County (A'). The stratigraphy shows a general west-to-east thickening trend. Gamma-ray log signatures are shown in green with the most organic-rich radioactive sections coloured in red. The blue line represents bulk density signature and the red lines that run between logs represent disconformities. Where GR. = Group; Mbr. = Member; Ls. = Limestone; Sh. = Shale; CHT. = Chert. Borehole A stratigraphy would be comparable to a combination of Washington County to Indiana County, whereas Borehole B would be more similar with Washington County stratigraphy (Carter et al., 2011).

7.5 Post-Deformation and Thermal Maturity

The Marcellus Subgroup was deformed during the Alleghanian Orogeny (during early Pennsylvanian to late Permian). This deformation of the Appalachians led to the formation of three structural provinces: the Plateau, the Blue Ridge and the Valley and Ridge, the latter is represented by numerous thrusts and folds (Manning & Elmore, 2012). The Alleghanian episode led to basin-wide fluid flow which altered the Onondaga Formation, producing authigenic illite, authigenic K-feldspar, authigenic quartz, and Fe-rich chlorites (Lu et al., 1991).

The Devonian strata was buried by younger sediments, causing the Devonian Shales e.g. Marcellus Shale to be subjected to variable temperatures and pressures (East et al., 2012). In northwest Pennsylvania the shale experienced low maximum temperatures and pressures, whereas the other site in this case study in West Virginia experienced enough burial to potentially produce oil (East et al., 2012) East et al. (2012) mapped the thermal maturity of the Appalachian Basin (Fig 7.9), using vitrinite reflection (VR) as the main indicator of maturation. However this method has limited usefulness in some shales due to the lack of organic matter, therefore the Conodont Alteration Index (CAI) was also used by East et al., (2012) and Repetski et al., (2008).

CAI is an index of thermal maturity that is used in marine rocks from Ordovician to Triassic (Fig. 7.8; East et al., 2012; Repetski et al., 2008). Marcellus shale CAI score of the samples described here varies from 0.5 to 1.5 and fits into the thermally immature to prolithic oil generation window.

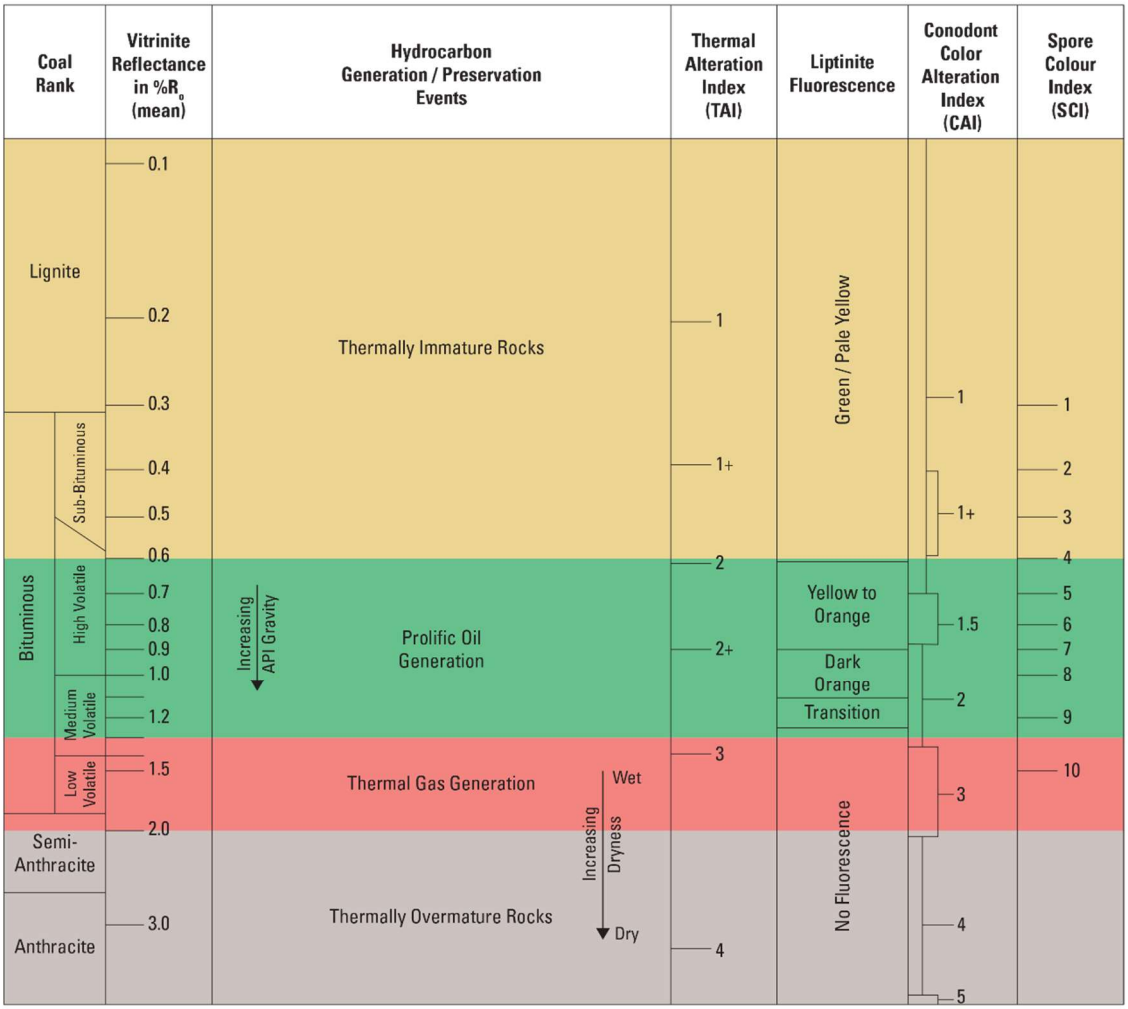

Figure 7.8. Relationship between the different methods used for determining maturity, and their relationship to hydrocarbon generation zones (East et al., 2012).

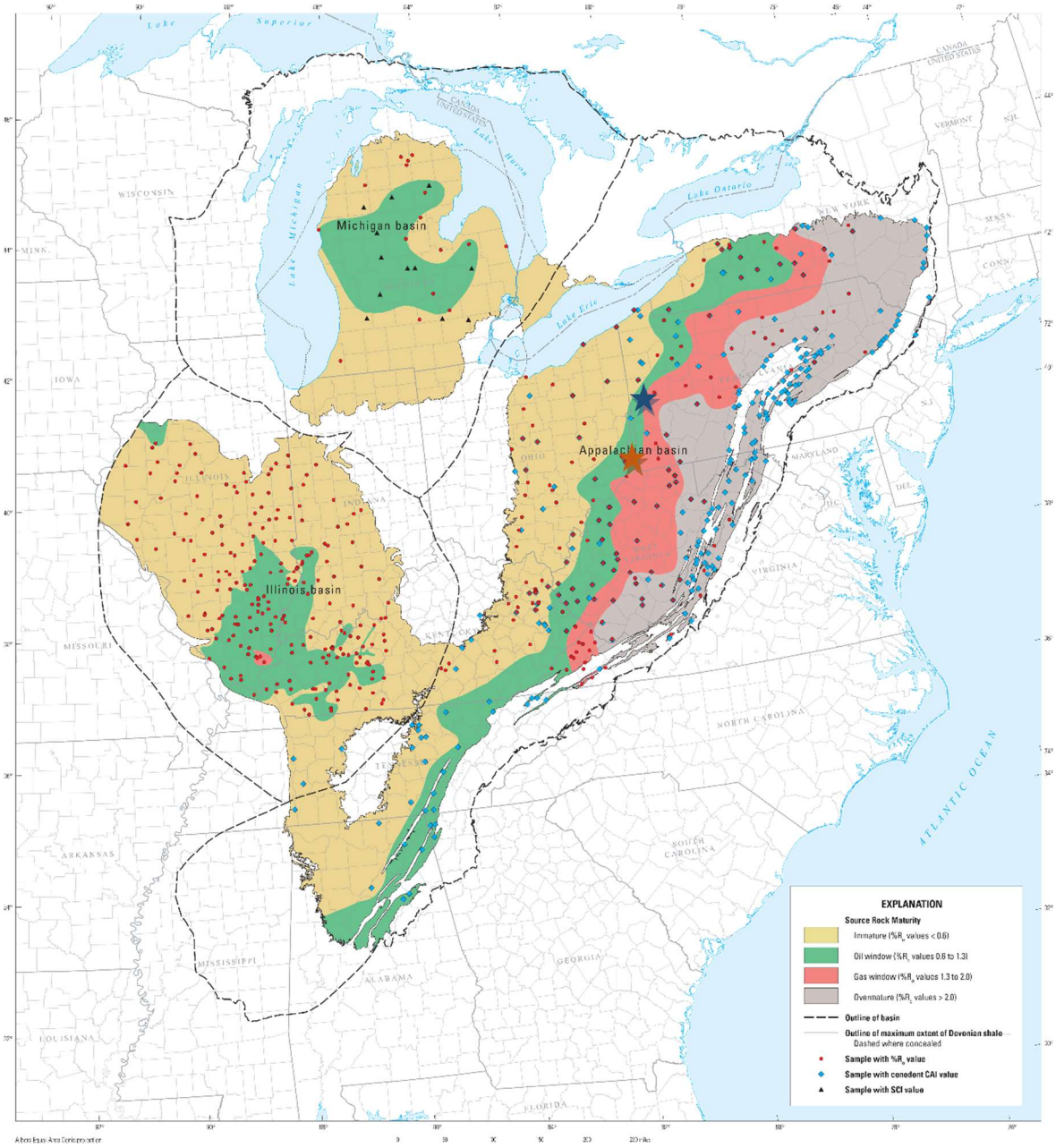

Figure 7.9. Different zones of hydrocarbon maturity in northeast USA. Dots shows CAI and VR sample locations (East et al., 2012). Borehole A and B have been marked on as a blue and orange star, respectively.

7.6 Previous Magnetic work on the Marcellus

Manning & Elmore (2012) performed rock magnetic characterisation, and determined magnetisation components on the Marcellus Shale in eastern Pennsylvania. Their study area was southeast of borehole A's location and their data will therefore reflect increased thermal maturity shown in its greater CAI score. They found: a viscous component that had a maximum unblocking temperature up to 275°C; an intermediate-temperature component that was removed by 250-290°C and was interpreted as a CRM in magnetite and a ChRM component with a higher unblocking temperature (480°C) that was interpreted as a late Carboniferous re-magnetisation produced during the Kiaman superchron (Lu et al., 1990).

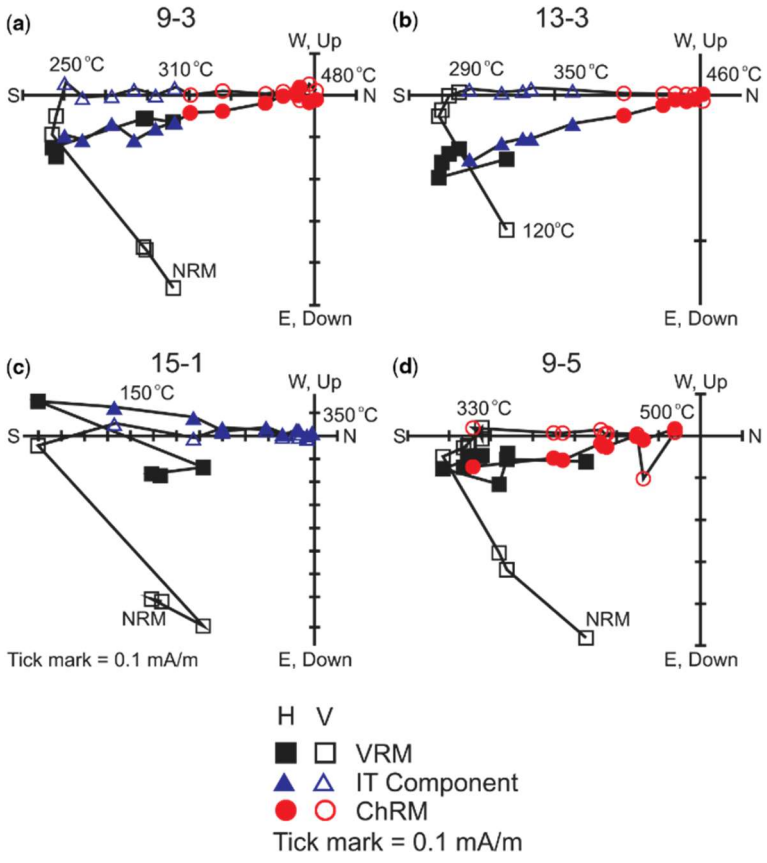

Figure 7.10. Vector orthogonal plots (Zijderveld 1967). There are three components highlighted, the black viscous component which is removed at 290°C, a blue south easterly intermediate temperature component and a red, shallow southern characteristic remanent component which represents the Kiaman overprint (Manning & Elmore, 2012).

Manning & Elmore (2012) found different groups of ChRM's which they concluded was the result of differences in the remanence carriers. The first showed southerly declinations and shallow up inclinations, interpreted as pyrrhotite as the remanence carrier. The second ChRM has more southerly declinations and shallow down inclinations, interpreted as magnetite being the main carrier of remanence.

Hirt et al. (1995) studied the AMS of Devonian shales on the Appalachian plateau. Their study area was in southwest New York State and included the Hamilton Group and younger groups such as the West Falls Group. The shales in this study would have experienced greater thermal maturity than those in borehole A but will have a similar thermal maturity and CAI values as found in borehole B. They concluded that the AMS fabrics reflect a well-defined bedding fabric associated with vertical compaction, as the degree of flattening (Kint/Kmin) was between 1-7% and the fabric had a lesser defined magnetic lineation (Kmax/Kint) >1%.

Hirt et al. (1995) measured the AMS at different temperatures to establish the AMS of ferrimagnetic and paramagnetic minerals. Room temperature measurements provided the AMS of the ferrimagnetic and paramagnetic minerals and those at liquid nitrogen temperatures measured the chlorite fabric. Anhysteretic remanent magnetisation (AARM) was also measured for the magnetic anisotropy of ferrimagnetic minerals. They found the best relationship between compaction and degree of anisotropy was in the low-temperature AMS which was predominantly influenced by the crystalline anisotropy of

chlorite or other platy minerals; these had P values of c.1.1. The chlorite is thought to have been recrystallised from an illite precursor that formed before the deformation and the Kmax direction of the chlorite (Fig. 7.11) corresponds directly to the fast direction of the seismic anisotropy (Fig 7.5; Hirt et al., 1995); the low-temperature AMS reflects a sedimentary fabric rather than a structural foliation of the Alleghanian orogeny (Hirt et al., 1995).

The presence of a small ferrimagnetic component is indicated in the difference between low and room temperature AMS (Fig 7.11) which is thought to be caused by the presence of pyrrhotite and magnetite which AARM has more northerly Kmax directions and has P values of c.1.16. In Western Pennsylvania (near borehole A) Kmax directions are orientated 270-290º reflecting the strike of coal joints. In Pennsylvania and West Virginia (similar to study area) Kmax directions are orientated 270-295º, reflecting tension joints that post-date the anticlines of the Appalachian Plateau (Hirt et al., 1995).

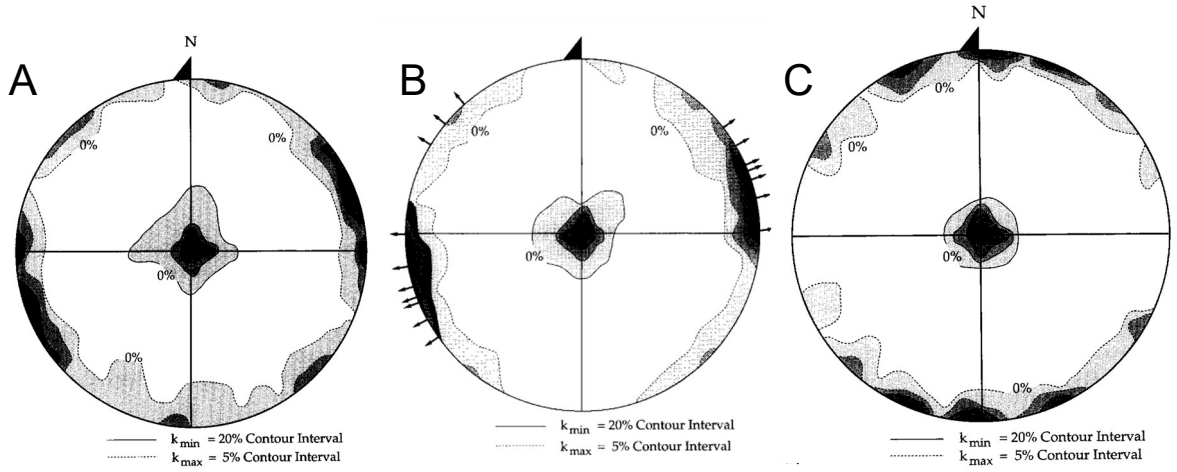

Figure 7.11. Equal-area, lower hemisphere stereoplots showing A) AMS magnitude ellipsoid measured at room temperature. B) AMS magnitude ellipsoid measured at liquid nitrogen temperature C) AARM magnitude ellipsoid. The Kmax direction for A and B are orientated to southwest-northeast, whereas C is orientated north-south (Hirt et al., 1995).

7.7 AMS Study

Samples used in the study were acquired from unoriented borehole cores. The bedding dip was zero in the cores and all the AMS measurements were taken at room temperature with field correction strike and dip of 0, 90° respectively.

To azimuthally re-orientate the samples, they were treated to conventional palaeomagnetic techniques to determine their recent remagnetisation components (TVRM), the Kiaman partial remagnetisation, and in some cases some remaining Devonian components. This was achieved by thermal demagnetisation up to 200°c and then demagnetising the samples using an alternating field up to 90 mT (Fig. 7.12). The difference between the samples' component declinations and in situ estimated component directions is used to establish the degree of rotation required to orientate the core specimens to true north. The reference TVRM component used was current magnetic north (0° declination) and the reference Kiaman component declination was 165° with a shallow southerly negative inclination, taken from the average calculated by Manning & Elmore (2012). The degree of rotation determined from the TVRM and Kiaman where averaged (if both present) to provide the overall estimated degree of rotation. All the sample AMS data was then rotated (about a vertical axis) using this angle to correct it back to geographic North. The re-orientation was only partially effective as the TVRM and ChRM's did not show a good clustering in borehole A which would be expected in the re-orientated stereoplots.

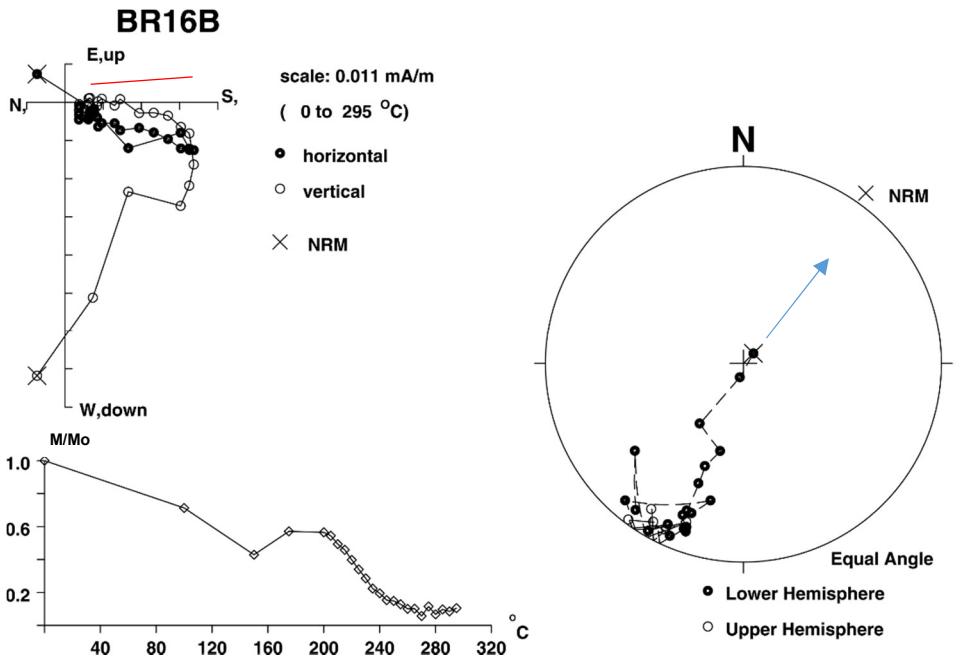

Figure 7.12. A) vector orthogonal plots (Zijderveld 1967). The red line shows the Kiaman component. B) Standardised demagnetisation plot and C) a stereoplot. The blue arrow highlights the thermo-viscous component

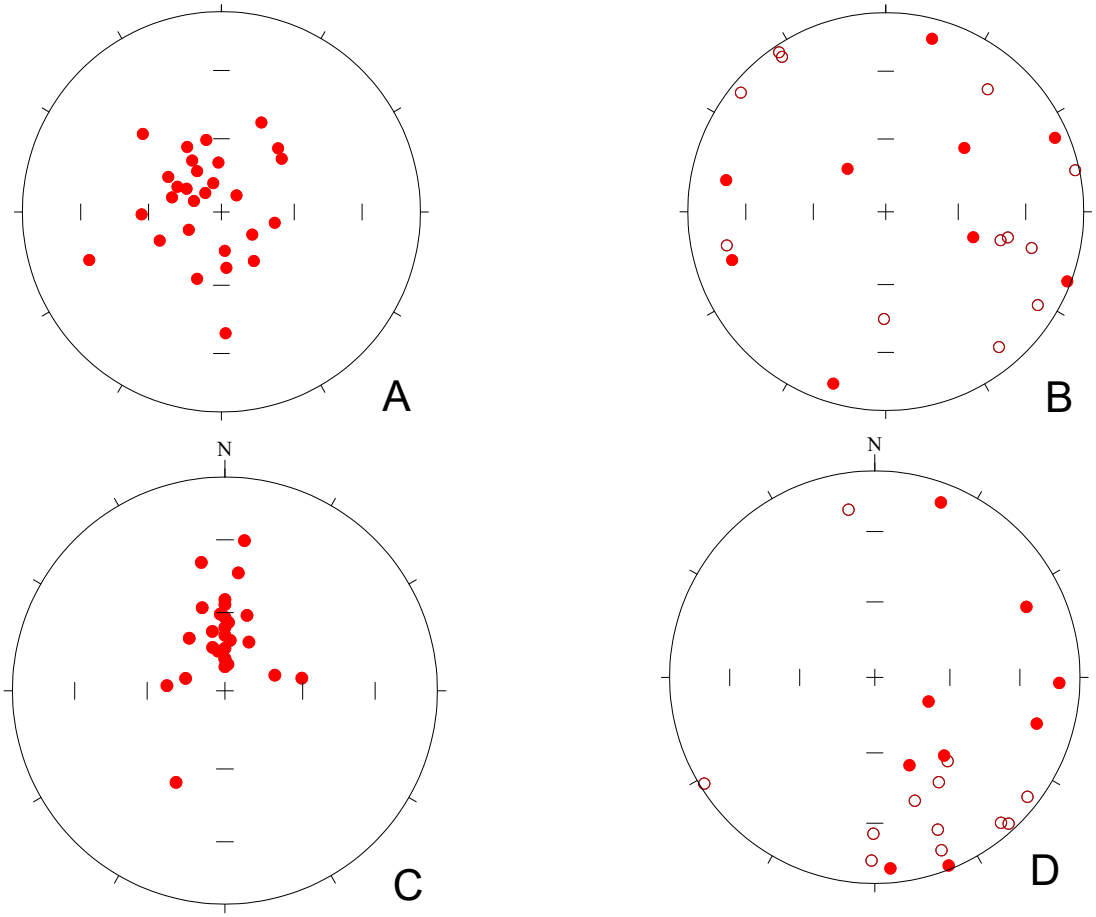

Figure 7.13. Stereoplots showing borehole A unorientated A) TVRM and B) Kiaman components. The samples show scatter which is expected if the samples were removed from unorientated cores. C) is the re-orientated TVRM which generally show steep northerly components and D) re-oriented Kiaman showing a shallow southeastly direction with some scatter. On the re-orientated stereoplots N is the current north. The re-orientated TVRM show a good clustering but the ChRM are more scattered indicating re-orientation was only partially effective.

7.7.1 Borehole A

Borehole A is located in Pennsylvania, north east of Pittsburgh. Twenty four core plugs were taken from this core. The rotated AMS shows a clear Kmax grouping in a northeast-southwest trend (Fig 7.14), there is also a smaller northwest Kmax group.

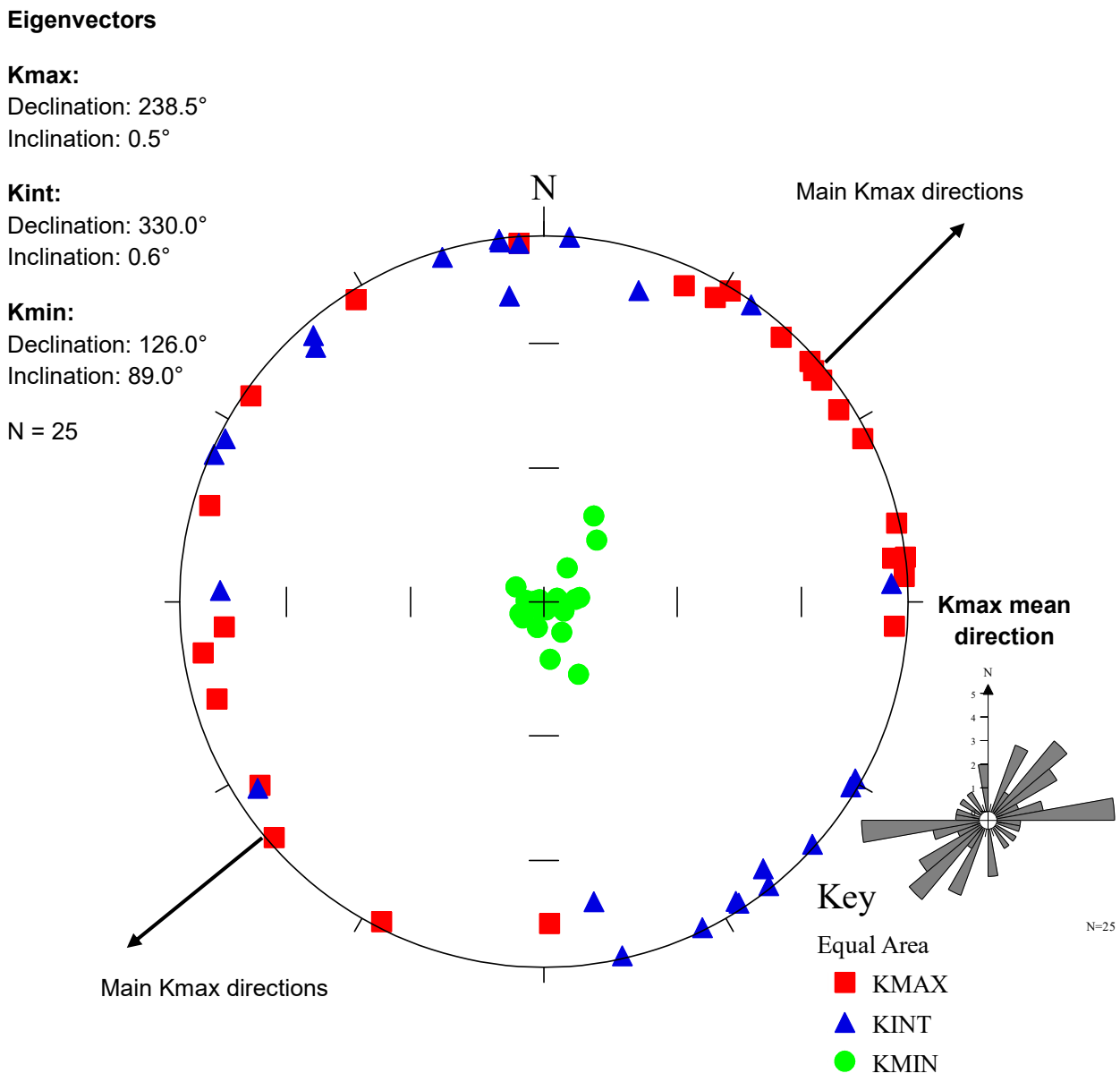

Figure 7.14. Two Kmax directional clusters are apparent, the dominat northeast-southwest and lesser north-westerly directed one. The Kmin imbrication is not present.

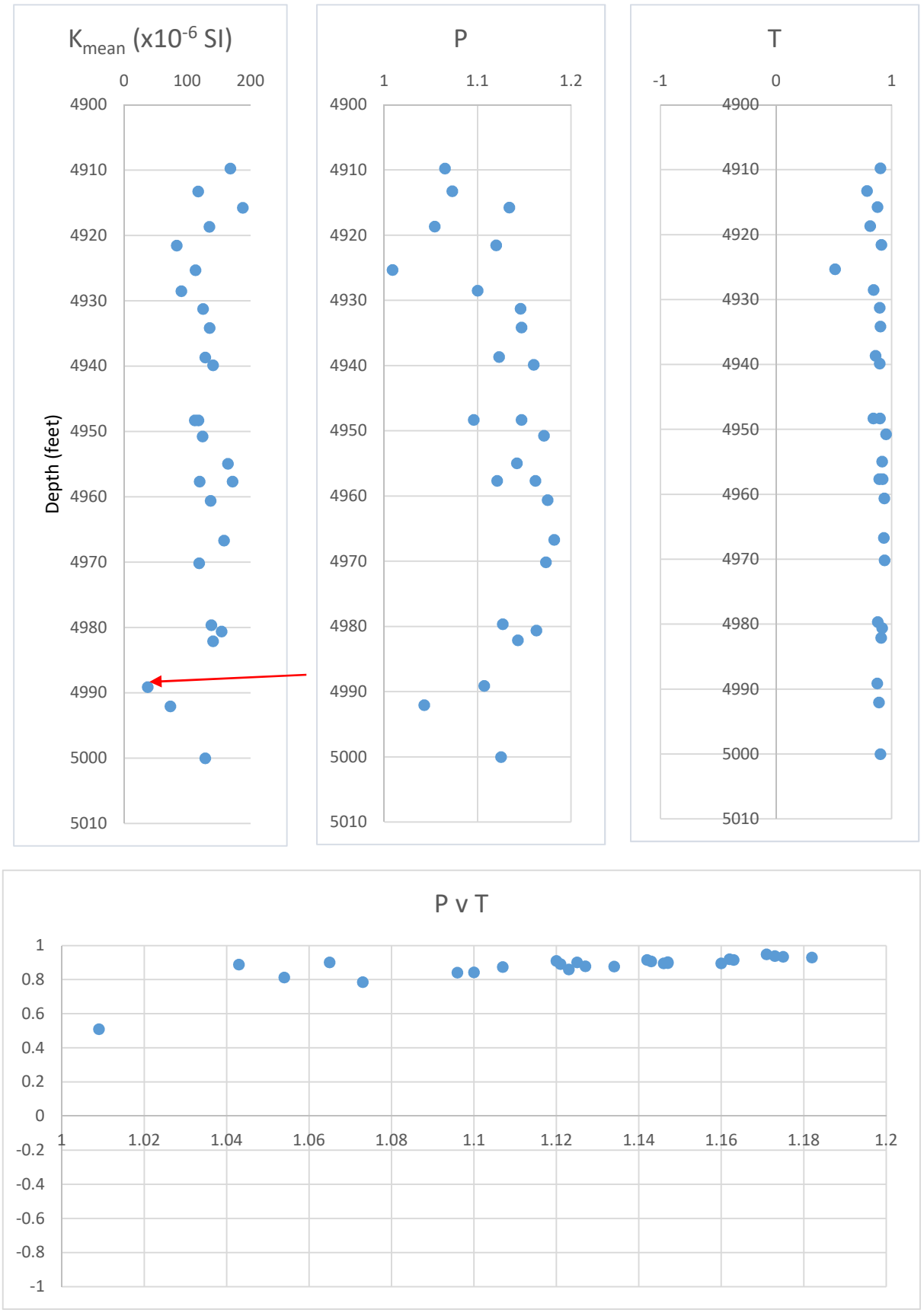

Figure 7.15. AMS parameters for borehole A. The top three graphs left to right are magnetic susceptibility, degree of anisotropy and shape and are plotted against depth (feet). The bottom graph is the degree of anisotropy against shape. A drop in mass susceptibility is marked by a red arrow.

The AMS results suggests that the Kmax reflects the long-grain axis in mudstone, the Kmax is perpendicular to Kmin values and AMS has high T and P values throughout the borehole (Fig. 7.15). These results reflect deposition from suspension showing well-defined bedding fabric which later underwent (vertical) compaction with the samples with greater P values having experienced greater compaction. Therefore, the Kmax direction can be attributed to the palaeoflow direction, therefore suggesting the currents were parallel to the basin axis which is supported by the seismic anisotropy data in Fig. 7.5 (Hirt et al., 1995).

The second observation is the presence of a small northeastly Kmax group. These anomalies are not restricted to a certain depth and there is no connection with a decrease in magnetic susceptibility or lesser degree of anisotropy. Hirt et al. (1995) observed similar patterns in their AMS results. They suggested that this could have been caused mineralogical differences, such as a small ferrimagnetic contribution, or associated with coal tension joints in this area. However, these north-westerly Kmax direction probably represent scatter associated with mineralogical changes rather than a structural fabric.

The third observation is the sharp drop in magnetic susceptibility at c.4490 feet, this has been attributed to a higher content of carbonate i.e. greater calcite content. The greater calcite content would lower the sample magnetic susceptibility and would explain the drop in susceptibility and degree of anisotropy. However, this cannot be confirmed owing to limited samples below that depth.

7.7.2 Borehole B

Borehole B is located in West Virginia, south of Wheeling. Ten samples were taken from this site. The TVRM data acquired from this site is similar to that of borehole A (Fig. 7.16) with rotated AMS results showing a clear Kmax trend in a northeast-southwest direction (Fig 7.17). The Kmin results are slightly more scattered in these samples, this may be the result of mineralogical differences associated with the sample's thermal maturity indicated by the CAI scores which increased from 0.5-1 in borehole A to 1.0-1.5 in borehole B.

Mineralogical differences between the two sites are also indicated by the mass susceptibility which is much smaller in borehole B samples when compared to borehole A. Mineralogical differences in samples would have been caused by geographical changes in sedimentation such as a greater carbonate influence rather than clay which may explain the greater scatter in borehole B. The regional differences in thermal maturity of the two sites (Fig. 7.9) imply that borehole B has experienced greater thermal maturity. This could have increased the K_m and P values as more chlorite is produced; however, these values decreased in borehole B which suggests the original composition rather than thermal maturity of the clays dominates the AMS fabric in these sites.

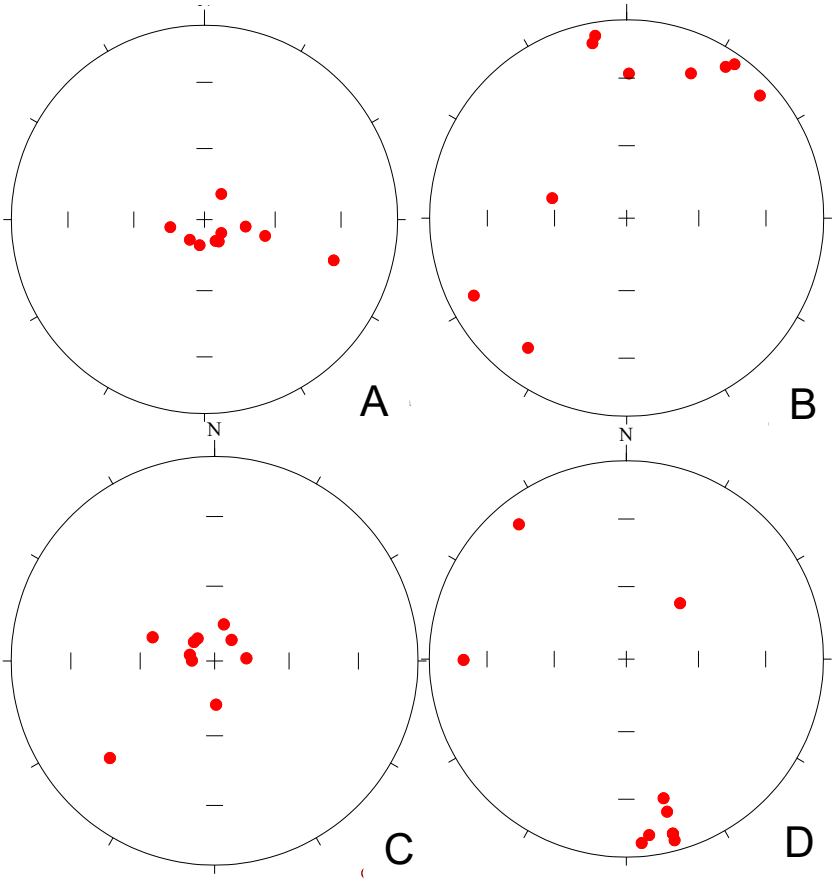

Figure 7.16. Stereoplots showing borehole A unorientated A) TVRM and B) Kiaman components. C) is the re-orientated TVRM which generally shows steep northerly components and D) largely shows a shallow southeastly direction with some scatter. On the re-orientated stereoplots N is the current north. The re-orientated TVRM are a bit scattered but the ChRM show a good grouping indicating re-orientation was effective except for three anomalous results.

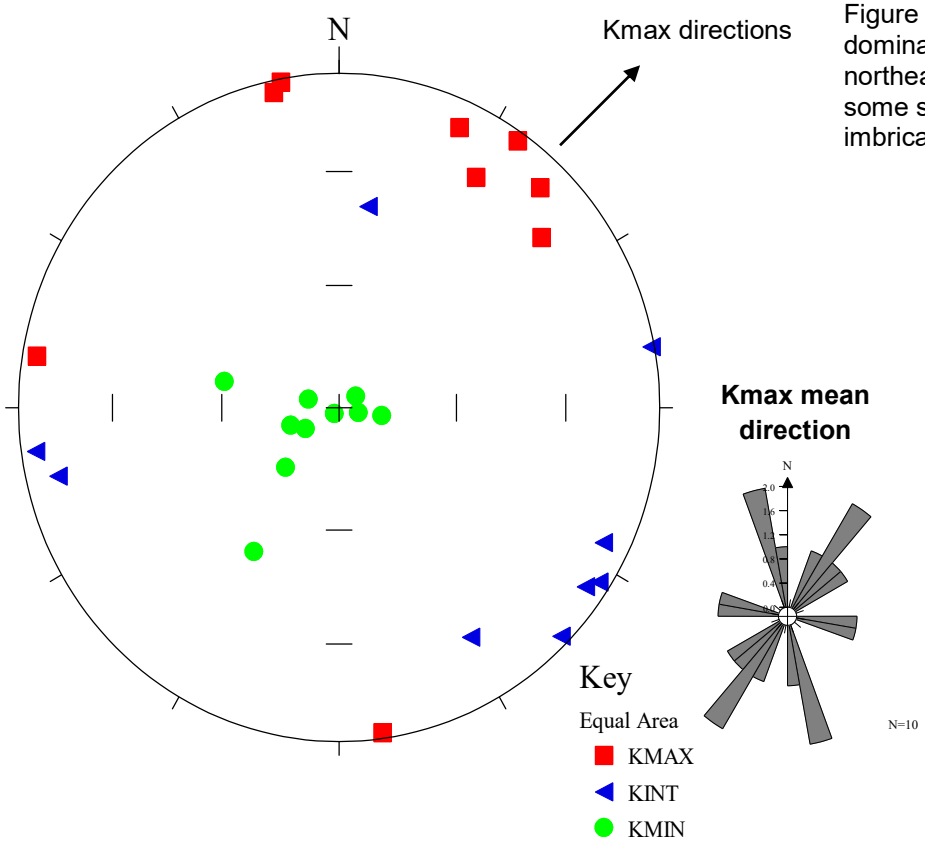

Figure 7.17. There is one dominant Kmax trend northeast-southwest with some scatter present. Kmin imbrication is not present.

Eigenvectors

Kmax:
Declination: 23.5°
Inclination: 9.1°

Kint:
Declination: 116.0°
Inclination: 3.1°

Kmin:
Declination: 235.2°
Inclination: 81.3°

N = 10

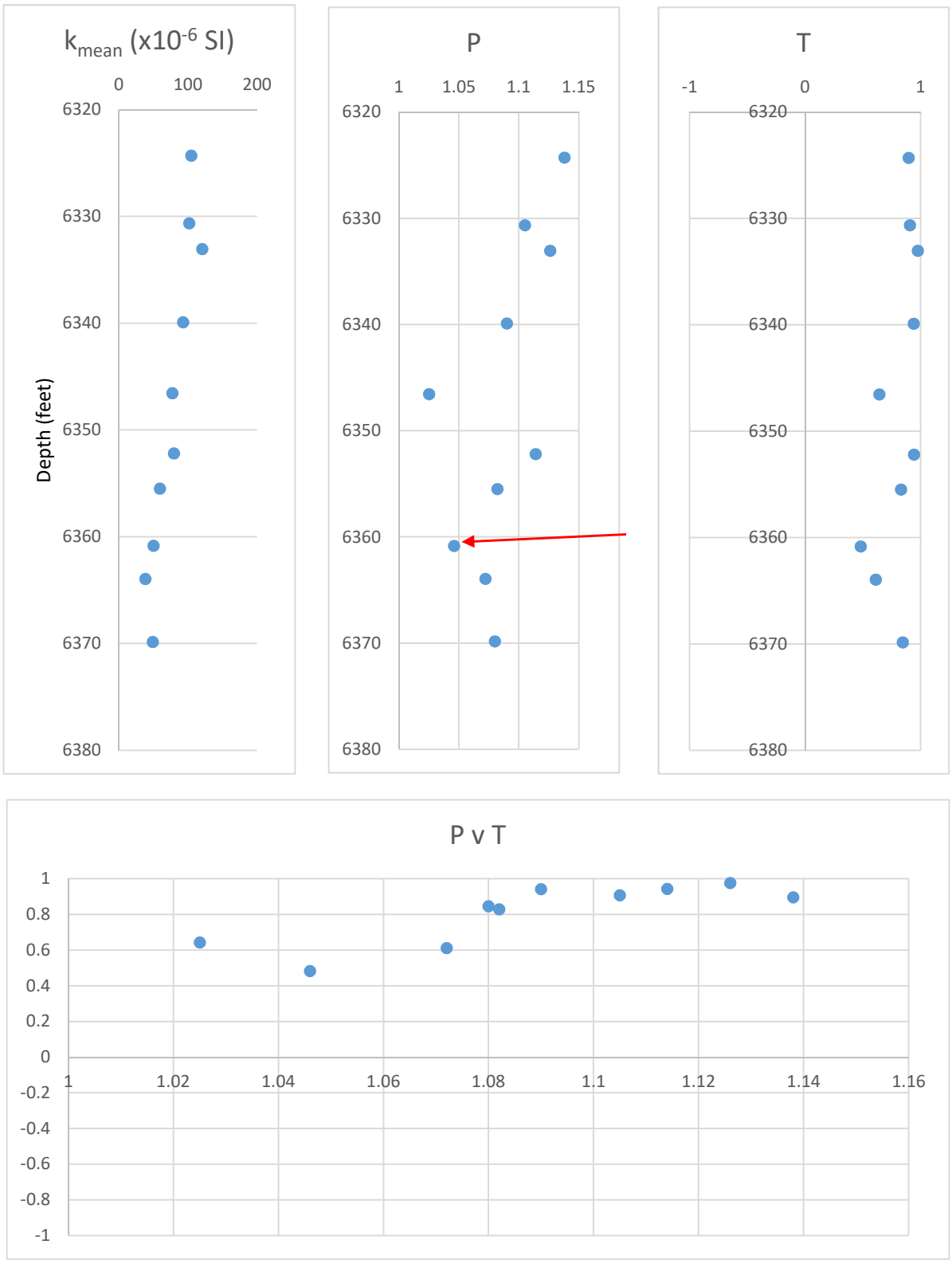

Figure 7.18. AMS parameters for borehole B. The top three graphs left to right are magnetic susceptibility, degree of anisotropy and shape and are plotted against depth (feet). The bottom graph is the degree of anisotropy against shape. A drop in degree of anisotropy is marked by a red arrow.

7.8 Hysteresis Study

A hysteresis study was performed to establish the paramagnetic mineral contribution to the induced magnetisation (Fig. 7.19). A grey shale specimen (Br.7) and black shale specimen (Cn 9) were compared and the estimated paramagnetic content from each specimen was estimated to be 74 and 93% respectively. This would suggest that the AMS in these rocks, particularly the organic rich shales, were dominated by a paramagnetic contribution. Hirt et al. (1995) found similar conclusions suggesting the AMS is chlorite dominated.

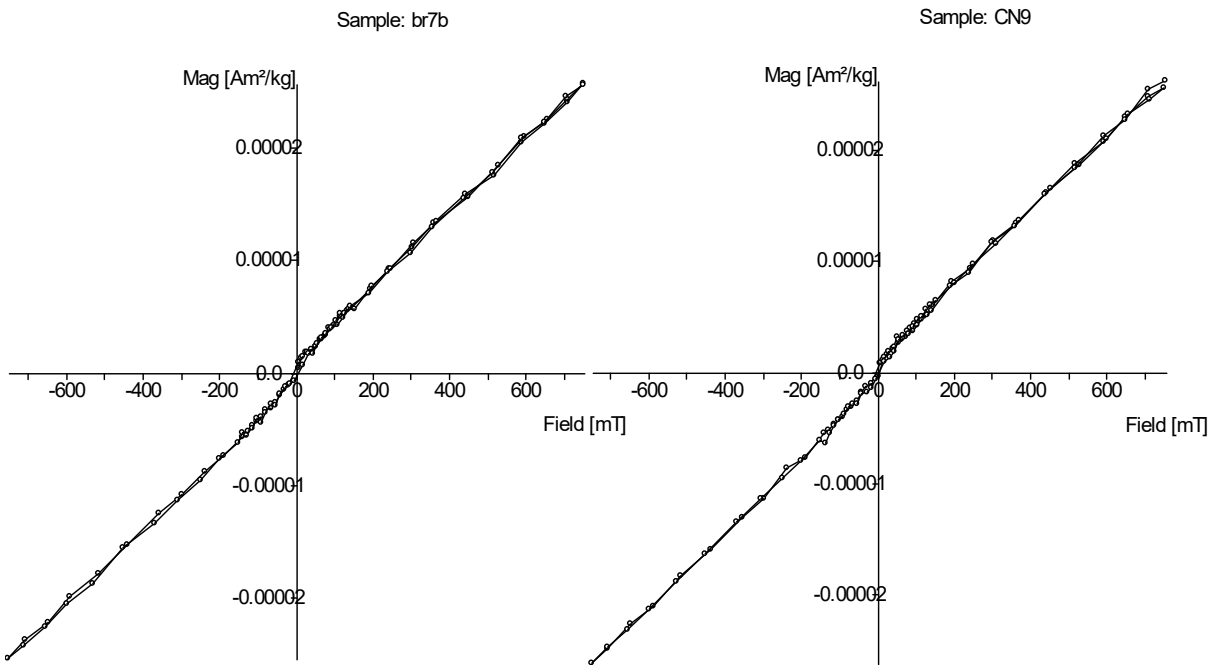

Figure 7.19. A) Sample Br7b, a grey shale B) Sample Cn9, a black shale. Both samples near linear-shape indicates that they have a large paramagnetic contribution, particularly the black shale.

Table 7.1. Hysteresis parameters for each of the sediment samples, MDST=mudstone. The percentage of ferrimagnetic paramagnetic/diamagnetic content. Ms=Saturation induced magnetisation, Mrs=Saturation remanent magnetisation. Hc/Hrh are coercivity and remanent coercivity respectively.

Spec	**Type**	**Ferromagnetic content (%)**	**Para/diamag-netic content (%)**	**Ms (Am^2/kg)**	**Mrs (Am^2/kg)**	**Hc (mT)**	**Hcr (mT)**
Br 7	Grey clay	26.1	73.9	$1.94x10^{-3}$	$4.80x10^{-4}$	12.93	18.39
Cn 9	Black shale	7.1	92.9	$1.82x10^{-3}$	$3.69x10^{-4}$	8.63	249.11

7.9 Conclusion

The results are supportive of the room temperature AMS studies by Hirt et al. (1995), finding that the AMS data reflects a sedimentary fabric that has experienced compaction rather than one created by tectonism (Baas et al., 2007). This is supported by the strongly oblate shape of the AMS fabric, and the Kmax orientations similar to previous fossil orientations of Jones & Dennison (1970) and seismic anisotropy of Evans et al. (1989). These studies would suggest the main palaeocurrent is orientated northeast - southwest.

It was important to establish if tectonism has had an impact on the data, as the hysteresis results and Hirt et al. (1995) suggest the magnetic fabric is dominated by crystalline anisotropy associated with paramagnetic minerals such as chlorite. This crystalline fabric would have been susceptible to deformation, as the chlorite plates could be re-aligned to the fold axis rather than the bedding plane. The chlorite has recrystallised from an illite precursor that's formation predates the Alleghanian deformation event (Hirt et al., 1995) and therefore more likely represents a depositional fabric.

Samples in borehole A have a large ferrimagnetic content (Table 7.1); the ferrimagnetic minerals formation postdate the chlorite and the deformation, Hirt et al. (1995) suggests the ferrimagnetic fabric was reflective of a growth of new phases which these ferrimagnetic minerals are carrying a younger magnetization. A greater ferrimagnetic contribution to the AMS would explain the anomalous northerly Kmax direction which was influenced by coal/tension joints (Hirt et al., 1995). The drop in magnetic susceptibility in the two boreholes can be explained as an interval with carbonate deposition, thus the drop is explained by an increase in calcite content.

The two boreholes show a similar AMS fabric, having similar Kmax directions, P and T values, although borehole B samples have a lower average magnetic susceptibility. This would suggest that the mode of deposition was consistent throughout the axis of the Appalachian Basin. Mineralogical differences would explain the decrease in

magnetic susceptibility between the two boreholes, as a higher carbonate content would explain the scatter in borehole B.

The increased thermal alteration between the two sites indicated by the increase in CAI from 0.5-1 in borehole A to 1.0-1.5 in borehole B, would have affected the AMS fabric. The higher maturity would have produced more chlorite in Borehole B, thus increasing B's K_{mean} and P values if the carbonate content were the same. However, this is not possible to examine owing to the increased carbonate content which lowers the susceptibility. Thus, the original composition rather than thermal maturity of the clays dominates the AMS fabric in these sites.

The AMS results were able to show direction of palaeoflow within an estuary-hemipelagic basin (Slingerland & Loule, 1988). The AMS indicates a dominant current orientated northeast to southwest, running parallel to the Appalachian Basin axis.

8. Conclusion

This study explored the applications of anisotropy of magnetic susceptibility (AMS) to examine fabrics in a variety of shale basins. There were four key areas that AMS was used to develop the understanding of each basin: 1) its application as a palaeoflow indicator; 2) understanding the magnetic mineralogy; 3) understanding the likely impact of tectonism on the AMS; and 4) to assist traditional methods in examining and interpreting palaeo-environments.

8.1 Implications of Using AMS as a Palaeoflow Indicator

The main aim of this project was to evaluate the petrofabric using AMS and examine how AMS could be applied to shale basin studies following the principles set out by the likes of Baas et al. (2007); Borradaile (2001); Hamilton & Rees (1970); Kissel et al. (1998) and Schieber & Ellwood (1993).

8.1.1 Ainsa System

The Eocene Ainsa System, the main focus of this project, comprises a series of turbiditic units between thick interfan-shales. The case study utilised the depositional models set out by Baas et al. (2007) of how different directional petrofabrics are produced in sand dominated turbidites. The results from Ainsa were in agreement with their observations, indicating two modes in the sandstone fabrics: 1) flow-aligned fabrics, where the grains aligned in the most stable position, parallel to the current flow indicated by tool marks and scour marks on the turbidites (Pickering & Corregidor, 2005); 2) flow-transverse

fabrics, where the Kmax directions were aligned perpendicular to flow, caused by high velocity depositional currents rolling the grains.

When examining the distribution of flow-aligned and flow–transverse fabrics, there were fewer flow-parallel fabrics at the base of the Anisa Quarry section than expected. These flow-aligned fabrics would have represented the facies associated with the upper parts of turbidite beds (e.g. Td, Te; So et al., 1997). This bias towards transverse fabrics in the Ainsa Quarry was explained when examining an individual turbidite (Fig. 2.24). The turbidite was mostly composed of the lower Bouma facies (Ta-Tc), with these facies representing rapid low-density turbidity flows which favour transverse fabric. At the top of the bed specimens showed a flow-aligned fabric that represented a change in the mode of transport. The sediments were transported in slower currents associated with upper Bouma divisions (Td-Te) but most of these upper facies had been removed by the overlying turbidite.

A key observation is that transverse flow directions are also seen in the interfan-shales. The shales are a mixture of hemipelagic mudstone deposits and debris flows. The findings in this project support previous studies by Parés & Dinarés-Turell (1993) which looked ‘grey marls’ around the Ainsa Basin sharing similar flow-aligned AMS fabrics, with similar shape anisotropy (T = 0.822) and a high degree of anisotropy (P’ = 1.044). However, they did not find transverse directions, but this can be explained by the small sample size they used and the focus on conventional marls and shales that would not have possessed transverse fabrics owing to their low viscous currents. Instead,

transverse fabrics in the interfan-shales are associated with the debris flows containing pebbles (Fig. 5.10). Baas et al. (2007) and Park et al. (2013) explain the depositional conditions in debris flows as high velocity shearing flows that caused the grains to interact and so align grains normal to flow.

Park et al. (2013) examined Miocene fan-deltas in South Korea, they found the mud dominated lithologies had varying AMS fabrics. The flow-aligned muds were similar to those mentioned in Parés & Dinarés-Turell (1993). There were transverse mud, sand and heterolithic debrites units which had oblate T values =~0.8 and Pj values =1.27. They suggested these transverse fabrics were generated by shear-induced rotation of the long axis of the grains. This would explain the two modes of fabric in Ainsa interfan-shales, a flow-aligned hemipelagic mode and transverse mode found in the coarser silts or debrites. The debrites are supported by the presence of pebble beds in the shales that show this transverse fabric.

8.1.2 Welsh Borderlands

The Welsh Borderlands study was used to compare low energy mudstones (possibly distal turbidites) and shelf-edge deposits with the Ainsa system. A series of samples of Telychian and Wenlock age units were taken from different parts of the shelf edge of the Midland Platform and the AMS of each site shared a common northeast-southwest Kmax trend with little to no flow-transverse fabrics. This Kmax trend is similar to the palaeoflow directions obtained from Underwood's (1994) fossil orientation study and the palaeoflow directions obtained by Soper & Woodcock (1990), suggesting the Kmax is indicative of shelf-parallel palaeoflow directions. Comparison to the depositional models in Baas et al. (2007) indicates that samples were deposited in low velocity systems (compared to those at Ainsa), insufficient to rotate and roll grains on the seabed. This assessment is supported by the high degree of anisotropy, the oblate fabric of the mud units and lack of Kmax- transverse fabrics.

Soper & Woodcock (1990) and Cherns et al. (2006) suggest possible sediment sources during the Silurian; they suggest the sediments were deposited by northerly (to north easterly) directed currents generated from turbidite and suspension deposition. This basin-wide direction would suggest either widespread distal turbidites or palaeoflow was influenced by topography. Ziegler et al. (1968) established the shoreline which the AMS Kmax directions are largely aligned parallel to; thus the Kmax directions reflect a basin-wide shore drift or perhaps contourite system.

Previous studies by Shor et al. (1984) and Taira & Scholle (1979) looked at the AMS of contourites with respect to turbidite deposits. Their AMS study used a range of mud and sand sediments from bottom current deposits. The AMS fabrics showed horizontal foliation planes and the Kmax directions were parallel to the shelf. The turbidites' AMS fabric was different from that of the bottom current deposits, as the T values were more isotropic and they had a smaller degree of anisotropy. The change in mode of deposition is further supported by the difference in their Kmax directions. Shor et al. (1984) study found the Kmax direction of the turbidite to be normal to the shoreline which was attributed to a new source of deposition. These previous case studies support the argument that the AMS fabric in the Welsh Borderlands reflects a contourite system rather than a turbidite dominated basin as this was not supported by the AMS fabric.

8.1.3 Marcellus Shale

The Marcellus shale is in many ways similar to the Welsh Borderlands Silurian, occurring in a shale dominated mid Devonian succession, but in this case in a more hemipelagic basin representing distal sources from a tidal estuary system (Slingerland et al., 2009). The Kmax directions reflect a northeast-southwest trend which is the expected palaeoflow direction from previous fossil orientation studies by Jones & Dennison (1970) and seismic anisotropy data from Hirt et al. (1995). Kmax long-grain axes show a well-developed foliation perpendicular to the Kmin values. The high T (oblate fabrics) and P values throughout the borehole suggest the fabric reflects deposition from suspension. The AMS fabric is therefore a well-defined bedding fabric which later underwent (vertical) compaction, with little apparent impact from folding, since the core material is far from the Appalachian deformation fronts.

Table 8.1. A summative table of the AMS fabrics and their interpretations for each of the case studies.

Case Study	Environment	Observations	Analysis
Ainsa System	Turbidite dominated system with inter-shales between sequences.	Two dominant modes of Kmax direction shown, one aligned with flow and one normal to flow (Pickering & Corregidor, 2005). Flow aligned Kmax directions are orientated NW-SE and found throughout the sequence but mainly at the top of turbidite beds and in the shales. Transverse fabrics Kmax directions are orientated NE-SW found in interfan shales and the base of the Ainsa Quarry.	Flow-aligned fabrics represent both high velocity turbulent flows and low velocity flows that are not able to rotate the grains. The transverse fabrics dominate the Ainsa turbidite facies as these are favourable conditions for transverse fabrics and the top Bouma facies are absent. The transverse fabrics in the interfan-shales, represent debris flows which cause the 'rolling' fabric.
Welsh Borderland	Hemipelagic mud dominated turbidite/ contourite basin.	One dominant Kmax direction across the three sites, which aligns with the palaeoflow, directed to NE. Dominantly high degree of anisotropy and oblate shape. Small sample sets responsible for some anomalous data Fig 6.18.	The dominant direction indicates the sites shared a similar source, throught the Silurian, interrupted as shore-parallel currents/contourites. Lower MS samples belong to sites which are richer in carbonates, e.g. the Eaton Trackway, Farley Member. Some of the Buttington Quarry anomalous results may be attributed to tectonism.
Marcellus shale	Hemipelagic estuary.	One Kmax trend across the two sites, orientated NE-SW. Dominantly high degree of anisotropy and oblate shape, with noticeable changes at certain depth.	The Kmax direction aligns with palaeocurrents obtained from fossil orientation and seismic anisotropic fabric No imbrication, strong degree of anisotropy and oblate shape suggest deposition from suspension. Changes in MS attributed to variations in chlorite content related to more carbonate or a higher quartz contents.

8.2 Compositional Factors Controlling the AMS

By examining the effects of ferrimagnetic or paramagnetic contributions to the AMS data, the study was able to distinguish the likely mineralogical source and if it was dominated by shape or crystalline anisotropy.

The Ainsa samples showed a mixture of ferrimagnetic and paramagnetic mineralogy within the sandstone units. A ferrimagnetic mineralogy was dominant in the coarser sediments and was identified as probable multi-domain magnetite agreeing with claims of a detrital ferrimagnetic source by Mochales et al. (2012). This would suggest that the shape anisotropy is current-carried by flow-transverse aligned magnetite in the coarser sediments.

AMS in samples that have a greater contribution from paramagnetic rather than ferrimagnetic minerals, reflect a preferred crystalline orientation of paramagnetic minerals. Studies by Rochete (1987) and Hounslow, (1985) have suggested that paramagnetic mineral-derived AMS (carried by phyllosilicates such as Fe-rich clays) can correspond to flow and bedding plane foliations in the rock fabric. The paramagnetic dominated samples in all three basins examined reflected the palaeoflow data obtained from tool marks, fossil orientation, seismic and X-ray data. The findings would suggest that AMS derived from paramagnetic minerals can be used to determine palaeoflow, providing they did not form authigenically or were later re-altered by post-deposition deformation.

8.3 Tectonism

It is important to examine the impact of tectonism as this can change the fabric of the rocks, so it is crucial to be able to distinguish between textures produced from initial deposition/compaction and those that formed from folding. Sedimentary fabrics can be confused with tectonic fabrics since both reflect block faulting or inversion in the basins, an example would be flows parallel to bounding faults (Cifelli et al., 2005). Thus palaeoflow indicators are essential to infer and determine if the AMS fabric is related to palaeocurrents or tectonism. This is particularly important when examining fabrics carried by phyllosilicates and clays which are more susceptible to crystallisation during burial or incipient deformation. AMS in highly deformed sediments can be useful as a strain indicator (Parés, 2015) but was not desired in this study when inferring palaeoflow.

Cifelli et al. (2005); Parés et al. (1999) have used AMS to infer deformation within basins. When beds are folded and the grain fabric deformed, the magnetic lineation within the sediments can re-orientated. Under these conditions the magnetic lineation will switch to being parallel to the axis of stretching, the fold-hinge or the intersection of cleavage and bedding (Hounslow, 1990; Cifelli et al. 2005; Pares, 2015).

Sedimentary rocks used in this study experienced little post-deformation (none showed cleavage development), with oblate AMS ellipsoids and foliations sub-parallel to bedding, and hence the AMS fabric is attributed to deposition and compaction (Baas et al., 2007; Cifelli et al., 2005). The Buttington Quarry samples in the Welsh Borderlands experienced folding (beds were dipping >75º) and faulting compared to the other sites, but no cleavage development, and have low conodont alteration indices (CAI) of about 2.5 (Aldridge, 1986). However, when bedding corrections are applied, the AMS fabric is comparable to the other Welsh Borderland sites and so it is possible to reasonably infer that the AMS reflects the palaeoflow. Other Silurian sites sampled had lower degrees of heat alteration of 1 to 1.5 CAI.

The two Marcellus sites experienced different levels of post deformation with borehole B experiencing slightly greater maximum temperatures than borehole A, indicated by the CAI index increase from 0.5-1 in borehole A to 1.0-1.5 in borehole B. However, the two sites both share similar AMS fabrics, suggesting that the effects of deformation on the AMS are minimal.

8.4 Anisotropy of Magnetic Susceptibility in Determining Environments

This study has been successful in showing that AMS can be used to establish paleoflow and some types of grain deposition, which makes it a useful tool to establish palaeoenvironment (Joseph et al., 1998). This is particularly important in shale basins, where traditional methods may not be applicable.

AMS could be used on a large scale to map flow in basins, such as the Marcellus Shale in the Appalachian Basin and the Welsh Borderlands, or to infer changes in sources directions or currents. On a smaller scale AMS could be used to evaluate individual beds (e.g. in the Ainsa System) to infer the type of grain-mode transport. An example would be the flow-transverse fabrics in the interfan shales which suggests that fabrics related to debrites are much more common than can be inferred in the field. Conversely, the flow aligned fabrics in similar looking mudstone facies indicate deposition from suspension and probably low-velocity turbidity currents. The fabrics in the turbidite sequence can be used to determine which parts of the Bouma sequences are present and if they are from the channel axis or levee/overbank units.

The main limitation of using AMS is that it can be influenced by tectonism which may distort the inferred palaeoflow direction. Veloso et al. (2007) was able to infer the extent of block rotation on the sediments within the Late Miocene Main Volcanic Unit of the Taitao ophiolite in Southern Chile. They were able to find an inferred northwest palaeoflow using un-orientated AMS data. However, the samples were re-orientated using palaeomagnetic corrections and the inferred direction was northwest west which better reflected the structure of the basin. Piper et al. 1996 used AMS fabric to determine the extent of Acadian tectonism on mudrocks in the Windermere Basin, northern England, establishing the impact of cleavage on the AMS fabric. Also sediments that show magnetically weak susceptibilities tend to have inconsistent AMS data and cannot be relied on.

Overall the project found AMS to be a reliable indicator for the paleo-schematics of basins. This project aimed to explore AMS as a potential technique to understand transport mechanisms in shale-prone basins where conventional methods were difficult to apply. AMS was successfully used to examine the petrofabric of shales but could not be used to definitely describe the transport mechanism without having an understanding of the structural geology of the basins. Therefore the future of AMS being used in these shale-prone basins is a supportive role and should be used when the structural geology is known. AMS studies of shales should be used in conjunction with sandstone fabrics in order to provide an accurate and reliable palaeocurrent direction.

List of References

AGICIO. 2016. Available at http://www.agico.com/manuals/ mfk1-man.pdf [accessed on 09/072016]

Aldridge, R.J., 1986. Conodont palaeobiogeography and thermal maturation in the Caledonides. *Journal of the Geological Society*, 143(1), pp.177-184.

Amorós, E.B., 2014. Paleomagnetism and Thermochronology in Tertiary Syntectonic Sediments of the South-central Pyrenees: Chronostratography, Kinematic and Exhumation Constraints (Doctoral dissertation, *Universitat de Barcelona*).

Baas J. H., Hailwood E. A., McCaffrey W. D., Kay M. & Jones R. 2007. Directional petrological characterisation of deep-marine sandstones using grain fabric and permeability anisotropy: Methodologies, theory, application and suggestions for integration. *Earth-Science Review* 82 pp101-142

Bassett, M.G., Bluck, B.J., Cave, R., Holland, C.H. and Lawson, J.D., 1992. Silurian. *Geological Society, London, Memoirs*, 13(1), pp17-56.

Battey M.H. & Pring A. 1997. Minerology for students (third edition) *Addison Wesley Longman Limited*. Harlow pp91-110.

Blakey, R., 2013. North American Paleogeography. https://www2.nau. edu/rcb7/nam.html [accessed 05/02/2017]

Borradaile, G.J., 1994. Paleomagnetism carried by crystal inclusions: the effect of preferred crystallographic orientation. *Earth and planetary science letters*, 126(1), pp171-182.

Borradaile, G.J. and Werner, T., 1994. Magnetic anisotropy of some phyllosilicates. *Tectonophysics*, 235(3), pp223-248.

Borradaile, G.J. and Henry, B., 1997. Tectonic applications of magnetic susceptibility and its anisotropy. *Earth-Science Reviews*, 42(1), pp49-93.

Borradaile G. J. 2001. Magnetic fabrics and petrofabrics: their orientation distributions and anisotropies. *Journal of Structual Geology* 23 pp1581-1596

Bouma A. H., 2000. Coarse-grained and fine-grained turbidite systems as end member models: applicability and dangers. *Marine and Petroleum Geology* 17 pp137-143.

Brett C. E., Baird G. C., Bartholomew A. J., Desantis M. K. & Ver Straeten C. A. 2011. Sequence stratigraphy and a revised sea-level curve for the Middle Devonian of eastern North America. *Palaeogeography, Palaeclimatology Palaeoecology* 304, pp21-53

Brenchley, P.J. and Rawson, P.F. eds., 2006. The geology of England and Wales. *Geological Society of London*.

Briden, J.C. and Arthur, G.R., 1981. Precision of measurement of remanent magnetization. *Canadian Journal of Earth Sciences*, 18(3), pp.527-538.

Brown T. C. and Kenig F. 2004. Water column structure during deposition of Middle Devonian-Lower Mississippian black and green/gray shales of the Illinois and Michigan Basins: a biomarker approach. *Palaeogeography, Palaeclimatology Palaeoecology* 215, pp59-85

Burgess, N.D. and Richardson J. B., 1991. Silurian cryptospores and miospores from the type Llandovery area, south-west Wales. *Palaeontology*, 34(3), pp575-599.

Butler R. F. 1992. Paleomagnetism: Magnetic Domains to Geologic Terranes. *Blackwell Scientific* p1-180

Cantalejo B & Pickering K. T. 2014. Climate forcing of fine-grained deep-marine systems in an active tectonic setting: Middle Eocene, Ainsa Basin, Spanish Pyrenees. *Palaeogeography, Palaeoclimatology, Palaeoecology.* 410 pp351-371

Carter, K.M., Harper, J.A., Schmid, K.W. and Kostelnik, J., 2011. Unconventional natural gas resources in Pennsylvania: The backstory of the modern Marcellus Shale play. En*vironmental Geosciences*, 18(4), pp.217-257.

Cawood, P.A. and Nemchin, A.A., 2001. Paleogeographic development of the east Laurentian margin: Constraints from U-Pb dating of detrital zircons in the Newfoundland Appalachians. *Geological Society of America Bulletin*, 113(9), pp1234-1246.

Chadima M., Pruner P., Šlechta S., Grygar T. & Hirt A. M. 2006. Magnetic fabric variations in Mesozoic black shales, Northen Siberia, Russia: Possible paleomagnetic implications. *Techonphysics* 418 pp145-162.

Chadima M. & Jelinek V., 2009. Anisoft (Version 4.2) software. Agico, Inc.

Cherns, L., Cocks, L.R.M., Davies, J.R., Hillier, R.D., Waters, R.A. and Williams, M., 2006. Silurian: the influence of extensional tectonics and sea-level changes on sedimentation in the Welsh Basin and on the Midland Platform. *The geology of England and Wales*, pp75-102.

Cifelli, F., Mattei, M., Chadima, M., Lenser, S. and Hirt, A.M., 2009. The magnetic fabric in “undeformed clays”: AMS and neutron texture analyses from the Rif Chain (Morocco). *Tectonophysics*, 466(1), pp79-88.

Cocks, L.R.M., 1989. The Geology of South Shropshire. *Proceedings of the Geologists' Association*, 100(4), pp505-519.

Collinson, D.W., 1965. Depositional remanent magnetization in sediments. *Journal of Geophysical Research*, 70(18), pp.4663-4668.

Collinson D.W. 1983. Methods in Rock Magnetism and Palaeomagnetism. *Chapman and Hall Ltd*, London, pp1-445

Crossley, J.D. and Clark, H.E., 2015. More gap than record? Qualitative and quantitative assessment of stratigraphic gaps in a field based study, with examples from the Lower Silurian Pentamerus Beds of Shropshire, England and the Lower Ordovician Ribband Gp of County Wexford, Ireland. *Geological Society, London, Special Publications*, 404(1), pp271-282.

Dakin N., Pickering K. T., Mohrig D. & Bayliss N.J. 2013. Channel-like features created by erosive submarine debris flows: Field evidence from the Middle Eocene Ainsa Basin, Spanish Pyrenees. *Marine and Petroleum Geology*. 41, pp62-71

Davies J. R., Ray D. C., Thomas A. T., Loydell D. K., Cherns L., Cramer B. D., Veevers S. J., Worton G. J., Marshall C., Molyneux S. G., Vandenbroucke T. R. A., Verniers J., Waters, M. Williams R. A. and Zalasiewicz J. A.. 2011. Siluria Revisited: A Field Guide. International Subcommission on Silurian Stratigraphy, Field Meeting 2011 (ed. D.C. Ray), pp1 -170

Day, R., Fuller, M. and Schmidt, V.A., 1977. Hysteresis properties of titanomagnetites: grain-size and compositional dependence. *Physics of the Earth and planetary interiors*, 13(4), pp.260-267.

DeSantis M. K. & Brett C. E. 2011. Late Eifelian (Middle Devonian) biocrises: Timing and signature of the pre-Kačák Bakoven and Stony Hollow Events in eastern North America. *Palaeogeography, Palaeclimatology Palaeoecology* 304, pp113-135.

Dewey, J. and Rosenbaum, M., 2008. Future avenues of research in the Welsh Borderland, with particular reference to terrane tectonics. *Proceedings of the Shropshire Geological Society*, 13, pp104-13.

Duke, W.L., 1990. Geostrophic circulation or shallow marine turbidity currents? The dilemma of paleoflow patterns in storm-influenced prograding shoreline systems. *Journal of Sedimentary Research*, 60(6).

Duke, W.L., Arnott, R.W.C. and Cheel, R.J., 1991. Shelf sandstones and hummocky cross-stratification: new insights on a stormy debate. *Geology,* 19(6), pp625-628.

Dunlop, D.J., 2002. Theory and application of the Day plot (Mrs/Ms versus Hcr/Hc) 1. Theoretical curves and tests using titanomagnetite data. *Journal of Geophysical Research: Solid Earth*, 107(B3).

East, J.A., Swezey, C.S., Repetski, J.E. and Hayba, D.O., 2012. Thermal maturity map of Devonian shale in the Illinois, Michigan, and Appalachian basins of North America. *US Geological Survey Scientific Investigations Map*, 3214(1).

EDINA. 2016. Available at https://digimap.edina.ac.uk/ [accessed on 15/06/2016]

Engelder T., 1979. The nature of deformation within the outer limits of the central Appalachian foreland fold and thrust belt in New York State. *Tectonphysics* 55 pp289-310

Enkin, R.J., 2003. The direction–correction tilt test: an all-purpose tilt/fold test for paleomagnetic studies. *Earth and Planetary Science Letters*, 212(1), pp.151-166.

Evans, K.F., Oertel, G. and Engelder, T., 1989. Appalachian stress study: 2. Analysis of Devonian shale core: Some implications for the nature of contemporary stress variations and Alleghanian deformation in Devonian rocks. *Journal of Geophysical Research: Solid Earth*, 94(B6), pp7155-7170.

Falivene, O., Arbués, P., Howell, J., Muñoz, J. A., Fernández, O. & Marzo, M. 2006. Hierarchical geocellular facies modelling of a turbidite reservoir analogue from the Eocene of the Ainsa basin, NE Spain *Marine and Petroleum Geology*, 23(6), pp679-701.

Faugères, J.C. and Stow, D.A., 1993. Bottom-current-controlled sedimentation: a synthesis of the contourite problem. *Sedimentary Geology*, 82(1-4), pp287-297.

Fedo, C.M., Sircombe, K.N. and Rainbird, R.H., 2003. Detrital zircon analysis of the sedimentary record. *Reviews in Mineralogy and Geochemistry*, 53(1), pp277-303.

Fisher, R., 1953, Dispersion on a sphere. *In Proceedings of the Royal Society of London* 217, pp295-305.

Fleet, A.J., Clayton, C.J., Jenkyns, H.C. and Parkinson, D.N., 1987. Liassic source rock deposition in western Europe. *Petroleum Geology of North West Europe*, pp59-70.

Hailwood, E.A., Kidd, R.B. and Dowling, L., 1987. THE MAGNETIC FABRIC OF NEOGENE AND QUATERNARY SEDIMENTS ON THE FENI AND GARDAR DRIFTS, NORTHEASTERN ATLANTIC, DEEP-SEA DRILLING PROJECT SITE-610 AND SITE-611. *INITIAL REPORTS OF THE DEEP SEA DRILLING PROJECT*, 94, pp1083-1089.

Hamilton, N. and Rees, A.I., 1970. Magnetic fabric of sediments from the Shelf at La Jolla (California). *Marine Geology*, 9(2), ppM6-M11.

Heard, T.G., Pickering, K.T. and Clark, J.D., 2014. Ichnofabric characterization of a deep-marine clastic system: a subsurface study of the Middle Eocene Ainsa System, Spanish Pyrenees. *Sedimentology*, 61(5), pp1298-1331.

Hirt A. M., Evans K. F. & Engelder T. 1995. Correlation between magnetic anisotropy and fabric for Devonian shales on the Appalachian Plateau. *Tectonophysics* 247 pp121-132

Hounslow, M.W., 1985. Magnetic fabric arising from paramagnetic phyllosilicate minerals in mudrocks. *Journal of the Geological Society*, 142(6), pp995-1006.

Hounslow, M.W., 1990. Grain fabric measured using magnetic susceptibility anisotropy in deformed sediments of the Barbados accretionary prism: Leg 110. *In Moore, JC, Mascle, A., et al., Proc. ODP, Sci. Results* 110, pp257-275.

Hounslow M. W., 2006. PMAG TOOLS (Version 5.0), software. Lancaster University

Hrouda, F., 1982. Magnetic anisotropy of rocks and its application in geology and geophysics. *Geophysical surveys*, 5(1), pp37-82.

Hrouda, F., 1992. Separation of a component of tectonic deformation from a complex magnetic fabric. *Journal of structural Geology*, 14(1), pp.65-71.

Hrouda, F., Plasienka, D. and Gregorová, D., 2002. Assumed Neogene deformation in the Central Western Carpathians as inferred from magnetic anisotropy investigations. *Stephan Mueller Special Publication Series*, 1, pp125-136.

Hughes S. R., Alexander J., & Druitt T. H. 1995. Anisotropic grain fabric: volcanic and laboratory analogues for turbidites. *Geological Society, London, Special Publications*, 94(1) pp51-62

Hunt, C.P., Moskowitz, B.M., Banerjee, S.K., 1995. Magnetic properties of rocks and minerals. In: Ahrens, T.J. (Ed.), *Rock Physics and Phase Relations. A Handbook of Physical Constants. American Geophysical Union*, pp. 189–204.

Jacobs J.A. (editor) 1989. Geomagnetism. *Academic Press* 3 pp1-248

Jelinek, V., 1981. Characterization of the magnetic fabric of rocks. *Tectonophysics*, 79(3-4), ppT63-T67.

Johnson, H.D. and Stewart, D.J., 1985. Role of clastic sedimentology in the exploration and production of oil and gas in the North Sea. *Geological Society, London, Special Publications*, 18(1), pp249-310.

Jones, M. L. and Dennison, J. M., 1970. Oriented fossils as paleocurrent indicators in Paleozoic lutites of southern Appalachians. *J. Sediment. Petrol.*, 40, pp642-649.

Joseph, L.H., Rea, D.K. and Van der Pluijm, B.A., 1998. Use of grain size and magnetic fabric analyses to distinguish. *Paleoceanography*, 13(5), pp491-501.

Ketcham, R.A., 2005. Three-dimensional grain fabric measurements using high-resolution X-ray computed tomography. *Journal of Structural Geology*, 27(7), pp1217-1228.

Kent, J.T., Briden, J.C. and Mardia, K.V., 1983. Linear and planar structure in ordered multivariate data as applied to progressive demagnetization of palaeomagnetic remanence. *Geophysical Journal International* 75(3) pp593-621.

Kissel, C., Laj, C., Mazaud, A. and Dokken, T., 1998. Magnetic anisotropy and environmental changes in two sedimentary cores from the Norwegian Sea and the North Atlantic. *Earth and Planetary Science Letters*, 164(3), pp617-626.

Langereis C.G., Krijgsman W., Muttoni G., & Menning M. 2010. Magnetostratigraphy – concepts, definitions, and applications. *Gebrüder Borntraeger* 43/3 pp207-233

Lash G.G. & Blood D.R. 2014. Organic matter accumulation, redox and diagenetic history of the Marcellus Formation, southwestern Pennsylvania, Appalachian basin. *Marine and Petroleum Geology* 57 pp244-263.

Leonhardt, R., 2006. Analyzing rock magnetic measurements: the RockMagAnalyzer (Version 1.0) software. *Computers & Geosciences*, 32(9), pp1420-1431.

Loydell, D.K., Frýda, J., Butcher, A. and Loveridge, R.F., 2014. A new high-resolution δ13C carbon isotope curve through the lower Wenlock Series of Buttington Quarry, Wales. *GFF*, 136(1), pp172-174.

Lu G., Marshak S. & Kent D. V. 1990. Characteristics of magnetic carriers responsible for Late Paleozoic remagnetization in carbonate strata of the mid-continent, U.S.A. Elsevier Science Publishers 99 pp351-361

Lüneburg, C.M., Lampert, S.A., Lebit, H.D., Hirt, A.M., Casey, M. and Lowrie, W., 1999. Magnetic anisotropy, rock fabrics and finite strain in deformed sediments of SW Sardinia (Italy). *Tectonophysics*, 307(1), pp51-74.

Magnetic Measurements Ltd, 2006, available at http://www.magnetic-measurements.com/ [Accessed 08/07/2016]

Manning E. B. & Elmore R. D. 2012. Rock magnetism and identification of remanence components in the Marcellus Shale, Pennsylvania. *Geological Society, London, Special Publications* 371, pp271-282

Maher B. A., Thompson R. 2010. Quaternary Climates, Environments and Magnetism. *Cambridge University Press*, Cambridge pp1-230

McElhinny, M.W. and Merrill, R.T., 1975. Geomagnetic secular variation over the past 5 my. *Reviews of Geophysics*, 13(5), pp.687-708.

McFadden, P.L. and McElhinny, M.W., 1988. The combined analysis of remagnetization circles and direct observations in palaeomagnetism. *Earth and Planetary Science Letters*, 87(1), pp161-172.

Menning M., Alekseev A. S., Chuvashov B. I., Davydov V. I, Devuyst F.-X., Forke H. C., Grunt T. A., Hance L., Heckel P. H., Izokh N. G., Jin Y.-G., Jones P. J., Kotlyar G. V., Kozur H. W., Nemyrovska T. I., Schneider J. W., X.-D Wang., Weddige K., Weyer D. & Work D. M. 2006. Global time scale and regional stratigraphic reffernces scales of Centeral and West Europe, East Europe, Tethys, South China, and North America as used in the Devonian-Carboniferous-Permian Correlation Chart 2003 (DCP 2003). *Palaeogeography, Palaeclimatology Palaeoecology* 240, pp318-372

Mochales, T., Barnolas, A., Pueyo, E.L., Serra-Kiel, J., Casas, A.M., Samsó, J.M., Ramajo, J. and Sanjuán, J., 2012. Chronostratigraphy of the Boltaña anticline and the Ainsa Basin (southern Pyrenees). Geological Society of America Bulletin, 124(7-8), pp.1229-1250.

Morton, A.C. and Hallsworth, C.R., 1999. Processes controlling the composition of heavy mineral assemblages in sandstones. *Sedimentary Geology*, 124(1), pp.3-29.

Mulder, T., 2011. Gravity processes and deposits on continental slope, rise and abyssal plains. *Deep-sea sediments*, pp25-148.

Mullins, G.L. and Loydell, D.K., 2001. Integrated Silurian chitinozoan and graptolite biostratigraphy of the Banwy River section, Wales. *Palaeontology*, 44(4), pp731-781.

Muñoz, J.A., Beamud, E., Fernández, O., Arbués, P., Dinarès- Turell, J. and Poblet, J., 2013. The Ainsa Fold and thrust oblique zone of the central Pyrenees: Kinematics of a curved contractional system from paleomagnetic and structural data. *Tectonics*, 32(5), pp1142-1175.

Néel, L., 1955. Some theoretical aspects of rock-magnetism. *Advances in physics*, 4(14), pp.191-243.

Opdyke N. D. & Channell J. E. T. 1996. Magnetic Stratigraphy. *Academic Press Limited*. London. 64 pp1-345

Parés, J.M. and Dinarés-Turell, J., 1993. Magnetic Fabric in Two Sedimentary Rock-Types from the Southern Pyrenees. *Journal of geomagnetism and geoelectricity*, 45(2), pp193-205.

Parés, J.M., van der Pluijm, B.A. and Dinarès-Turell, J., 1999. Evolution of magnetic fabrics during incipient deformation of mudrocks (Pyrenees, northern Spain). *Tectonophysics*, 307(1), pp.1-14.

Parés, J.M., 2015. Sixty years of anisotropy of magnetic susceptibility in deformed sedimentary rocks. *Frontiers in Earth Science*, 3, pp4

Park M. E., Cho H., Son M & Sohn Y. K. 2013. Depostional processes, Paleoflow patterns, and evolution of a Miocene gravelly fan-delta system in SE Korea constrained by anisotropy of magnetic susceptibility analysis of interbedded mudrocks. Marine and Petroleum Geology 48 pp206-223

Pavlov V. & Gallet Y. 2005. A third superchron during the Early Paleozoic. *Episodes* 28/2 pp1-7

Peters, C., 1995. Unravelling magnetic mixtures in sediments, soils and rocks. Ph.D. thesis, *University of Edinburgh*.

Peters, C. and Thompson, R., 1998. Magnetic identification of selected natural iron oxides and sulphides. Journal of Magnetism and Magnetic Materials, 183(3), pp.365-374.

Peters, C. and Dekkers, M.J., 2003. Selected room temperature magnetic parameters as a function of mineralogy, concentration and grain size. *Physics and Chemistry of the Earth, Parts A/B/C*, 28(16), pp659-667.

Pickering K. T. & Corregidor J. 2005. Mass-transport complexes (MTCs) and tectonic control on basin-floor submarine fans, Middle Eocene, south Spanish Pyrenees. *Journal of Sedimentary Research*, 75, pp761–783

Pickering, K.T. and Corregidor, J., 2005. Tectonic control, rates of lateral migration and growth patterns of confined basin-floor submarine fans (seismosequences), and importance of mass transportcomplexes (MTCs), mid-Eocene, south-central Pyrenees: Core Display H5 (with posters): *Geological Society of London. In Petroleum Geology of NW Europe*, Proceedings of the 6 th Conference, London, UK.

Piper, J.D.A., Elliot, M.T. and Kneller, B.C., 1996. Anisotropy of magnetic susceptibility in a Palaeozoic flysch basin: the Windermere Supergroup, northern England. *Sedimentary Geology*, 106(3), pp235-258.

Pohl, F. & McCann, T. 2014. Architecture and depositional development of the Eocene deep-marine Morillo and Coscojuela Formations, Aínsa Basin, Spain. *Geological Journal*, 49(3), pp221-238.

Rasmussen, S.L. and Surlyk, F., 2012. Facies and ichnology of an Upper Cretaceous chalk contourite drift complex, eastern Denmark, and the validity of contourite facies models. *Journal of the Geological Society*, 169(4), pp435-447.

Rees, A.I., Brown, C.M., Hailwood, E.A. and Riddy, P.J., 1982. Magnetic fabric of bioturbated sediment from the Northern Rockall Trough: Comparison with modern currents. *Marine Geology*, 46(1-2), pp161-173.

Repetski, J.E., Ryder, R.T., Weary, D.J., Harris, A.G. and Trippi, M.H., 2008. Thermal Maturity Patterns (CAI and% Ro) in Upper Ordovician and Devonian Rocks of the Appalachian Basin. A Major Revision of USGS Map I–917–E Using New Subsurface Collections. *US Geological Survey Scientific Investigations Map, 3006*, pp26.

Robertson, D.J. and France, D.E., 1994. Discrimination of remanence-carrying minerals in mixtures, using isothermal remanent magnetisation acquisition curves. *Physics of the Earth and Planetary Interiors*, 82(3-4), pp.223-234.

Rochette, P., 1987. Magnetic susceptibility of the rock matrix related to magnetic fabric studies. *Journal of Structural Geology*, 9(8), pp1015-1020.

Rochette, P., Jackson, M. and Aubourg, C. 1992. Rock magnetism and the interpretation of anisotropy of magnetic susceptibility. *Reviews of Geophysics*, 30(3), pp209-226

Schieber, J. and Ellwood, B.B., 1988. The coincidence of macroscopic paleocurrent indicators and magnetic lineation in shales from the Precambrian Belt Basin. *Journal of Sedimentary Research*, 58(5).

Schieber J. & Ellwood B. B., 1993. Determination of basinwide Paleocurrent patterns in a shale succession from Anisotropy of Magnetic Susceptibility (AMS): a case study of the Mid-Proterozoic Newland formation, Montana*. SEPM Journal of Sedimentary Research* 63 pp874-880

Scotchman J. I., Bowna P., Pickering K. T., BouDagher-Fadel M., Bayliss N. J.& Robinson S. A. 2015. A new age model for the middle Eocene deep-marine Ainsa Basin, Spanish Pyrenees. *Earth-Science Reviews.* 144, pp10–22.

Shanmugam, G., 1997. The Bouma sequence and the turbidite mind set. *Earth-Science Reviews*, v.42(4), pp.201-229

Shor, A.N., Kent, D.V. and Flood, R.D., 1984. Contourite or turbidite?: Magnetic fabric of fine-grained Quaternary sediments, Nova Scotia continental rise. *Geological Society, London, Special Publications*, 15(1), pp257-273.

Slingerland, R., Patzkowski, M. and Peterson, D., 2009. Facies and Sedimentary Environments of the Catskill Systems Tract in Central Pennsylvania. *Pittsburgh Association of Petroleum Geologists and Pennsylvania State University*, 46.

So, Y.S., Rhee, C.W., Choi, P.Y., Kee, W.S., Seo, J.Y. and Lee, E.J., 2013. Distal turbidite fan/lobe succession of the Late Paleozoic Taean Formation, western Korea. *Geosciences Journal*, 17(1), pp.9-25.

Soper, N.T. and Woodcock, N.H., 1990. Silurian collision and sediment dispersal patterns in southern Britain. *Geological Magazine*, 127(06), pp527-542.

Southard, J. 2007. Avaible at https://ocw.mit.edu/courses/earth-atmospheric-and-planetary-sciences/12-110-sedimentary-geology-spring-2007/lecture-notes [accessed on 25/01/2017]

Stamatakos, J., Hirt, A.M. and Lowrie, W., 1996. The age and timing of folding in the central Appalachians from paleomagnetic results. *Geological Society of America Bulletin*, 108(7), pp815-829.

Stow D. A. V., Faugères J-C., Howe J. A., Pudsey C. J. & Viana A. R. 2002. Bottom currents, contourites and deep-sea sediment drifts: current state-of-the-art. *Geological Society, London, Memoirs*, 22(1), pp7-20

Taira, A. and Scholle, P.A., 1979. Deposition of resedimented sandstone beds in the Pico Formation, Ventura Basin, California, as interpreted from magnetic fabric measurements. *Geological Society of America Bulletin*, 90(10), pp952-962.

Tarling, D. and Hrouda, F. eds., 1993. Magnetic anisotropy of rocks (first edition). *Chapman & Hall, London*, pp1-31

Tauxe, L., 2005. Inclination flattening and the geocentric axial dipole hypothesis. *Earth and Planetary Science Letters,* 233(3), pp247-261.

Thellier, E., 1967. Methods of sample collection and orientation for Archaeomagnetism. Methods in Palaeomagnetism. Elsevier Publishing Company, Amsterdam.

Tilmann, S.E. and Bennett, H.F., 1973. A Sonic Method for petrographic analysis. *Journal of Geophysical Research*, 78(35), pp8463-8469.

Toghill, P. and Chell, K., 1984. Shropshire geology—stratigraphic and tectonic history. *Field studies*, 6(1), pp59-101.

Toghill, P., 1992. The Shelveian event, a late Ordovician tectonic episode in southern Britain (Eastern Avalonia). *Proceedings of the Geologists' Association,* 103(1), pp31-35.

Torsvik T. H., Van der Voo R., Preeden U., Mac Niocaill C., Steinberger B., Doubrovine P. V., Van Hinsbergen D. J.J., Domeier M., Gaina C., Tohver E., Meert J. G., McCausland P. J.A., Cocks L. R. M. 2012. Phanerozoic polar wander, palaeogeography and dynamics. *Earth-Science Reviews*, 114(3-4), pp325-368

Travé, A., Labaume, P., Calvet, F., Soler, A., Tritlla, J., Buatier, M., Potdevin, J.L., Séguret, M., Raynaud, S. and Briqueu, L., 1998. Fluid migration during Eocene thrust emplacement in the south Pyrenean foreland basin (Spain): an integrated structural, mineralogical and geochemical approach. *Geological Society, London, Special Publications*, 134(1), pp163-188.

Underwood, C.J., 1994. Faunal transport within event horizons in the British Upper Silurian. *Geological Magazine*, 131(04), pp485-498.

Van der Pluijm, B.A., Ho, N.C. and Peacor, D.R., 1994. High-resolution X-ray texture goniometry. *Journal of Structural Geology*, 16(7), pp1029-1032.

Veloso, E.E., Anma, R., Ota, T., Komiya, T., Kagashima, S.I. and Yamazaki, T., 2007. Paleocurrent patterns of the sedimentary sequence of the Taitao ophiolite constrained by anisotropy of magnetic susceptibility and paleomagnetic analyses. *Sedimentary Geology*, 201(3), pp446-460.

Ver Straeten, C.A., Brett, C.E. and Sageman, B.B., 2011. Mudrock sequence stratigraphy: a multi-proxy (sedimentological, paleobiological and geochemical) approach, Devonian Appalachian Basin. *Palaeogeography, Palaeoclimatology, Palaeoecology,* 304(1), pp54-73.

Wignall, P.B., 1991. Model for transgressive black shales?. *Geology*, 19(2), pp167-170.

Wignall, P.B. and Newton, R., 2001. Black shales on the basin margin: a model based on examples from the Upper Jurassic of the Boulonnais, northern France. *Sedimentary Geology*, 144(3), pp335-356.

Woodcock, N.H. and Gibbons, W., 1988. Is the Welsh Borderland Fault System a terrane boundary?. *Journal of the Geological Society*, 145(6), pp915-923.

Woodcock N. and Strachan R., 2000. (First edition) Geological History of Britain and Ireland. *Blackwell Publishing*. Oxford pp. 141-205

Wynn, R.B. and Stow, D.A., 2002. Classification and characterisation of deep-water sediment waves. *Marine Geology*, 192(1), pp7-22.

Ziegler, A.M., Cocks, L.R.M. and Bambach, R.K., 1968. The composition and structure of Lower Silurian marine communities. *Lethaia*, 1(1), pp1-27.

Zijderveld, J.D.A., 1967. AC demagnetization of rocks: analysis of results. *Methods in paleomagnetism*, 1, pp.254-286.

Appendix

Palaeomagnetic data

Ainsa Quarry

	Treatment	Intensity	TVRM	TVRM	TVRM	TVRM	Chrm	Chrm	Chrm	Chrm	
AQP	**Bedding corrected**		**Range**	**dec**	**inc**	**a95**	**Range**	**dec**	**inc**	**a95**	**Class**
11.1	0-350-80mt	0.13	nrm-200	297.2	63.6	10.4	250-20mt	238.8	-58.8	11.5	s2
12.5	0-350-80mt	0.33	100-250	311.6	40.1	19.1	20-60mt	188.5	-60.2	26.7	s2
13.1	0-350-80mt	0.15	nrm-200	357.5	74.1	9.2	350-phi	224.2	-37.6	12.6	s2
12.3	0-350-80mt	0.22	nrm-250	326.9	70.9	10.7	250-40mt	243.1	-43.5	7.9	s1
16.1	0-350-80mt	0.19	nrm-150	308	65.5	6.2	350-10mt	265.3	-45.9	32.4	s3
18.5	0-600	0.29	nrm-150	254.4	67.1	13.2	150-400	237	-53.6	8.3	s2
22.3	0-600	1.5	100-300	54.5	27.5	5.2	350-500	244.2	-27	13.6	s1

	Treatment	Intensity	TVRM	TVRM	TVRM	TVRM	planes	planes	planes	planes	
AQP	**Bedding corrected**		**Range**	**dec**	**inc**	**a95**	**Range**	**dec**	**inc**	**a95**	**class**
2.1	0-350-80mt	0.26	100-200	8.6	54	9.2	200-400	306.8	36	19.6	t2
2.4	0-350-80mt	0.26	100-150	348.9	59	3.7	10-phi	333.1	13.2	21.4	t2
3.2	0-600	0.13	100-200	8.6	54	18.4	0-400	303.3	8.2	18.4	t2
3.3	0-600	0.26	100-200	2.5	60.8	12.3	200-450	128.6	-17.2	13.1	t1
4.3	0-350-80mt	0.18	nrm-150	6	65.4	2.8	20mt-phi	234.7	35.7	13	t2

Appendix

4.4	0-350-80mt	0.2	nrm-250	21.3	68	4.5	250-420	204.8	32.4	14.3	t1
5.1	0-600	0.62	nrm-200	285.4	48.2	32.3	250-phi	149.2	10.6	7.9	t2
5.2	0-600	0.71	nrm-150	225.4	14.1	5.2	450-phi	225.4	14.1	5.2	t2
6.3	0-350-80mt		?				420-PHI	354.9	-6.3	17.9	t3
7.2	0-350-80mt	0.32	nrm-150	308.9	72.4	5.8	100-phi	177.2	16.1	15	t1
7.3	0-350-80mt	0.26	nrm-200	305.7	67.3	5.2	0-phi	173.7	11.7	6.7	t1
8.2	0-350-80mt	0.16	100-200	288.6	52.6	5.2	350-phi	329.5	-30	11.5	t2
8.4	0-350-80mt	0.27	100-200	308.4	55.5	5.4	350-phi	28.5	-66.2	16.6	t2
9.1	0-350-80mt	0.21	nrm-250	265.9	63.7	5.4	250-phi	146.5	-6.4	17.8	t2
9.2	0-350-80mt	0.55	nrm-250	260.4	76.6	4.3	350-380	277.6	12.7	6.2	t2
10.1	0-600	0.2	nrm-250	302.4	40.3	4.3	150-350	177.5	20.1	5.5	t2
10.3	0-600		nrm-300	224.9	21.6	8.4	360-420	98.1	-48.4	21.9	t3
11.4	0-350-80mt	0.0877	nrm-250	311.3	59.4	4.1	300-390	322.8	-5.4	14.1	t1
13.2	0-350-80mt	0.83	100-300	79.2	8.9	5.5	10-40mt	343.3	-42.1	24.8	t2
14.2	0-350-80mt	0.14	100-150	334.6	61.5	7.6	360-phi	350.2	-6.8	12.3	t2
16.2	0-350-80mt	0.11	nrm-150	323.9	63.2	3.6	300-380	228.6	56.3	19	t2
17.4	0-350-80mt	0.19	nrm-250	105.3	65.5	5.1	250-360	252.1	13.6	6.8	t3
18.3	0-600	0.23	100-250	5	78	12.9	300-phi	91.5	-31.2	18.3	t2
19.4	0-350-80mt	0.17					50-phi	55.6	18.4	23.3	t1
19.5	0-350-80mt	0.21	NRM-200	195.1	72.6	11.4	200-350	34	-36	18.5	t2
22.4	0-600	0.63	No TVRm				0-phi	314.5	47.3	27.4	t1
23.1	0-350-80mt	0.6	nrm-300	313.5	72.2	5.1	0-60mt	33.6	-3.1	10.1	t2
23.3	0-350-80mt	1.3	100-300	207	53.3	3.1	370-phi	125.3	21.7	19.6	t1

Appendix

Barranco Forcaz

	intensity	Treatment	TVRM	TVRM	TVRM	TVRM	Chrm	Chrm	Chrm	Chrm	
BFP			**Range**	**dec**	**inc**	**a95**	**Range**	**dec**	**inc**	**a95**	**Class**
1.2	0.28	0-350-80mt					10-40mt	265.5	-58.4	5	s1
2.5	0.29	0-350-80mt	nrm-200	272.3	74.2	5.2	250-450	234	-61.4	5.9	s1
4.2	0.32	0-350-80mt					250-30mt	251.8	-56.7	10	s1
6.1	0.27	0-350-80mt					350-500	226.6	-63.1	13.2	s1
7.1	0.36	0-350-80mt					250-70mt	233	-46.5	6.2	s1
8.2	0.3	0-350-80mt	NRM-300	260	68.9	5.1	30-50MT	212.9	-45.5	7.5	s2
9.1	0.32	0-350-80mt	NRM-250	281.4	75.6	11.9	350-70MT	199.1	-55.6	7	s2
10.1	0.41	0-350-80mt	NRM-200	266.7	55.8	8.8	20-40MT	217.8	-51.9	13.3	s2
10.3	0.11	0-350-80mt	NRM-250	350.3	69.4	2.6	40-50MT	200.8	-38	12.6	s2
11.3	0.33	0-350-80mt	nrm-250	285.7	35.6	18.5	350-50MT	230.4	-50.4	7	s1
12.1	0.37	0-350-80mt	NRM-200	263.6	62.8	7.2	10-50MT	213.5	-57.1	5.6	s1
18.1	0.34	0-600	nrm-250	315.4	77.8	4.1	250-350	254.6	-37.4	9.1	s2
22.1	0.48	0-350-80mt					10mt-60mt	237.8	-56	9.4	s1
22.2	0.67	0-350-80mt					200-60mt	217.8	-45.2	2.7	s2
24.4	0.8	0-350-80mt					10-50mt	201.2	-39.4	6.4	s1
25.4	0.49	0-350-80mt	100-250	287.6	86	6.1	300-350	212.1	-36.2	23.3	s3
28.1	0.2	0-350-80mt	nrm-200	311.9	74.6	15	200-20mt	261	-45.1	15.2	s2
31.2	0.15	0-350-40mt					350-40mt	203.9	-64.9	14.2	s1
35.5	0.14	0-350-80mt	nrm-200	262.6	68.9	8.2	350-40mt	216.5	-48.2	14.2	s3
39.3	0.26	0-350-80mt					10-40mt	220.4	-56.8	3.6	s1
42.4	0.45	0-350-80mt	nrm-200	212.5	68.1	4.6	300-10	248.6	-52.5	14	s2

Appendix

46.2	0.22	0-350-80mt	nrm-250	293.2	66.6	4.4	300-20mt	199.2	-67	22.8	s2

	intensity	Treatment	TVRM	TVRM	TVRM	TVRM	planes	planes	planes	planes	
BFP			**Range**	**dec**	**inc**	**a95**	**Range**	**dec**	**inc**	**a95**	**Class**
2.3	0.34	0-350-80mt	nrm-300	273.7	73.6	4.3	350-550	107.8	-14.6	12.9	t1
5.3	0.33	0-350-80mt					360-410	284.2	38.3	17.7	t2
13.2	0.31	0-350-80mt	NRM-200	14.1	69.8	4.3	200-PHI	267.1	-60.2	7.9	t3
14.2	0.43	0-350-80mt	100-250	61.4	60.2	3.7	390-phi	113.8	-33	12.5	t2
16.1	0.34	0-350-80mt	nrm-250	220.8	67	12.6	370-410	180.8	7.9	5.9	t1
17.1	0.45	0-350-80mt					360-400	229.5	39.4	26.9	t2
19.3	0.64	0-350-80mt	nrm-250	256.5	66.3	6.2	360-390	326.1	-36.2	16	t3
20.2	0.74	0-350-80mt	nrm-250	36.8	60.4	6.5	350-400	126.6	1.9	7.6	t2
21.2	0.17	0-350-80mt	100-250	100.4	54.6	8.9	250-390	46.3	-42.8	12.8	t3
24.1	0.58	0-350-80mt					350-400	102.5	-16.2	26	t1
26.1	0.37	0-350-80mt	200-10	312.2	2.8	7.6	350-400	303.9	58.4	6.5	t2
27.1	0.28	0-350-80mt	nrm-150	320	71.6	5.2	390-phi	139.4	14.9	28.2	t1
33.3	0.18	0-350-80mt	nrm-200	81.9	68.2	9	350-400	201.7	52.3	17.5	t2
33.5	0.64	0-350-80mt	100-300	260.1	8.9	5.6	350-410	45.2	67.7	11.2	t2
38.4	0.46	0-350-80mt	nrm-200	331.5	55.2	3.3	360-400	3.9	18	10.1	t2
42.5	0.47	0-350-80mt					350-400	285.5	-24.8	18.9	t2
43.4	0.71	0-350-80mt	nrm-250	241.3	32.3	8.9	370-400	57.2	-25.5	12.7	t2
45.3	1	0-350-80mt	nrm-250	227.4	61.5	6.8	250-390	122.6	26.3	14.1	t1
47.2	0.24	0-600					300-450	301.4	-4.3	27.2	t1
47.5	0.23	0-600					250-400	235.1	16.1	18.2	t1

Appendix

48.1	0.15	0-350-80mt	150-250	285.8	41.8	24.6	250-phi	76.6	-36.7	18.5	t2
48.5	0.21	0-350-80mt	nrm-200	68.1	62.7	6	360-390	230.4	15.7	33.7	t2

Marcellus Shale - Borehole A

			TVRM	**TVRM**	**TVRM**	**TVRM**	**Kiaman**	**Kiaman**	**Kiaman**	**Kiaman**	**Kiaman**	**Intermediates**			**Polarity**
sample	NRM Intensity	Range	dec	inc	a95	Range	dec	inc	a95	Rho		dec	inc	a95	
2	0.23	0-200	268	57	5.8	225-255	104	-25	30	0.6	205-225	75	76	19	N
5	0.15	0-225	299.3	69.4	6.8	225-275	51.2	47.8	14.9	0.8					
6	0.553		250	30			40	-21				287	19		K
7b	0.284	0-205	286	69	15					1					N
8	0.11	0-220	241	74.8	7.3	220-280	66.6	7.6	10.3	0.75					
9	0.84	100-225	319	80	3	225-265	111	2	16	1					N??
10	0.13	0-205	200	60.7	6.4	205-245	318	66.5	12.6	2					
11	0.056	0-225	245	62						1.2					weak and scattered
12	0.1	0-200	178	39	40	235-@	326	-4	27	1.1	205-225	50	75	27	K
13	0.3889	0-210	43	81	4						210-265	96	-19	6	N
14	0.092	0-205	175	74	11	235-295	281	19	24		215-235?	17	-41	27	N?
16a	0.316		303	73			140	-12				160	37		R??
16b	0.08	0-205	24.3	49.6	4.7	215-280	197	10.4	6	1.3	205-215	187	74.6	26.9	
17	0.075	0-210	303	64	21	210-255	102	-37	20						too scattered
18	0.086	0-215	344	78	21					0.8					R?
19a	0.104	210-235	42	55	19	275-@	181	-45	23	0.8					K
19b	0.694		291	78								111	58		R
20	0.072	0-200	314.5	43.9	6	215-@	106.4	52	7.5	1.2		127.2	0.9	28.2	
21															
22a	0.076	0-215	126.6	74.3	12.2	235-@	77.8	-2.4	17	0.5	215-235	346.6	-3.9	37.4	

Appendix

23	0.073	0-210	101.9	67.7	5.6	210-@	252.5	19.8	8.2	1.4					
24															
26	0.11	0-205	49	57	6					1.2	205-215	264	88	13	R
27b	0.075	0-210	356.4	70	17.5	210-@	15.1	11	9.6	0.5					
28	0.121	0-210	328.8	70.8	3.2	210-@	121.5	-10.9	3.5	1					
29a	0.502	100-210	146.6	65.8	7.4	210-@	309.2	-6.2	1.9	1.2					
B2h_30	0.406		330	66											R
B2h_31	0.343		332	60			104	-40							K
32															
b2h_33	0.313		175	67			326	-7				334	25		K
b2h_38	0.1029	0-200	348	60	35	285-@	258	-19	28	0.8	200-275	251	62	17	K

Marcellus Shale – Borehole B

		TVRM	**TVRM**	**TVRM**	**TVRM**	**Kiaman**	**Kiaman**	**Kiaman**	**Kiaman**		**Intermediates**			
sample	NRM Intensity	Range	dec	inc	a95	Range	dec	inc	a95		dec	inc	a95	
1	0.2	0-200	107.6	30.5	4.6	210-@	284.6	57.9	4.4	200-210	78.9	55.3	17	
3	0.268	0-210	147.4	78.9	4.4	210-@	0.9	28	4.2					
4	0.333	0-210	129	80.9	4.8	210-@	24.1	21.2	4.6					
6	0.499	0-215	215.7	79.4	3.8	260-@	348.8	11.2	23	215-235	351.8	22.4	27.7	
8	0.728	0-200	105.4	63.4	9.2	200-@	350.1	7.4	2.7					
10	0.243	100-200	100	72.4	5.5	220-240	243.1	14.1	19.5	200-220	211.8	77.1	4.8	
11	0.241	0-210	190.5	78.9	3.3	250-@	33.4	9.6	16	210-250	63	33.9	18.9	
13	0.442	0-200	33.7	77.3	4.6	210-@	217.3	18.5	8.8	200-210	146.2	79	20.2	
14	0.316	0-210	256.9	75.2	4.1	210-@	47.6	9.3	6.9					
16	0.389	0-210	153.2	79.8	5.1	210-@	35.2	5.8	3					

Appendix

Bedding and AMS data

Ainsa Quarry

Sample	Field Strike	Field Dip	Bedding strike	Bedding dip	Km	P	T	B1-Dec	B1-inc	B2-Dec	B2-Inc	B3-Dec	B3-inc
Ainsa Roadside													
ar1	168	38	166	22	123	1.034	0.193	353.3	1.9	84	2.9	222.9	85
ar2	158	45	166	22	132	1.024	0.473	345.7	3.2	82.4	42.9	252.4	44.3
ar3	139	23	166	22	108	1.021	0.386	115.1	4.1	24.2	7.2	258.8	83.1
ar4	136	13	159	23	65.3	1.027	0.884	43	11.2	133.8	3.9	242.7	78.1
ar5	164	30	159	23	69.2	1.014	0.427	51.6	2.9	321.3	6.7	165.2	82.7
ar6	149	10	159	23	64.6	1.011	-0.139	46.9	18.1	141.4	12.7	263.4	67.2
ar7	336	74	159	23	104	1.004	-0.597	235.9	3.6	326.6	11.6	109.1	80.6
ar8			159	23									
ar9	162	29	159	23	101	1.016	0.748	58.1	3.4	327.7	6.4	175.5	82.8
ar10	341	37	159	23	61.5	1.018	-0.71	58.8	52.2	244.6	38.1	152.3	2.4
ar11	162	29	159	23	127	1.053	0.952	6.3	1.7	276.1	3.6	119.2	86.2
ar12	212	15	159	23	118	1.039	0.927	314.9	5.7	45.5	8.6	192.1	79.8
Ainsa Quarry													
2	220	32	160	20	46.1	1.03	0.288	331.4	14.1	243.3	2.9	144.5	78.7
90	272	72	176	26	59.3	1.007	0.478	22.2	9.9	305	36.8	246.2	76.4
91	332	53	176	26	92.3	1.004	0.703	73.6	11.5	287.9	31.5	267.9	78.1
3	172	32	160	20	59.3	1.014	0.8	222.2	7.4	312.7	4.5	74.2	81.4
92	330	54	176	26	75	1.016	0.603	78.6	16.6	344.9	19.3	266	73.2

Appendix

93	76	11	176	26	53.8	1.032	0.784	270.5	6.1	88.6	31.1	180.7	-2.2
4	170	25	160	20	54.2	1.018	0.383	249.3	6.9	340.5	8.6	120.8	79
95	244	76	176	26	65.5	1.016	0.847	34.4	10.1	309.1	24.1	273.8	70.8
94	162	24	176	26	89	1.016	0.616	129.4	9.6	213.5	26.9	267.1	77.1
5	138	22	160	20	65	1.016	0.845	52.9	11.3	144.7	8.7	271.1	75.6
6	158	21	160	20	60.6	1.014	0.945	52.5	3.2	142.9	6.7	297.2	82.6
7	150	19	160	20	61.9	1.015	0.625	123.6	4.1	34.1	1.1	280.3	85.4
8	170	06	160	20	75.5	1.02	0.202	1.6	5.8	271.1	4.4	144.6	82.7
9	190	20	160	20	79.3	1.014	0.59	342.8	2.4	73.1	6.1	234.4	83.6
10	120	20	160	20	80.7	1.019	0.813	38.8	1	129.5	37.8	307.5	52.2
11	122	24	160	20	53.3	1.022	0.864	60.9	11	151.1	0.5	243.5	79.1
12	160	15	160	20	76.7	1.02	0.79	59.6	9.2	329.1	2.8	222.7	80.3
13	168	20	156	21	84.1	1.017	0.715	201.9	6.4	111.8	1.4	8.5	83.5
14	226	10	156	21	82.2	1.028	0.622	312.7	4.4	44.4	21.1	211.4	68.5
15	160	21	156	21	67.2	1.013	0.655	172.9	3	82.9	0.8	339.6	86.9
16	156	18	156	21	65.5	1.017	0.55	119.6	5.1	29.3	4.5	258	83.2
17	136	21	156	21	85.5	1.02	0.6	144	13.8	238.4	17.6	17.8	67.3
18	164	17	156	21	96.9	1.013	0.556	306.2	6.2	216.1	0.2	124.2	83.8
19	200	21	156	21	80.3			29.2	19.6	294.9	11.5	176	67
20	172	15	156	21	39.1	1.012	-0.184	354.6	2.7	85.5	2	219.3	86.9
21	182	25	156	21	49.4	1.019	0.4	312.7	8.6	43.4	4.4	160.7	80.3
22	138	20	156	21	59.4	1.016	0.894	130.1	11	153.7	10.2	342.2	79.7
23	130	26	156	21	50.6	1.005	-0.257	112.2	15.8	204.2	6.6	316.2	72.8
Ainsa Interfan-shales I													

Appendix

50-52	n/a	n/a	160	21	135	1.066	0.922	358.6	0.3	268.3	1.6	79.3	87.5
53	294	56	160	21	105	1.029	0.597	99.2	19.9	6.7	7.6	258.4	68.8
54	284	49	160	21	125	1.026	0.713	53.8	14.4	148.5	21.9	287	63.7
56	164	16	160	21	112	1.041	0.823	110.2	20.5	200.3	1.3	294	69.3
57	230	16	160	21	109	1.043	0.728	113.9	16.9	22.1	5.1	275.5	72.2
58	216	22	160	21	119	1.026	0.924	73	12.1	341.8	13.5	220.2	77.8
60	202	16	160	21	131	1.021	0.655	0.1	10.2	89.9	1.8	202.5	79.4
62	141	19	141	19	126	1.037	0.702	353.5	14.9	84.6	6.2	200.8	75.8
63	236	12	141	19	169	1.038	0.717	101.2	9.9	191.4	1.7	290.2	79.8
64	268	18	141	19	109	1.035	0.572	25.3	25.8	300.3	4.1	201.8	64.4
65	278	10	141	19	128	1.038	0.878	73.7	16.3	164.1	1.5	255.9	74.2
80	340	27	176	20	128	1.052	0.699	118.2	19.5	23.3	13.5	261.3	65.9
81	12	60	176	20	137	1.048	0.718	122.1	18.9	35.2	1.3	298.6	71.5
82	228	28	176	20	93.9	1.024	-0.06	289.3	1.4	199.5	15	17.5	76.1
83	53	72	176	20	112	1.023	0.303	98.7	9	6.2	14.9	219.6	72.3
84	182	71	153	22	146	1.03	0.305	297	7.4	201.5	33.6	38.5	55
85	206	26	153	22	145	1.045	0.708	129.3	7.4	37.2	10.5	254.9	77
86	297	15	153	22	124	1.059	0.805	125	12.1	32.8	10.3	261.8	74.2

Appendix

Barranco Forcaz

Sample	Field strike	Field dip	Bedding strike	Bedding dip	Km	P	T	B1-Dec	B1-inc	B2-Dec	B2-Inc	B3-Dec	B3-inc
1	109	20	134	30	76.6	1.021	0.505	357.7	9.7	88.6	5.2	206.4	78.9
2	138	30	134	30	79.5	1.009	0.237	328.5	9.2	103.2	10.3	234.5	79.5
4	148	32	134	30	74.5	1.003	0.006	319.8	6.3	59.6	57.1	225.8	32.1
5	156	30	134	30	85.2	1.015	0.409	10.5	17.7	102.7	6.8	213.1	70.8
6	136	33	134	30	61.6	1.018	0.676	324.7	4.3	55.3	7.5	205.2	81.4
7	130	27	134	30	79.9	1.01	-0.101	311.9	8.8	44.3	15.7	193.6	71.9
8	136	31	134	30	74.9	1.017	0.621	141.5	12.4	50.1	6.4	292.9	76
9	098	28	134	30	88.9	1.022	0.301	97	39.1	196.4	11.6	299.7	48.6
10	138	20	134	30	67.3	1.012	0.536	135	4.9	41.2	37.6	231.2	51.9
11	119	30	134	30	57.8	1.02	0.38	144.5	5.8	53.8	8.2	273.3	79.6
12	112	35	134	30	82.1	1.018	0.779	147.7	24	239.9	4.3	339.1	66.1
13	142	25	134	30	61.6	1.005	0.066	59.8	1.6	150.3	15.6	324.4	74.3
14	140	35	134	30	68.6	1.026	0.687	290.5	1.6	20.6	1.9	160.2	87.6
15	139	37	137	30	89.1	1.015	0.376	138	3.3	228.1	1.5	342.9	86.4
16	149	30	137	30	47.3	1.014	0.455	302.4	1.2	32.7	13.2	207	76.8
17	090	26	137	30	74.1	1.006	0.492	124.1	25.9	29	10.3	278.9	61.8
18	120	24	137	30	80	1.006	0.552	141.2	1.9	50.7	16.6	237.5	73.2
19	119	26	137	30	83.3	1.013	0.222	121.3	31.6	30.3	1.4	297.9	58.4
20	148	26	137	30	59.2	1.019	0.563	320	9	229.8	3.1	121.1	80.4
21	150	26	137	30	51.6	1.011	-0.189	100.5	11.7	192.9	12.1	327.7	72.3
22	134	30	137	30	100	1.004	0.895	323.4	2.4	54.3	17.6	225.6	72.2

Appendix

23	148	28	137	30	93.5	1.005	0.885	143.2	9.5	52.6	3.6	301.9	79.9
24	113	29	137	30	101	1.034	0.727	118.6	10.3	208.8	1.2	305.1	79.5
25	189	27	137	30	93	1.005	-0.196	32.3	4.2	122.4	0.7	218.2	85.7
26	126	27	137	30	102	1.003	-0.417	37.9	36.8	186.2	49.7	294.8	14.6
27	152	40	137	30	98.9	1.006	0.149	38.1	13.9	143.6	47.2	296.3	39.6
28	146	26	137	30	87	1.008	0.514	325.5	9.3	57.6	12.5	200	74.3
30	158	27	141	32	89	1.008	0.74	150.5	3	60.4	2.6	288.7	85.9
31	160	36	141	32	44.2	1.018	0.408	310.2	14.5	40.9	3.9	143.4	75.1
32	168	32	141	32	102	1.009	0.433	310.4	15.2	43.3	10.1	166	71.6
33	180	35	141	32	84.6	1.006	-0.316	341.3	5.3	250.1	13.7	92	75.4
34	340	24	141	32	102	1.004	0.111	265	58.4	7.4	7.7	101.9	30.4
35	184	20	141	32	105	1.004	0.006	127.1	67.7	235.3	7.2	328.1	20.8
37	140	21	141	32	69.1	1.002	-0.612	131.4	34.2	276.6	50.3	28.9	17.5
38	120	24	141	32	76.5	1.012	0.747	127	13.9	35.2	7.3	278.4	74.3
39	120	25	141	32	60.4	1.009	0.748	60.5	11.2	152.3	8.8	279.6	75.7
41	154	30	141	32	95.7	1.006	0.789	293.7	24.6	32.1	17.6	154	59.1
42	138	40	141	32	76.1	1.004	0.835	75.5	14.1	341.8	13.8	209.2	70.1
43	130	26	141	32	80	1.011	0.366	49.9	7.4	142.2	17.4	297.6	71
44	138	36	141	32	103			146.4	6.9	236.8	3.5	353.2	82.3
45	119	38	141	32	103	1.007	0.086	129.9	10.4	225.8	31.2	21.6	56.4
46	142	30	141	32	70.3	1.004	-0.097	337.4	20.7	82.7	54.4	245.3	33
47	100	22	141	32	95.2	1.007	0.622	170.8	26.9	68.4	22.8	304.1	53.4
48	152	40	141	32	74.5	1.005	-0.437	130.3	3.6	38.5	25.5	227.8	64.2
60	264	11	140	29	112	1.049	0.476	45.8	2.2	312.1	65.1	137	24.9

61	272	36	148	25	119	1.024	-0.429	34.2	14.2	128.1	20.1	270.2	65.3
62	136	41	148	25	115	1.012	0.197	354.4	6.7	263.4	6.7	130.4	80.7
63	98	23	148	25	122	1.027	0.602	38.5	6.4	128.9	7.1	255.3	82
64	104	10	146	26	143	1.039	0.6	202.4	3.2	292.7	2.6	42.7	86.4
68	138	32	146	26	116	1.019	0.49	0.7	12.4	93.5	11.3	224.7	73.1
69	132	28	142	22	121	1.017	0.501	4.2	12	98.1	17.3	241.6	68.4
70	136	31	142	22	93.9	1.021	0.459	350.8	12.7	84.6	16.3	225.1	68.8
71	140	27	146	22	108	1.026	0.624	3.3	10.6	95.5	13	234.8	73
72	148	31	148	29	106	1.017	0.391	356.3	15.5	92.8	21	231.5	63.4
73	156	34	156	23	102	1.005	-0.478	36.6	25.2	127.5	1.3	219.1	64.4
88	142	29	132	22	124	1.016	0.336	359.9	8	91.4	10.5	234.1	76.8
89	128	31	132	22	143	1.029	0.751	320.4	10.6	54.1	18.5	201.8	68.4
90	146	22	132	22	88.2	1.023	0.464	0	12	92.3	9.2	217.7	74.3

Welsh borderlands

Hillend Farm

Spec	Field strike	Field dip	Bedding strike	Bedding-dip	Km	P	T	B1-Dec	B1-Inc	B2-Dec	B2-Inc	B3-Dec	B3-Inc
HEF1.2	40	14	53	20	240.1	1.009	-0.226	223.4	2.9	133.2	8.3	332.2	80.9
HEF2.2	130	14	53	20	374.7	1.092	0.543	54.6	1.5	325	6	156.4	83.8
HEF3.3	35	13	53	20	258.6	1.097	0.602	49	3.6	139.3	3	267.6	85.3
HEF5.1	50	20	50	20	297.1	1.087	0.557	227.9	5.6	137.2	3	24	84.4
HEF5.3	50	20	50	20	259.8	1.088	0.563	48	9	139	6	259	79
HEF6.3	55	20	50	20	333.9	1.083	0.534	229.7	9.5	139.1	5	23.8	79.9
HEF7.2	39	10	39	10	299.2	1.101	0.708	337	0.1	67	10	246.9	80
HEF10.1	60	15	55	15	279.7	1.09	0.967	194.8	6.9	103.7	6.1	332	81

HEF10.2	60	15	55	15	342.3	1.119	0.675	59.2	4.1	328.9	2	213.9	85.4
HEF10.3	60	15	55	15	431.3	1.12	0.668	56.5	1.7	146.9	1	264	88.1
HEF11.1	90	55	55	21	295.9	1.086	0.351	228.2	32.5	126.5	17.7	12.9	51.9
HEF12.2	70	25	55	21	255.1	1.092	0.42	221.8	1.8	131.8	1.6	1.4	87.6
HEF12.3	70	25	55	21	298.9	1.096	0.35	225.8	1.7	135.9	0.2	51.7	88.8
HEF13.2	55	21	55	21	263.4	1.086	0.568	47	2.9	317	4	177.3	85
HEF14.3	75	13	55	21	314	1.101	0.62	246.9	2.4	157	1.5	33.4	87.6
HEF15.2	67	21	67	21	320.3	1.097	0.598	62	3	152	7	310	83
HEF15.3	67	21	67	21	312.9	1.099	0.6	56	2	146	2	294.1	87
HEF16.2	71	20	71	20	314.9	1.091	0.629	42	4	132	1	234	86
HEF17.2	89	21	69	21	307.5	1.096	0.518	227.7	3.1	317.8	2.6	97	86.5
HEF19.2	95	76	69	21	328.6	1.096	0.59	262.3	15.7	152.2	49.3	4	35.4
HEF42.2	90	45	90	45	98.51	1.012	0.767	85.8	2.8	176.1	17.2	345.1	72.5
HEF43.2	54	34	54	34	112.5	1.002	0.801	346.5	41.1	81.4	6	178.1	48.3
HEF43.3	54	34	54	34	126.5	1.005	0.042	42	12.8	134.7	11.6	264.9	72.8

Buttington Quarry

Spec	Field strike	Field dip	Bedding strike	Bedding dip	Km	P	T	B1-Dec	B1-Inc	B2-Dec	B2-Inc	B3-Dec	B3-Inc
BQ2A	2	17	51	86	135	1.003	0.44	175	7.8	75	51.2	271.4	37.7
BQ2B	2	17	51	86	145.3	1.009	0.152	298.1	58.4	103.6	30.3	197.2	6.4
BQ2C	2	17	51	86	124	1.005	-0.692	155.9	20.5	42.4	46.5	261	36.7
BQ4A	0	0	51	86	193.2	1.007	-0.177	134.8	80.9	320.8	9	231	1
BQ4B	0	0	51	86	190.2	1.016	0.543	132	17.3	224.4	6.4	336.3	71.3
BQ10A	102	10	51	86	385.8	1.024	0.419	233.1	0.9	143.3	8.5	327.3	80.9
BQ10B	102	10	51	86	420.3	1.029	0.411	45.6	5.6	315.4	1.8	208.9	84.6
BQ10C	102	10	51	86	386.3	1.024	0.074	222.4	6.5	132.1	5.7	356.6	81.4
Minor Fault													
BQ13C	40	5	50	85	114.8	1.016	0.429	179	10.2	86.8	12.6	306	73.5

BQ14A	85	10	50	85	172.4	1.018	0.729	197.9	18.7	105.9	5.3	0.8	70.2
BQ14B	85	10	50	85	165.5	1.016	0.68	200.4	24.2	108.9	3.8	11.1	64.5
BQ15B	338	34	50	85	209.2	1.005	0.329	194.1	22.5	286.9	6.6	33.6	66
BQ15C	338	34	50	85	266.8	1.007	0.107	178	2.7	269.2	14.5	77.7	74.5
BQ16B	58	90	50	85	489.8	1.034	0.592	219.5	6.8	128	10.1	340	78.3
BQ17A	50	90	50	85	219.4	1.089	0.755	213.2	3.4	122.3	9.1	320	80
BQ17C	50	90	50	85	224.6	1.095	0.767	205.2	3.9	115.1	8.7	320	80
BQ18A	50	78	50	85	314.2	1.009	-0.295	195.2	13.5	287.1	7.1	46.8	75
BQ18B	50	78	50	85	381	1.009	0.202	186.9	0.5	76.8	87.8	276.6	2.6
Minor Fault													
BQ19.2	69	69	63	83	196.1	1.031	0.826	267.9	10	358.8	6.4	119.3	77.9
BQ21.2	64	80	64	80	366.4	1.104	0.931	221	2.1	130.6	3.9	334	86
BQ26.1	346	27	67	75	312.7	1.082	0.854	8.1	49.4	174.2	39.8	270.1	7.5
BQ26.3	346	27	67	75	308.6	1.082	0.884	14.9	53.7	174.1	34.7	271.1	10.2
BQ27B	325	41	67	75	406	1.088	0.894	55.8	3.1	146.6	8.6	310.4	81.1
BQ28.2	22	17	67	75	352.6	1.096	0.92	250.2	11.6	160.1	2.4	58.7	78.2
BQ28.3	22	17	67	75	354	1.094	0.968	250.8	6.2	340.8	0.5	76.4	83.2
BQ30A	80	68	67	75	307.8	1.063	0.862	205.5	7.8	295.9	4.2	55.2	81
BQ30B	80	68	67	75	353.3	1.064	0.942	213.9	8.3	304.6	5.4	68.3	80.3
BQ30C	80	68	67	75	329.8	1.064	0.898	208.6	7.9	299.8	10.9	81.5	76.2
BQ31B	82	75	67	75	339.1	1.061	0.877	220.7	16.7	312.9	6.3	62.7	72.4
BQ31C	82	75	67	75	359.2	1.061	0.9	235.6	17	326.7	3.3	69.3	72.6
BQ32.1	173	71	67	75	327.8	1.082	0.792	207.7	64.1	106.1	4.8	14.4	24.8
BQ33.2	320	41	67	75	342.8	1.072	0.895	359.9	1.4	89.7	4	246.5	86.1
BQ34A	74	78	67	75	369.3	1.107	0.93	233.7	4.5	143.4	6.2	0.1	82.4
BQ34B	74	78	67	75	358.2	1.1	0.924	226.3	8.3	135.8	5.2	14	80.1
BQ34C	74	78	67	75	385.1	1.088	0.944	217.2	9.3	126.3	4.5	10.8	79.2
BQ36.1	70	76	67	75	295.4	1.087	0.861	87.3	1.4	177.6	9.1	349.5	80.8
BQ44.2	327	85	69	81	316.5	1.092	0.756	251.9	11.7	345.1	17.3	130.4	69.2

BQ46.1	69	81	69	81	309.4	1.11	0.955	43.5	0.7	313.6	0.4	23.6	90
BQ47.2	70	87	69	81	246.6	1.1	0.898	192.8	3.6	102.3	0.7	357.4	86.8
BQ50.1	188	37	69	81	355	1.064	0.127	305.1	18	204.3	29.3	61.4	54.7
BQ63.3	72	84	64	85	367.9	1.06	0.741	191.6	13.1	283	5.5	34	76.1
BQ65.2	72	12	64	85	237.9	1.098	0.949	257.1	38.7	36.4	43.4	148.7	22.3
BQ72.3	80	72	80	72	278.4	1.066	0.757	63	12	153	0.8	248.7	77.6
BQ74.3	170	-27	80	72	234.8	1.087	0.938	168.2	21.6	258.7	2.5	355.3	67.9
BQ75.3	80	90	80	72	374.3	1.08	0.809	257.1	0.9	167.2	19.4	350	70
BQ76.1	160	75	80	72	284.5	1.086	0.963	337.4	57.3	176.3	31.9	80.4	8.5
BQ77.3	90	85	80	72	316.5	1.126	0.957	264.4	7	171.6	19.4	13.3	69.4
BQ78.3	70	60	80	72	293.9	1.084	0.968	100.5	8.4	9.8	2.1	265.3	81.4
BQ80.2	64	88	80	72	262.1	1.069	0.812	225.1	2.8	134.1	24.3	320.6	65
BQ85.1	308	41	80	72	355.9	1.112	0.957	86.8	15.6	177.7	3.9	283.7	73.9
BQ85.2	308	41	80	72	327.5	1.112	0.949	47.5	9.4	139.9	14.7	285.1	72.6
BQ90.3	85	48	85	48	313.5	1.129	0.966	289.5	1.4	199.2	3.7	52.8	86.4

Eaton Trackway

Spec	**Field strike**	**Field dip**	**Bedding strike**	**Bedding Dip**	**Km**	**P**	**T**	**B1-Dec**	**B1-Inc**	**B2-Dec**	**B2-Inc**	**B3-Dec**	**B3-Inc**
ET1.1	226	15	12	11	241.6	1.059	0.849	265.1	3.5	175.2	8	18.6	81.6
ET1.3	226	15	12	11	243.1	1.058	0.872	264	5.5	173.1	8.6	27	79.6
ET7.3	298	11	65	8	240.9	1.05	0.827	275.1	1	5	3.9	177.2	86.6
ET8.2	63	8	65	8	187.1	1.048	0.849	252.8	2.1	161.8	6.1	3.9	83.5
ET15.1	291	9	306	12	181.2	1.047	0.733	76.3	0.9	166.2	2.7	334.5	87.4
ET19.3	118	36	38	11	227.4	1.063	0.947	121.8	26.1	317.5	62.9	214.7	6.5
ET21.2	36	11	38	11	211.2	1.044	0.802	263.4	0.8	353.7	1.7	149	87.8
ET23.1	33	15	42	13	191.1	1.049	0.859	268.2	3.4	359.1	4.9	142.2	83.8
ET27.1	58	20	60	20	156.2	1.054	0.876	71.1	1.3	340.9	7.6	170.3	82.2
ET27.4	58	20	60	20	148	1.053	0.846	71.8	3.2	341.8	6.6	187.7	82.9

ET27.5	58	20	60	20	170.9	1.053	0.849	67.7	3.6	338	9.8	178.5	79.8
ET29.1	45	18	45	18	170.6	1.053	0.834	55.1	2	325	8.7	162	81.4
ET29.1	45	18	45	18	150.5	1.056	0.883	255.9	1.2	345.8	0.4	81	88.2
ET29.2	45	18	45	18	147.1	1.053	0.866	255.9	1.2	346.1	2.4	135	88
ET29.4	45	18	45	18	153.1	1.056	0.887	245.3	2.2	155	0.1	71.4	87.4
ET29.5	45	18	45	18	166.3	1.057	0.888	257.1	4.6	348	2	103	85
ET3.2	328	13	12	11	198.3	1.03	-0.644	26.7	17.5	295	5.7	187.9	72.4
ET31.2	150	6	40	8	100.6	1.007	0.72	111.3	2.4	201.6	1.5	327.9	86.9
ET33.2	40	8	40	8	101.2	1.012	0.574	67.6	3.3	158.2	9	317.1	80
ET33.4	40	8	40	8	105.2	1.019	0.619	75.3	0.4	165.1	7.5	344.4	82.3
ET35.1	235	10	60	10	97.76	1.018	0.559	85.8	2.7	355.7	1	233.1	87.6
ET35.2	235	10	60	10	94.7	1.023	0.91	68.8	9.6	338	4.9	222.2	79.6
ET37.2	62	6	60	10	99.18	1.023	0.605	256.9	1.9	167.3	8.5	358.2	80.4
ET37.3	62	6	60	10	99.34	1.024	0.652	257.9	2.1	167.2	9.5	358.2	80.4
ET37.4	62	6	60	10	109.3	1.023	0.689	237.5	2.6	148.1	6	353.1	83.7
ET39.2	72	14	52	7	112.1	1.019	0.733	257.1	1	166.9	16.7	349.9	73.4
ET39.4	72	14	52	7	102.4	1.028	0.813	69.2	9	339	2.7	231.7	80.2
ET39.4	72	14	52	7	97.69	1.029	0.784	75.7	13.3	345.1	4.4	235.7	76
ET41.3	314	7	52	7	97.53	1.023	0.597	86.9	7	177.7	1.3	273.3	82.7
ET41.4	314	7	52	7	101.9	1.026	0.759	101.8	6.7	191.5	3.5	312.1	82.9
ET43.1	176	7	52	7	108.7	1.031	0.721	273	2.6	3.1	4.3	151.9	84.7
ET43.3	176	7	52	7	110.3	1.03	0.625	254.1	0.6	163.8	0.5	54	89.5
ET43.4	176	7	52	7	101.6	1.031	0.853	250	1.2	159.9	0.3	56	89
ET45.3	90	3	37	6	92.55	1.021	0.872	274.1	1	184.6	2.8	13.3	86.6
ET45.4	90	3	37	6	91.17	1.018	0.635	235	0.9	144.8	4.3	333.5	85.7
ET47.3	40	8	40	8	185.5	1.051	0.873	79.5	1.9	169.5	2.8	318.9	86
ET51.3	50	13	70	7	88.18	1.029	0.726	66.9	7.4	159	14	308.8	74.3
ET51.4	50	13	70	7	89.81	1.03	0.741	63.9	7.8	156.2	16	307.8	71.2
ET51.5	50	13	70	7	88.84	1.031	0.668	79.2	17	173.5	13.2	301.6	67.8

Appendix

Marcellus Shale – Borehole A

Spec	Depth (feet)	strike	dip	Km	P	T	Rotation angle	k1-Dec	k1-Inc	k2-Dec	k2-Inc	k3-Dec	k3-Inc
4	4909.75	0	90	168.2	1.065	0.902	76.5	77.5	1	167.5	1	290.5	89
5	4913.25	0	90	117.1	1.073	0.786	87.25	237.25	8	147.25	3	35.25	81
6	4915.75	0	90	187.7	1.134	0.878	117.5	265.5	13	170.5	18	30.5	68
7A	4918.65	0	90	59.99	1.015	0.695							
7B	4918.65	0	90	134.9	1.054	0.814	354	328	3	237	7	84	82
8	4921.55	0	90	83.38	1.12	0.911	109	48	2	318	7	150	82
9	4925.3	0	90	113.1	1.009	0.51	47.5	261.5	6	353.5	17	154.5	72
10	4928.5	0	90	90.46	1.1	0.844	156.5	51.5	3	141.5	1	253.5	87
11	4931.25	0	90	125	1.146	0.897	171.5	253.5	7	343.5	2	86.5	83
12	4934.15	0	90	135.5	1.147	0.903	171.5	29.5	5	119.5	2	231.5	84
13	4938.65	0	90	128.5	1.123	0.861	317	179	13	272	12	41	72
14	4939.85	0	90	140.7	1.16	0.896	185	86	1	356	2	217	88
16A	4948.3	0	90	111.8	1.096	0.842	41	63	2	154	1	269	88
16B	4948.3	0	90	117.5	1.147	0.898	183.9	82.9	4	352.9	0	257.9	86
18	4954.95	0	90	164.2	1.142	0.917	16	42	3	132	1	244	87
19A	4957.65	0	90	171.6	1.162	0.921	318	356	2	87	5	243	84
20	4960.6	0	90	137	1.175	0.935	52	83	0	353	1	173	89
21	4963.6	0	90	162.4	1.128	0.958							
22A	4966.7	0	90	158.1	1.182	0.931	160	94	4	4	0	272	86
22B	4966.7	0	90	100.9	1.022	0.573							
23	4970.15	0	90	118.9	1.173	0.939	173	305	2	35	1	165	88
24	4972.75	0	90	130.6	1.145	0.925							
26	4979.65	0	90	138.1	1.127	0.879	311	57	4	147	2	259	86
27A	4980.6	0	90	91	1.132	0.888							
27B	4980.6	0	90	154.4	1.163	0.917	77	286	5	17	12	174	77
28	4982.1	0	90	140.8	1.143	0.908	37	24	6	294	1	194	84

29a	4989.1	0	90	37.47	1.107	0.875	179	31	1	121	2	264	88
29B	4989.1	0	90	106.9	1.173	0.934							
30	4992.05	0	90	73.1	1.043	0.889	30	229	2	319	4	116	85
31	4994.95	0	90	42.8	1.028	0.205							
31rpt	4994.95	0	90	42.37	1.03	0.146	44.5	49.5	3	140.5	6	296.5	83
32	4998.6	0	90	40.32	1.005	-0.281							
38	#N/A	0	90	128.5	1.125	0.902	93	207	2	297	2	77	87

Marcellus Shale – Borehole B

Spec	depth (feet)	strike	dip	Km	P	T	Rotation angle	k1-Dec	k1-Inc	k2-Dec	k2-Inc	k3-Dec	k3-Inc
1	6324.3	0	90	104.9	1.138	0.896	119.6	108.6	12	8.6	39	211.6	48
3	6330.65	0	90	102	1.105	0.907	164.1	24.1	9	116.1	9	250.1	77
4	6333.05	0	90	120.6	1.126	0.975	140.9	34.9	3	124.9	7	283.9	82
6	6339.9	0	90	92.87	1.09	0.941	183.8	347.8	4	256.8	11	100.8	79
8	6346.55	0	90	77.71	1.025	0.642	185.1	51.1	20	149.1	21	282.1	60
10	6352.2	0	90	79.81	1.114	0.943	78.1	172.1	2	262.1	5	58.1	85
11	6355.5	0	90	59.39	1.082	0.829	131.6	43.6	10	134.6	3	238.6	80
13	6360.85	0	90	50.23	1.046	0.482	52.3	279.3	5	9.3	0	105.3	85
14	6363.95	0	90	38.5	1.072	0.611	117.4	349.4	1	79.4	1	218.4	88
16	6369.85	0	90	49.23	1.08	0.845	129.8	31.8	20	122.8	4	222.8	70